ACTIVATION OF CARBON OXIDES: CHEMICAL REACTIONS AND TRANSFORMATIONS FACILITATED BY GROUPS 6, 7 & 8 METAL COMPLEXES

A Dissertation

by

SAMUEL JOHN KYRAN

Submitted to the Office of Graduate and Professional Studies of
Texas A&M University
in partial fulfillment of the requirements for the degree of

DOCTOR OF PHILOSOPHY

Chair of Committee,	Donald J. Darensbourg
Committee Members,	François P. Gabbaï
	Oleg V. Ozerov
	Jodie L. Lutkenhaus
Head of Department,	François P. Gabbaï

December 2015

Major Subject: Chemistry

ABSTRACT

Small molecules carbon dioxide and carbon monoxide produced *via* the oxidation and partial oxidation of carbonaceous matter, respectively, have distinct chemical functions and reactivity. A fairly stable species and a greenhouse gas, carbon dioxide has risen to an unprecedented level of 400 ppm in the atmosphere by the increased consumption of fossil fuels. To address this undesired accumulation of carbon dioxide, various solutions are being introduced and the utilization of carbon dioxide as a C1 feedstock in chemical synthesis can contribute towards this goal. The levels of carbon monoxide are unaffected as it is relatively short-lived in the atmosphere and is considered a temporary pollutant. High concentrations are toxic to humans due to its ability to displace oxygen from red blood cells. Nanomolar concentrations of carbon monoxide, however, are endogenously-produced and are beneficial to physiology due to its unexpected role as a regulatory molecule. Herein, results on various chemical transformations of carbon dioxide and studies on reactions involving carbon monoxide are presented.

A promising endeavor is the synthesis of polycarbonates from carbon dioxide and epoxides. The use of a naphthalene derived epoxide to produce poly(1,4-dihydronaphthalene carbonate) exhibiting high thermal transitions comparable to bisphenol-A polycarbonate is illustrated. Being a large monomer, employing traditional *tert*-butyl substituted (salen)Cr(III) catalysts show poor polymer selectivity, whereas the use of a planar tetraazaannulene bound Cr(III) catalyst is successful in chain propagation and subsequently displays higher activity. Fundamental studies on direct carboxylation of

hydrocarbons were also investigated. Carbon dioxide insertions into Ru-H and Ru-Me bonds proceed favorably at electron rich metal centers and the formation of an acetate is thermodynamically more stable when compared with formate formation. Bond dissociation energies of acrylates from ruthenium and iron complexes, prepared synthetically as model compounds of an ethylene and carbon dioxide coupled product, were measured through kinetic experiments. Ruthenium complexes show lower BDEs.

Rhenium and manganese carbonyls bound by a hemi-labile pyrrolyl carboxyaldehyde and a bulky diazabutadiene ligand, respectively, are evaluated as carbon monoxide releasing molecules. Additionally, a detailed mechanistic investigation on an unusual carbon monoxide reaction with a synthetic analogue of a biomimetic iron dinitrosyl complex is described.

ACKNOWLEDGEMENTS

You know what the Chinese philosopher, Confucius said about work? That if you enjoy what you do, you'd never work another day in your life. This has been absolutely the case over the past 5 years in Don's lab. I couldn't have asked for a better boss. Don gave me the freedom and opportunity to tackle a variety of projects and to learn to grow as a chemist. He certainly didn't stifle my corny jokes or antics either, of which there were plenty. I truly appreciate his genuine interest in his students and his wonderful ability to find humor in every situation.

I have met, interacted and made friends with many a colorful character who have made my graduate school experience quite lively. Two in particular stand out. Much like an older brother, Andrew, taught me to be curious about everything. He always listened and gave me sound advice as I mapped my way through an hurdle. And Joanna, my lab mate, motivates me to live a balanced life – be it getting up early for a run, be passionate about travel and eating (the latter of which she does a lot) or groan loudly to relieve stress.

Netflix – an exceptional entertainment platform which has helped me relax and pass many a dull night, and subscribing to which has been one of my best decisions. That, and fantastic books by Dolores Cannon, Brandon Sanderson, Brent Weeks to name a few.

Always supportive of whatever I chose to do is my wonderful family. Mom for making delicious food whenever I visited, dad for always making sure I was on top of things, Sally for being the best sister to goof around with and my spirit guides for walking with me on this journey, reminding me to take a deep breath and just be.

I can take up to four pages for my acknowledgement section, so how about a short story? Writing stories was something I began in graduate school. I'm sure it'd be alright including one here for you the reader. Why not? I'll add that I do acknowledge the below story for playing a small but integral part of my grad school experience. This way it won't make the cut by the Thesis Office review, eh? So without further ado, here is "The Lapse":

It was a tense evening in lab 43, as pouring rain battered the windows. Its insistent drumming only worsened the throbbing in his head. Andy was lost in silicon limbo. Search as he might his glaring screen, the transition state eluded him for the fifth time that day.

Separated by a wall, Joan was squeezing into her second sweater in lab 44. The darn ventilation system was blowing air straight from North Pole. Walking and tugging her sweater down around her midriffs, she stopped short in front of her hood. A string of loud curses escaped her lips. The mini pressure reactor was leaking again.

Fingers a blur over keyboard, narrowed eyes flitting across orbitals and energy profiles, Andy was jarred out of his trance by a loud clatter. He looked to his right and found his colleague, the troublesome one, standing by the tool drawer a few feet away. She had emptied it on the floor. And now she was walking away.

Where is that ugly wrench when you need it? wondered Joan. Rummaging through the tool drawer, it dawned on her that she had to pee, and quite badly so. The cold was making her body relieve its fluids to decrease the increasing blood pressure from the

constricted blood vessels. As she hurriedly stepped away, one of her sweaters snagged the handle, pulling the drawer all the way out, dropping it and all its contents. Picking them up will have to wait.

"Hey! You gonna pick those up?" asked Andy, frustrated at the sudden unwelcome disturbance.

"Later. Or maybe you can pick it up!" said Joan in a high cadence, as she hurried out looking for blessed relief.

"What? Girl! I will cut you!" exclaimed Andy in an outraged drawl. And then he flushed a bright red. His true ghetto slang had come unbidden at an unguarded moment.

In reality, those two were engaged in trimming some steel tubing for the reactors with a pipe cutter. So let's call it as loosely inspired by true events.

TABLE OF CONTENTS

Page

ABSTRACT ii

ACKNOWLEDGEMENTS iv

TABLE OF CONTENTS vii

LIST OF FIGURES ix

LIST OF TABLES xvi

CHAPTER I INTRODUCTION 1

CO_2 as Chemical Feedstock 2
Carbon Monoxide Chemistry 12

CHAPTER II A CARBON DIOXIDE COPOLYMERIZATION STUDY WITH A STERICALLY ENCUMBERING NAPHTHALENE DERIVED OXIDE 14

Introduction 14
Results and Discussion 17
Concluding Remarks 36
Experimental Section 38

CHAPTER III MODEL STUDIES ON THE DIRECT CARBOXYLATION OF HYDROCARBONS WITH CARBON DIOXIDE 46

CO_2 Insertion Reactions into Ru-Me and Ru-H Bonds 46
Acrylic Acid Derivatives of Iron and Ruthenium Carbonyls 71
Triphos Derivatives of Mo & W Carbonyls and Their Reactivity with Olefins 94

CHAPTER IV CARBON MONOXIDE INDUCED REDUCTIVE ELIMINATION OF DISULFIDE FROM DINITROSYL IRON COMPLEXES: A MECHANISTIC STUDY 108

Introduction 108
Results and Discussion 112
Concluding Remarks 125
Experimental Section 127

CHAPTER V CARBON MONOXIDE RELEASING MOLECULES (CORMS) 129

An Unusually Labile Rhenium Carbonyl Complex 130
Reactivity of a Bulky Diazabutadiene Manganese Carbonyl Complex.....144
Bis(cycloamine) Complexes of Molybdenum Carbonyls 151

CHAPTER VI CONCLUSIONS 163

REFERENCES.....168

LIST OF FIGURES

Page

Figure 1 The carbon cycle.[2] 2

Figure 2 Catalytic coupling of CO_2 and epoxide to provide poly- and cyclic carbonates. 3

Figure 3 (salen)$M^{III}X$ catalyst (left) with onium salt cocatalysts (right). Activity and selectivity of catalyst can be tuned by altering groups R, M and X. Typical M = Cr, Co while X = azide, chloride and 2,4-dinitrophenolate. 6

Figure 4 Acrylic acid formation from coupling of CO_2 and ethylene. 8

Figure 5 A long-lived CO_2 and ethylene coordinated intermediate observed in the formation of an acrylate over a triphos bound molybdenum center. 9

Figure 6 Proposed catalysis of carboxylic acids with CO_2. 11

Figure 7 Free energy of reactions for carboxylation of methane, benzene and dihydrogen. 11

Figure 8 From left to right: CO_2 derived PCs - Poly(indene carbonate), PCXC, Poly(1,4-dihydronaphthalene carbonate) and the industrial PC derived from phosgene: BPA polycarbonate. 15

Figure 9 Cobalt(III) catalysts: a) (salen)Co^{III}-2,4-dinitrophenoxide, 1 b) bifunctional (salen)CoIII, 2 and c) biphenol-linked dinuclear Co^{III} complex, 3. 16

Figure 10 (Salen)Cr^{III} catalysts used for CO_2/DNO coupling. 19

Figure 11 Cocatalyst effect on product selectivity for CO_2/DNO coupling with (salen)CrCl, 4. 22

Figure 12 Cartoon representation of the increased nucleophilic competition of a cocatalyst due to the steric hindrance felt by an approaching DNO. The grey spheres depict the t-butyl groups of catalyst 4. 22

Figure 13 Tetraazaannulene derived catalyst, (tmtaa)Cr^{III}Cl, 9 (left) vs the sterically crowded catalyst, (salen)Cr^{III}Cl, 4 (right). 24

Figure 14 Cocatalyst effect on product selectivity for CO_2/DNO coupling with (tmtaa)CrCl, 9. 25

Figure 15 Illustration of dinuclear Co^{III} complexes and its catalytic cavity (top). Higher activity observed when the cavity is more open and bearing smaller substituents.[42] 27

Figure 16 Sketched representations: a) Total energetic barrier of 25.8 kcal/mol for carbonate backbiting of PCHC from its lowest energy chair conformation b) With the boat conformation as the energy minimum, PDNC has a lower backbiting barrier of 22.7 kcal/mol. Free energies calculated using the CBS-QB3 composite method.[6] The anionic polymer chain, X, is modeled as methyl carbonate. 29

Figure 17 Crystal structures: Thermal ellipsoid representations of *cis*-CHDC (left) and *cis*-DNC (right) with ellipsoids at 50% probability surfaces.[32,10c] 31

Figure 18 T_g vs MW comparison of PDNC and PIC. 32

Figure 19 X-ray crystal structure of dctaa. Thermal ellipsoids shown at 50% probability level. 35

Figure 20 Preliminary structure of dataa showing highly disordered atoms on the triethyl ammonium arms. Counteranion and hydrogens omitted for clarity. ... 36

Figure 21 ^{1}H NMR spectrum showing the appearance of new formate and methyl resonances of an unidentified complex relative to the signals of *trans*-$Ru(dmpe)_2(Me)(O_2CH)$ complex. Spectrum collected after 13 h at r.t. showing a 25% conversion. 50

Figure 22 a) Three-dimensional IR stack plots showing the growth of the Ru-acetate bands and b) the reaction profiles of the product formation upon CO_2 insertion in benzene at 30 °C. 52

Figure 23 Natural log plot of absorption data *versus* time of the Ru-acetate band at 1378 cm^{-1} of 2a at 30 °C. A linear trend consistent with a first-order condition in 2 gives a k_{obs} value of 4.85 x 10^{-5} s^{-1}. 52

Figure 24 Transformation of methyl signals in ^{1}H NMR for the reaction of 2 with CO_2 (4.1 atm) at 25 °C in d_6-benzene. Reactant: (■) 6H, [Ru](*Me*)$_2$. Product: (▲) 3H, [Ru]-O_2C*Me* and (♦) 3H, [Ru]-*Me*. 54

Figure 25 Plot of k_{obs} *versus* $[CO_2]$ for the formation of complex 2a at 25 °C. The equation of the trend line was $y = 0.000353x + 0.000003$, with an R^2 value of 0.9996. Solubility data of CO_2 in benzene was obtained from literature.[71] 54

Figure 26 Natural log plots of reaction rate for the conversion of 2 to 2a in benzene under 1 atm of CO_2 at various temperatures. 55

Figure 27 Eyring plot of the reaction of *trans*-$Ru(dmpe)_2(Me)_2$ with CO_2 (1 atm). The equation for the trend line is y = -6.375x + 7.713, with an R^2 value of 0.991. 56

Figure 28 Proposed transition state for CO_2 insertion.[64,72] 57

Figure 29 The two possible conformations of $L_2RuX(CO_2Y)$ complexes. The conformation labels (i) and (ii) are used hereafter. 60

Figure 30 Relative enthalpies for the reactions between $Ru(dmpe)_2$ complexes with carbon dioxide; the corresponding free energy diagram is qualitatively the same. *trans*-$Ru(dmpe)_2$ is abbreviated [Ru]. 62

Figure 31 Enthalpies of CO_2 insertion into the Ru-Y bond for compounds of the form, $Ru(dmpe)_2XY$. 63

Figure 32 The transition state for $Ru(dmpe)_2H_2$ leading to carboxylation. The immediate product of this elementary reaction is the formate complex of conformation (i). Hydrogen atoms on the dmpe ligand have been omitted for clarity. Distances: Ru-H (a) 2.471 Å; Ru-C (b) 2.936 Å; Ru-O (c) 3.003 Å; Ru-H (d) 1.575 Å. 64

Figure 33 Enthalpies of CO_2 insertion into the Ru-Y bond for complexes of the form RuL_2XY and the corresponding APT charges on the hydride. 65

Figure 34 X-ray structures: Thermal ellipsoid representations of A, $(CH_2=CHCOOH)Ru(CO)_4$, and B, $(CH_2=CHCOOH)Fe(CO)_4$ with ellipsoids at 50% probability surfaces. 75

Figure 35 Capped sticks representation of $(CH_2=CHCOOH)Ru(CO)_4$ indicating intermolecular hydrogen-bonding, d(O5–O6') and d(O5'–O6) = 2.656 Å (similarly in the iron derivatives = 2.630 Å). 76

Figure 36 Infrared spectrum of $(CH_2=CHCOOH)Ru(CO)_4$ in the carbonyl region. 77

Figure 37 ^{13}C NMR spectra of of (acrylic acid)$Ru(CO)_4$ in $CDCl_3$ at (a) 20 °C (194.3 ppm) and (b) -40 °C (192.7, 193.7, 193.9, and 196.4 ppm). 77

Figure 38 A. Infrared ν_{CO} peak profiles as a function of time for (acrylic acid)$Ru(CO)_4$ (red), $(PPh_3)Ru(CO)_4$ (green), and *trans*-$(PPh_3)_2Ru(CO)_3$ (black) at 283 K in CH_2Cl_2. B. Plot of $\ln(A_t/A_0)$ *vs* time for disappearance of (acrylic acid)$Ru(CO)_4$, R^2 = 0.997 79

Figure 39 Thermal ellipsoid representation of the X-ray structure of $(Ph_3P)Ru(CO)_4$ with ellipsoids at 50% probability surfaces. 80

Figure 40 Infrared ν_{CO} profiles for (acrylic acid)$Ru(CO)_4$ disappearance (red) and appearance of $(Ph_3P)Ru(CO)_4$ (green) and *trans*-$(Ph_3P)_2Ru(CO)_3$ (black). Tenfold excess PPh_3 (solid lines) and thirtyfold [PPh_3] (hollow lines) in CH_2Cl_2 at 283 K.....81

Figure 41 Infrared ν_{CO} peak profiles as a function of time for (acrylic acid)$Ru(CO)_4$ (red), $(PPh_3)Ru(CO)_4$ (green), and *trans*-$(PPh_3)_2Ru(CO)_3$ (black) at 288 K in CH_2Cl_2. Hollow lines with piperidine and solid lines without piperidine...83

Figure 42 X-ray structure of $(CH_2{=}CHCOO)Fe(CO)_4^-H_2NC_5H_{10}^+$ along with its H-bonding motif with ellipsoids at 50 % probability. The Fe – C(5) and Fe – C(6) distances of 2.1049 (19) and 2.1149 (19) Å as well as the C(5) – C(6) distance of 1.410 (3) Å are not statistically different from those found in the parent acrylic acid complex. The d(O6 – N1) and d(O5 – N1') were determined to be 2.710 and 2.703 Å, respectively. 85

Figure 43 X-ray structure of $(CH_2{=}CHCOOMe)Fe(CO)_4$. The Fe–C(5) and Fe–C(6) distances of 2.108 (2) and 2.101 (2) Å are not statistically different from those found for the acrylic acid and acrylate derivatives. 87

Figure 44 Reaction profiles for $(CH_2{=}CHCOOMe)Fe(CO)_4$ + 10 equivalents of PPh_3 in chlorobenzene at 343 K. $(CH_2{=}CHCOOMe)Fe(CO)_4$ (red), $PPh_3Fe(CO)_4$ (green), and *trans*-$(PPh_3)_2Fe(CO)_3$ (black). 88

Figure 45 A proposed reaction pathway which accommodates processes described in the above study. 90

Figure 46 Three-dimensional stack plots for the substitution reaction of *cis*-$Mo(CO)_4(pip)_2$ with Triphos in $CHCl_3$ at 308 K, where the starting material is subtracted out. Reaction profiles for the formation of (κ^2-Triphos)$W(CO)_4$ (1891 cm^{-1}) and (κ^3-Triphos)$W(CO)_3$ (1842 cm^{-1}).....95

Figure 47 ^{31}P NMR Spectra. A. Purified sample of (κ^3-Triphos)$W(CO)_3$. B. Isolated sample of (κ^2-Triphos)$W(CO)_4$ from mild condition synthesis. 96

Figure 48 X-ray structures. A. Thermal ellipsoid representation of complex 3a with elipsoids at 50% probability surfaces. Hydrogen atoms have been omitted for clarity. B. Ball-and-stick drawing of complex 3b. 98

Figure 49 Spectral changes observed upon photolysis of (κ^2-Triphos)$W(CO)_4$ in the presence of [1-hexene] = 3.2 M at 288 K. The peaks at 1944 and 1860 cm^{-1} assigned to the (κ^2-Triphos)$W(CO)_3$(η^2-1-hexene) complex decrease

in intensity while those at 1933 cm^{-1} and 1841 cm^{-1} due to the (κ^3-Triphos)$W(CO)_3$ complex grow at the same rate (see inset). The spectra were obtained 0, 5.8, 17.3, and 46.2 seconds after photolysis.....100

Figure 50 Effect of increasing 1-hexene concentration upon the decay rate of the (κ^2-Triphos)$W(CO)_3(\eta^2$-1-hexene) complex at 288 K.....101

Figure 51 Reversible dissociation of 1-hexene prior to (κ^3-Triphos)$W(CO)_3$ formation.....101

Figure 52 (Top) (a) A sketch of the calculated collision complex,[142] involved in the rate determining step for CO and (NHC)(RS)$Fe(NO)_2$, proceeding through a 5-coordinate intermediate I.[142] Theory finds that as the Fe-CO bond becomes linear as in (b), the Fe-SR bond lengthens, and releases a thiyl radical, either by direct homolytic Fe-S bond cleavage or *via* homolytic C-S cleavage from a transient metallothioester group.[142] (Bottom) Corresponding plots of the transition state SOMOs: (a) the unpaired electron on the {$Fe(NO)_2$} donates into the π^* orbital of the side-on entering CO; and (b) the shift of the unpaired electron releases thiyl radical.[142] 112

Figure 53 Overlaid IR Spectra of RRE, 1 and 2 in THF. [Green: RRE: ν_{NO} 1783(s), 1757(s) cm^{-1}], [Blue: 1: ν_{NO} 1763(s), 1715(vs) cm^{-1}], [Red: 2: ν_{CO} 1986(s), ν_{NO} 1747(s), 1705(vs) cm^{-1}].....113

Figure 54 Molecular structures of complexes (a) 1 and (b) 2in ball-and-stick view. 114

Figure 55 Three-dimensional stacked plot of the reaction of complex 1 with $CO_{(g)}$ at 333 K in toluene.....115

Figure 56 Reaction profiles of infrared bands for the conversion of 1 (ν_{NO} 1708, 1753 cm^{-1}) to 2 (ν_{CO} 1992, ν_{NO} 1720, 1768 cm^{-1})) at 348 K in toluene.....115

Figure 57 Natural log plot of absorption data versus time of the ν_{CO} of complex 2 at 323 K. A linear trend consistent with a first-order condition in 2 gives a k_{obs} value of 4.03 x 10^{-5} s^{-1} calculated from the slope. 116

Figure 58 Plot of k_{obs} vs [CO] for the formation of complex 2 at 323 K. The R^2 value of 0.9996. 117

Figure 59 Natural log plots of absorption data versus time of the ν_{CO} of complex 2 at various temperatures. 118

Figure 60 Eyring plot obtained from the temperature dependence of *k*. The R^2 value is 0.999. 119

Figure 61 Overlaid IR spectra for 1, 1a-1e.....120

Figure 62 Overlaid cyclic voltammograms (THF solution, scan rate 100 mV/s, 100 mM [*n*-Bu_4N][BF_4] as supporting electrolyte) of 1a (red), 1b (brown), 1 (blue), 1c (green), 1d (purple), 1e (grey). All are referenced to Cp_2Fe/Cp_2Fe^+.....121

Figure 63 Plot of $E_{1/2}$ for 1a-1e *vs* the Hammett substituent parameter σ_p. All are referenced to Cp_2Fe/Cp_2Fe^+.....122

Figure 64 Hammett plot of rate constants from reactions of DNICs (1a-1d, 1) with CO. Error bars are 10% of original value. Slope of trend line is -0.831 with an R^2 of 0.901. 125

Figure 65 Pyrrole- aldehyde/acetyl bound rhenium carbonyls prepared by Bideau and coworkers.[9].....131

Figure 66 Difference FTIR spectra observed as a function of time upon reaction of a 3 mM solution of **1a** with 0.17 M PPh_3 in heptane at 303 K. The positive peaks are due to the growth of the product complex, **2a**, while the negative peaks are due to the disappearance of the reactant, **1a**. 133

Figure 67 Difference FTIR spectra obtained at the start of the reaction between a 3 mM solution of 1a and 0.17 M PPh_3 at 303 K in heptane. The peaks marked with IM are due to the formation of an intermediate species that grows in rapidly and then decays over the course of the reaction at the same rate as the growth of the product complex 2a. The inset shows spectral changes in the 1700−1500 cm^{-1} region due to the C═O stretching of the aldehyde. 134

Figure 68 The temporal profile of the intermediate complex, IM, monitored at 2103 cm^{-1} obtained upon reaction of a heptane solution of 1a with 0.17 M PPh_3 at 303 K. The time dependence of this species demonstrates a fast rise followed by a slower decay. The solid black line represents a biexponential fit to the data. 135

Figure 69 Proposed structure of intermediate. 135

Figure 70 Spectral changes observed when a heptane solution initially containing 1a, IM, and 2a is left standing at 298 K. The spectra are consistent with complete conversion of IM to the reactant 1a while the concentration of 2a is left unchanged. Due to the overlap between the CO bands of the various species, the conversion is best observed at 2103 cm^{-1} (IM) and 2112 cm^{-1} (1a). The intensities of the product bands at 1939 cm^{-1} and 1912 cm^{-1} due to 2a are unchanged. 137

Figure 71 A plot of Abs vs. time for the reaction of 1a and 1b with PPh_3 monitored at 2009 cm^{-1} and 2000 cm^{-1}, respectively. A heptane solution of 1a or 1b was reacted with 0.17M PPh_3 at 303 K. 139

Figure 72 Crystal Structure of {2-$(CF_3CO)C_4H_3N$}$Re(CO)_3(PPh_3)$, 2b. 139

Figure 73 Crystal Structure of {2-$(CHO)C_4H_3N$}$Re(CO)_3$(pyridine), 3a. 140

Figure 74 Thermal ellipsoid (probability level at 50%) plot of 2 with select atom labeling. Hydrogen atoms and counteranion omitted for clarity. 145

Figure 75 Thermal ellipsoid (probability level at 50%) plot of 3a with select atom labeling. Hydrogen atoms and counteranion omitted for clarity. 146

Figure 76 Spectral changes observed upon reaction of a dichloromethane solution of 2 with 0.5 M CH_3CN at 288 K to yield 3a. 147

Figure 77 Thermal ellipsoid (probability level 50%) plot of 3b with select atom labeling. Hydrogen atoms and counteranion omitted for clarity. 148

Figure 78 Common methylene bridged cyclic amines. 152

Figure 79 Infrared spectra of $[CH_2(pyr)_2]Mo(CO)_4$, 1 (red) and $[CH_2(pip)_2]Mo(CO)_4$, 2 (blue) complexes in dichloromethane. 157

Figure 80 Structures of $[CH_2(pyr)_2]Mo(CO)_4$, 1 (left) and $[CH_2(pip)_2]Mo(CO)_4$, 2 (right). Thermal ellipsoids, probability level 50%, with select atom labeling. Hydrogen atoms omitted for clarity. Select bond distances (Å) - Complex 1: N-Mo_{ave} = 2.326(2); axial C-O_{ave} = 1.147(3); equatorial C-O_{ave} = 1.166(3). Complex 2: N-Mo_{ave} = 2.338(3); axial C-O_{ave} = 1.123(7); equatorial C-O_{ave} = 1.157(4). 159

Figure 81 View down the axial carbonyls of *cis*-$(pip)_2Mo(CO)_4$,[21] 3 (left), $[CH_2(pip)_2]Mo(CO)_4$, 2 (center) and $[CH_2(pyr)_2]Mo(CO)_4$, 1 (right). Capped stick representations with angles around the molybdenum center. Average distance to the closest ligand hydrogens from the equatorial carbonyl carbon is shown by arrow. Inset figures display the angle facing away from ligand and between the axial carbonyls. 159

LIST OF TABLES

Page

Table 1 Copolymerization of 1,4-dihydronaphthalene oxide and CO_2 with (salen)Cr^{III} catalysts. 21

Table 2 Copolymerization of DNO and CO_2 with (tmtaa)$Cr^{III}Cl$, 9. 25

Table 3 Enthalpies and free energies calculated for epoxide to react with CO_2 to yield polymer and cyclic carbonate. 28

Table 4 Selected Bond Distances (Å) and Angles (deg) for *cis*-CHDC and *cis*-DNC. ... 31

Table 5 Temperature dependent rate constants for the formation of 2a in benzene under 1 atm of CO_2. 55

Table 6 Rate constants calculated from following the methyl peaks via ^1H NMR and from the *in situ* IR monitoring of acetate bands of 2a for the reaction of 2 with CO_2. 57

Table 7 Rate constants and reaction half-lives of CO_2 insertions into 2 carried out in benzene. 58

Table 8 Relative energies of conformation (ii) *vs* conformation (i) for complexes of the form Ru(dmpe)$_2$X(formate). 60

Table 9 Enthalpies of species involved in CO_2 insertion reactions, transition state relative to reactant plus CO_2 (energies in kcal/mol). (B3LYP/BS2++, gas phase). 64

Table 10 Enthalpies of CO_2 insertion into the M-Y bond for complexes of the form, M(dmpe)$_2$XY. 66

Table 11 Positions of CO stretching frequencies for the Ru & Fe complexes..... 79

Table 12 Temperature dependent rate constants for the substitution reactions of (CH_2=CHCOOH)Ru(CO)$_4$ with PPh_3.[a] 81

Table 13 Temperature dependent rate constants for the substitution reactions of (CH_2=CHCOOH)Ru(CO)$_4$ with PPh_3 in the presence of piperidine.[a]..... 83

Table 14 Summary of activation parameters for olefinic ligand dissociation determined in these studies using Eyring analysis.[a] 84

Table 15 Temperature dependent rate constants for the substitution reactions of $(CH_2=CHCOOH)Fe(CO)_4$ with PPh_3 in the presence[a] and absence[b] of piperidine. 86

Table 16 Temperature dependent rate constants for the substitution reactions of $(CH_2=CHCOOMe)Fe(CO)_4$ with PPh_3.[a] 87

Table 17 Enthalpy (kcal/mol) of the reaction: $M(CO)_4L \rightarrow M(CO)_4 + L$. 89

Table 18 Kinetic parameters obtained from a linear fit of the natural log plots. CO concentrations in toluene at 1 atm were derived from literature.[29] 118

Table 19 Kinetic parameters for reactions of 1a-1e with CO obtained from linear fits of natural log plots. 124

Table 20 CO stretching frequencies for manganese complexes in dichloromethane 145

Table 21 Calculated Mn−L BDEs for manganese complexes demonstrating the steric influence of the diimine ligand upon the strength of this interaction. 150

Table 22 Conditions investigated for the reaction of piperidine with dichloromethane. 155

CHAPTER I

INTRODUCTION

Carbon oxides are chemicals solely composed of the elements carbon and oxygen. The simplest and most common of these class of molecules are the gaseous species, carbon monoxide and carbon dioxide. A carbon connected to an oxygen *via* a triple bond, carbon monoxide (CO) is produced naturally in photochemical reactions in the troposphere. It is also a product of incomplete combustion arising from volcanoes, burning of fossil fuels as well as natural and man-made fires. CO is eventually oxidized to carbon dioxide, having a short atmospheric life-time of two months.[1] A carbon doubly bonded to two oxygen atoms, carbon dioxide (CO_2) makes up 0.04% of earth's atmosphere, a significantly larger volume than CO which is present in very trace amounts. Following nitrogen (78%), oxygen (21%) and argon (0.93%), CO_2 is the fourth largest component of air and plays a key role in the carbon cycle on earth (Figure 1). With its recycling capacity perfected over millions of years to be around 200 gigatons (Gt) of CO_2 per year, the natural carbon cycle now faces an imbalance with an additional 35 Gt/y of CO_2 released *via* anthropogenic emissions through burning of fossil fuels.[1] Being a greenhouse gas, the increased levels of CO_2 is linked to adverse climate changes across the planet. It is thus imperative to find sustainable technologies and effective solutions to minimize the accumulation of CO_2 in the atmosphere. The primary focus of this dissertation falls on CO_2 utilization and is addressed shortly, while a secondary concentration on select chemical reactions of CO and its significance are introduced further on in this chapter.

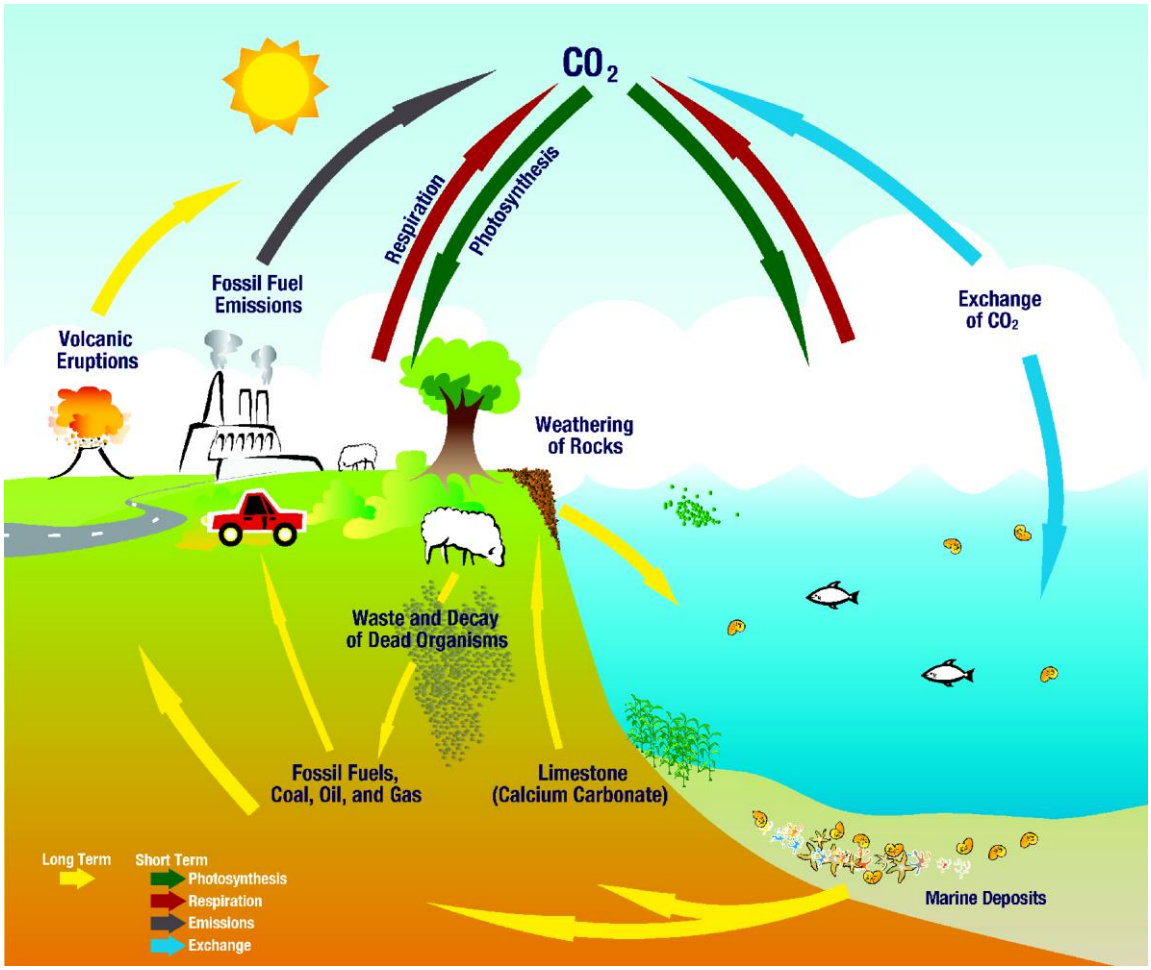

Figure 1 The carbon cycle.[2]

CO_2 as Chemical Feedstock

There is no silver bullet that can remedy CO_2 accumulation in the atmosphere but rather a combination of technologies need to be implemented over the next several years in mitigating its rising volume. Foremost of which will be finding clean and alternate fuel sources given that nearly 60% of emissions come from the energy sector. A medium-term solution is seen to be the capture and storage of CO_2 in geological formations which can be expensive and energy intensive as well.[1,3] However, finding profitable uses for CO_2

can drive such an effort forward. Notably, its use as a C1 feedstock in chemical synthesis can efficiently contribute to the reduction of CO_2 emissions as well as a means for storage.

Currently, around 130 Mt/y of CO_2 is already employed in the chemical industry primarily for the synthesis of urea, salicylic acid, methanol, cyclic carbonates and inorganic carbonates.[1] Large efforts are now carried out by researchers around the world in expanding the utilization of CO_2 for various chemical synthesis. An area of active interest is the preparation of polycarbonates by the coupling of CO_2 with cyclic ethers or epoxides (Figure 2).[4] Showing 100% atom economy and without the need for a solvent, this route provides a greener alternative to the traditional synthesis involving polycondensation of a diol and phosgene in a basic media. An entropically favored side product, cyclic carbonate, is also produced in the coupling reaction. While the research herein is focused on the selective preparation of polycarbonates, it should be noted that cyclic carbonates also find use industrially. Their polar and aprotic nature renders them suitable as electrolytes in lithium-ion batteries and as high-boiling solvents.[5]

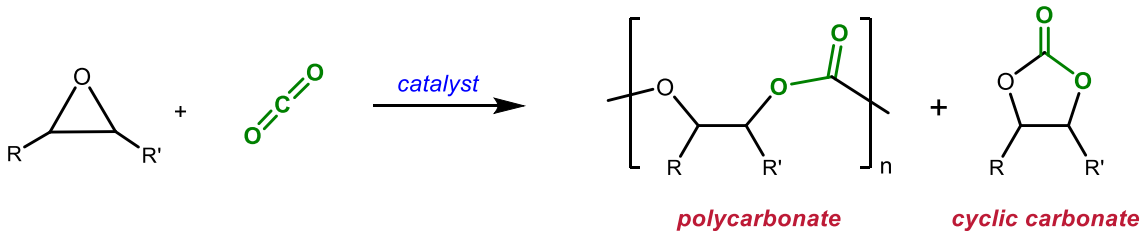

Figure 2 Catalytic coupling of CO_2 and epoxide to provide poly- and cyclic carbonates.

The copolymerization of CO_2 and epoxides require the use of a metal catalyst and a nucleophilic cocatalyst that helps initiate the reaction *via* ring-opening of the epoxide upon its coordination to the metal center (Scheme 1).[4f] The resulting alkoxide undergoes carboxylation followed by the ring-opening of another epoxide. An alternating enchainment process of epoxide and CO_2 ensues producing the desired polycarbonate. Cyclic carbonates can be produced when the growing anionic chain strays far away from the metal center and proceeds to back bite on itself either from an alkoxide or carbonate end group (Scheme 2).[4f] The choice of the catalyst, cocatalyst, reaction conditions and the identity of the epoxide then plays an important role in producing polycarbonate selectively over cyclic carbonate.

Scheme 1

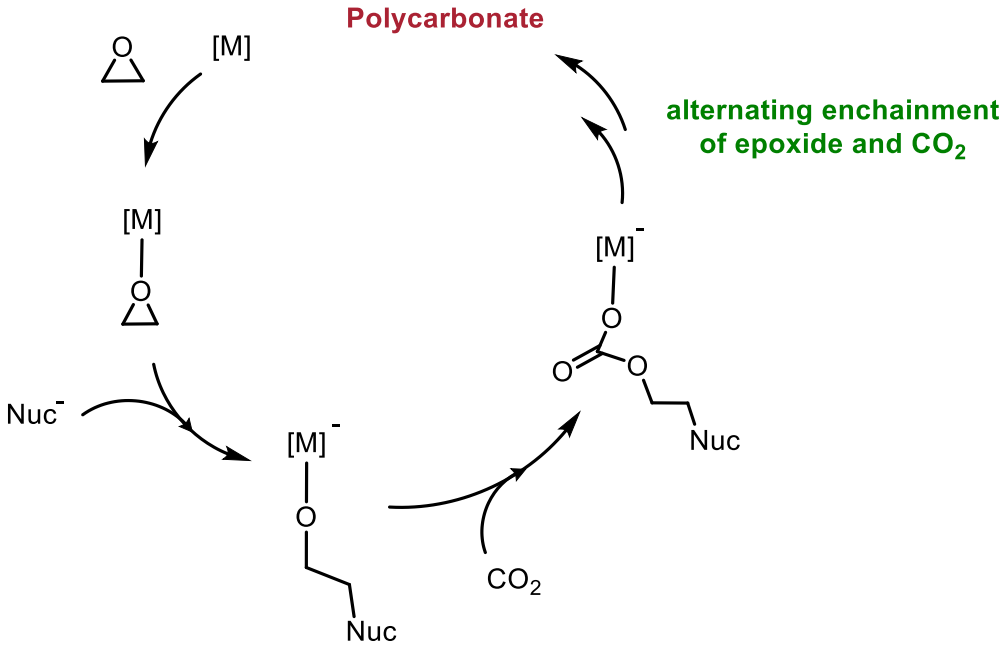

Scheme 2

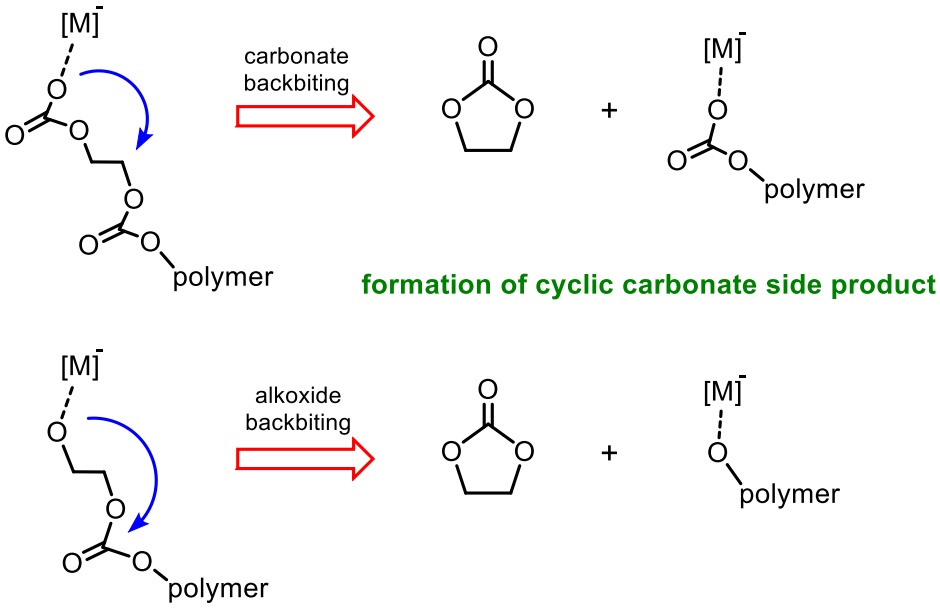

Since Inoue's first observation in 1969 of a CO_2 coupling reaction with propylene oxide catalyzed by diethyl zinc in water at a very low turnover frequency (TOF),[6] this chemistry has grown considerably, especially in the past two decades. A class of robust and active catalysts studied widely are the (salen)$M^{III}X$ species, where typically M = Cr or Co with X = Cl, N_3 or 2,4-dinitrophenolate (Figure 3).[4f] When paired with an onium salt cocatalyst, these binary catalytic systems exhibit good activity and selectivity for copolymerizing CO_2 with a variety of epoxides. Further progress was achieved with salen catalysts designed to have one or more tethered ammonium arms. While the counteranion of the salt behaved as a built-in nucleophilic cocatalyst, the ammonium side arm prevented the back-biting mechanism of the growing anionic polymer chain leading to the undesired cyclic carbonate byproduct (Scheme 3).[4k] Kinetic studies on reactions carried out with these bifunctional catalysts revealed lower and higher activation energies for polymer and

cyclic carbonate formation, respectively in comparison to their binary counterparts.[7] Enhanced activity and high molecular weights are hence observed, with the best bifunctional systems thus far showing TOFs in the tens of thousands with MWs in the hundreds of thousands for producing poly(propylene carbonate).[8]

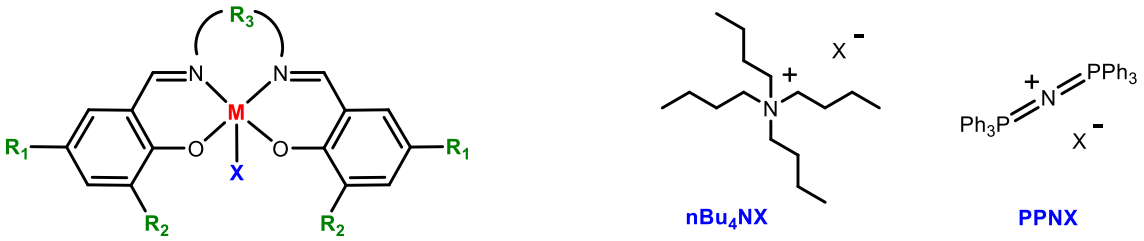

Figure 3 (salen)$M^{III}X$ catalyst (left) with onium salt cocatalysts (right). Activity and selectivity of catalyst can be tuned by altering groups R, M and X. Typical M = Cr, Co while X = azide, chloride and 2,4-dinitrophenolate.

When it comes to epoxides, cyclohexene oxide (CHO) and propylene oxide (PO) and derivatives thereof are very well-studied in the copolymerization reactions. In fact, poly(cyclohexene carbonate), PCHC and poly(propylene carbonate), PPC are now commercially synthesized from CO_2 by companies such as Novomer, Empower Materials, Econic Technologies, and Bayer.[9] Their uses, however, are limited due to their physical properties which falls short when compared to industrial standards such as bisphenol-A (BPA) derived polycarbonate. In order to expand the application of CO_2-derived polycarbonates, two topics are of current interest. One is the synthesis of water soluble PCs targeted towards biomedical applications. A strategy involves monomers bearing an olefinic backbone that can be modified post-polymerization with desirable hydrophilic functional groups.[10] The second is the preparation of PCs with high thermal transition

properties which can then compete with the likes of BPA polycarbonate. This then calls for the use of bulky and rigid epoxides to couple with CO_2. Chapter II of this dissertation addresses this latter interest by presenting our investigations with a naphthalene derived epoxide.

Scheme 3

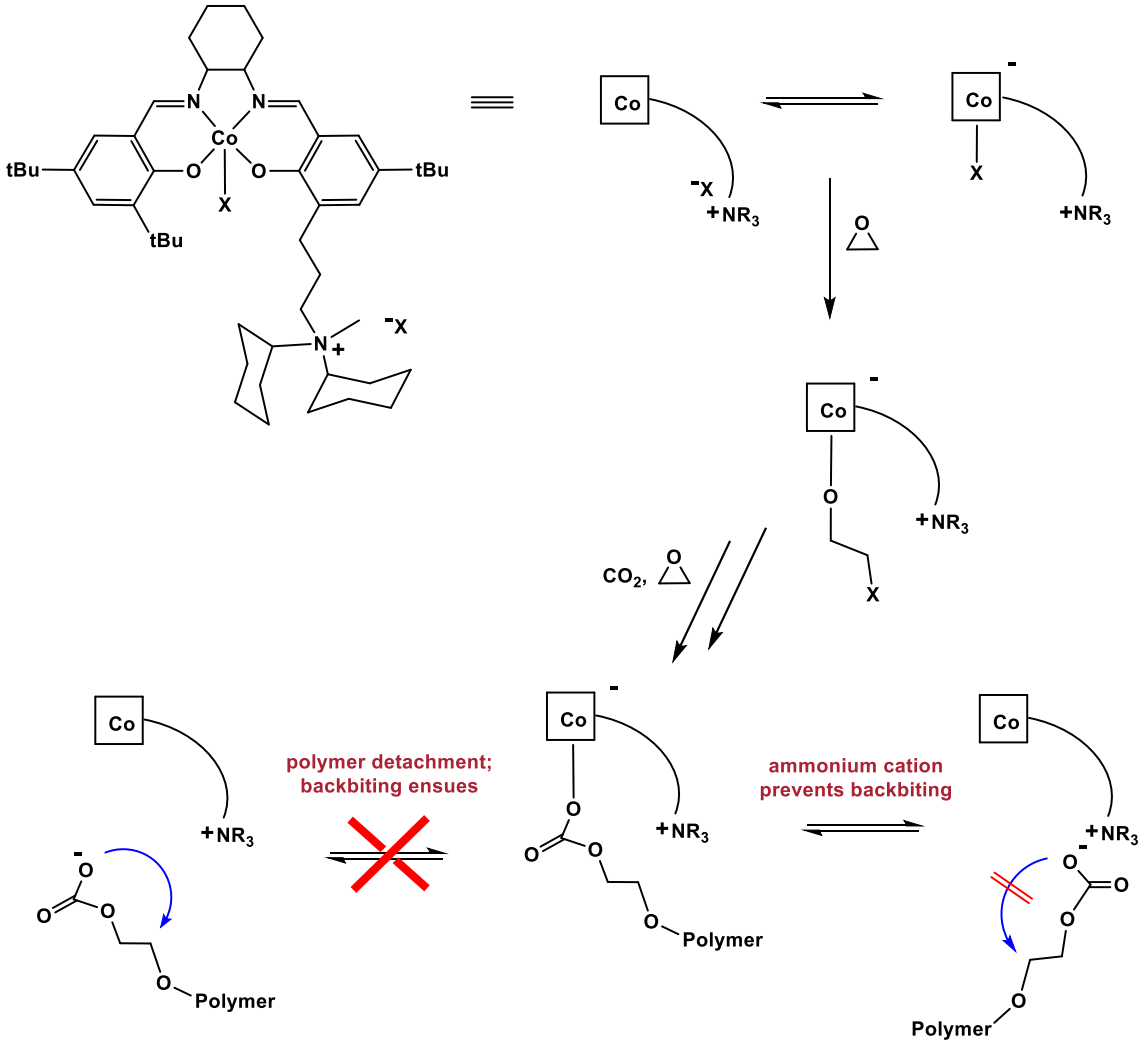

Another sought-after conversion of CO_2 involves its coupling with olefins such as ethylene to generate acrylic acid (Figure 4). A high-demand monomer produced in millions of tons, acrylic acid and its derivatives are polymerized to give polyacrylates that have uses ranging from coatings and adhesives to the manufacture of plastics and superabsorbent polymers.[11] Current industrial synthesis involves the oxidation of propylene gas, a byproduct of gasoline production, utilizing a high-energy and intensive process.[11] Ethylene is usually produced *via* steam cracking of petroleum, but it can be obtained alternatively from a biosource, i.e. through the dehydration of bioethanol produced by fermentation of biomass (corn, sugarcane, etc.).[12] This together with CO_2 offers a greener route for the synthesis of acrylic acid.

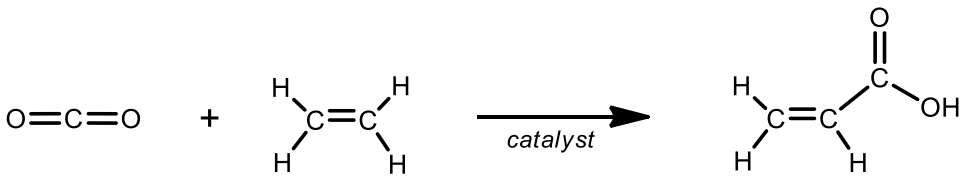

Figure 4 Acrylic acid formation from coupling of CO_2 and ethylene.

Hoberg and coworkers showed the first coupling of CO_2 and ethylene in 1983 to occur over nickel centers, but the product obtained was a nickelalactone which was unable to undergo a β-H elimination to provide an acrylate.[13] Later in 1985, Carmona and coworkers revealed the successful formation of acrylates over molybdenum centers.[14] DFT calculations carried out by Papai and coworkers showed β-H elimination to be quite facile for Mo *vs* Ni centers.[15] Bernskoetter and coworkers revisited these molybdenum

systems in 2011 and have shown through detailed kinetic studies that a pre-coordination of CO_2 is important for its coupling with ethylene (Figure 5).[16] This was also supported by calculations and is found to be unlike the nickel systems where it isn't required.[15]

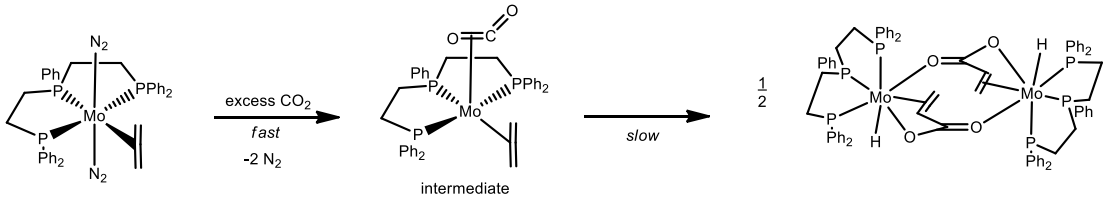

Figure 5 A long-lived CO_2 and ethylene coordinated intermediate observed in the formation of an acrylate over a triphos bound molybdenum center.

Scientists working at BASF in Germany have recently shown that by employing a strong base, the metallalactone formed on nickel centers can be driven to give the acrylate salt and can further be displaced from the nickel center to regenerate the original ethylene bound precursor (Scheme 4).[17] A TON of 10 was achieved, however, the reaction was complicated by the fact that the base employed, an alkoxide, is incompatible with CO_2 and the catalytic cycle had to be carried out first in a CO_2-rich regime followed by a CO_2-poor regime. While further studies are clearly warranted, they have shown the importance of the use of a base to act as a sink for the acid and drive the reaction forward. Bernskoetter and coworkers have employed MeI to remove the acrylate from the metal center to give methyl acrylates though it is accompanied by the decomposition of the metal complex.[18] Finding appropriate reagents to safely remove the resulting acrylate product from a CO_2 and ethylene coupling reaction on a metal center is thus currently under investigation.

Scheme 4

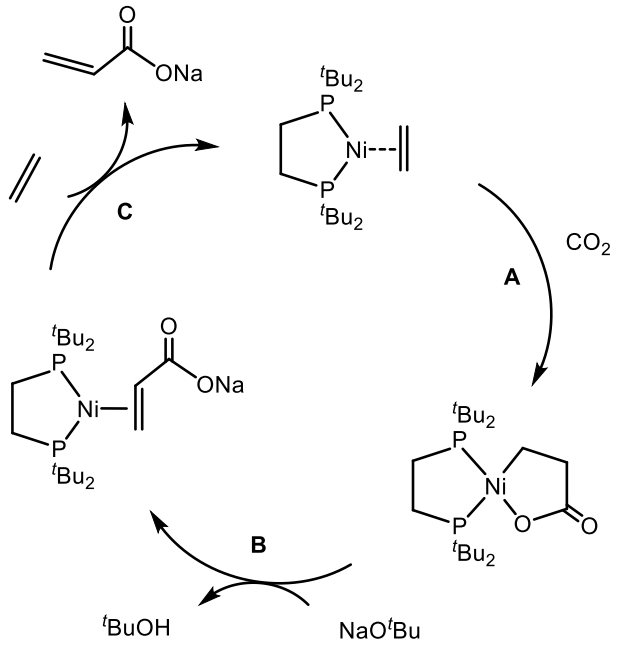

Steps **B** & **C** have to be carried out in the absence of CO_2

The catalytic carboxylation of aliphatic and aromatic carbons to produce carboxylic acids by direct use of CO_2 is a more challenging reaction. This process involves three distinct steps that each need to happen at a suitable metal center: 1) the activation of a C-H bond *via* oxidative addition, 2) CO_2 insertion into the M-C bond to give a metal-carboxylate and 3) reductive elimination from the metal to yield carboxylic acid (Figure 6). The unfavorable thermodynamics involved in the direct carboxylation of hydrocarbons such as methane or benzene to provide acetic or benzoic acids (Figure 7), will also require the addition of a base to drive the reaction to completion.[19] Noyori and coworkers have shown the catalysis of formic acid in supercritical CO_2 and H_2 using a Ru catalyst and in the presence of triethylamine, which aided product isolation by forming an adduct with

the acid in a 1:2 ratio.[20] New experimental investigations on C-H bond carboxylations over Cu and Au were carried out under basic conditions to yield carboxylate salts which were then converted to carboxylic acids by acid hydrolysis.[21,22]

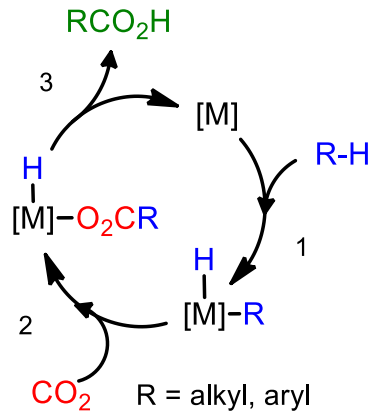

Figure 6 Proposed catalysis of carboxylic acids with CO_2.

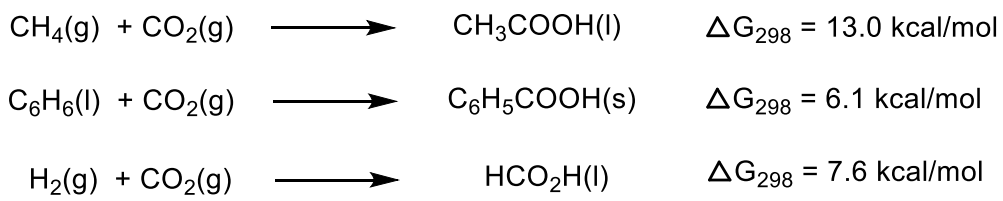

Figure 7 Free energy of reactions for carboxylation of methane, benzene and dihydrogen.

In Chapter III, we present model studies to understand the fundamentals of such transformations. The kinetics and thermodynamics of CO_2 insertions into Ru-H and Ru-Me bonds are investigated through experiments and computations. In addition, the structural characterizations of acrylic acid bound ruthenium and iron complexes prepared synthetically are described along with an evaluation of their bond dissociation energies

from the metal centers. Preparation of triphos bound molybdenum and tungsten carbonyls and their interactions with olefins is also included.

Carbon Monoxide Chemistry

CO is produced industrially as it is employed in the production of various commodity chemicals. Two main production methods are 1) coal gasification where carbon is directly oxidized to CO by passing air over a bed of coal at high temperatures and 2) the steam reformation of methane which produces CO along with H_2 gas.[23] Major bulk chemicals manufactured by utilizing carbon monoxide are as listed: a) the production of methanol *via* catalytic reduction with H_2 b) the Monsato process which produces acetic acid by the carbonylation of methanol c) the synthesis of phosgene by its reaction with Cl_2 d) the hydroformylations of olefins to produce aldehydes and e) the production of inorganic carbonyls such as $Ni(CO)_4$ and $Fe(CO)_5$.[23]

Carbon monoxide is also known as the "silent killer" as this odorless, tasteless gas has a strong binding affinity to hemoglobin.[24] It can displace oxygen from the blood cells resulting in irreversible damage to the heart and brain upon a prolonged exposure. It is thus classified as a toxic gas, with levels greater than 100 ppm deemed dangerous to human health. Surprisingly, CO is also produced in the human body by the hemeoxygenase enzymes as was discovered in the late 1960's.[25] It wasn't until 1990's that its role as an important regulatory gas molecule in mammalian biology was elucidated.[25] These findings were spurred along with the discovery of NO, another important signaling molecule within cells, around that time. CO is now known to induce vasodilations and

possess anti-inflammatory and various other therapeutic properties when present in nanomolar amounts.

Currently, administration of CO is carried out through inhalation of the gas as a mixture with air.[26] This process requires careful monitoring on the supplied volume and the formation of CO-bound hemoglobin for the gas permeates the entire body once in the lungs. A better option would be to deliver the CO to a desired location in controlled quantities. For this purpose, active research is being carried out on the use of metal carbonyls as CO releasing molecules (CORMs). A promising compound, $Ru(CO)_3Cl$(glycinate) shows very good activity with low toxicity against cardiovascular and inflammatory conditions in animal trials.[25] Several other metal carbonyls based on Mn, Re and Mo metal centers are being studied to understand their biological activity and stability, as well as cell-targeting by attachment of peptides and polymers.

In Chapter IV of this dissertation, we present an example of gaseous CO reacting with a synthetic analogue of a biological dinitrosyl iron complex (DNIC) under mild conditions. DNICs are noted to be NO storage and supply agents in the cellular milieu, and there is strong evidence of interactions between CO and NO producing enzymes in the body. Details on the unusual mechanism observed in the reaction are given. And finally in Chapter V, we introduce two new CORMs that are highly labile and discuss the effect of the ligands coordinated on to metal carbonyls that facilitate the CO release.

CHAPTER II

A CARBON DIOXIDE COPOLYMERIZATION STUDY WITH A STERICALLY ENCUMBERING NAPHTHALENE DERIVED OXIDE[*]

Introduction

Epoxides employed in the catalytic copolymerization reactions with CO_2 are largely aliphatic and alicyclic in nature for producing polycarbonates.[4] The most common and well-studied in literature are propylene oxide (PO) and cyclohexene oxide (CHO) along with their functionalized derivatives. Poly(propylene carbonate), PPC and poly(cyclohexene carbonate), PCHC have been commercialized in recent years and are used as sacrificial binding agents, additives in coatings and as low molecular weight PC-polyol precursors for polyurethane synthesis.[9] Of late, there is an interest in preparing CO_2-derived polycarbonates that display high thermal resistance comparable to that of the widely applicable industrial standard BPA polycarbonate (T_g = 154 °C). We began work in this area when we first presented poly(indene carbonate) with a T_g of 138 °C as a result of its fused cyclopentene and benzene ring in the polymer backbone (Figure 8).[27,28] Lu and coworkers then described the preparation of CO_2 copolymers with 3,5-dioxaepoxides where their use of 4,4-dimethyl-3,5,8-trioxabicyclo[5.1.0]octane (CXO) in particular gave the respective polycarbonate, PCXC with a T_g of 140 °C.[29]

---

[*] Reprinted (adapted) with permission from: Darensbourg, D. J.; Kyran, S. J. *ACS Catal.* **2015**, *5*, 5421. Darensbourg, D. J.; Chung, W. C.; Arp, C. J.; Tsai, F.-T.; Kyran, S. J. *Macromolecules* **2014**, *47*, 7347. Copyright 2015 & 2014, respectively, American Chemical Society.

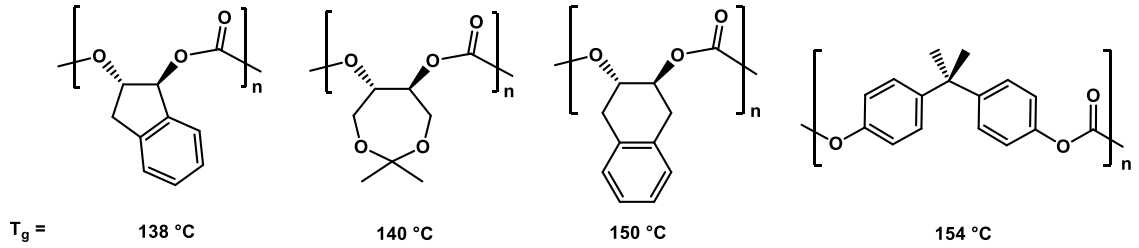

Figure 8 From left to right: CO_2 derived PCs - Poly(indene carbonate), PCXC, Poly(1,4-dihydronaphthalene carbonate) and the industrial PC derived from phosgene: BPA polycarbonate.

The copolymerization of indene oxide with CO_2 proved to be a challenge. Our initial attempts with the (salen)Co^{III}-2,4-dinitrophenoxide catalyst, **1** (Figure 9) along with an onium salt cocatalyst at its normal working temperature range (25 - 40 °C) was met only with the production of the entropically favored product, *cis*-indene carbonate.[27] After lowering the temperature to 0 °C, a polymer selectivity of about 60% was observed with very low TOFs (2 h^{-1}). The tendency to produce the cyclic byproduct is enhanced for epoxides with a π system near the methine carbon due to a resonance stabilized transition state that provides a lower barrier for polymer backbiting as seen through computations.[30] The use of a bifunctional (salen)Co^{III} catalyst, **2** then proved fruitful in producing PIC with high selectivity (>99%) at 25 °C.[28] The ammonium side arm of **2** prevents disassociation of the growing anionic polymer chain, keeping it closer to the metal center *via* electrostatic interactions. This encourages long-chain propagation, averting the detrimental polymer backbiting process leading to cyclic carbonates.[4k] Furthermore, the built-in cocatalyst helps increase the activity at lower loadings along with the thermal stability of the complex. This gave us PIC in higher MWs with M_n reaching 10,000 g/mol. The catalytic activity still remained low with TOFs of no more than 12 h^{-1}.

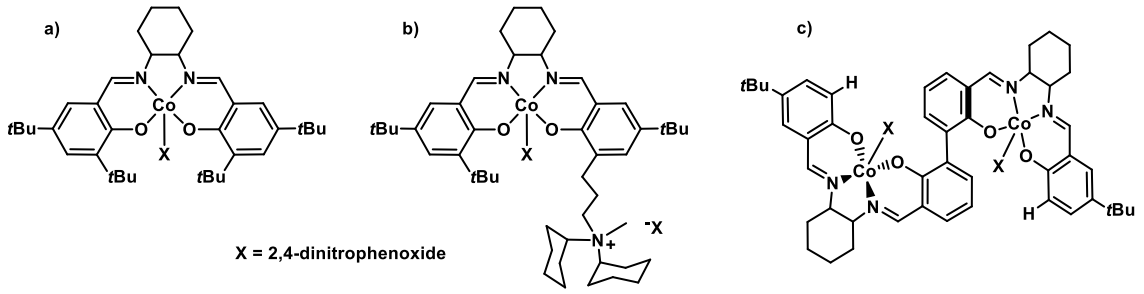

Figure 9 Cobalt(III) catalysts: a) (salen)Co^{III}-2,4-dinitrophenoxide, **1** b) bifunctional (salen)CoIII, **2** and c) biphenol-linked dinuclear Co^{III} complex, **3**.

We felt the need to improve upon the results described above and decided to look for other aromatic epoxides that could fare well in the catalysis. Our focus then shifted to 2,3-epoxy-1,2,3,4-tetrahydronaphthalene or 1,4-dihydronaphthalene oxide (DNO). There were a few reasons that made DNO an appropriate monomer for the next study: 1) The aromatic ring is one carbon away from both the methine carbons which will diminish the electronic effects that leads to polymer backbiting 2) DNO can be viewed as a benzene fused with a cyclohexene oxide; cyclohexene oxide selectively produces the copolymer as it has a large activation barrier for making cyclic carbonate.[30,31] Hence, DNO could have an analogous property, and 3) the resulting polymer could display a higher glass transition temperature than PIC due to its bulkier backbone.

We had previously worked with DNO as early as 2004, at which time we communicated the crystal structure of *cis*-1,4-dihydronaphthalene carbonate (DNC) and showed this cyclic carbonate to be the only isolable product from the catalysis of CO_2 with DNO using a (salen)Cr^{III} catalyst.[32] We have now reexamined this reaction with various chromium(III) catalysts and would like to report here the successful preparation of

poly(1,4-dihydronaphthalene carbonate), PDNC (Scheme 5).[33] Parallel to our efforts, Lu and coworkers have very recently communicated their preparation of the same copolymer by employing a dinuclear cobalt(III) catalyst, **3** (Figure 9c).[34] They show high molecular weight isotactic PDNC to exhibit a T_g of 150 °C, very close to that of BPA polycarbonate (**Figure 8**). Their work also substantiates our further findings regarding a strong steric influence from the catalyst when copolymerizing a large monomer such as DNO which is described in detail (*vide infra*).

Scheme 5

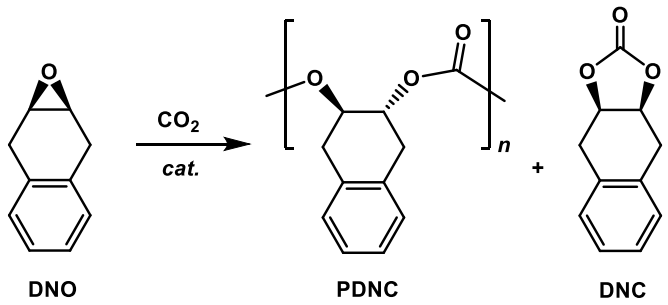

Results and Discussion

Naphthalene, the readily available polycyclic aromatic hydrocarbon occurring as the largest component in coal tar (10 wt. %),[35] can be reduced to 1,4-dihydronaphthalene and epoxidized to 1,4-dihydronaphthalene oxide (DNO) suitable for CO_2 coupling (Scheme 6**).**[36,37] A pale yellow solid that melts above 40 °C, DNO would require the addition of a solvent such as CH_2Cl_2 or toluene for the copolymerization reaction with CO_2 at ambient temperature, as was previously done with indene oxide (MP = 32 °C). Surprisingly, catalysts **1** and **2** showed no sign of a coupling reaction to produce either

cyclic or polycarbonates. Long reaction times (up to 5 days), varying reaction temperature (0 - 25 °C with solvents; neat reactions with **1** & **2** at 45 °C & 70 °C, respectively) and varying cocatalyst initiators (2,4-dinitrophenoxide, azide, chloride, trifluoroacetate) under pressures of 25-35 CO_2 bar proved ineffective at our typically employed catalyst loading of 0.2%. However, Lu and coworkers show the catalysis to occur at a higher loading of **1** (0.5%) albeit with a TOF of only 15 h^{-1}.[34] Hence, it was decided to examine the catalysis using the Cr^{III} complexes.

Scheme 6

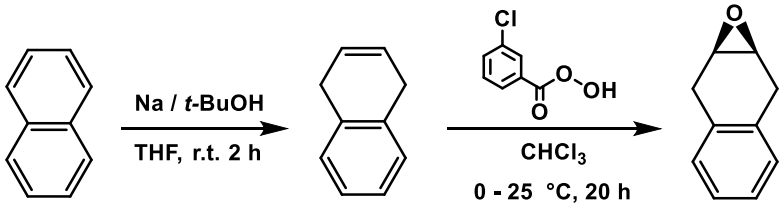

Gratifyingly, a reaction at 70 °C with (salen)Cr^{III}Cl, **4** (Figure 8) and an equivalence of PPNCl as cocatalyst at a loading of 0.2% provided poly(1,4-dihydronaphthalene carbonate), PDNC with a polymer selectivity of 78% and a TOF of 8 h^{-1} (Table 1, entry 4). The working temperatures for chromium catalysts are higher than cobalt (≥70 °C), so the use of solvents can be abated as DNO is a liquid at that temperature. Solvents are known to lower both the conversion and polymer selectivity due to epoxide dilution and it is also seen here (Table 1, entries 1-3). When the more active bifunctional (salen)Cr^{III} catalyst, **8** is used at a loading of 0.13%, both higher polymer selectivity (93%) and TOFs (29 h^{-1}) are observed at 100 °C (Table 1, entry 12). A molecular weight of 6,700

g/mol displaying a T_g of 136 °C was noted. Lowering the loading of **8** to 0.1% failed to produce higher MWs (Table 1, entry 13).

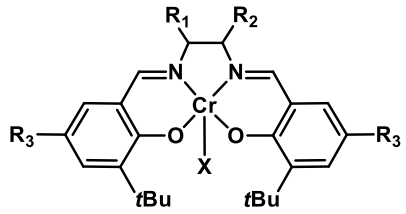

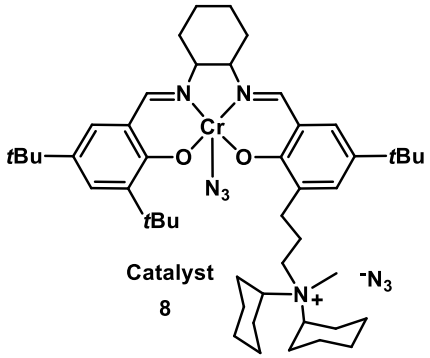

Catalyst	
4	R_1, R_2 = -C_4H_8-; R_3 = *t*Bu; X = Cl
5	R_1 = R_2 = H; R_3 = *t*Bu; X = Cl
6	R_1, R_2 = -C_4H_8-; R_3 = OMe; X = N_3
7	R_1 = R_2 = R_3 = H; X = Cl

Figure 10 (Salen)Cr^{III} catalysts used for CO_2/DNO coupling.

Cocatalyst Effects. We noticed an odd occurrence for the catalysis carried out with the binary salenCr^{III} catalyst/cocatalyst systems. Specifically, there seemed to be a large cocatalyst effect on the resulting product ratio based on the identity of the nucleophile and the amount utilized in the reaction (Table 1, entries 4-7). More PDNC was obtained when employing PPNCl *vs* $PPNN_3$ but changing to two equivalents of the cocatalysts drastically increased the cyclic product with less than 5% polymer selectivity seen for two azides. Figure 11 depicts this observation more clearly. The role of a cocatalyst is to help intiate the ring-opening of an epoxide and the addition of two equivalence can also help accelerate the copolymerization as was shown previously in a CHO/CO_2 study.[38] Based on the data at hand, we believe this trend to originate as a result of a steric hindrance from the catalyst. It is now much harder for a bulkier DNO, *versus* a PO or CHO molecule, to

access the metal center surrounded by four *t*-butyl groups in catalyst **4**. In fact, we have shown that a highly sterically encumbered catalyst bearing six *t*-butyl groups, including on the R_1 & R_2 positions of the salen backbone, shows little activity for CHO/CO_2 coupling.[39]

Here, when a DNO molecule gets ring-opened and carboxylated, the nucleophilic cocatalysts become increasingly competitive to coordinate and displace the one-mer unit rather than allow chain propagation *via* ring-opening of another epoxide due to unfavorable steric effects (Figure 12). The displaced one-mer unit can then backbite to give cyclic carbonate. This will explain the observed higher cyclic carbonate selectivity for the more nucleophilic azide cocatalyst *versus* chloride, a better leaving group, if backbiting was the exclusive reason. Prior results showing only cyclic carbonate formation may well be due to the use of 2.25 equivalence of *N*-methyl imidazole (NMI), another good nucleophile (Table 1, entry 8).[32] On the other hand, the lack of catalysis with the cobalt complexes in our earlier attempts can presumably be due to its smaller metal center more effectively shrouded by the salen ligand towards an approaching DNO molecule. The effective ionic radii of six-coordinate low spin Co^{III} and Cr^{III} are 54.5 and 61.5 pm, respectively.[40] Considering spherical volume which is of a cubic function, Co^{III} is nearly a third smaller than the size of Cr^{III}. While we note that increased catalyst loading plays a role in enhancing polymer production as seen with both the Co^{III} catalyst, **1** (our results *vs* Lu's, *vide supra*) and the Cr^{III} catalysis (Table 1, entries 3 *vs* 7), the trend in product selectivity because of steric hindrance cannot be ruled out.

Table 1 Copolymerization of 1,4-dihydronaphthalene oxide and CO_2 with (salen)Cr^{III} catalysts.

	cat/cocat [loading][a]	*T (°C) [solv.]*[b]	*Time (h)*	*% conv.*[c]	*% PDNC*[c]	*TOF (h^{-1})*[d]	*M_n (g/mol)*[e]	*PDI*	*T_g (°C)*
1[f]	**4**/$TBAN_3$ [1:2:250]	70 [tol]	6	37	47	16	2,600 [7,900]	1.06	119
2	**4**/$TBAN_3$ [1:2:250]	70 [dcm]	6	36	45	15			
3	**4**/$TBAN_3$ [1:2:250]	70	6	47	67	19	4,000 [14,800]	1.06	128
4	**4**/PPNCl [1:1:500]	70	15	24	78	8			
5	**4**/$PPNN_3$ [1:1:500]	70	14	32	61	11	3,500 [17,500]	1.07	
6	**4**/PPNCl [1:2:500]	70	14	41	28	15			
7	**4**/$PPNN_3$ [1:2:500]	70	14	54	4	20			
8[g]	**5**/NMI [4:9:1000]	80 [tol]	12	20	<1	3			
9	**6**/PPNCl [1:1:500]	70	14	25	76	9	3,000 [18,200]	1.09	
10	**6**/$PPNN_3$ [1:2:500]	70	18	36	5	10			
11	**7**/PPNCl [1:1:500]	70	14	17	60	6			
12	**8** [1:750]	100	15	58	93	29	5,300[h]; 6,700 [76,200]	1.11	130; 136
13	**8** [1:1000]	100	7	17	83	23	3,000 [25,300]		

All reactions carried out at a CO_2 pressure of 30 bar with the following exceptions: entries 3, 12 & 13 at 25 bar; entries 1 & 8 at 45 & 55 bar, respectively. [a]Loading ratio depicts catalyst:cocatalyst:DNO, respectively and catalyst:DNO for last two entries. [b]1 mL solvent per 1 g of DNO, except entry 8 which used 1.6 mL Tol / g DNO. [c]Determined using ^{1}H NMR spectroscopy. [d]Turnover frequency of DNO to products (PDNC and DNC) as determined *via* ^{1}H NMR spectroscopy. [e]Determined *via* gel permeation chromatography in THF. Values in square brackets denote theoretical M_n = (M/I) × (% conversion) × (MW of DNC). [f]$TBAN_3$ used for its solubility in toluene [g]Data based on isolated yields from ref. 32. NMI is *N*-methyl imidazole. [h]A low MW polymer sample was recovered from the CH_2Cl_2/MeOH work-up solution after initial precipitation of the high MW polymer.

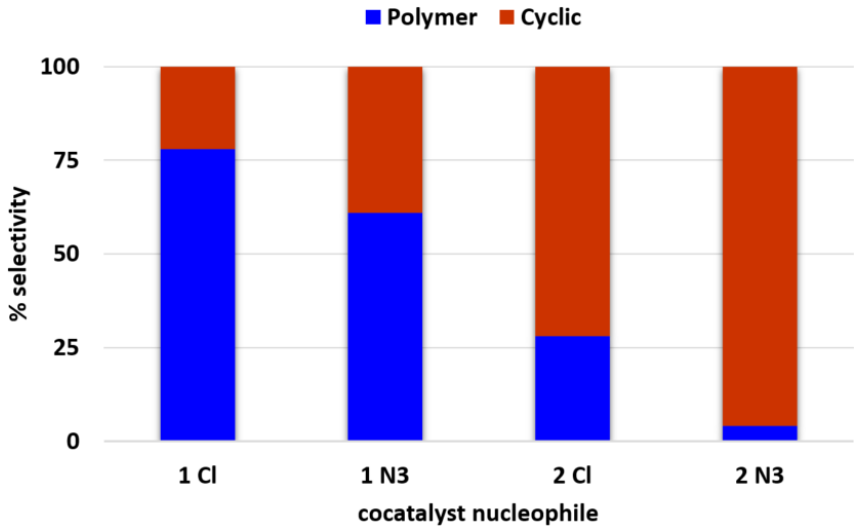

Figure 11 Cocatalyst effect on product selectivity for CO_2/DNO coupling with (salen)CrCl, **4**.

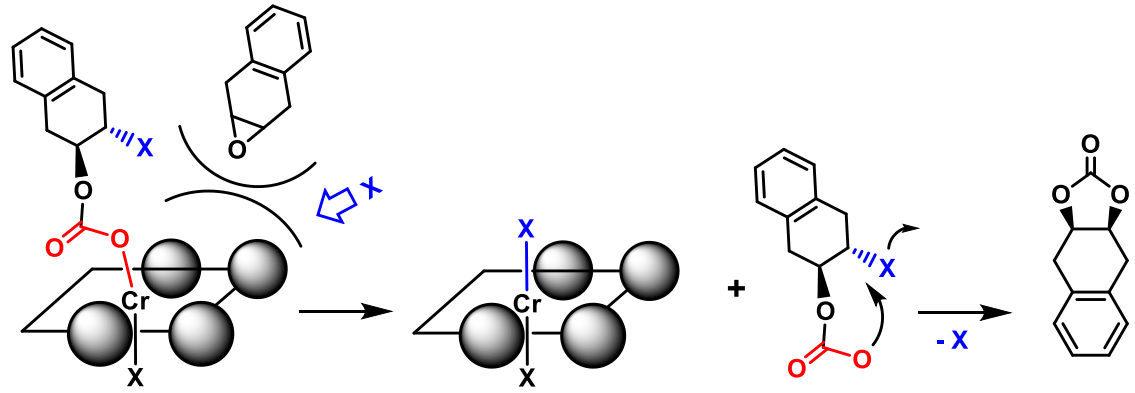

Figure 12 Cartoon representation of the increased nucleophilic competition of a cocatalyst due to the steric hindrance felt by an approaching DNO. The grey spheres depict the t-butyl groups of catalyst **4**.

Steric Effects. If the observed cocatalyst effect is indeed a reflection of the steric around the metal center, then a better polymer selectivity and activity should be achieved by using (salen)Cr^{III} complexes bearing smaller substituents. For this purpose, we used catalyst **6** with smaller methoxy groups in the 5-positions with an equivalence of PPNCl

and the resulting polymer selectivity was now 15% higher when compared with catalyst **4** (Table 1, entry 9 *vs* 5. Note: catalyst **6** has a coordinated azide). But if the cocatalyst was switched to two equivalence of $PPNN_3$, it quickly shuts down polymer production with PDNC selectivity no greater than 5% (Table 1, entry 10). This indicated that the change in the steric environment is slight when reducing the substituent size in the 5-positions alone. Catalyst **7** with hydrogens *vs* methoxy groups and an ethylene *vs* cyclohexene backbone didn't show any improvements either (Table 1, entry 11). Replacing all four *t*-butyls with smaller substituents is not a good choice as it results in a poorer solubility of the chromium catalyst in the epoxide medium, thus leading to poorer activity.[39] Facing this limitation with (salen)Cr^{III} complexes, we chose to look at a different ligand altogether for optimizing the polymerization condition.

A tetramethyltetraazaannulene chromium complex, (tmtaa)$Cr^{III}Cl$, **9** was shown to be highly active (TOF = 1,500 h^{-1}) for the copolymerization of CHO with CO_2 by our group in 2007.[41] The less sterically congested and planar motif of this azaannulene ligand seemed to be a suitable candidate in producing PDNC with high selectivity (Figure 13). Upon performing a catalytic run at 0.2% loading of **9** with an equivalence of PPNCl, we found nearly 90% polymer selectivity with three times the activity of the binary (salen)Cr^{III} complex, **3** (Table 2, entry 1 *vs* Table 1, entry 4). The resulting PDNC also had a MW of 5,800 g/mol with a T_g of 136 °C, comparable to that obtained with the bifunctional (salen)Cr^{III} catalyst, **8**. A series of experiments varying the cocatalyst and their loading with **9** further showed that though there were more cyclic product with two equivalents, it was not a drastic change as seen with catalyst **4** (Table 2, entries 2-5; Figure

14). Lower catalyst loadings (0.13%) show reduced activity but maintain moderate to good polymer selectivity (Table 2, entries 6&7). These results suggest that as we expand our epoxide toolset towards bulkier monomers for producing polycarbonates with high thermal resistance, the catalysts we employ needs to evolve as well, particularly taking steric into consideration.

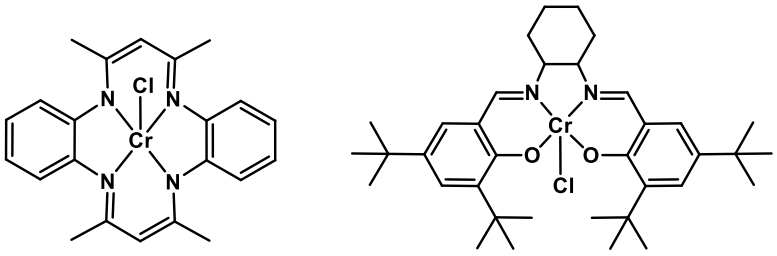

Figure 13 Tetraazaannulene derived catalyst, (tmtaa)$Cr^{III}Cl$, **9** (left) vs the sterically crowded catalyst, (salen)$Cr^{III}Cl$, **4** (right).

Table 2 Copolymerization of DNO and CO_2 with (tmtaa)$Cr^{III}Cl$, **9**.

	cat/cocat [loading][a]	*T (°C)*	*Time (h)*	*% conv.*[b]	*% PDNC*[b]	*TOF (h^{-1})*[c]	*M_n (g/mol)*[d]	*PDI*	*T_g (°C)*
1	**9**/PPNCl [1:1:500]	70	14	63	89	23	5,800 [53,400]	1.11	136
2	**9**/PPNCl [1:1:500]	70	7	40	84	28	4,700 [31,000]	1.10	
3	**9**/$PPNN_3$ [1:1:500]	70	7	42	85	30	4,600 [34,100]	1.10	
4	**9**/PPNCl [1:2:500]	70	7	44	58	32			
5	**9**/$PPNN_3$ [1:2:500]	70	7	55	71	39	4,500 [36,500]	1.11	
6	**9**/PPNCl [1:1:750]	70	14	27	80	15	3,800 [31,226]	1.09	
7	**9**/$PPNN_3$ [1:1:750]	70	14	23	47	13			

All reactions carried out at a CO_2 pressure of 30 bar [a]Loading ratio depicts catalyst:cocatalyst:DNO, respectively. [b]Determined using ^{1}H NMR spectroscopy. [c]Turnover frequency of DNO to products (PDNC and DNC) as determined *via* ^{1}H NMR spectroscopy. [d]Determined *via* gel permeation chromatography in THF. Values in square brackets denote theoretical M_n = (M/I) × (% conversion) × (MW of DNC).

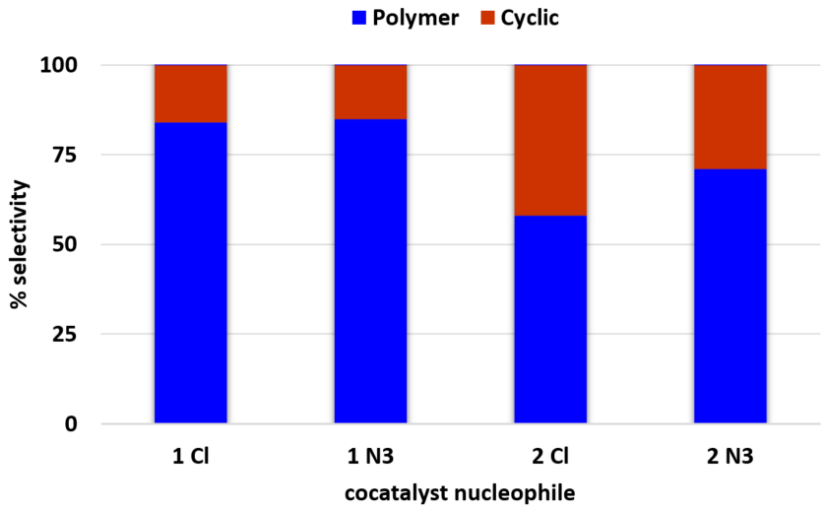

Figure 14 Cocatalyst effect on product selectivity for CO_2/DNO coupling with (tmtaa)CrCl, **9**.

With the use of their biphenol-linked dinuclear Co^{III} catalyst, **3** Lu and coworkers were able to prepare PDNC with high activity and selectivity. For example, at a loading of 0.2% and two equivalents of PPNDNP as cocatalyst, they observed a TOF of 125 h^{-1} yielding only the copolymer after 4 h at 25 °C.[34] A TOF of 900 h^{-1} was also noted for a 30 min reaction at an elevated temperature of 50° C. In a prior work, they have shown the copolymerization with catalyst **3** proceeds *via* an intramolecular bimetallic mechanism.[42] This involves an alternating chain growth through the carbonate attack of the copolymer from one metal center on to an activated epoxide on the next metal. This cooperative nature gives **3** its superior catalytic rate and polymer selectivity than in a monometallic mechanism as seen with **1**. Important to note here is the ability of **3** to accommodate both the growing polymer chain and an epoxide displaying its open environment with very little steric impact. In fact, based on experimental and theoretical results it was observed that the substituent size on the dinuclear Co^{III} complex and the width of catalytic cavity (influenced by the linker utilized) clearly dictated the activity of CHO/CO_2 copolymerization (Figure 15).[42] The *t*-butyl groups in the 5-positions are found to be remote from the catalytic centers, whereas when the substituents on the 3-positions are changed from an H to *t*-butyl to adamantyl groups, the TOFs drop from 1409 to 1269 to 173 h^{-1}. The activities mentioned go along with the biphenol linker which displays a fairly wide cavity arising from the large *endo* phenol-phenol dihedral angle of about 140° (Co-Co distance ≈ 8.2 Å). When a binaphthol bridge is used instead, the opening of the catalytic cavity is reduced as a result of an *endo* naphthol-naphthol dihedral angle of no more than

90° (Co-Co distance ≈ 6.5 Å). Consequently, the resulting activity is poorer with TOFs around 50 h^{-1} for PCHC production.[42]

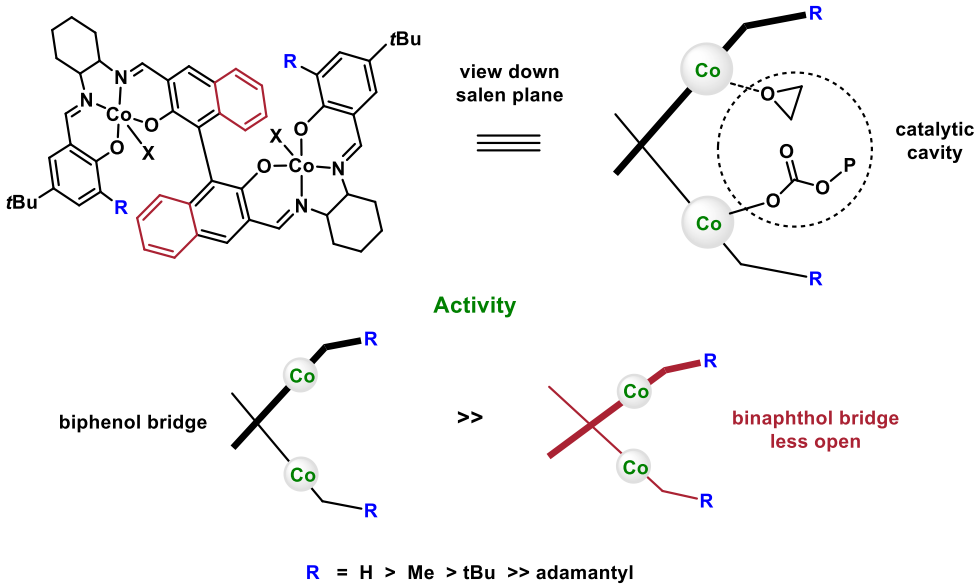

Figure 15 Illustration of dinuclear Co^{III} complexes and its catalytic cavity (top). Higher activity observed when the cavity is more open and bearing smaller substituents.[42]

Computational Insight. Additional understanding on the formation of the 1,4-dihydronaphthalene carbonates were obtained with the help of computations. Thermodynamically, CHO and DNO behave similarly having nearly the same calculated enthalpies and free energies of reactions with CO_2 to give poly and cyclic carbonates (Table 3). When it comes to kinetics, PCHC has the highest free energy barrier among all polycarbonates towards carbonate backbiting to produce *cis*-CHC.[30] Indeed, very little cyclic byproduct is seen experimentally which has made CHO an initial benchmark for testing new catalysts for CO_2 copolymerization reactions. This is the result of an

endergonic conformational change of its cyclohexene backbone from a chair to boat conformation ($\Delta = 4.7$ kcal/mol) prior to achieving its backbiting transition state ($\Delta = 21.1$ kcal/mol). This gives PCHC an overall barrier of 25.8 kcal/mol while other aliphatic polycarbonates exhibit 18-20 kcal/mol.[30] A sketched representation of the conformations are indicated in Figure 16. In the case of PDNC, the benzene ring fused to the cyclohexene ring reduces the latter's flexibility such that the only energy minimum conformation observed is boat-shaped. Hence, the free energy barrier for carbonate backbiting is lower for PDNC at 22.7 kcal/mol. This lower barrier may also explain why some *cis*-DNC (the only isomer seen experimentally) is produced even under the best catalytic conditions thus far with Cr^{III} complexes that work at higher temperatures.

Table 3 Enthalpies and free energies calculated for epoxide to react with CO_2 to yield polymer and cyclic carbonate.

	ΔH_r (kcal/mol)		**ΔG_r (kcal/mol)**	
Epoxide	**Polymer**	**Cyclic carbonate**	**Polymer**	**Cyclic carbonate**
CHO[6]	-22.6	-16.7 (*cis*)	3.4	-4.6 (*cis*)
		-13.0 (*trans*)		-0.9 (*trans*)
DNO	-22.6	-15.8 (*cis*)	2.5	-4.1 (*cis)*
		-11.7 (*trans*)		+0.6 (*trans*)

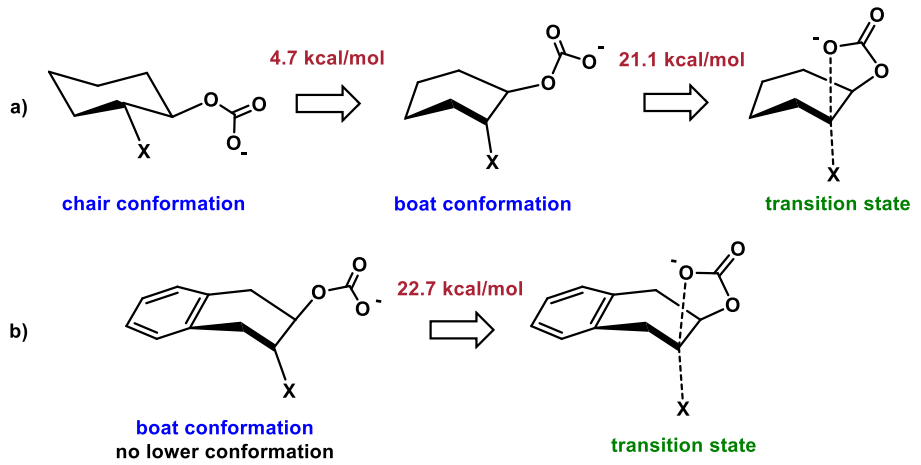

Figure 16 Sketched representations: a) Total energetic barrier of 25.8 kcal/mol for carbonate backbiting of PCHC from its lowest energy chair conformation b) With the boat conformation as the energy minimum, PDNC has a lower backbiting barrier of 22.7 kcal/mol. Free energies calculated using the CBS-QB3 composite method.[6] The anionic polymer chain, X, is modeled as methyl carbonate.

A Reduced Structural Analog of DNC. The identity of the 1,4-dihydronaphthalene carbonate byproduct in the copolymerization reaction was confirmed previously to be the *cis* isomer through an X-ray diffraction study.[32] An additional interest is its similarity to a naturally occurring cyclic carbonate, *cis*-1,4-cyclohexadiene carbonate (CHDC). This cyclic carbonate is found covalently bound to the serine residues at the active site of a (-) γ-lactamase enzyme of an *Aureobacterium* species as reported by Littlechild and coworkers.[43] When refining the crystal structure of the protein, the authors found additional electron density at its active site indicative of a small molecule. The identity of this naturally expressed molecule was confirmed to be *cis*-CHDC *via* rigorous modeling experiments and subsequent independent synthesis of the compound. Its role as a ligand to protect the active site from foreign inhibitors, but itself being displaced by the lactam substrate was illustrated.[43]

Synthetically, CHDC can be prepared from the *cis*-diol using triphosgene or by the coupling of 1,2-epoxy-4-cyclohexane with CO_2 using a $ZnCl_2/nBu_4NI$ catalyst system (Scheme 7).[10c] Though lacking a fused benzene ring, CHDC has an unsaturated bond in the same region of the cyclohexene ring as DNC. This may impart CHDC with a structural conformation similar to DNC and is indeed the case as we found through structural analysis. Long rod shaped crystals of *cis*-CHDC suitable for X-ray diffraction were grown *via* slow evaporation of a diethyl ether solution. The thermal ellipsoids are illustrated in Figure 17 along with *cis*-DNC. Selected bond distances and angles are provided in Table 4. It can be seen that *cis*-CHDC is a simpler and reduced structure of *cis*-DNC with identical bond distances and angles within three standard deviations. The six-membered alicyclic rings of both compounds adopt a boat conformation and the only notable difference is the shorter length of the C(4)–C(5) double bond in *cis*-CHDC, as expected.

Scheme 7

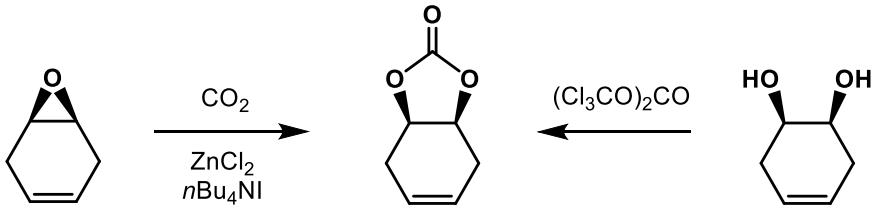

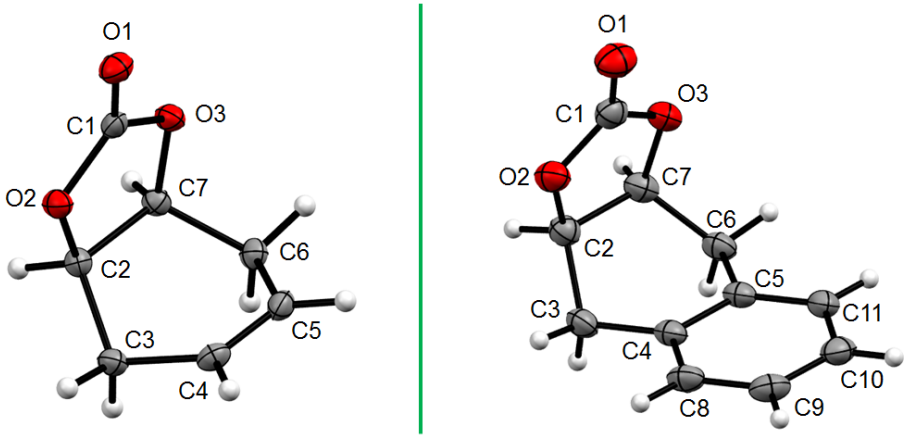

Figure 17 Crystal structures: Thermal ellipsoid representations of *cis*-CHDC (left) and *cis*-DNC (right) with ellipsoids at 50% probability surfaces.[32,10c]

Table 4 Selected Bond Distances (Å) and Angles (deg) for *cis*-CHDC and *cis*-DNC.

	***cis*-CHDC**	***cis*-DNC[8]**
C(1) – O(1)	1.197(2)	1.203(2)
C(1) – O(2)	1.337(1)	1.345(2)
C(2) – O(2)	1.455(1)	1.460(2)
C(2) – C(7)	1.543(1)	1.550(2)
C(2) – C(3)	1.519(1)	1.525(3)
C(4) – C(5)	1.326(2)	1.406(2)
O(1) – C(1) – O(2)	124.1(1)	123.8(2)
C(1) – O(2) – C(2)	110.67(9)	110.7(1)
C(2) – C(7) – O(3)	103.35(8)	103.2(1)
O(2) – C(2) – C(3)	108.50(8)	109.2(1)

A Bifunctional Azaannulene Ligand. The highest molecular weight of PDNC isolated in the current study is 6,700 g/mol displaying a T_g of 136 °C. Comparing the T_g values to those of low MW PIC shows PDNC to be greater by about 5 °C because of its increased bulk (Figure 18). The true measure of a polymer's thermal transition is past 10,000-15,000 g/mol whereby its T_g becomes independent of the MW. Using catalyst **3**, this was shown to be 150 °C for PDNC.[34] With a similar interest in making higher MWs using Cr^{III} complexes, we began to look into newer and effective ligand designs. We decided to prepare a tetraazaannulene ligand with ammonium side arms, much like the salen bifunctional ligands. With less sterics and the added benefit of the pendant arms that prevent polymer backbiting, a Cr^{III} or even a Co^{III} complex bearing this ligand could prove to be an effective catalyst in producing high MW PDNC.

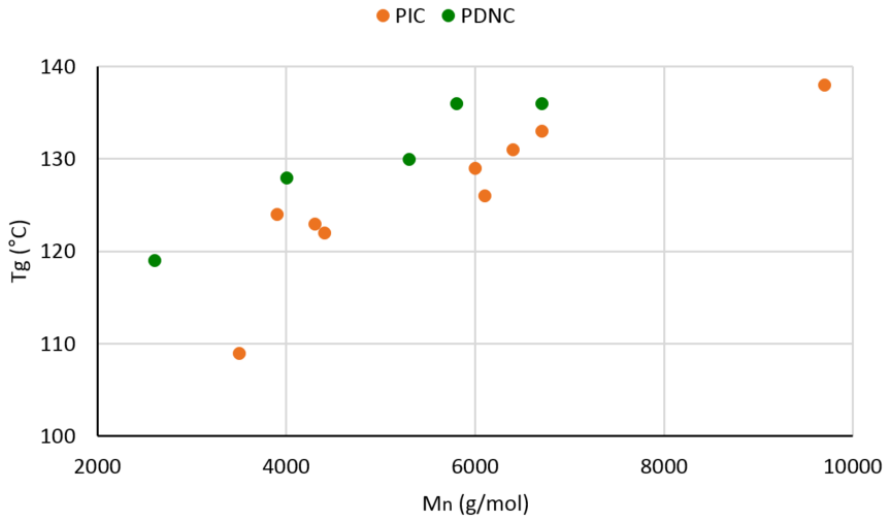

Figure 18 T_g vs MW comparison of PDNC and PIC.

Another advantage of a bifunctional tetraazannulene chromium(III) catalyst would be the range of epoxides that could now be utilized. Previously, we had shown catalyst **9**, (tmtaa)$Cr^{III}Cl$ to be successful in producing polycarbonates with high selectivity and activity for CHO and 4-vinyl-CHO but other epoxides such as PO and styrene oxide (SO) produced mostly the cyclic carbonate product.[41] This is a result of a more electron-rich metal center bearing four nitrogen donors. The growing anionic polymer chain is thus not as tightly bound leading to a higher propensity to backbite. Electrostatic interactions with the ammonium side arms of a bifunctional catalyst can then mitigate this process. CHO is unaffected as it is reticent towards backbiting as described in the previous section.

The first step towards preparing this new ligand involves the synthesis of a dihydroxytetraazaannulene, dhtaa compound *via* the ring opening and condensation reaction of 3,4-dihydro-2*H*-pyran-5-carbaldehyde and *o*-phenylenediamine (OPD) as shown previously by Breitmaer and coworker (Scheme 8).[44] This results in a tetraazaannulene bearing two propyl arms with an OH group at the end which can be further transformed for our purposes. Mesylation of this dihydroxy compound provides the dimesylatetetraazaannulene (dmtaa) in near quantitative yields. We found the use of ionic liquids, 1-Butyl-3-methylimidazolium chloride and bromide salts, ([BMIM]X; X = Cl, Br) to successfully convert the dimesylate compound into the dichloro- and dibromotetraazaannulene, dctaa and dbtaa, as per the protocol developed by Chae and coworkers for transformation of sulfonate esters.[45] Single crystals of dctaa suitable for X-ray diffraction were grown from the slow cooling of a hot MeCN solution and its structure is shown in Figure 19. The final step involves the alkylation of NEt_3 in DMF with the

dihalo compounds. While we did not have success with the dichloro derivative, reaction with the dibromo compound proceeds smoothly giving us a diammoniumtetraazaannulene (dataa) ligand in a high yield. The overall synthesis is relatively quick (5 steps) without any tedious purification as otherwise seen with the preparation of the asymmetrical bifunctional salen ligands.[10b,46] The presence of more than one pendant ammonium arm on the ligand for a bifunctional catalyst has been previously shown to be highly active as well.[8] This diammonium ligand, dataa, has been fully characterized and a preliminary crystal structure is presented in Figure 20. There is also room for modification of the length of the pendant arms (furan *vs* pyran derived aldehyde), the electronics (substituted OPDs) and the bulkiness of the onium salt (various tertiary amines) which will make it desirable for optimization studies. Our preliminary work shows the coordination of dataa onto a cobalt center by refluxing with $Co(OAc)_2{\cdot}4H_2O$ in DMF to give the (dataa)Co^{II} complex. Further work on the preparation of Co^{III} and Cr^{III} complexes and their use in catalysis for copolymerizing various epoxides with CO_2 will be the subject of another paper.

Scheme 8

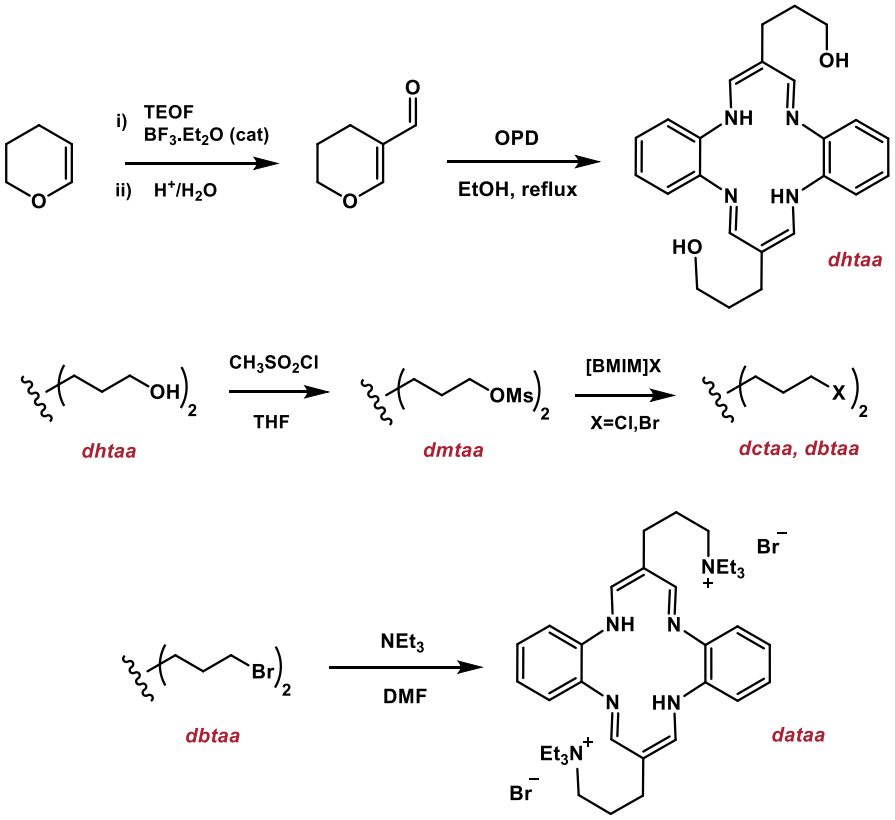

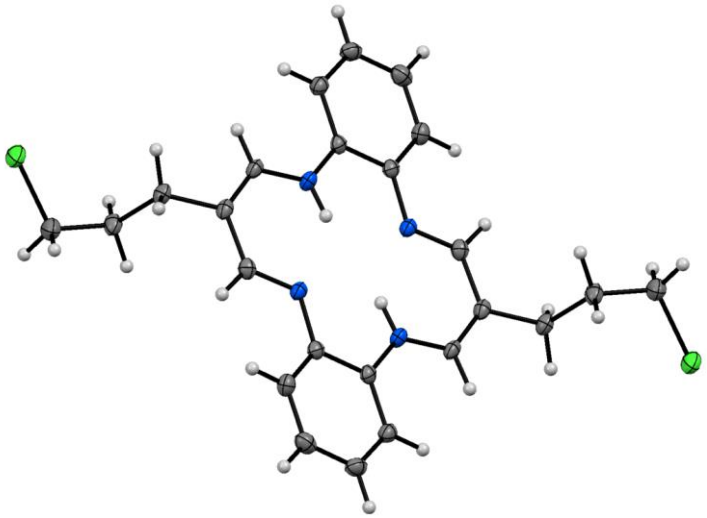

Figure 19 X-ray crystal structure of dctaa. Thermal ellipsoids shown at 50% probability level.

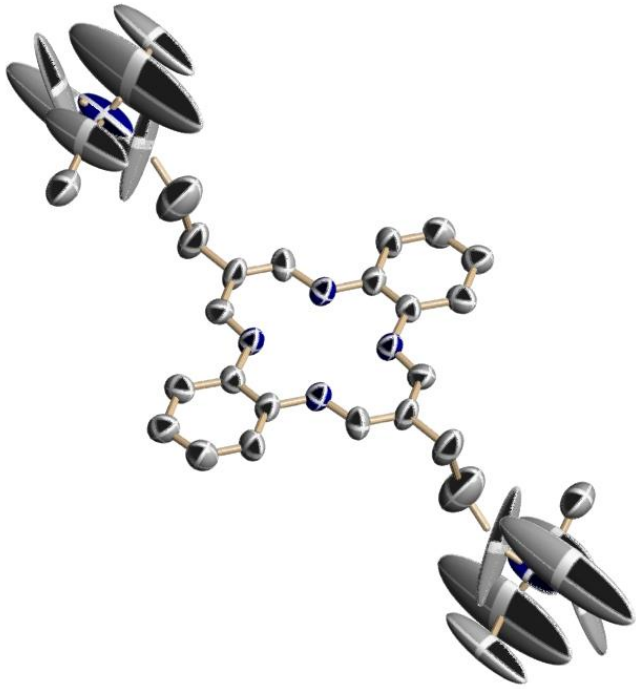

Figure 20 Preliminary structure of dataa showing highly disordered atoms on the triethyl ammonium arms. Counteranion and hydrogens omitted for clarity.

Concluding Remarks

Our renewed interest in exploring the CO_2 coupling reaction with 1,4-dihydronaphthalene oxide was in part due to the demanding but nevertheless a successful catalytic copolymerization observed with a related bicyclic monomer, indene oxide.[3,4] Results from the latter also indicated advantages of using 1,4-dihydronaphthalene oxide over indene oxide. An earlier attempt at making poly(1,4-dihydronaphthalene carbonate) involved the use of a binary (salen)Cr^{III} catalyst/cocatalyst system optimized at that time for making poly(propylene carbonate) and poly(cyclohexene carbonate).[1f,8] This mostly afforded the cyclic byproduct, *cis*-1,4-dihydronaphthalene carbonate, which we assumed

to be the result of an electronic difference when compared to its simpler analog, cyclohexene oxide that primarily provides the copolymer. With a more detailed study, we have shown here that poly(1,4-dihydronaphthalene carbonate) can indeed be produced with high selectivity using chromium(III) catalysts.

The formation of the copolymer is highly dependent on the steric environment provided by the ligands in a catalyst. A bulkier monomer, 1,4-dihydronaphthalene oxide now faces a large steric hindrance at a Cr^{III} center surrounded by a salen ligand bearing four *t*-butyl groups. As a result, its chain growth is inhibited due to an increased preference for displacement by the coordination of the smaller cocatalysts. The displaced anionic polymer chain then proceeds to backbite yielding cyclic carbonate. Increasing the cocatalyst ratio to two equivalents or employing more nucleophilic anions produces almost exclusively cyclic carbonates.

The use of a less sterically demanding tetramethyltetraazaannulene catalyst, (tmtaa)Cr^{III}Cl, increases the catalytic activity by three-fold (23 vs 8 h^{-1}) in comparison to (salen)Cr^{III}Cl with polymer selectivity reaching 90%. The competitive binding of the cocatalyst are also subdued reflecting the more spacious catalyst. When utilizing a bifunctional salenCr^{III} complex, copolymer selectivity of greater than 90% is achieved but the molecular weights remain low around 6,500 g/mol. Computations indicate that poly(1,4-dihydronaphthalene carbonate) is somewhat more susceptible to carbonate backbiting with a lower energy barrier (22.7 kcal/mol) than poly(cyclohexene carbonate) (25.8 kcal/mol). This is a result of the fused benzene ring of the former which prevents the cyclohexyl ring from adopting the lower energy chair conformation.

We have also developed a new bifunctional tetraazaannulene ligand that can be easily prepared and further optimized. Supporting two pendant ammonium arms and having less steric with respect to salen, this ligand can yield a Cr^{III} or Co^{III} catalyst that could display enhanced activity and polymer selectivity. This may then prove fruitful for producing high molecular weight polycarbonates from sterically demanding monomers, such as 1,4-dihydronaphthalene oxide, and realizing high thermally resistant properties in CO_2 derived polycarbonates.

Experimental Section

Materials and Methods. Unless otherwise specified, all syntheses and manipulations were carried out on a double-manifold Schlenk vacuum line under an atmosphere of argon or in an argon-filled glovebox. Tetrahydrofuran was purified by an MBraun Manual Solvent Purification system packed with Alcoa F200 activated alumina desiccant. Triethylamine (EMD) was freshly distilled from CaH_2 prior to use. Naphthalene (Aldrich), *t*-BuOH (Alfa Aesar), meta-chloroperoxybenzoic acid, mCPBA (Aldrich), 1-Butyl-3-methylimidazolium chloride and bromide salts, [BMIM]X; X = Cl, Br (Alfa Aesar), methanesulfonyl chloride (Acros) and dry *N*,*N*-dimethylformamide (Aldrich) were used as received. (R,R)-*N,N'*-bis(3,5-di-tertbutylsalicylidene)-1,2-cyclohexanediaminochromium(III) chloride, (salen)CrCl was purchased from Strem. Other (salen)CrCl derivatives,[39] (salen)CoDNP,[47] bifunctional salen Cr^{III} and Co^{III} catalysts,[10b,46] [PPN]DNP[48] and [PPN]N_3[49] were prepared as per literature. The tetramethyltetraazaannulene Cr^{III} complex, (tmtaa)CrCl was synthesized per a

modification of Cotton's procedure.[41] 6,13-Bis(3-hydroxypropyl)-dibenzo[*b*,*i*][1,4,8,11]tetraazacyclotetradecine or dihydroxytetraazaannulene (dhtaa) was prepared starting from 3,4-Dihydro-2*H*-pyran.[44,50] Research Grade 99.999% carbon dioxide supplied in a high-pressure cylinder and equipped with a liquid dip tube was purchased from Airgas. The CO_2 was further purified by passing through two steel columns packed with 4 Å molecular sieves that had been dried under vacuum at ≥ 200 °C.

Measurements. NMR spectra were recorded on either a Varian INOVA 300 or 500 MHz spectrometer. Infrared spectra were obtained on a Bruker Tensor 27 FTIR spectrometer. Elemental Analyses were determined by Atlantic Microlab (Norcross, GA). Molecular weight determinations (Mn and Mw) were carried out with a Malvern Modular GPC apparatus equipped with ViscoGEL I-series columns (H+L) and Model 270 dual detector comprised of RI and light scattering detectors. Glass transition temperatures (T_g) were measured using a Mettler Toledo polymer DSC equipped with a liquid nitrogen cooling system and 50 mL/min purge of dry nitrogen gas. Samples (~8 mg) were weighed into 40 μL aluminum pans and subjected to two heating cycles. The first cycle covered the range from 25 to 200 °C at 10 °C/min and was then cooled back to 0 °C at −10 °C/min. Midpoint T_g data were obtained from the second heating cycle which ranged from 0 to 300 °C at a heating rate of 5 °C/min.

2,3-epoxy-1,2,3,4-tetrahydronaphthalene or 1,4-dihydronaphthalene oxide (DNO). The first step involving reduction of naphthalene was prepared per literature[36]:

Sodium (11.6 g, 0.504 mol) as small cut and flattened pieces were added over a period of 15 min to a solution of naphthalene (25.0 g, 0.195 mol) in THF (250 mL). After stirring for 30 min, the blue solution was chilled in an ice bath and treated drop wise with *t*-BuOH (47 mL, 0.491 mol) dissolved in THF (50 mL) over the next 20 min. The solution was let stir for 2.5 h and the THF rotovaped after removing the excess sodium pieces. The resulting pinkish red oil was taken into 150 mL Et_2O and washed with distilled H_2O (5x100 mL) until the organic layer turns clear yellow. *Caution*: The first addition of water needs to be done very slowly as the flask heats up causing Et_2O to boil when the salt dissolves. The organic layer is further washed with brine (3x50 mL) and dried over anhydrous $CaCl_2$ by stirring overnight. *Note*: $CaCl_2$ also removes excess *t*-BuOH. Filtration and removal of Et_2O give a viscous yellow oil. ^{1}H NMR on crude product shows ~80% 1,4-dihydronaphthalene while the rest is made up of the 1,2-isomer and tetralin. The product composition varies depending on the amount of excess sodium and reaction time involved, but the crude product can be used for the next step without additional purification.

Epoxidation of 1,4-dihydronaphthalene is carried out similar to a literature prep[37]: mCPBA (17.5 g, 0.101 mol) was added slowly to an ice-cooled solution of 1,4-dihydronaphthalene (16 g, 0.123 mol) in $CHCl_3$ (100 mL). It was then treated with a saturated aqueous $NaHCO_3$ solution (80 mL) and the biphasic medium was let stir at r.t. for 4 h. The solution was chilled again and treated with additional $CHCl_3$ (100 mL) and mCPBA (14.0 g, 0.081 mol). Continued stirring for 17 h resulted in the complete conversion of starting material as seen *via* TLC. The reaction mixture was transferred to

a 1000 mL Erlenmeyer flask and the acid generated was neutralized by addition of more $NaHCO_3$ solution (70 mL), stirring until bubbling ceased. Excess mCPBA was then killed with a saturated sodium thiosulfate solution (150 mL, added in 50 mL increments and tested with starch paper). Finally, distilled water (50 mL) was added, stirred and the organic layer allowed to separate. The organic layer was further washed with water (3x70 mL) in a separation funnel, dried with anhydrous $MgSO_4$ and filtered to give a clear yellow solution. Following removal of solvent, the crude epoxide was purified *via* flash chromatography with gradient elution of ethyl acetate in hexane on a silica column using Teledyne ISCO's CombiFlash® R_f 150. DNO is obtained as a pale yellow solid (14 g) with a total yield of about 50%. Characterizations match that previously reported.[32] MP = 40 - 42 °C. NMR in $CDCl_3$: ^{1}H δ 3.15-3.40 (m, 4H, C*H*$_2$), 3.50 (s, 2H, C*H*), 7.05-7.27 (m, 4H, aromatic *H*); ^{13}C{^{1}H} δ 29.7, 51.7, 126.5, 129.2, 131.4. Anal. Calcd. for $C_{10}H_{10}O$: C, 82.16; H, 6.89. Found: C, 82.25; H, 6.90%.

Poly(1,4-dihydronaphthalene carbonate) (PDNC): Representative Coupling Reaction of CO_2 and 1,4-dihydronaphthaleneoxide. A stir bar, (tmtaa)CrCl (3.0 mg, 7.0 μmol), PPNCl (3.8 mg, 6.6 μmol), and 1,4-dihydronaphthaleneoxide (0.500 g, 3.42 mmol, 500 equiv.) were added to a 12 mL stainless steel autoclave reactor which had been previously dried at 150 °C for 6 h. The reactor was pressurized to 27 bar and heated to 70 °C in an oil bath with magnetic stirring. After 7 h, the reactor was cooled in an ice bath and depressurized slowly. Sublimated epoxide is observed on the inside of the reactor cap, but it is very minimum (10-30 mg). A ^{1}H NMR spectrum of the reaction mixture was taken

immediately. The crude mixture was dissolved in CH_2Cl_2 and added drop wise to an acidified methanol (10% HCl) solution to precipitate the polymer. The polymer was collected *via* filtration and purified twice more by precipitation from CH_2Cl_2/MeOH. The pale yellow to off-white PDNC is dried *in vacuo* before further analysis by GPC and DSC. Note: A 50/50 mix of C_6D_6 and $CDCl_3$ is used to obtain a well-resolved NMR spectrum to determine the polymer to cyclic carbonate ratio in the crude mixture. The peaks of both species overlap in $CDCl_3$ making it harder to do so and using only C_6D_6 underestimates the amount of polymer as it is not completely soluble in benzene. NMR in $CDCl_3$: ^{1}H δ 3.05 (br s, 2H, C*H*$_2$), 3.40 (br s, 2H, C*H*$_2$), 5.23 (br s, 2H, C*H*), 7.05-7.31 (m, 4H, aromatic *H*); ^{13}C{^{1}H} δ 31.3, 73.7, 126.5, 128.6, 131.7 and 153.5. ^{1}H NMR (C_6D_6/$CDCl_3$): δ 2.75 (br s, 2H, C*H*$_2$), 3.13 (br s, 2H, C*H*$_2$), 5.06 (br s, 2H, C*H*), 6.70-7.00 (m, 4H, aromatic *H*). IR (CH_2Cl_2): 1753 cm^{-1}. Anal. Calcd. for $(C_{11}H_{10}O_3)_n$: C, 69.46; H, 5.30. Found: C, 69.36; H, 5.48%.

cis-1,4-dihydronaphthalene carbonate (cis-DNC). Pure *cis*-DNC was obtained after removal of the acidified methanol filtrate from a polymer work-up under reduced pressure and recrystallization of the residue from methanol/hexane. Characterizations of the white product matches that previously described.[32] MP = 155 °C. ^{1}H NMR in $CDCl_3$: δ 2.90 (s, 2H, C*H*$_2$), 3.15 (s, 2H, C*H*$_2$), 5.19 (s, 2H, C*H*), 7.20-7.30 (m, 4H, aromatic *H*); C_6D_6/$CDCl_3$: δ 2.22 (s, 2H, C*H*$_2$), 2.62 (s, 2H, C*H*$_2$), 4.36 (s, 2H, C*H*), 6.75-7.05 (m, 4H, aromatic *H*). IR in CH_2Cl_2: 1807 (s), 1794 (sh); THF: 1811 (s) cm^{-1}. Anal. Calcd. for $C_{11}H_{10}O_3$: C, 69.46; H, 5.30. Found: C, 69.47; H, 5.49%.

Synthesis of 6,13-Bis(3-methanesulfonylpropyl)dibenzo[b,i][1,4,8,11]-tetraazacyclotetradecine or dimesylatetetraazaannulene (dmtaa). A 500 mL round bottom flask was charged with dhtaa (0.955 g, 2.36 mmol) and dry THF (250 mL). To this red mixture, NEt_3 (2.0 mL, 14 mmol) followed by methanesulfonyl chloride (1.0 mL, 13 mmol) were added using a syringe. The reaction was stirred at room temperature until complete conversion of the dihydroxy compound is observed *via* TLC (24-32 h). The solvent is rotovaped and the crude mixture washed thoroughly with distilled H_2O (150 mL) to remove triethylammonium chloride. Further washings using MeOH (50 mL), Et_2O (50 mL) and drying *in vacuo* gives the orange-red product (1.28 g, 97%). ^{1}H NMR (d_6-DMSO): δ 1.89 (p, 4H, -C*H*$_2$-), 2.32 (t, 4H, -C*H*$_2$-), 3.19 (s, 6H, C*H*$_3$), 4.24 (t, 4H, -C*H*$_2$-), 6.90 (m, 4H, aromatic H), 7.28 (m, 4H, aromatic H), 7.85 (m, 4H, C*H*), 13.61 (t, 2H, N*H*). Poor solubility precluded the collection of ^{13}C NMR. ESI-MS (m/z): 561.20 (MH^+). MP = 198 °C (dec). Anal. Calcd. for $C_{26}H_{32}N_4O_6S_2$: C, 55.70; H, 5.75; N, 9.99. Found: C, 54.79; H, 5.86; N, 9.55%.

Synthesis of 6,13-Bis(3-chloropropyl)-dibenzo[b,i][1,4,8,11]tetraaza-cyclotetradecine or dichlorotetraazaannulene (dctaa). A 30 mL tall vial with a stir bar was packed with dmtaa (0.600 g, 1.07 mmol) followed by [BMIM]Cl (1.92 g, 11.0 mmol) on top. The vial was placed in a 90 °C oil bath to let the ionic liquid melt down (~15 min). Stirring was then begun and after 24 h TLC shows complete conversion of the dimesylate to the dichloro compound. *Note*: If needed, some acetonitrile can be used to rinse down the sides of the vial during the course of the reaction to achieve complete mixing after

lowering the temperature to 80 °C. The resulting brown sludge is taken into CH_2Cl_2 (125 mL), washed with 20% aqueous NaCl solution (3x100 mL) and dried with magnesium sulfate. The solvent is then rotovaped and the residue washed with Et_2O (75 mL) to give a brown product after drying *in vacuo* (0.325 g, 69%). NMR in $CDCl_3$: ^{1}H δ 1.95 (p, 4H, -C*H*$_2$-), 2.41 (t, 4H, -C*H*$_2$-), 3.63 (t, 4H, -C*H*$_2$-), 6.92 (m, 4H, aromatic H), 7.05 (m, 4H, aromatic H), 7.63 (m, 4H, C*H*), 13.71 (t, 2H, N*H*); ^{13}C{^{1}H} δ 29.8, 34.5, 43.9, 106.0, 113.5, 124.3, 137.5, 147.0. ESI-MS (m/z): 441.18 (MH^+). MP = 224 °C (dec). X-ray quality crystals grown *via* slow cooling of a hot MeCN solution.

Synthesis of 6,13-Bis(3-bromopropyl)-dibenzo[b,i][1,4,8,11]tetraaza-cyclotetradecine or dibromotetraazaannulene (dbtaa). Prepared in a similar manner to dctaa described above by using [BMIM]Br. A brownish red product is isolated in greater than 60% yield. Characterizations match those previously reported.[51] ^{1}H NMR (d_6-DMSO): δ 2.02 (p, 4H, -C*H*$_2$-), 2.34 (t, 4H, -C*H*$_2$-), 3.55 (t, 4H, -C*H*$_2$-), 6.91 (m, 4H, aromatic H), 7.28 (m, 4H, aromatic H), 7.85 (m, 4H, C*H*), 13.61 (t, 2H, N*H*). Anal. Calcd. for $C_{24}H_{26}Br_2N_4$: C, 54.36; H, 4.94; N, 10.57. Found: C, 55.22; H, 5.23; N, 10.42%.

Synthesis of 6,13-Bis[3-(N,N,N-triethylammonium)propyl)]-dibenzo[b,i]-[1,4,8,11]tetraazacyclotetradecine dibromide or diammoniumtetraazaannulene (dataa). A 100 mL Schlenk flask charged with dbtaa (0.365 g, 0.688 mmol) is treated with 50 mL DMF and NEt_3 (10 mL, 72 mmol) and placed in an oil bath set at 50 °C. The dark red solution is let stir for 3 days after which the solvents are removed under reduced pressure.

The resulting red residue is washed down the sides of the flask with CH_2Cl_2 (< 5 mL) and treated with THF (50 mL). It is stirred for a few minutes, filtered, and dried *in vacuo* to give the product as a red solid (0.462 g, 92%). NMR in d_6-DMSO: ^{1}H δ 1.17 (t, 18H, NCH_2CH_3), 1.81 (m, 4H, -CH_2-), 2.27 (t, 4H, -CH_2-), 3.13 (m, 4H, -CH_2-), 3.25 (q, 12H, NCH_2CH_3), 6.93 (m, 4H, aromatic H), 7.31 (m, 4H, aromatic H), 7.91 (m, 4H, C*H*), 13.64 (t, 2H, N*H*); ^{13}C{^{1}H} δ 7.31, 23.7, 28.8, 52.2, 55.6, 106.7, 114.1, 124.4, 136.9, 148.0. ESI-MS (m/z): 286.22 [$(M-2Br^-)^{2+}$]. Anal. Calcd. for $C_{36}H_{56}Br_2N_6 \cdot 3H_2O$: C, 54.96; H, 7.94; N, 10.68. Found: C, 54.12; H, 7.29; N, 10.54%. X-ray quality crystals grown *via* vapor diffusion of methyl *t*-butyl ether into a MeOH solution.

CHAPTER III

MODEL STUDIES ON THE DIRECT CARBOXYLATION OF HYDROCARBONS WITH CARBON DIOXIDE*

CO_2 Insertion Reactions into Ru-Me and Ru-H Bonds

The insertion reactions of CO_2 into metal-hydrogen and metal-carbon sigma bonds at different metal centers are well-studied processes.[52-61] As indicated in Equations 1 and 2 the insertion products are metal formates and metal carboxylates. The former process proceeds via an H•••CO_2 interaction leading to cleavage of the M–H bond with concomitant formation of a metal-bound formate ligand. That is, in general, no prior coordination of CO_2 to the metal center is required. A similar conclusion was reached for insertion of CO_2 into metal-carbon sigma bonds. In early studies, we have performed extensive mechanistic comparisons between these two insertion reactions utilizing group 6 metal carbonyl anionic derivatives, e.g., $M(CO)_5R^-$, where R = H, alkyl or aryl.[62-67] The results of these investigations can be summarized as follows:

(a) Equation **1** is highly reversible, whereas equation **2** is irreversible.

(b) CO_2 insertion into M–H bonds is much faster than insertion into the corresponding M–C sigma bonds.

---

* Reprinted (adapted) with permission from: Darensbourg, D. J.; Kyran, S. J.; Yeung, A. D.; Bengali, A. A. *Eur. J. Inorg. Chem.* **2013**, 4024. Copyright 2013 Wiley-VCH Verlag GmbH & Co. KGaA, Weinham. Li, B.; Kyran, S. J.; Yeung, A. D.; Bengali, A. A.; Darensbourg, D. J. *Inorg. Chem.* **2013**, *52*, 5438. Copyright 2013 American Chemical Society. Kyran, S. J.; Muhammad, S.; Knestrick, M.; Bengali, A. A.; Darensbourg, D. J. *Organometallics* **2012**, *31*, 3163. Copyright 2012 American Chemical Society.

(c) The rate of CO_2 insertion increases with the nucleophilicity of the M–H and M–C moieties, e.g., M–Me >> M–Ph.

(d) The CO_2 insertion process occurs at coordinatively saturated metal centers, i.e., prior coordination of CO_2 at the metal center is not required.

(e) CO_2 insertion into M–C sigma bonds occurs with retention of configuration about the α carbon center.

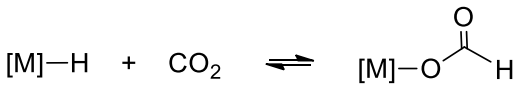

1

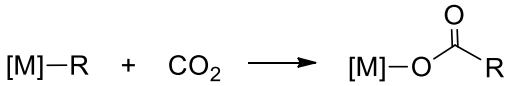

2

Although the relative reactivity of CO_2 at *isolated* metal-hydrogen and metal-carbon sigma bonds in analogous metal complexes is as indicated in (b) and decarboxylation readily occurs in the formate derivative, it has only recently been established that thermodynamics favor formation of carbon-carbon bonds. That is, Field and coworkers have shown the reaction sequence illustrated in Scheme 9 to be operative for the $Ru(dmpe)_2(Me)H$ complex.[68] Whereas CO_2 insertion into the ruthenium-hydride bond to afford the formate complex was the kinetic product, the thermodynamically more stable insertion product was acetate derivative. The reaction pathway of the rearrangement presumably involves decarboxylation of the formate complex with concomitant insertion of CO_2 into the Ru-Me bond. Further insertion of CO_2 to provide an acetate-formate ruthenium derivative was not observed.

Scheme 9

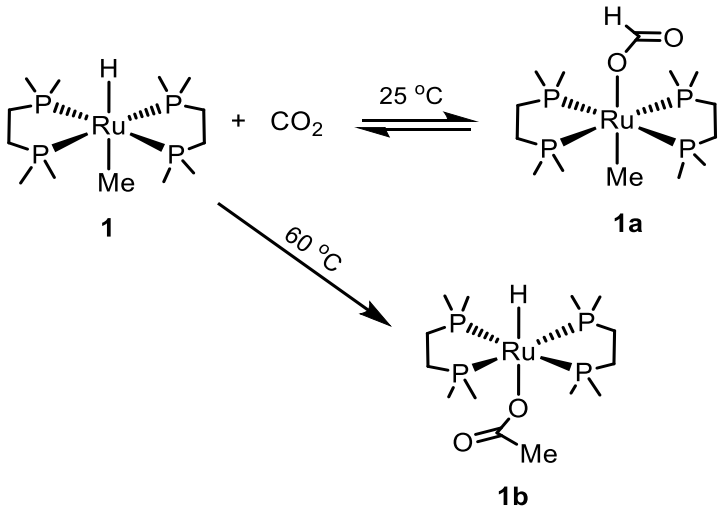

This represents an important observation which may be useful in the functionalization of hydrocarbons, since reductive elimination would afford the more desirable carboxylic acid *versus* the alkyl formate alternative. Nevertheless, because methane plus CO_2 to acetic acid is a non-spontaneous process, it will be necessary to couple this reaction to another, such as acid/base chemistry in order to drive it forward. This is analogous to the pathway employed by Jessop and Noyori for the production of formic acid from the coupling of CO_2 and hydrogen.[20,69]

In this section, we wish to present kinetic data for these CO_2 insertion processes, as well as computational studies, to define the various activation barriers and thermodynamic driving forces for these and closely related processes.[70] Changes in ancillary ligands on the metal center will be investigated in efforts to better optimize the kinetic and thermodynamic parameters for these CO_2 insertion reactions.

Kinetic Studies. The carbon dioxide insertion reactions depicted in Scheme 9 have been well-described by Field and coworkers;[68] nevertheless, there is a need to assess the kinetic parameters for these and related processes. Under an atmosphere of CO_2, the *trans*-Ru(dmpe)$_2$(Me)H complex, **1** readily converts completely to the formate complex, *trans*-Ru(dmpe)$_2$(Me)(O_2CH), **1a** within a few minutes at 0 °C. This can be clearly seen in the ^{1}H NMR with the appearance of a formate hydrogen at 8.68 ppm and the disappearance of the hydride signal from the starting material at -12.3 ppm in d_6-benzene. The reaction is reversible and the formate complex reverts to the hydride complex in the absence of a CO_2 atmosphere. Consistent with this observation, the introduction of an excess of $^{13}CO_2$ to a solution of complex **1a** also shows a complete exchange to *trans*-Ru(dmpe)$_2$(Me)($O_2{}^{13}$CH) within 20 minutes at room temperature. An unexpected observation is the slow conversion of the formate complex to a yet to be identified product at room temperature. The ^{1}H NMR spectrum indicates this new species with a growing formate signal at 8.82 ppm along with an upfield methyl resonance at -1.36 ppm (Figure 21). A corresponding ^{31}P NMR signal is seen as a singlet peak at 42.0 ppm with the decay of the original formate complex resonance at 44.2 ppm. A 50% conversion is seen after 2.5 days. Although our plans are to better establish the nature of this *time-dependent* species in solution, relevant to this study both formate species are eventually converted to the *trans*-Ru(dmpe)$_2$(O_2CMe)H derivative (*vide infra*).

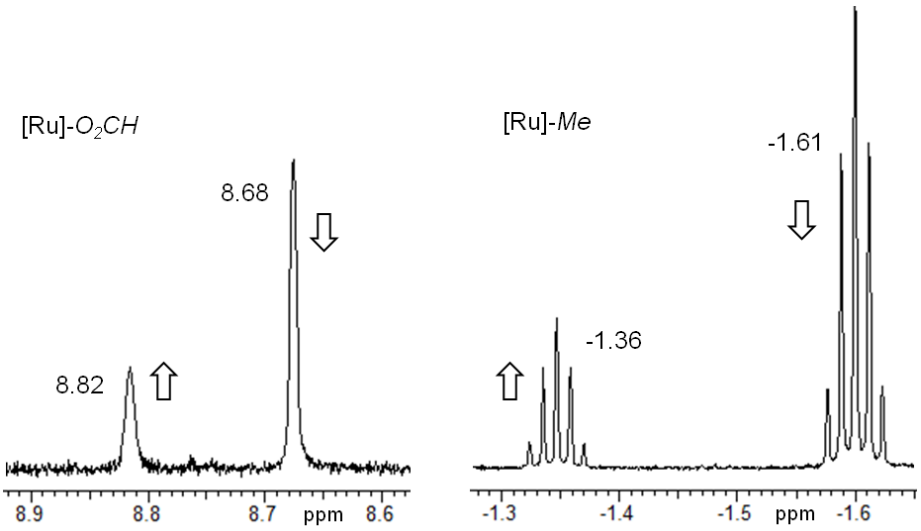

Figure 21 ^{1}H NMR spectrum showing the appearance of new formate and methyl resonances of an unidentified complex relative to the signals of *trans*-Ru(dmpe)$_2$(Me)(O$_2$CH) complex. Spectrum collected after 13 h at r.t. showing a 25% conversion.

Upon heating the formate complex, *trans*-Ru(dmpe)$_2$(Me)(O$_2$CH), under 10 atm of CO_2 over a period of 5 days at 60 °C, the acetate hydride complex, *trans*-Ru(dmpe)$_2$(O$_2$CMe)H is produced and the ^{1}H NMR shows a singlet acetate signal at 2.10 ppm and a pentet hydride resonance at -22.5 ppm. This complex has been characterized structurally by Field and coworkers, prepared by an alternate route involving Ru(dmpe)$_2$(H)$_2$ and acetic acid.[68] As previously reported, the acetate hydride complex, **1b** does not afford further reaction with CO_2 to produce an acetate-formate ruthenium complex. This deactivation towards CO_2 insertion with regards to the presence of an electron withdrawing ligand on the ruthenium center is also distinctly observed in the case of the hydride chloride complex, *trans*-Ru(dmpe)$_2$(Cl)H. With a *trans* chloride ligand

versus an electron donating methyl, the hydride does not undergo insertion to produce a formate even at 13 atm of CO_2 at room temperature. Computations show that this is not only due to a high activation barrier but also due to a thermodynamically disfavored formate product and is discussed in more detail later.

The dimethyl complex, *trans*-$Ru(dmpe)_2(Me)_2$, **2** when exposed to an atmosphere of CO_2, results in the formation of a mono-acetate product, *trans*-$Ru(dmpe)_2(Me)(O_2CMe)$, **2a** within 24 h at room temperature as noted by Field and coworkers.[68] Kinetic experiments were carried out to investigate the mechanistic aspect of this reaction. Figure 22 depicts the 3D stack plots from *in situ* infrared monitoring of this process in benzene along with the reaction profiles indicating the same growth rate in the IR bands of the resulting mono-acetate product.

The concentration of CO_2 present in solution (under 1 atm CO_2) is only four times that of the ruthenium complex, but it does not change over the course of the long reaction time (12 hours or more) as the CO_2 consumed is replaced concomitantly by the dissolution of CO_2 gas, which is present in 200 times excess above the solution in the sealed flask. Thus, this reaction is essentially of a pseudo-first-order condition with respect to the ruthenium complex (Equation 3) as evidenced by the linear natural log plot over three half-lives of the absorption data of the Ru-acetate band (1378 cm^{-1}) of **2a** at 30 °C (Figure 23).

$$\text{rate} = k_{obs}[Ru]^1, \text{ where } k_{obs} = k[CO_2]^n \qquad 3$$

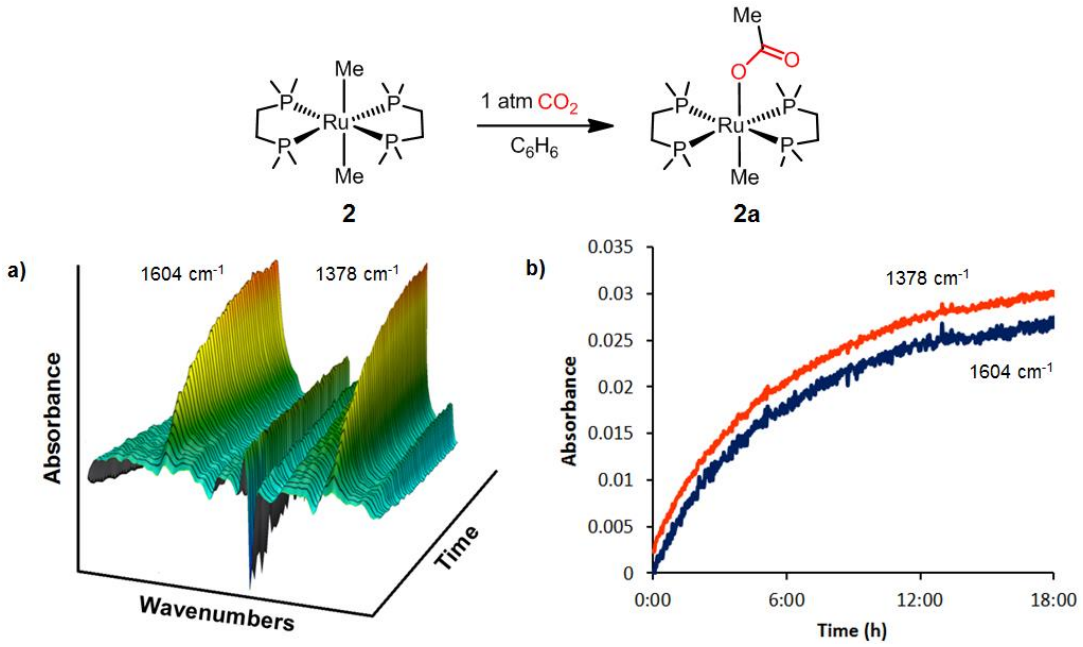

Figure 22 a) Three-dimensional IR stack plots showing the growth of the Ru-acetate bands and b) the reaction profiles of the product formation upon CO_2 insertion in benzene at 30 °C.

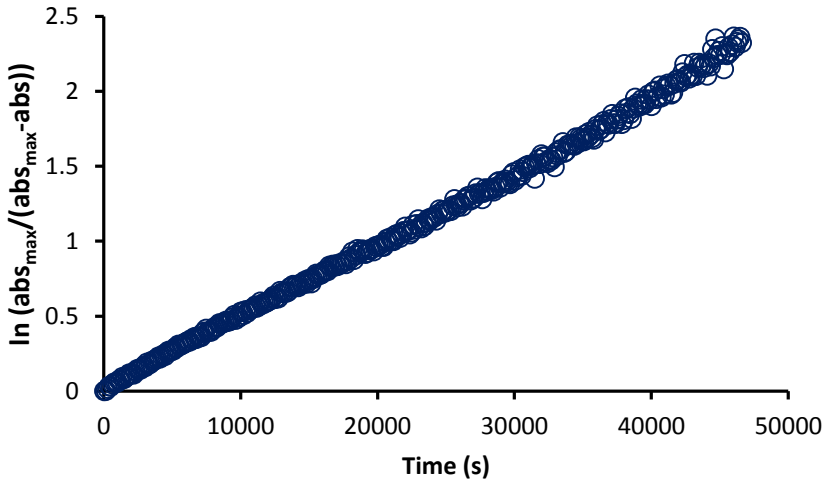

Figure 23 Natural log plot of absorption data *versus* time of the Ru-acetate band at 1378 cm^{-1} of **2a** at 30 °C. A linear trend consistent with a first-order condition in **2** gives a k_{obs} value of 4.85 x 10^{-5} s^{-1}.

The reaction rate for the insertion of CO_2 into the Ru-C bond of **2** was also monitored by ^{1}H NMR, where the decay of the methyl signals from *trans*-Ru(dmpe)$_2$(Me)$_2$ complex (-1.20 ppm) and the growth of the new acetate and methyl signals (2.00 and -1.60 ppm, respectively) of the product *trans*-Ru(dmpe)$_2$(Me)(O_2CMe), **2a** can be followed (Figure 4). At 25 °C, the reaction was complete within 24 h under 1 atm of CO_2, whereas the experiment conducted at 4.1 atm in a high pressure NMR tube is complete within 7 h, showing a reaction dependence on CO_2 concentration. Plotting the k_{obs} vs [CO_2] at different pressures results in a linear graph with a y-intercept of zero as anticipated for a first-order reaction with respect to the concentration of CO_2 (Figure 25). Thus, the complete rate expression reveals a first-order rate dependence in both complex **2** and CO_2 (Equation 4).

$$\text{rate} = k\,[\text{Ru}]^1\,[CO_2]^1 \qquad 4$$

The temperature dependence of the rate constant, *k*, for the CO_2 insertion into **2** to give **2a** was measured over a 21 °C range (Figure 26) and the resulting *k* values, derived as per Equation 4, are listed in Table 5.

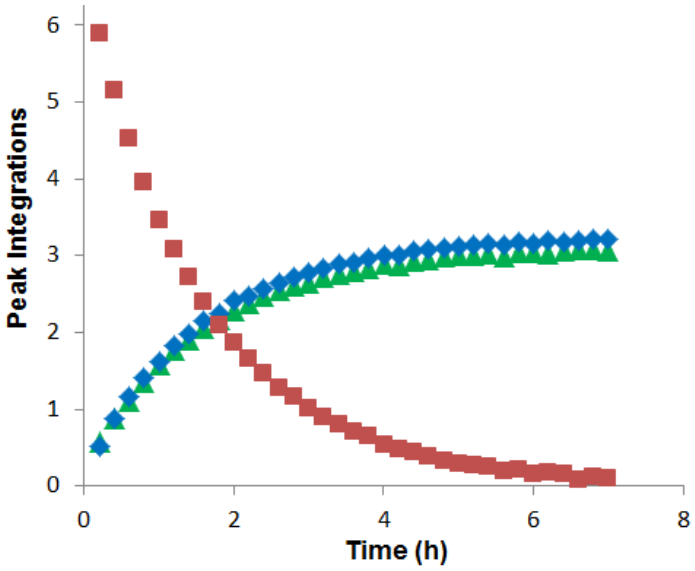

Figure 24 Transformation of methyl signals in ^{1}H NMR for the reaction of **2** with CO_2 (4.1 atm) at 25 °C in d_6-benzene. Reactant: (■) 6H, [Ru](*Me*)$_2$. Product: (▲) 3H, [Ru]-O_2C*Me* and (♦) 3H, [Ru]-*Me*.

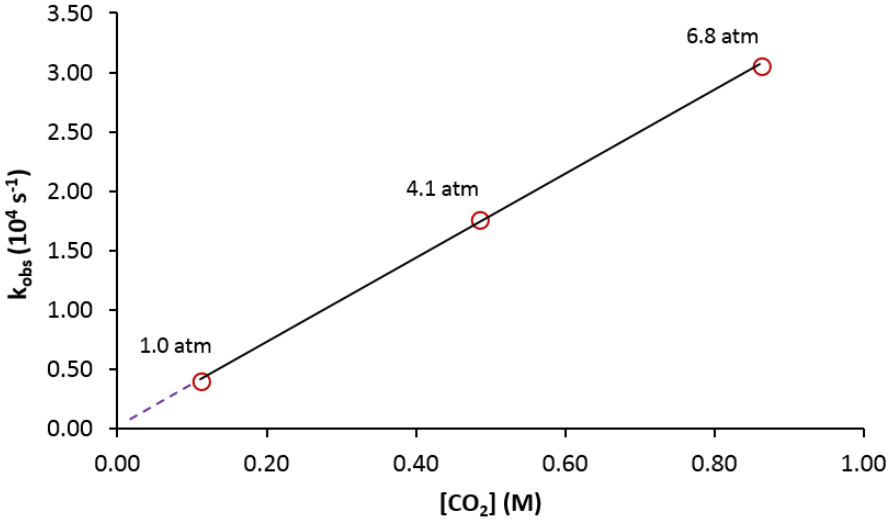

Figure 25 Plot of k_{obs} *versus* [CO_2] for the formation of complex **2a** at 25 °C. The equation of the trend line was y = 0.000353x + 0.000003, with an R^2 value of 0.9996. Solubility data of CO_2 in benzene was obtained from literature.[71]

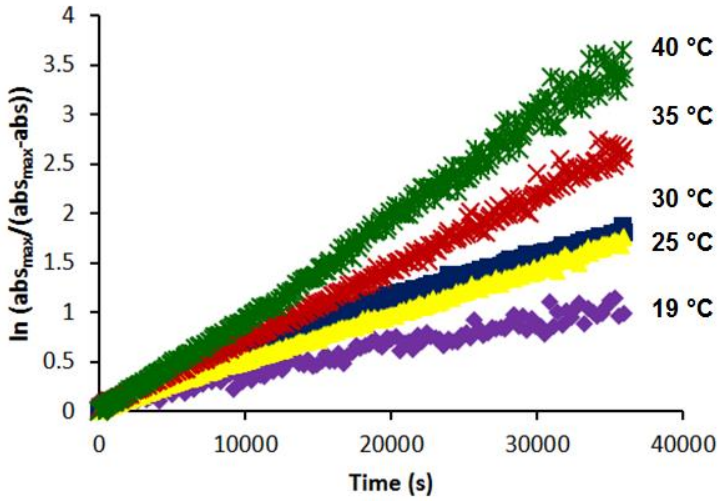

Figure 26 Natural log plots of reaction rate for the conversion of **2** to **2a** in benzene under 1 atm of CO_2 at various temperatures.

Table 5 Temperature dependent rate constants for the formation of **2a** in benzene under 1 atm of CO_2.

T (°C)	[a][CO_2] (M)	k_{obs} (10^4 s^{-1})	k (10^4 M^{-1} s^{-1})
19	0.118	0.261	2.21
25	0.111	0.401	3.61
30	0.106	0.485	4.57
35	0.101	0.721	7.15
40	0.095	0.999	10.5

[a]Solubility data of CO_2 obtained from literature.[71]

The activation parameters for the formation of **2a** were determined through Eyring analysis and found to have values for $\Delta H^{\ddagger}$ of 12.7 ± 0.6 kcal•mol^{-1} and a $\Delta S^{\ddagger}$ of -31.9 ± 2.0 e.u. (Figure 27). The large negative value of $\Delta S^{\ddagger}$ indicates a highly ordered transition state and, along with the small value of $\Delta H^{\ddagger}$, shows an associative reaction mechanism.

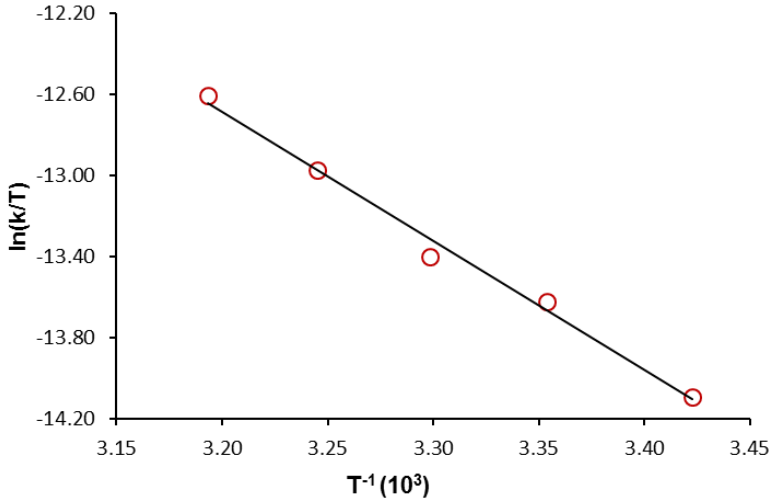

Figure 27 Eyring plot of the reaction of *trans*-Ru(dmpe)$_2$(Me)$_2$ with CO_2 (1 atm). The equation for the trend line is y = -6.375x + 7.713, with an R^2 value of 0.991.

Earlier studies from our laboratory have demonstrated that the CO_2 insertion reaction into the tungsten-Me bond also obeys first-order kinetics with respect to both [W-Me] and [CO_2], with rate increases occurring upon increasing the electron density at the metal center by ancillary phosphorus donor ligands.[64] The reaction barriers observed herein are similar to those determined for CO_2 insertion into the W-C bond of *cis*-W(CO)$_4$[P(OMe)$_3$]Me, $\Delta H^{\ddagger}$ = 10.2 ± 0.2 kcal•mol^{-1} and $\Delta S^{\ddagger}$ = -43.3 ± 0.9 e.u. where a highly ordered transition state of the form in Figure 28 was proposed.[64,72] Consistent with this interpretation, CO_2 insertion into the W-C bond of *threo*-PhCHDCHDW(CO)$_5^-$ led to production of the corresponding *threo* carboxylate complex, indicative of retention of configuration at the α-carbon center.[73]

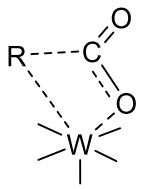

Figure 28 Proposed transition state for CO_2 insertion.[64,72]

With regards to the kinetic data obtained for the formation of **2a** via ^{1}H NMR spectroscopy *versus in situ* IR spectroscopy, we would like to note that they are comparable as can be seen from the similar rate constants calculated from both methods (Table 6). In the ^{1}H NMR spectra, we also observed an unidentified side product (~ 10%) that grows in with peaks at -1.70 (pentet) and 44.3 (singlet) ppm in the ^{1}H and ^{31}P NMR, respectively. This species was reported previously, but rather as a transient intermediate that diminished over the course of the reaction.[68] In this latter instance, its disappearance is likely due to the presence of adventitious water which reacts with the transient species. In our reactions, we have seen it grow in at a similar rate, however it persists at the end of the reaction. Upon spiking the sample with water, the transient species disappears quickly.

Table 6 Rate constants calculated from following the methyl peaks via ^{1}H NMR and from the *in situ* IR monitoring of acetate bands of **2a** for the reaction of **2** with CO_2.

	Product		**Reactant**	**IR acetate band**
	[Ru]-O_2C*Me*	[Ru]-*Me*	[Ru](*Me*)$_2$	
k (10^4 M^{-1} s^{-1}) at 25 °C	3.79	3.63	3.53	3.61

The diacetate complex, *trans*-Ru(dmpe)$_2$(O_2CMe)$_2$, produced via a second CO_2 insertion was much slower and can be observed only at high pressures of CO_2.[68] A reaction

followed by *in situ* IR spectroscopy at 19 °C, required 5 days to go to completion at a CO_2 pressure of 6.8 atm. The rate constant and reaction half-life are provided in Table 7. This rate deceleration can be rationalized based on the presence of the less electron-donating acetate ligand in the *trans*-Ru(dmpe)$_2$(Me)(O$_2$CMe) complex, which reduces the electron density at the ruthenium center, thereby resulting in a higher activation barrier for the second CO_2 insertion process.

Table 7 Rate constants and reaction half-lives of CO_2 insertions into **2** carried out in benzene.

	1st insertion	**2nd insertion**
k (10^4 M^{-1} s^{-1}) at 19 °C	2.21	0.0959
$t_{1/2}$	7.5 h (1 atm)	22.5 h (6.8 atm)

Computational Studies. In order to better understand these observations, Dr. Andrew Yeung from our group carried out DFT computational studies to assess the thermodynamics and kinetics behavior of these important transformations of CO_2. Initially, the enthalpies of the reaction of various ruthenium and iron complexes with carbon dioxide to yield carboxylate complexes (Scheme 10) were calculated. Using the B3LYP/BS1 geometry (basis sets are defined in the Computational Methods section), single-point energy calculations were performed using various functionals (B3LYP, BP86, TPSS, M06) using the BS2 basis set. The enthalpies of reaction were qualitatively the same between different functionals, giving us confidence in the results. There was no experimental thermodynamic data for comparison, so the B3LYP functional was chosen

for subsequent work. Basis set effects were also examined, and BS2 was chosen because it gave results identical to that obtained with a larger basis set.

In the working model for this reaction, CO_2 insertion converts the strongly sigma-donating methyl or hydride ligand into a more weakly-donating carboxylate ligand, thereby reducing the electron-density at the metal center. As a result, the carboxylation reaction is more favored when the electron-density at the metal center is greater.

Scheme 10

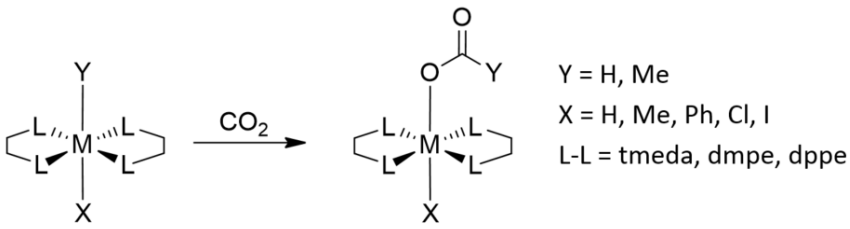

The reaction depicted in Scheme 10 has been somewhat simplified, i.e., complexes of the form L_2RuXCO_2Y have two possible conformations (Figure 29). Where Y = H, we found that the geometries having both oxygen atoms point toward the metal center (ii) are lower in energy than the geometries with only one oxygen atom pointing toward the metal center (i). The difference in enthalpy for these formate complexes is non-trivial, approximately 8-9 kcal/mol (Table 8). Indeed, the structure in (ii) is generally observed in the solid-state by X-ray crystallography.

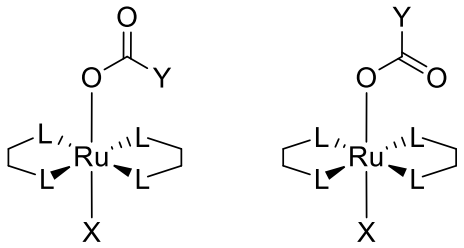

Figure 29 The two possible conformations of $L_2RuX(CO_2Y)$ complexes. The conformation labels (i) and (ii) are used hereafter.

Table 8 Relative energies of conformation (ii) *vs* conformation (i) for complexes of the form $Ru(dmpe)_2X(formate)$.

X	**ΔH, (ii)-(i) (kcal/mol)**
H	-9.2
Me	-8.9
Ph	-8.3
Formate	-7.9
Acetate	-7.5
Cl	-8.6
I	-8.3

The lower energy for complexes of conformation (ii) is probably due to a favorable electrostatic interaction between the carbonyl oxygen with the metal. Acetate complexes appear not to adopt conformation (i) due to steric repulsion. As a simple rotation about the C-O bond transforms one conformer to the other, the additional barrier is expected to be low. Conformation (i) remains significant because it is the immediate product when carbon dioxide inserts into a ruthenium-hydride bond, *vide infra*.

As noted earlier, Field and coworkers reported that *trans*-Ru(dmpe)$_2$Me$_2$ undergoes two sequential CO_2 insertion reactions to give the diacetate complex. In comparison, *trans*-Ru(dmpe)$_2$MeH inserts CO_2 into the Ru-H bond to give the formate complex as the kinetic product. The methyl formate complex yields the acetate hydride upon heating, but the latter does not insert a second equivalent of carbon dioxide.[68] Our computational results explain those observations: the two sequential carboxylation reactions of *trans*-Ru(dmpe)$_2$Me$_2$ are strongly exothermic (-28 and -21 kcal/mol, see Figure 30). Both possible reactions between *trans*-Ru(dmpe)$_2$MeH and CO_2 are exothermic. Addition of another equivalent of carbon dioxide to convert the acetate hydride complex to acetate formate complex (i) is endothermic, and the overall reaction to give acetate formate complex (ii) is barely exothermic. The loss of entropy encountered upon CO_2 insertion also helps make this reaction quite unfeasible.

This carboxylation of the hydride acetate complex is disfavored because the acetate ligand is a poor electron donor. With the electron-withdrawing chloride X ligand, the carboxylation is similarly unfavorable. Overall, no double insertion product is observed, presumably because the activation barrier from *trans*-Ru(dmpe)$_2$Me(formate) complex to yield the dicarboxylate product is higher than the overall barrier for it to transform into the *trans*-Ru(dmpe)$_2$(O_2CMe)H that does not react further.

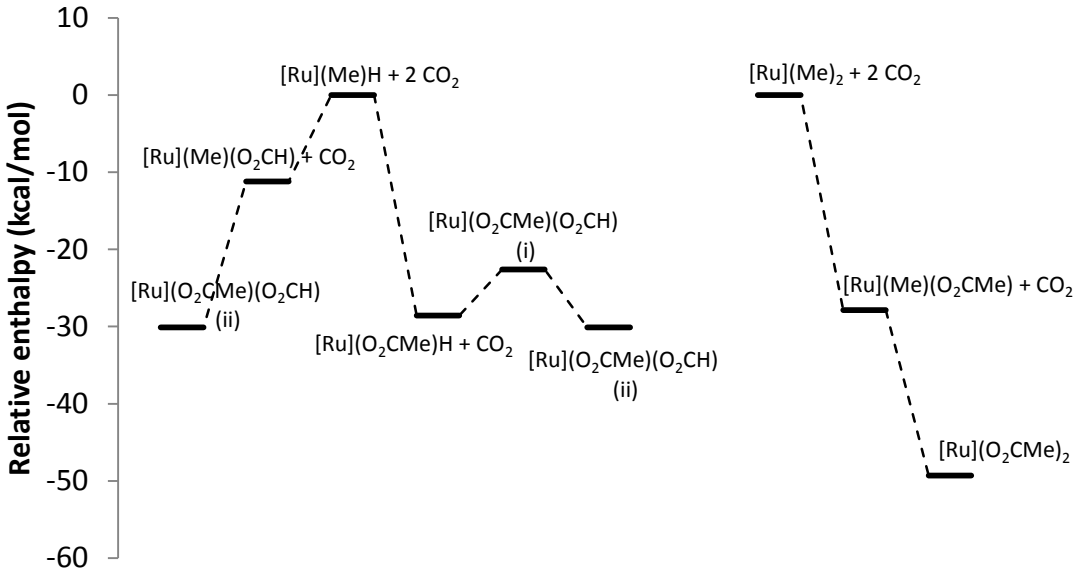

Figure 30 Relative enthalpies for the reactions between $Ru(dmpe)_2$ complexes with carbon dioxide; the corresponding free energy diagram is qualitatively the same. *trans*-$Ru(dmpe)_2$ is abbreviated [Ru].

Effect of the X Ligand

The effect of several X ligands were examined for the $Ru(dmpe)_2XY$ system. Electron-donating X-ligands were found to favor CO_2 insertion; the enthalpy of CO_2 insertion decreases as follows (Figure 31):

X = H ≈ Me > Ph >> acetate ≈ formate ≈ Cl > I

Incidentally, acetate formation is generally more exothermic than formate formation by approximately 17 kcal/mol.

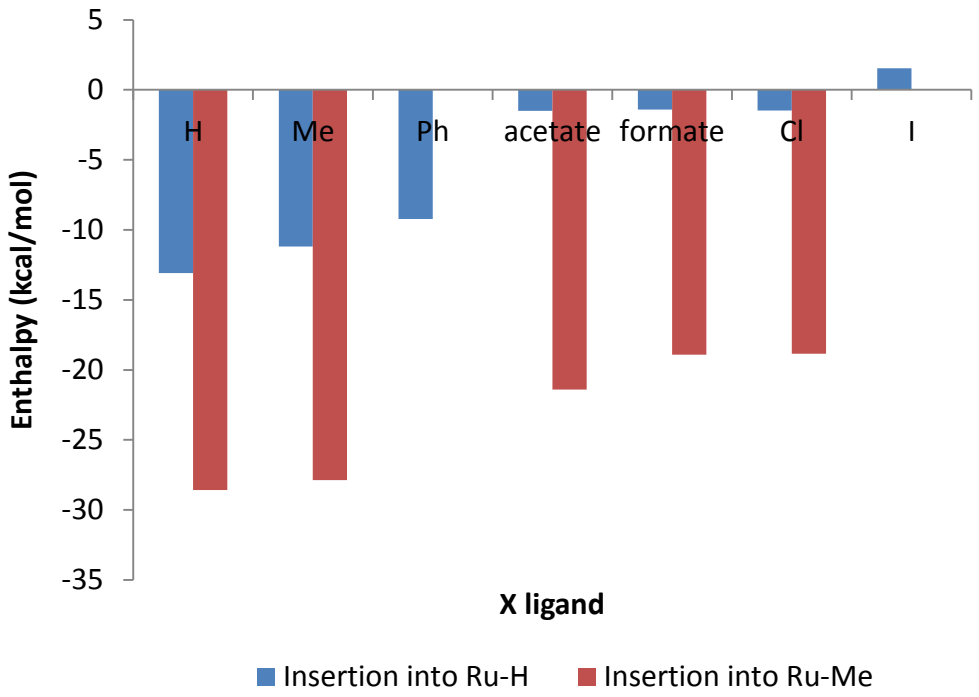

Figure 31 Enthalpies of CO_2 insertion into the Ru-Y bond for compounds of the form, $Ru(dmpe)_2XY$.

We were able to successfully locate the gas phase transition state for CO_2 insertion for three complexes of the form $Ru(dmpe)_2XH$ using the B3LYP functional and the BS2++ basis set. The calculated enthalpies listed in Table 9 indicate that the electron donating ability of the X ligands *trans* to the hydride ligand undergoing CO_2 insertion influences both the enthalpy of the reaction, as well as its activation barrier. It is important to note that decarboxylation of these formate complexes require that they adopt the less stable conformation (i) (Figure 32). Accordingly, the overall barriers to decarboxylation are 7.5 – 9.2 kcal/mol higher than they appear here, *vide supra*. Unfortunately, efforts to locate the analogous transition states yielding acetate complexes were fruitless, so the free

energy barriers presented in this section cannot be directly compared to the experiment, and the kinetics of acetate formation cannot be discussed.

Table 9 Enthalpies of species involved in CO_2 insertion reactions, transition state relative to reactant plus CO_2 (energies in kcal/mol). (B3LYP/BS2++, gas phase).

X	Ru(dmpe)$_2$XH + CO_2	Transition State	Ru(dmpe)$_2$X(formate) (i)
H	0	7.3	-5.1
Cl	0	27.9	6.4
Me	0	10.2	-3.3

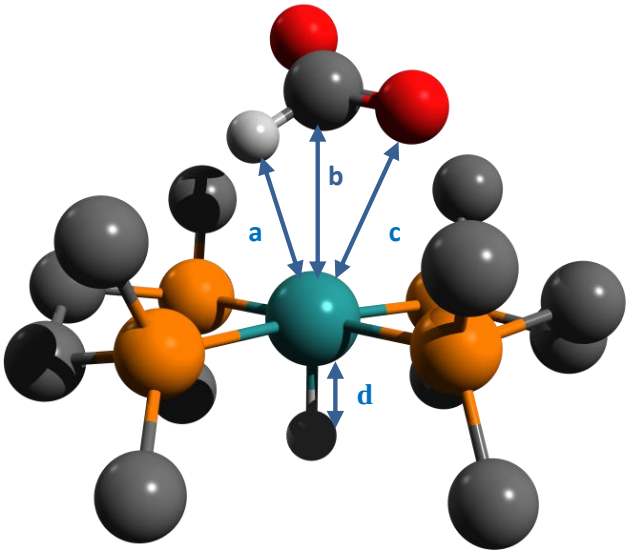

Figure 32 The transition state for Ru(dmpe)$_2$H$_2$ leading to carboxylation. The immediate product of this elementary reaction is the formate complex of conformation (i). Hydrogen atoms on the dmpe ligand have been omitted for clarity. Distances: Ru-H (a) 2.471 Å; Ru-C (b) 2.936 Å; Ru-O (c) 3.003 Å; Ru-H (d) 1.575 Å.

At the transition state for Ru(dmpe)$_2$H$_2$ to undergo carboxylation, the Ru-H and Ru-O distances (2.471 Å and 3.003 Å , respectively) are significantly elongated compared to the dihydride starting material, and the formate product (1.694 Å and 2.276 Å,

respectively). At the transition state, the supporting Ru-H bond is shortened (1.575 Å), compensating for the central ruthenium atom's weaker interactions with the developing formate ligand.

Supporting Ligand Effects

With dmpe supporting ligands, formate formation is favored for X = Me and poorly so for X = Cl (Figure 33). Both reactions were slightly more favored where a chelating dicarbene was used (1,1'-dimethyl-3,3'-methylenediimidazoline-2,2'-diylidene), whereas when dppe was used, both reactions were now endothermic. In contrast, both reactions were strongly favored when tmeda was used.

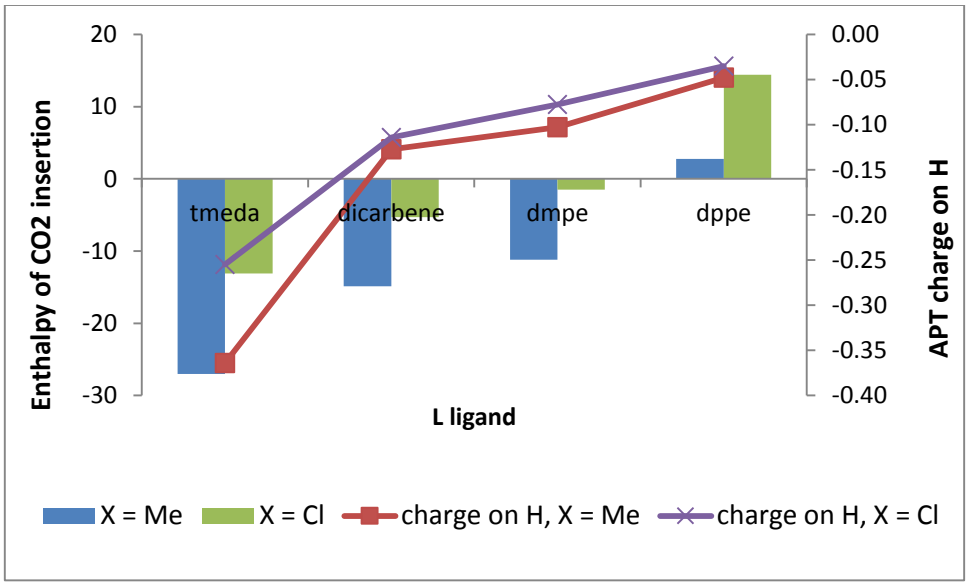

Figure 33 Enthalpies of CO_2 insertion into the Ru-Y bond for complexes of the form RuL_2XY and the corresponding APT charges on the hydride.

The amount of negative charge on H, represented by its atomic polar tensor (APT) atomic charge[74] (Figure 33), is a function of how pi-acidic the L ligands are: Strongly pi-

acidic L ligands like dppe cause the hydride ligand (that undergoes CO_2 insertion) to be less hydridic, whereas poorly pi-acidic L ligands like tmeda cause the hydride ligand to be more so. As the hydride ligand becomes more negatively charged, CO_2 insertion into the Ru-H bond becomes more exothermic and favored.

Ruthenium *vs* Iron

The iron complexes were calculated to react with carbon dioxide more exothermically than the ruthenium analogs do. Notably, carboxylation of trans-$Fe(dmpe)_2(O_2CMe)H$ is exothermic by 14.4 kcal/mol vs. 1.5 kcal/mol for *trans*-$Ru(dmpe)_2(O_2CMe)H$ (Table 10, entry 6). Insertion of carbon dioxide into the Fe-H bond is exothermic by approximately16 kcal/mol, whereas insertion into the Fe-Me bond is consistently exothermic by approximately 31 kcal/mol.

Table 10 Enthalpies of CO_2 insertion into the M-Y bond for complexes of the form, $M(dmpe)_2XY$.

No.	**X/Y**	**Enthalpy (kcal/mol)**	
		M = Fe	**M = Ru**
1	H/H	-18.0	-13.1
2	formate/H	-14.6	-1.4
3	Me/Me	-32.7	-27.9
4	acetate/Me	-32.0	-21.4
5	H/Me	-31.9	-28.6
6	acetate/H	-14.4	-1.5
7	Me/H	-16.8	-11.2
8	formate/Me	-29.5	-18.9

The computational results indicate that the carboxylation of the iron formate hydride complex is favorable whereas the same for ruthenium is unfavorable, and that the

sequential carboxylation reactions for the iron and ruthenium dimethyl complexes are favorable. These findings are in excellent agreement with published experimental work,[68,75,76] lending weight to our predictions.

Iron complexes react more exothermically than the ruthenium complexes due to its greater electron density. In fact, a leveling effect is observed for iron, in that its high electron density swamps the contribution of the X ligands. Regardless of the X ligand, acetate and formate production are consistently exothermic by 32 and 8 kcal/mol, respectively, though the carboxylation of *trans*-Ru(dmpe)$_2$(formate)H deviates somewhat (Table 10, entry 2). To further illustrate, ruthenium is able to discriminate between a strongly donating hydride or methyl ligands from a more poorly donating carboxylate ligands, whereas iron is unable to do so.

Summary and Conclusions. Kinetic measurements for the CO_2 insertion reactions into the Ru-H and Ru-Me bonds of the complexes *trans*-Ru(dmpe)$_2$(Me)H and *trans*-Ru(dmpe)$_2$(Me)$_2$ were determined by *in situ* infrared and NMR spectroscopies. These studies revealed a significantly higher activation energy for CO_2 insertion into Ru-Me bonds *versus* Ru-H bonds. Whereas CO_2 insertion into the Ru-H to afford the corresponding formate complex occurred instantaneously at 0 ^{o}C, CO_2 insertion into the Ru-Me bond had $\Delta H^{\ddagger}$ and $\Delta S^{\ddagger}$ values of 12.7 ± 0.6 kcal•mol^{-1} and -31.9 ± 2.0 e.u., respectively. These activation parameters are indicative of a highly ordered transition state. In both instances, the presence of less electron-donating *trans* ligands greatly retard the rate of CO_2 insertion. For example, although *trans*-Ru(dmpe)$_2$(CH)$_3$H readily inserts

CO_2 to provide the formate derivative, *trans*-Ru(dmpe)$_2$(O_2CMe)H does not provide a stable formate complex upon reaction with CO_2. Similarly, *trans*-Ru(dmpe)$_2$(Cl)H upon reaction with 13 atm of CO_2 does not lead to formate productions.

Computational studies support these experimental observations. Furthermore, these studies predict that upon replacing dmpe in these ruthenium complexes with tmeda, these CO_2 insertion processes will be more thermodynamically and kinetically favored over their dmpe counterparts. On the other hand, replacing dmpe by dppe has the opposite negative effect of retarding the insertion reaction. Additionally, these calculations assert that CO_2 insertions into the corresponding Fe-H and Fe-Me derivatives are both thermodynamically and kinetically favored over their ruthenium analogs.

Experimental Section. The starting materials *trans*-Ru(dmpe)$_2$(Me)$_2$,[77] *trans*-Ru(dmpe)$_2$(Cl)H,[78] and *trans*-Ru(dmpe)$_2$(Me)H[68] were synthesized according to literature. Benzene was purified by an MBraun Manual Solvent Purification System packed with Alcoa F200 activated alumina desiccant. Deuterated solvents d_6-benzene and d_8-toluene (Sigma-Aldrich) were dried over molecular sieves. Bone Dry grade carbon dioxide (99.999%) was purchased from Airgas Specialty Gases and passed through molecular sieves before use. *In situ* IR monitoring was carried out using a Mettler Toledo iC10 ReactIR with an AgX fiber conduit probe having a SiComp ATR crystal. NMR spectra were recorded on a Varian INOVA 500 (operating at 499.42 and 202.17 MHz for ^{1}H and ^{31}P, respectively). ^{1}H NMR spectra were referenced to residual solvent resonances, while ^{31}P NMR spectra were referenced to an external H_3PO_4 in D_2O at 0.0 ppm.

Kinetic Measurements

IR: In a typical experiment, a 0.03 M solution of *trans*-Ru(dmpe)$_2$(Me)$_2$ (**2**) was prepared in a 250 mL 3-neck round bottom flask fitted with the probe by dissolving the compound in 5 mL of CO_2-saturated benzene under an atmosphere of CO_2. Once completely dissolved (within 1 min of stirring), the FTIR monitoring was started and the reaction followed until completion. The reactions were conducted over a 21 °C temperature range and the solubility data of CO_2 was obtained from literature.[71] The high pressure reaction was monitored using an ASI ReactIR 1000 reaction analyses system with stainless steel Parr autoclave modified with a permanently mounted ATR crystal (SiComp) at the bottom of the reactor (purchased from Mettler Toledo). **NMR:** A high pressure NMR tube was charged with 0.2 mL of d_6-benzene or d_8-toluene solution of the compound. Upon freezing the solution with liquid nitrogen, the tube was evacuated on a Schlenk line for 30 s after which it was thawed back to room temperature. The tube was then filled with CO_2 to the desired pressure and shaken multiple times (this process was repeated again to account for slight loss in pressure upon CO_2 solvation). Data collection was started within 15 minutes.

Computational Methods

Reference 70 and therein: All calculations were performed with the Gaussian 09 suite of programs. To determine the thermodynamics of CO_2 insertion, geometry optimizations were performed using the B3LYP functional and the Pople-style all-electron 6-31G(d',p') basis set on all non-metal atoms except for iodine, and the SDD basis set with an effective core potential for the iron, ruthenium, and iodine atoms (BS1). Local

minima were confirmed by their vibrational frequencies (no imaginary vibrational modes). Single-point energy calculations using the B3LYP, TPSS, BP86, and m06 functionals were performed with the 6-311G(d,p) basis set on non-metal atoms except for iodine, and the SDD basis set for iron and ruthenium atoms (BS2). Thermal corrections obtained from the B3LYP/BS1 frequency calculation were applied thereafter. Enthalpies discussed in this article were obtained from the B3LYP/BS2 single-point energy calculations, apart from the comparison of different functionals.

APT atomic charges on the hydride ligands were obtained from frequency calculations performed at the B3LYP/BS1 level. Further such calculations were performed using a triple zeta basis set (BS2), and using this basis set with additional polarization and diffuse functions were performed. The APT charges did not change by more than 0.01 e, indicating that the BS1 level was adequate for this purpose.

To determine the barrier heights for CO_2 insertion, geometry optimizations were performed using the B3LYP functional and the 6-311++G(d,p) basis set on all non-metal atoms, and the SDD basis set with an effective core potential for the metal atoms (BS2++). The saddle points found were confirmed to be the correct ones by visualizing the imaginary vibrational modes with AGUI or Avogadro.

Acrylic Acid Derivatives of Iron and Ruthenium Carbonyls

Introduction. A chemical process under investigation dating back several decades involves the oxidative coupling of CO_2 and ethylene at transition metal centers. This problem was initially addressed by Hoberg in the 1980s using nickel(1,5,9-cyclododecatriene) in the presence of 1,2-*bis*(dicyclohexylphosphino)ethane (dcpe) or 2,2'-bipyridine (bipy).[13] In this manner, ethylene and CO_2 react to provide an oxanickel cyclopentanone which can be decomposed to other organic compounds (Scheme 11). Unfortunately, these processes are stoichiometric in nickel(0) complexes, and catalytic reactions would be highly desirable.

Scheme 11

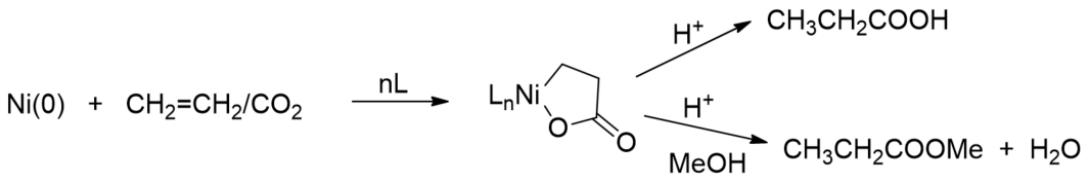

The oxidative coupling of ethylene and CO_2 to afford acrylic acid in the gas phase is slightly endothermic with an enthalpy of reaction of 4.65 kcal/mol (Equation 5). This along with a sizable negative entropy of reaction makes the process thermodynamically non-spontaneous at all temperatures. In the presence of hydrogen bonding solvents such as methanol, ΔH of reaction can become exothermic with an estimated value of -4.40 kcal/mol.[79] Similar thermodynamic behavior holds true for the coupling of CO_2 with most saturated and unsaturated hydrocarbons. In the closely related case of the hydrogenation

of CO_2 to formic acid, this issue can be overcome in the presence of certain additives, e.g., MeOH or Et_3N.[20,80,81]

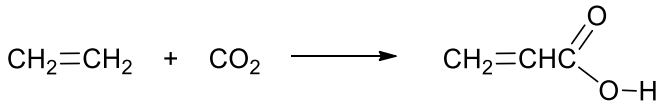

5

Recent kinetic and mechanistic studies of the reaction of (Triphos)Mo$(N_2)_2$(ethylene) with carbon dioxide have shown the oxidative coupling of ethylene and CO_2 to provide the dimeric complex depicted in Equation 6.[16] This process is similar to that previously reported by Carmona and coworkers.[14,82] Subsequently, Wolfe and Bernskoetter have demonstrated that reaction of the tungsten acrylate complex with an excess of methyl iodide results in the formation of methyl acrylate.[18] An analogous observation has been noted upon reacting the oxanickel cyclopentanone derivative with MeI.[83]

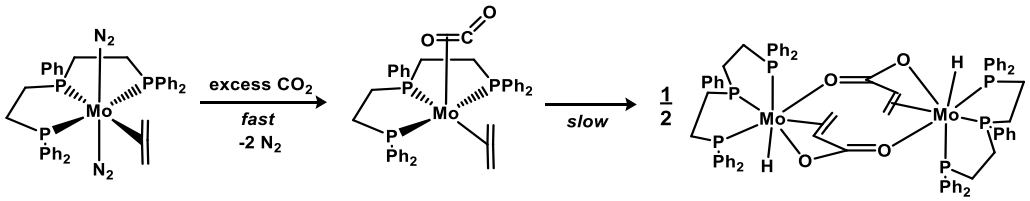

6

Since ethylene obtained from corn or sugar cane is a renewable resource, preparation of acrylic acid from ethylene and CO_2 would represent an alternative approach

to that currently under investigation for the production of bio-acrylic acid and its derived poly(acrylic acid). This latter process entails the catalytic dehydration of 3-hydroxypropionic acid (3-HP) produced by microbial conversion of sugar.[84] Recently, Novomer has described a process for the synthesis of polypropiolactone (PPL) from ethylene oxide and CO.[85] Since this stable polymer decomposes cleanly to acrylic acid above 200 ^{o}C, it provides a good method for shipping acrylic acid. In this section, we wish to communicate our studies of group 8 metal carbonyls with acrylic acid. Specifically, we will describe the binding and removal of the potential product of ethylene/CO_2 coupling, i.e., acrylic acid, to zero-valent ruthenium and iron tetracarbonyl derivatives. Our ultimate goal is to find metal complexes which will efficiently couple ethylene and CO_2 in the presence of a base to provide an adduct of acrylic acid. Subsequently, the base can be released upon heating and recycled, thereby, leading to a catalytic cycle for the production of this useful carboxylic acid (Scheme 12). The nature of the interaction of the acrylate with the metal center is undefined at this time in the transformations outlined. This is similar to the mechanism put forth by Buntine and coworkers for the nickel-mediated coupling reaction of CO_2/ethylene to acrylic acid, however in Scheme 12 triethylamine is used to overcome the unfavorable Gibbs free energy, and ultimately can be recycled upon the addition of thermal energy.[19a] Pápai, Aresta and coworkers have similarly investigated theoretically the mechanism for the coupling of CO_2 and ethylene involving a (bipy)Ni complex.[15a]

Scheme 12

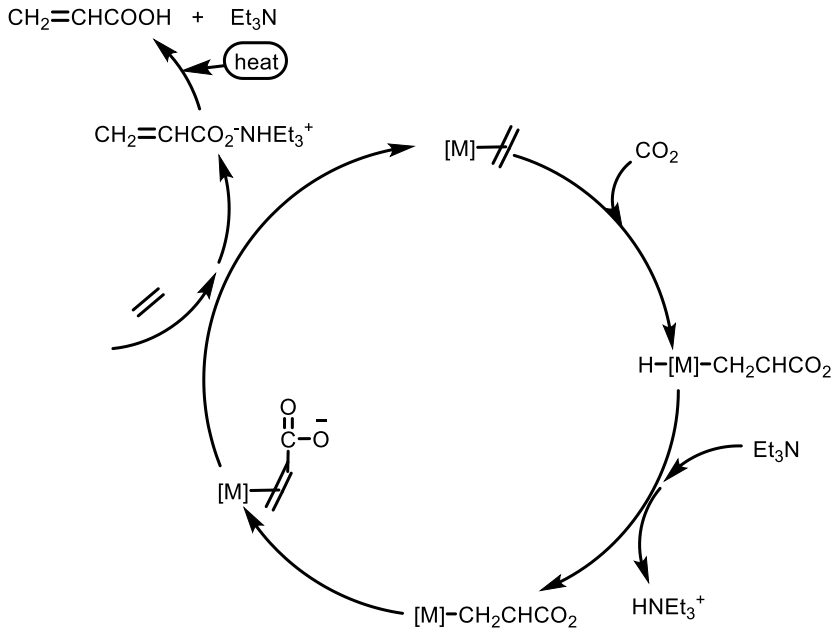

Results and Discussion. The published work presented herein were done in collaborations with Drs. Bo Li and Andrew Yeung.[86] The synthesis and kinetic studies were largely carried out by Dr. Li, while Dr. Yeung provided calculations corroborating our experimental data. My contribution involves all the structural characterizations along with some synthesis and kinetics as well. The major results of this study are included below.

Synthesis, Kinetics and Structural Characterizations

The synthesis of (acrylic acid)$Fe(CO)_4$ was achieved by photolysis of $Fe(CO)_5$ with acrylic acid at ambient temperature in a modified procedure to that previously published.[87] X-ray quality yellow crystals of this iron derivative were obtained from diethyl ether/heptane. Alternatively, the ruthenium analog was synthesized in a manner similar to that described by Poë and coworkers.[88] In this instance, it was necessary to first

prepare $Ru(CO)_5$ *in situ* by UV irradiation of $Ru_3(CO)_{12}$ in the presence of CO. Upon removal of excess CO, acrylic acid was added to the solution of $Ru(CO)_5$ and photolysis continued. Following isolation of (acrylic acid)$Ru(CO)_4$, the complex was purified by recrystallization from CH_2Cl_2/hexane to provide pale yellow crystals suitable for X-ray structural analysis. The solid-state structures of these (acrylic acid)$M(CO)_4$ (M = Fe, Ru) complexes display trigonal bipyramidal geometry with the acrylic acid ligand bound by its olefinic function at an equatorial site (Figure 34). Figure 35 depicts the intermolecular hydrogen-bonding seen between the acrylic acid ligands in the solid-state structures of $(CH_2{=}CHCOOH)Ru(CO)_4$.

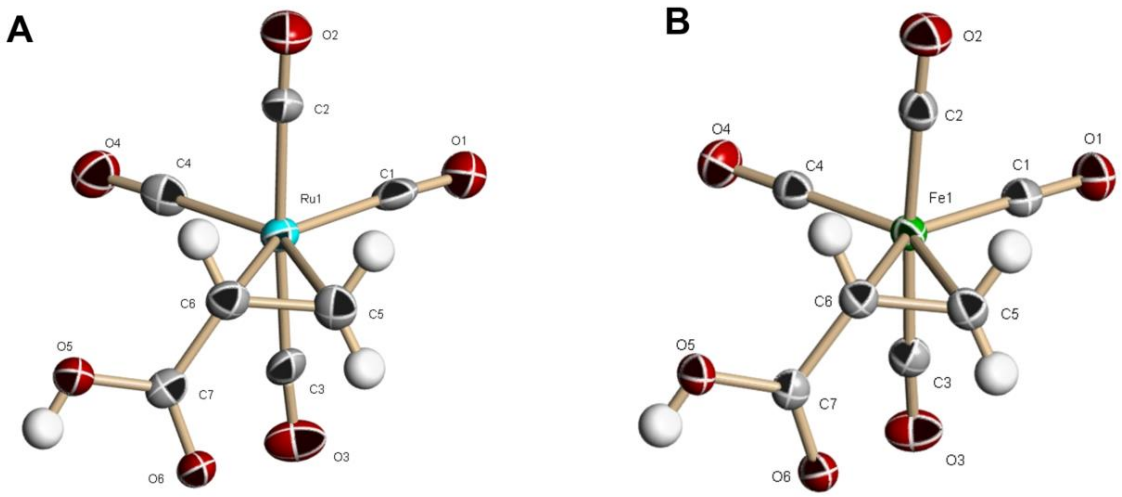

Figure 34 X-ray structures: Thermal ellipsoid representations of **A**, $(CH_2{=}CHCOOH)Ru(CO)_4$, and **B**, $(CH_2{=}CHCOOH)Fe(CO)_4$ with ellipsoids at 50% probability surfaces.

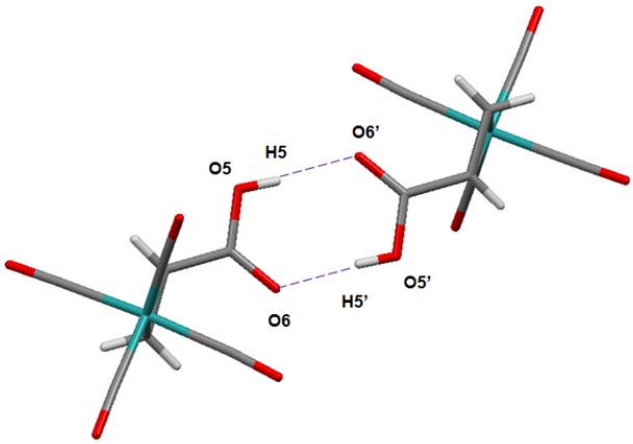

Figure 35 Capped sticks representation of $(CH_2{=}CHCOOH)Ru(CO)_4$ indicating intermolecular hydrogen-bonding, d(O5–O6') and d(O5'–O6) = 2.656 Å (similarly in the iron derivatives = 2.630 Å).

The infrared spectra of the two group 8 metal derivatives as expected displayed four bands in the ν_{CO} region, along with a carboxyl stretching vibration at ~1670 cm^{-1}. Figure 36 contains the spectrum of the ruthenium analog determined in hydrocarbon solvent. At ambient temperature, the four carbonyl ligands are fluxional as indicated by the ^{13}C NMR spectrum of $(CH_2{=}CHCOOH)Ru(CO)_4$ where one broad signal at 194.3 ppm is observed which resolves into four resonances upon lowering the temperature to -40 ^oC (Figure 37). Intramolecular rearrangement of the carbonyl ligands in olefin tetracarbonyl ruthenium complexes have been reported previously by Grevels, Reuvers and Takats.[89] Furthermore, Takats and coworkers have determined the energy of activation barriers for this process for several iron derivatives to be 11 – 14 kcal/mol.[90] It should be noted that the rearrangement of the CO ligands *via* a Berry process is accompanied by an olefin rotation which likely accounts for the higher barrier for intramolecular rearrangement compared to that seen in $Fe(CO)_5$.[90]

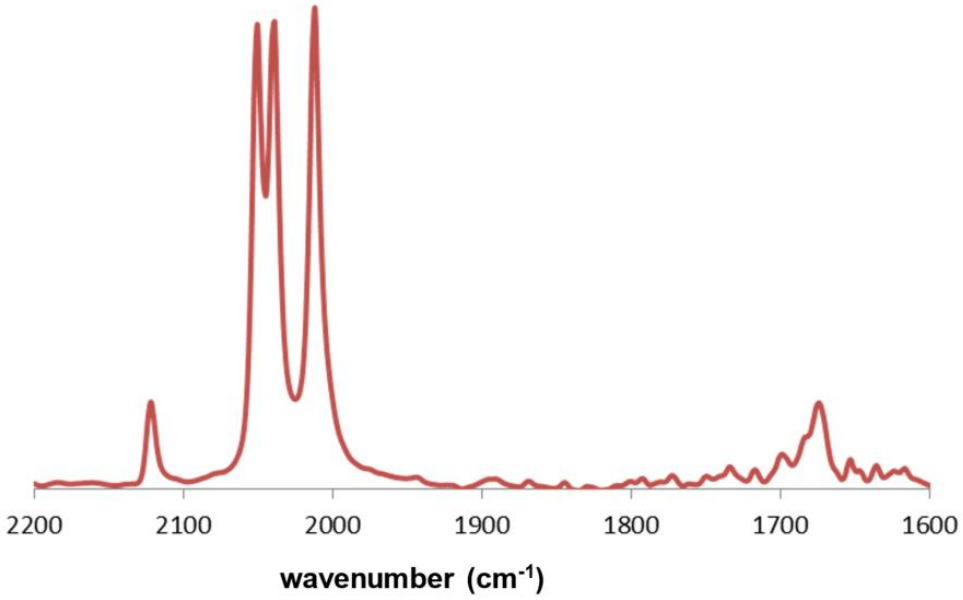

Figure 36 Infrared spectrum of $(CH_2{=}CHCOOH)Ru(CO)_4$ in the carbonyl region.

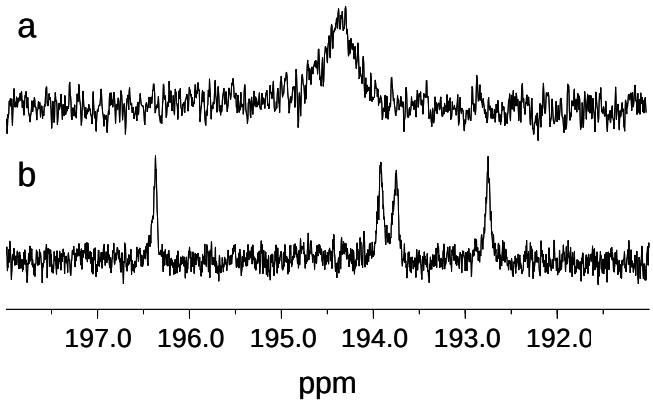

Figure 37 ^{13}C NMR spectra of of (acrylic acid)$Ru(CO)_4$ in $CDCl_3$ at (a) 20 °C (194.3 ppm) and (b) -40 °C (192.7, 193.7, 193.9, and 196.4 ppm).

The olefin ligand substitution reactions of (η^2-alkene)$Ru(CO)_4$, where alkene = ethylene and methyl acrylate, with phosphines or phosphites have been shown to proceed

via an alkene dissociative process by Chen and Poë.[91] Undoubtedly, the intermediate in this process, {$Ru(CO)_4$}, is solvated by the weakly binding solvents used in the reaction (Scheme 13). A similar mechanism is anticipated for substitution of acrylic acid in (acrylic acid)$Ru(CO)_4$ in this study with perhaps minor modifications due to its acidic function. Assuming a steady-state treatment for formation of the intermediate, the dependence of k_{obsd} on the [alkene] and [PR_3] is shown in Equation 7. Hence, for the processes carried out in excess [PR_3], k_1 can simply be approximated by k_{obsd}.

Scheme 13

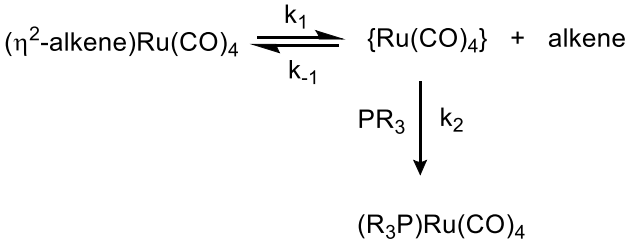

$$k_{obsd} = \frac{k_1 k_2 [PR_3]}{k_{-1} [\text{alkene}] + k_2 [PR_3]} \qquad 7$$

The kinetic parameters for the displacement of acrylic acid from (acrylic acid)$Ru(CO)_4$ with triphenylphosphine were determined using *in situ* infrared monitoring of the ligand substitution process with an iC10 ReactIR instrument. Table 11 contains the ν_{CO} frequencies of the relevant complexes investigated in this study. Figure 38 contains a reaction profile illustrating the disappearance of the parent complex with the concomitant appearance of the mono- and di-substituted triphenylphosphine derivatives in CH_2Cl_2.

Table 11 Positions of CO stretching frequencies for the Ru & Fe complexes.

Complex	ν_{CO} (cm^{-1})
$Ru(CO)_4(CH_2{=}CHCOOH)$	2011, 2039, 2050, 2122
$Ru(CO)_4(CH_2{=}CHCOO^-NH_2C_5H_{10}^+)$	1987, 2033, 2109
$Ru(CO)_4PPh_3$	1954, 1988, 2060
$Ru(CO)_3(PPh_3)_2$	1904
$Fe(CO)_4(CH_2{=}CHCOOH)$	2001, 2025, 2038, 2102
$Fe(CO)_4(CH_2{=}CHCOO^-NH_2C_5H_{10}^+)$	1975, 2004, 2016, 2085
$Fe(CO)_4(CH_2{=}CHCOOH)\bullet PPh_3$	1985, 2011, 2029, 2087
$Fe(CO)_4PPh_3$	1944, 1977, 2052
$Fe(CO)_3(PPh_3)_2$	1894
$Fe(CO)_4(CH_2{=}CHCOOMe)$	1997, 2021, 2034, 2100

[a]All spectra determined in hexane solution.

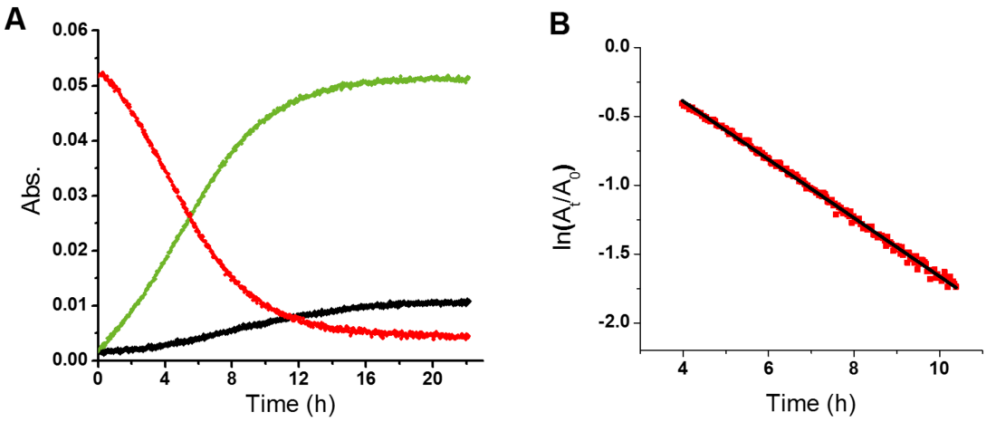

Figure 38 A. Infrared ν_{CO} peak profiles as a function of time for (acrylic acid)$Ru(CO)_4$ (red), $(PPh_3)Ru(CO)_4$ (green), and *trans*-$(PPh_3)_2Ru(CO)_3$ (black) at 283 K in CH_2Cl_2. **B**. Plot of $\ln(A_t/A_0)$ *vs* time for disappearance of (acrylic acid)$Ru(CO)_4$, $R^2 = 0.997$.

The temperature dependent rate constants for the substitution of acrylic acid in an equatorial site in (acrylic acid)$Ru(CO)_4$ with triphenylphosphine in an axial site in $(Ph_3P)Ru(CO)_4$ (see X-ray structure in Figure 39) are listed in Table 12 for reactions carried out in tenfold excess of phosphine. In an accompanying, less productive pathway, a small but significant quantity of *trans*-$(Ph_3P)_2Ru(CO)_3$ was afforded during the substitution process.[92] The extent of CO substitution appears to be slightly dependent on the amount of excess [PPh_3] utilized, as well as the reaction temperatures. See, for example, Figure 40 where the excess [PPh_3] was increased from 10-fold to 30-fold with the %*trans*-$(Ph_3P)_2Ru(CO)_3$ increasing from 17.2% to 24.4%. The negligible change in k_{obsd} upon a three-fold increase in [PPh_3] is further evidence of the reaction occurring under conditions where $k_{obsd} \approx k_1$.

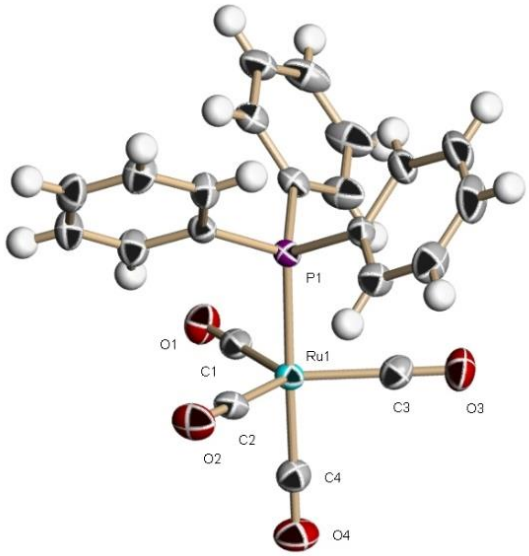

Figure 39 Thermal ellipsoid representation of the X-ray structure of $(Ph_3P)Ru(CO)_4$ with ellipsoids at 50% probability surfaces.

Table 12 Temperature dependent rate constants for the substitution reactions of $(CH_2{=}CHCOOH)Ru(CO)_4$ with PPh_3.[a]

Temperature (K)	k_{obsd} x 10^4 (sec^{-1})	% *trans*-$(Ph_3P)_2Ru(CO)_3$
273	0.102	16.4
283	0.571	17.2
288	1.22	17.9
298	5.09	18.5

[a]Reactions carried out in CH_2Cl_2 with a tenfold excess of triphenylphosphine.

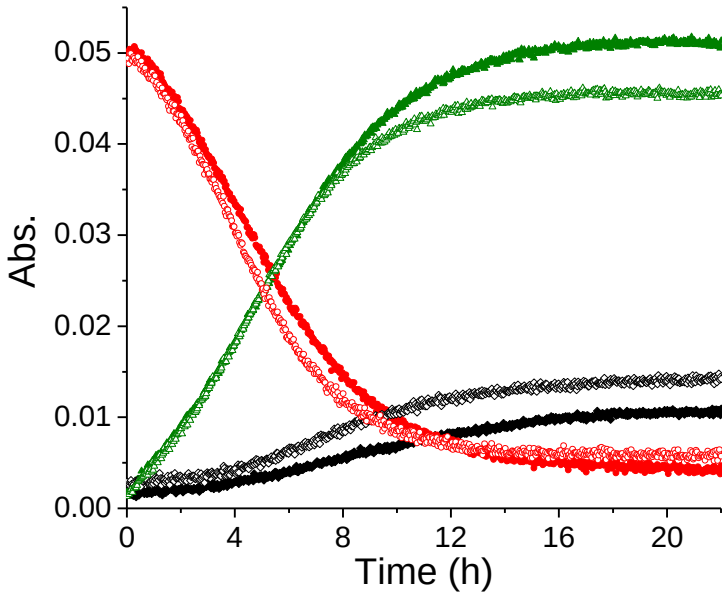

Figure 40 Infrared ν_{CO} profiles for (acrylic acid)$Ru(CO)_4$ disappearance (red) and appearance of $(Ph_3P)Ru(CO)_4$ (green) and *trans*-$(Ph_3P)_2Ru(CO)_3$ (black). Tenfold excess PPh_3 (solid lines) and thirtyfold [PPh_3] (hollow lines) in CH_2Cl_2 at 283 K.

The slight inhibition noted during the onset of the olefin substitution process (see Figure 38), is thought to be due to adduct formation in the form of hydrogen-bonding between the phosphine ligand and the carboxylic acid functional group (Scheme 14).

Indeed, there is a small red shift observed in the ν_{CO} frequencies upon the addition of PPh_3 to a solution of the ruthenium acrylic acid complex, consistent with partial proton abstraction. This red shift is more discernible (10-15 cm^{-1}, see Table 11) for the iron analog (*vide infra*). On the other hand, as noted in Table 11, deprotonation of the (acrylic acid)$Ru(CO)_4$ complex with one equivalent of piperidine results in a red shift of the ν_{CO} bonds of 15-20 cm^{-1}. This in turn leads to significantly enhanced rate of olefin loss concomitantly without the inhibition step (see Figure 41 and Table 13). As previously noted, the percentage of disubstitution increases with an increase in temperature. Eyring analysis yields the activation parameters for olefin substitution in the presence and absence of piperidine base and are listed in Table 14.

Scheme 14

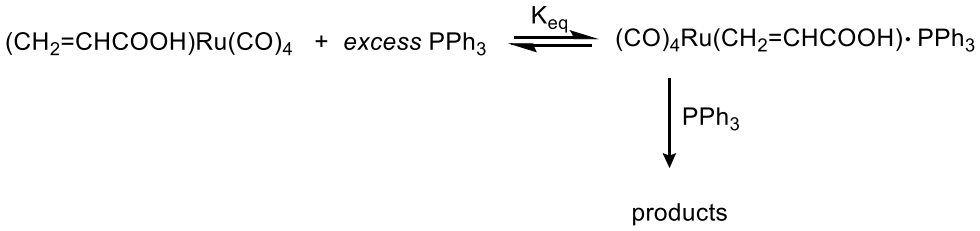

Table 13 Temperature dependent rate constants for the substitution reactions of $(CH_2{=}CHCOOH)Ru(CO)_4$ with PPh_3 in the presence of piperidine.[a]

Temperature (K)	k_{obsd} x 10^4 (sec^{-1})	% *trans*-$(Ph_3P)_2Ru(CO)_3$
273	0.152 (*0.102*)	7.75 (*16.4*)
278	0.473	8.40
288	2.20 (*1.22*)	9.61 (*17.9*)
298	9.86 (*5.09*)	11.1 (*18.5*)

[a]Reactions carried out in CH_2Cl_2 with a tenfold excess of triphenylphosphine and one equivalent of piperidine. [b]Values in parentheses are from Table 3 for measurements carried out in the absence of piperidine.

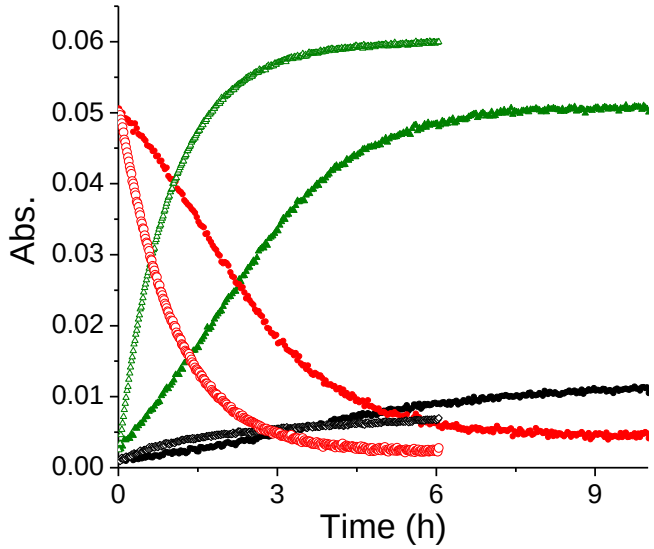

Figure 41 Infrared ν_{CO} peak profiles as a function of time for (acrylic acid)$Ru(CO)_4$ (red), $(PPh_3)Ru(CO)_4$ (green), and *trans*-$(PPh_3)_2Ru(CO)_3$ (black) at 288 K in CH_2Cl_2. Hollow lines with piperidine and solid lines without piperidine.

Table 14 Summary of activation parameters for olefinic ligand dissociation determined in these studies using Eyring analysis.[a]

Compound	$\Delta H^{\ddagger}$ (kcal/mol)	$\Delta S^{\ddagger}$ (e.u.)	$\Delta G^{\ddagger}$ (scaled At 298 K)
$(CH_2{=}CHCOOH)Ru(CO)_4$	24.8 ± 0.4	9.4 ± 1.4	22.0
$(CH_2{=}CHCO_2)Ru(CO)_4^-H_2NC_5H_{10}^+$	26.0 ± 1.1	14.8 ± 3.9	21.6
$(CH_2{=}CHCOOH)Fe(CO)_4$	28.0 ± 1.2	8.8 ± 3.7	25.4
$(CH_2{=}CHCO_2)Fe(CO)_4^-H_2NC_5H_{10}^+$	34.1 ± 1.5	25.7 ± 4.5	26.4
$(CH_2{=}CHCOOMe)Fe(CO)_4$	31.7 ± 0.5	13.4 ± 1.3	27.7

[a]Ruthenium and iron data determined in CH_2Cl_2 and chlorobenzene, respectively, in the presence of a tenfold excess of triphenylphosphine.

In an effort to better understand the ligand substitutional behavior of acrylic acid bound to low-valent metal derivatives, we have also studied this process in the iron analog and its ester derivative, $(CH_2{=}CHCOOMe)Fe(CO)_4$. Upon examining the displacement of the acrylic acid ligand in $(CH_2CHCOOH)Fe(CO)_4$ by PPh_3 some striking differences from the ruthenium analog are noted. The inhibition step is more pronounced in this instance, and the percentage of disubstituted phosphine complex is much larger (>70%). In addition, the ν_{CO} infrared bands for the PPh_3 adduct are red shifted significantly (Table 11) which allows for monitoring the decrease in both iron carbonyl species with time. Once the equilibrium distribution is established, both forms of the complex disappear at the same rate.

The addition of one equivalent of piperidine to $(CH_2{=}CHCOOH)Fe(CO)_4$ leads to the formation of the olefin bound acrylate iron carbonyl anion and $H_2NC_5H_{10}^+$. X-ray quality crystals of this complex were grown from CH_2Cl_2/hexane, and its structure is

illustrated in Figure 42 along with its hydrogen-bonding motif. As noted in Table 11, the ν_{CO} bands in the deprotonated derivative are more red shifted than in the presumably hydrogen bonded adduct with PPh_3. As seen before with the ruthenium analogue, the inhibition step is now absent during olefin substitution. The rate constants for olefin ligand dissociation were slightly smaller than those measured for the process in the absence of piperidine (Table 15), with concomitantly larger values of $\Delta H^{\ddagger}$ and $\Delta G^{\ddagger}$ (see Table 14).

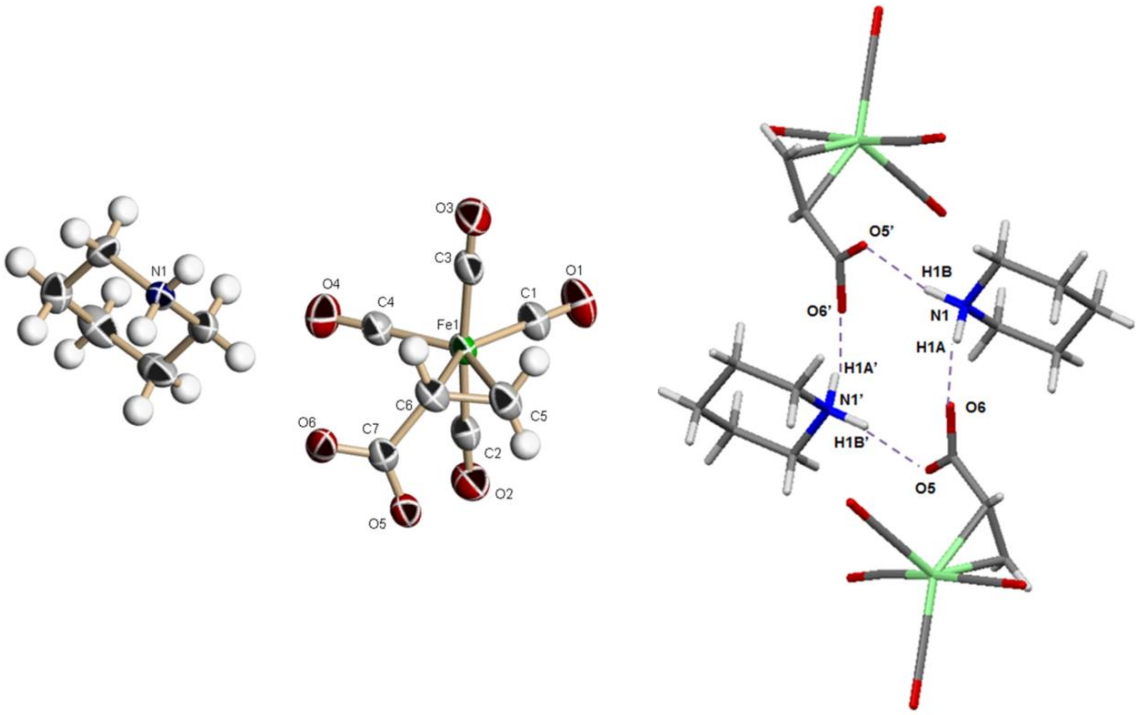

Figure 42 X-ray structure of $(CH_2{=}CHCOO)Fe(CO)_4^{-}H_2NC_5H_{10}^{+}$ along with its H-bonding motif with ellipsoids at 50 % probability. The Fe – C(5) and Fe – C(6) distances of 2.1049 (19) and 2.1149 (19) Å as well as the C(5) – C(6) distance of 1.410 (3) Å are not statistically different from those found in the parent acrylic acid complex. The d(O6 – N1) and d(O5 – N1') were determined to be 2.710 and 2.703 Å, respectively.

Table 15 Temperature dependent rate constants for the substitution reactions of $(CH_2=CHCOOH)Fe(CO)_4$ with PPh_3 in the presence[a] and absence[b] of piperidine.

Temperature (K)	**$(CH_2=CHCOO)Fe(CO)_4^-H_2NC_5H_{10}^+$ k_{obsd} x 10^4 (sec^{-1})**	**$(CH_2=CHCOOH)Fe(CO)_4$ k_{obsd} x 10^4 (sec^{-1})**
323	0.243	0.667
328	0.608	1.145
333	1.47	2.58
343	5.72	8.57

[a]Reactions carried out in CH_2Cl_2 with a tenfold excess of triphenylphosphine and one equivalent of piperidine. [b]Reactions carried out in chlorobenzene with a tenfold excess of triphenylphosphine

Further evidence that interaction of the proton in metal bound acrylic acid has influence on the rate of its displacement from the metal center is seen in substitution reactions of the closely related complex, $(CH_2=CHCOOMe)Fe(CO)_4$, containing the methyl ester of acrylic acid. As noted in Table 11, the binding abilities of the two olefinic ligands are quite similar, with the ν_{CO} frequencies being within 2-4 cm^{-1} of each other. Furthermore, the solid-state structure and relevant bond distances are correspondingly comparable, Figure 43. Rate constants for the substitution of the methyl ester derivative of acrylic acid are listed in Table 16 with reaction profiles provided in Figure 44. As is apparent from Table 16 and Figure 44, the substitution reaction is much slower in this instance, and by way of contrast, the mono-phosphine product is dominant and insensitive to temperature. The activation parameters for the dissociation of the methyl ester of acrylic acid indicated the barrier to be significantly higher in this instance (Table 14). The $\Delta H^{\ddagger}$ and $\Delta S^{\ddagger}$ for the dissociation of the methyl ester of acrylic acid from $(CH_2=CHCOOMe)Ru(CO)_4$ were previously reported by Chen and coworkers to be 28.1

kcal/mol and 20.5 e.u., respectively and are also much higher in comparison to the protonated ruthenium derivative studied here.[31]

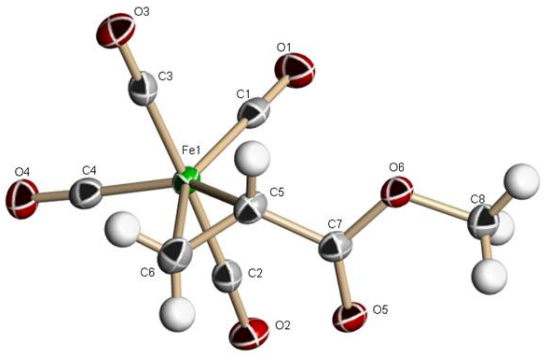

Figure 43 X-ray structure of $(CH_2{=}CHCOOMe)Fe(CO)_4$. The Fe–C(5) and Fe–C(6) distances of 2.108 (2) and 2.101 (2) Å are not statistically different from those found for the acrylic acid and acrylate derivatives.

Table 16 Temperature dependent rate constants for the substitution reactions of $(CH_2{=}CHCOOMe)Fe(CO)_4$ with PPh_3.[a]

Temperature (K)	k_{obsd} x 10^4 (sec^{-1})[b]	% *trans*-$(Ph_3P)_2Fe(CO)_3$
343	0.394	42
353[c]	1.46 (1.58) 1.43[d] (1.61) 1.23[e] (1.30)	42 (42)
358	2.79	42
363	5.45	41

[a]Reactions carried out in chlorobenzene with a tenfold excess of triphenylphosphine. [b]Rate constants determined from the disappearance of $(CH_2{=}CHCOOMe)Fe(CO)_4$. [c]Rate constant in parenthesis were carried out in the presence of a thirtyfold excess of triphenylphosphine. [d]Rate constants determined from the appearance of $PPh_3Fe(CO)_4$. [e]Rate constant determined from the appearance of *trans*-$(PPh_3)_2Fe(CO)_3$.

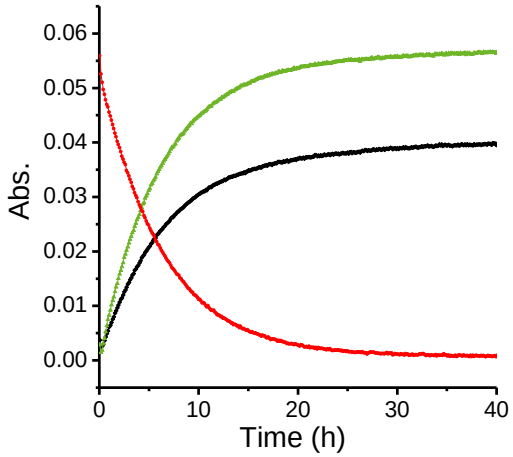

Figure 44 Reaction profiles for $(CH_2{=}CHCOOMe)Fe(CO)_4$ + 10 equivalents of PPh_3 in chlorobenzene at 343 K. $(CH_2{=}CHCOOMe)Fe(CO)_4$ (red), $PPh_3Fe(CO)_4$ (green), and *trans*-$(PPh_3)_2Fe(CO)_3$ (black).

Theoretical Modeling

In an effort to provide support for the experimental findings, DFT calculations were performed on several of these complexes. Specifically, bond dissociation energies (BDEs) for the olefin-metal bond were calculated for comparison with the experimental activation enthalpies in order to better assess the ligand substitution pathway. The olefin-metal bond dissociation energy was treated as the energy required for $M(CO)_4L$ to yield two isolated fragments, $M(CO)_4$ and L.

In the experiment used to determine the Ru-acrylic acid bond dissociation energy, triphenylphosphine is used to trap the ruthenium tetracarbonyl fragment: $Ru(CO)_4 + PPh_3 \rightarrow Ru(CO)_4PPh_3$. Unfortunately, triphenylphosphine behaves as a Bronsted base, and it is believed to partially afford a polar adduct with the carboxylic acid moiety of $Ru(CO)_4$(acrylic acid) in solution. By increasing the electron density on the acrylic acid ligand (more like its conjugate base), it acts as a poorer π-acid, and is more easily

dissociated from ruthenium than for L = methyl acrylate. Such interactions are not accounted for in the computations, possibly explaining the small discrepancy between the computed and the experimental results (Table 17). Compared with ruthenium, the bond dissociation energies for the iron carbonyl complexes were found to be consistently higher by approximately 4 kcal/mol. The iron complexes' greater bond dissociation is attributed to iron's greater back-donating ability compared to ruthenium to the olefinic ligand, which results in a stronger iron-olefin bond.

Table 17 Enthalpy (kcal/mol) of the reaction: $M(CO)_4L \rightarrow M(CO)_4 + L$.

L	Ru (theor.)	Ru (expt.)	Fe (theor.)	Fe (expt.)
C_2H_4	27.7	24.3[91]	32.3	
acrylic acid	30.5	24.8[a]	34.4	28.0[a]
methyl acrylate	30.4	28.1[91]	34.3	31.7[a]
CO	30.1	27.6[91]	38.8	48[93]

[a]Our results.

Carbon Dioxide and Ethylene Coupling Reactions

Our preliminary attempts at the oxidative coupling of CO_2 and ethylene involving group 8 metal carbonyls have been unsuccessful. Nevertheless, these studies have suggested future experiments which may be more productive. For example, upon irradiation of $Ru_3(CO)_{12}$ in hexane in the presence of a slow purge of ethylene, complete conversion of $Ru_3(CO)_{12}$ to $(ethylene)_nRu(CO)_{4-n}$ (n = 1 or 2) occurred (Equation 8).[94] However, subsequent introduction of CO_2 at atmospheric pressure led to no coupling of CO_2 and ethylene in the presence or absence of triethylamine. A similar observation was noted upon simultaneous introduction of ethylene and CO_2 at atmospheric pressure during

irradiation of $Ru_3(CO)_{12}$. Comparable observations were noted when $Ru_3(CO)_{12}$ was replaced with $Fe(CO)_5$. Hence, this would suggest as was observed in the group 6 metal derivatives that a more electron rich metal center is needed to promote the oxidative coupling process.[14,16,82] Since chelating electron rich diphosphine ligands readily afford ax-eq. substituted (diphosphine)$Ru(CO)_3$ derivatives, these species upon irradiation in the presence of ethylene/CO_2 may lead to more productive chemistry.[95,96] Importantly, this approach might lead to an olefin bound intermediate which, as shown herein, could be readily displaced in the presence of olefin to provide a catalytic cycle (Figure 45).

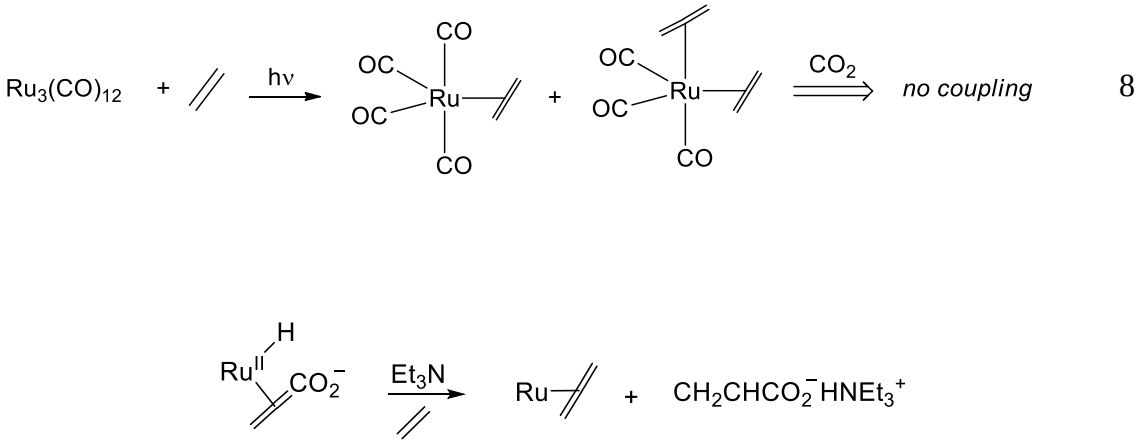

8

Figure 45 A proposed reaction pathway which accommodates processes described in the above study.

Concluding Remarks. Although these studies have not accomplished our ultimate goal of catalytic oxidative coupling of ethylene and CO_2 to afford acrylic acid or its derivatives as mediated by group 8 metal carbonyls, some useful fundamental chemistry closely related to the long term aims of the study has been forthcoming.[17] That is, the

kinetic parameters for the dissociation of the η^2-olefin bound acrylic acid from a conceivable product of ethylene/CO_2 coupling, (acrylic acid)$M(CO)_4$ (M = Fe or Ru) and its deprotonated analog, have been determined. Not unexpectedly, ligand dissociation from the second row transition metal was found to be more facile than from its first row analog. In addition, although there is little difference in the olefin dissociation kinetic parameters for the protonated or deprotonated forms, the alkylated species is much more kinetically stable toward ligand dissociation. Density Functional Theory computational studies reveal the activation enthalpies for the metal-olefin dissociation to correlate well with the calculated bond dissociation energies.

Experimental Section. All manipulations were carried out using a double manifold Schlenk vacuum line under an argon atmosphere or an argon filled glovebox unless otherwise stated. Reagent grade solvents were purified by an MBraun Manual Solvent Purification System packed with Alcoa F200 activated alumina desiccant. $Fe(CO)_5$ and $Ru_3(CO)_{12}$ were purchased from Strem Chemicals. Acrylic acid, methyl acrylate, piperidine, and PPh_3 were purchased from Sigma-Aldrich. PPh_3 was recrystallized prior to use. $(CH_2{=}CHCOO)Fe(CO)_4^-H_2NC_5H_{10}^+$ was prepared according to literature.[97] $Ru(CO)_4PPh_3$ was prepared by treating a solution of $Ru(CO)_5$ with PPh_3 and stirring overnight.[98] $(CH_2{=}CHCOOMe)Fe(CO)_4$ was prepared in an analogous manner to $(CH_2{=}CHCOOH)Fe(CO)_4$ starting with $Fe(CO)_5$ instead of $Fe_2(CO)_9$.[99,87] Research grade CO and ethylene were obtained from Matheson Tri-Gas. ^1H NMR spectra were recorded on a Varian INOVA 300 operating at 299.96 MHz and ^{13}C NMR spectra

were recorded on a Varian INOVA 500 operating at 125.59 MHz. The NMR spectra were referenced to residual solvent resonances. Infrared spectra were obtained on a Bruker Tensor 27 FTIR spectrometer. *In situ* IR monitoring was carried out using a Mettler Toledo iC10 ReactIR with an AgX fiber conduit probe having a SiComp ATR crystal. X-ray crystallography was done on a Bruker-AXS APEXII CCD diffractometer in a nitrogen cold stream maintained at 110 K. Elemental analyses were determined by Atlantic Microlab (Norcross, GA).

Synthesis of $(CH_2{=}CHCOOH)Ru(CO)_4$

A solution of $Ru(CO)_5$ was prepared and used *in situ* as follows: $Ru_3(CO)_{12}$ (63.9 mg, 0.10 mmol) was dissolved in hexane (100 mL) in a 250 mL Pyrex Schlenk flask. The solution was placed in an ice bath and irradiated using a high-pressure mercury UV lamp (100 W) under a CO atmosphere with slow bubbling for 3 h. During this time the orange solution turned colorless. After removing the excess CO, acrylic acid (69 uL, 1.0 mmol) was added to the above $Ru(CO)_5$ solution and irradiated at room temperature for another 4 h. Removal of solvent under vacuum followed by washing the residue with 5 mL degassed water and recrystallization from CH_2Cl_2/hexane yielded pale yellow crystals of $(CH_2{=}CHCOOH)Ru(CO)_4$ (36 mg, 42%). IR data in hexane (ν_{CO}): 1675 (m), 2011 (vs), 2039 (s), 2050 (s), 2122 (m). NMR data in $CDCl_3$: ^1H δ 2.27 (m, 1 H, CH_2), 2.55 (m, 1 H, CH), 3.04 (m, 1 H, CH_2), 9.20 (s, 1H, COOH); $^{13}C\{^1H\}$ δ 23.5, 34.4, 182.6, 194.4. Anal. Calcd for $C_7H_4O_6Ru$: C, 24.48; H, 1.41 Found: C, 29.66; H, 1.51%.

Synthesis of $(CH_2=CHCOOH)Fe(CO)_4$

Similar to literature method,[87] acrylic acid (0.34 mL, 5.0 mmol) and $Fe(CO)_5$ (10 mL, 74.0 mmol) were added into a 50 mL Pyrex Schlenk flask. The solution was irradiated using a high-pressure mercury UV lamp (100 W) under a CO atmosphere with slow bubbling for 4 h at room temperature. Excess $Fe(CO)_5$ was removed and the residue was washed with 10 mL degassed water. Recrystallization from Et_2O/heptane yielded yellow crystals of $(CH_2=CHCOOH)Fe(CO)_4$ (0.385 g, 32%). IR data in hexane (ν_{CO}): 1680 (m), 2001 (vs), 2025 (vs), 2038 (s), 2102 (m); ^{13}C NMR could not be collected due to decomposition in solution overnight. Anal. Calcd for $C_7H_4O_6Fe$: C, 35.04; H, 1.68. Found: C, 35.15; H, 1.81%.

Kinetic Measurements

An example of a typical experiment is as follows: $Ru(CO)_4(CH_2=CHCOOH)$ (25 mg, 0.087 mmol) and PPh_3 (230 mg, 0.877 mmol) were treated with 5 mL of CH_2Cl_2 under an argon atmosphere in a 3-neck round bottom flask fitted with the *in situ* IR probe. Once completely dissolved, the FTIR monitoring was started and the reaction followed till completion. The reactions were conducted over a 25 K temperature range from 273 to 298 K. In the case of iron tetracarbonyl derivatives, chlorobenzene was used as the solvent and the reactions were conducted over a 20 K temperature range from 323 to 343 K.

Triphos Derivatives of Mo & W Carbonyls and Their Reactivity with Olefins

Inspired by the kinetic and mechanistic studies reported by Bernskoetter and Tyler on the reaction of (Triphos)Mo(N_2)$_2$(C_2H_4), Triphos = ($Ph_2PCH_2CH_2$)$_2$PPh with CO_2 (Equation 6) to give acrylates (introduced in the prior section),[16] we wish to communicate herein some of our results covering the reactivity of phosphine derivatives of group 6 carbonyls with terminal olefins.[100] Subsequent studies of these systems with carbon dioxide will also be described.

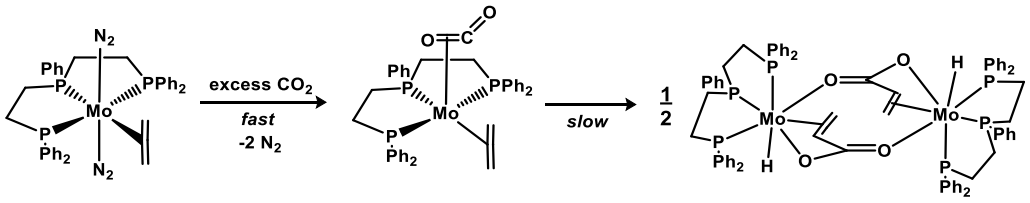

6

Synthesis and Characterization. The reactions of *cis*-M(CO)$_4$(pip)$_2$ (M = Mo, W and pip = piperidine) with the tripodal version of Triphos, i.e., 1,1,1-tris(diphenylphosphinomethyl)ethane, provided the κ^2 or κ^3 coordination depending on reaction conditions. Although the κ^2-Triphos derivatives of the group 6 tetracarbonyls have been prepared by direct substitution of the parent hexacarbonyl in refluxing ethanol,[101] replacement of the labile piperidine ligands in *cis*-M(CO)$_4$(pip)$_2$ derivatives represents milder reaction conditions for the synthesis of κ^2-[MeC(CH_2PPh_2)$_3$]M(CO)$_4$ complexes (M = Mo(**1a**) or W(**1b**)).[102,103] In a similar manner where the reactions temperature and time were increased the κ^3-Triphos derivatives of molybdenum and

tungsten tricarbonyls were formed. Interestingly, during the synthesis of the bidentate coordination of Triphos to either molybdenum or tungsten carbonyls under mild conditions, small quantities of the tridentate chelated ligand were observed. This was true in the short term reactions carried out in refluxing dichloromethane (313 K) or over longer reaction times at ambient temperature. Figure 46 depicts the three-dimensional stack plots for the substitution reaction of *cis*-$Mo(CO)_4(pip)_2$ with Triphos in $CHCl_3$ at 308 K, along with the reaction profiles for the growth of κ^2- and κ^3-Mo carbonyl species. As is readily visible from the *in situ* infrared monitoring of the substitution reaction, formation of this κ^3 complex occurs concurrently with the κ^2 species, albeit at a slower rate.

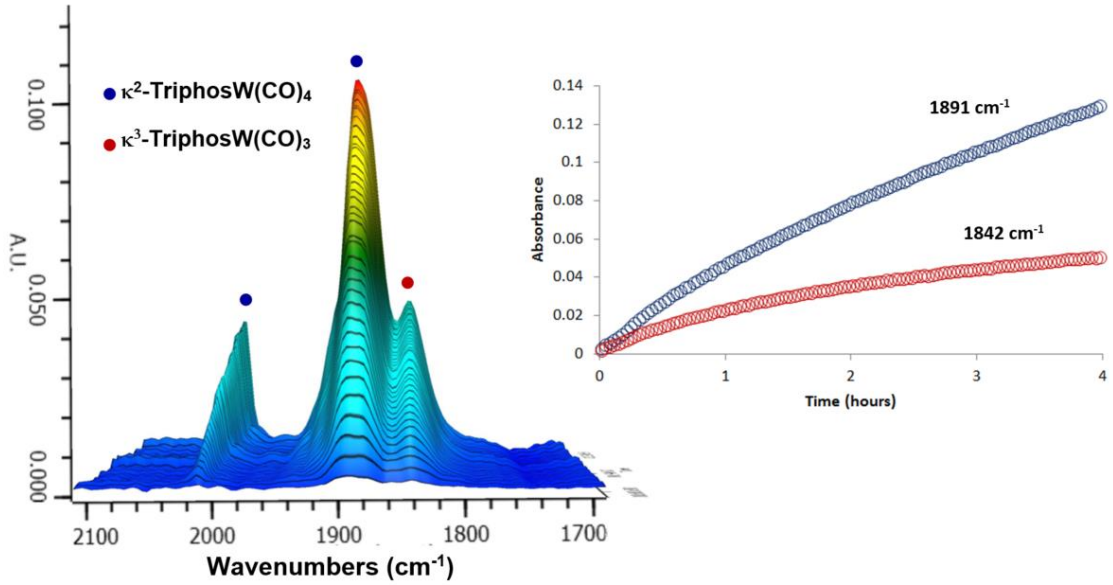

Figure 46 Three-dimensional stack plots for the substitution reaction of *cis*-$Mo(CO)_4(pip)_2$ with Triphos in $CHCl_3$ at 308 K, where the starting material is subtracted out. Reaction profiles for the formation of (κ^2-Triphos)$W(CO)_4$ (1891 cm^{-1}) and (κ^3-Triphos)$W(CO)_3$ (1842 cm^{-1}).

Further evidence for simultaneous formation of the κ^3 derivative is noted in the ^{31}P NMR spectrum (see Figure 47). This behavior is suggestive of a phosphine assisted (I_a) pathway for the displacement of CO in the κ^2-Triphos complexes.[104] Support for such a process is noted from our observation that CO substitution in $Mo(CO)_4$(diphos) by PPh_3 takes place much more slowly by a dissociative mechanism.

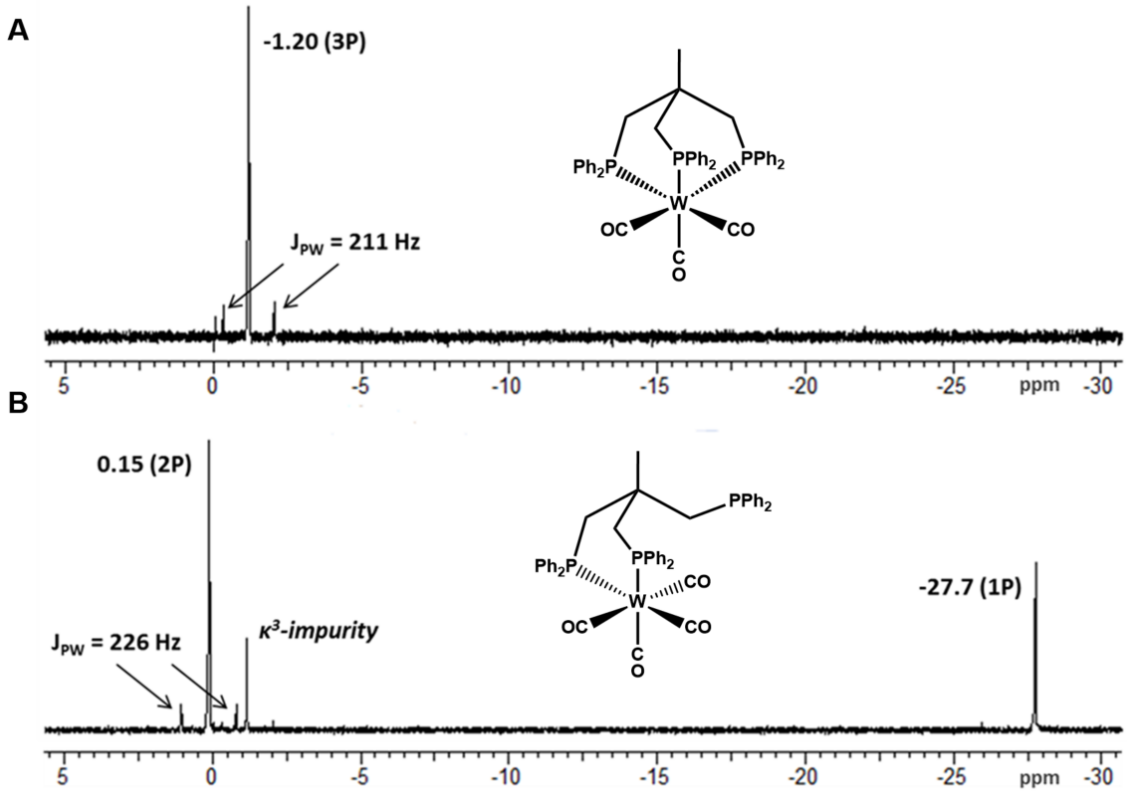

Figure 47 ^{31}P NMR Spectra. **A**. Purified sample of (κ^3-Triphos)$W(CO)_3$. **B**. Isolated sample of (κ^2-Triphos)$W(CO)_4$ from mild condition synthesis.

The crystal structures of the (κ^3-Triphos)$M(CO)_3$ (M = Mo(**2a**) or W(**2b**)) complexes have been reported.[105] However, in all of our attempts at obtaining X-ray

quality crystals of the κ^2-Triphos metal tetracarbonyls we obtained two crystalline forms, a cluster of needles and cubes, only the latter were suitable for X-ray analysis. X-ray crystallography established these cube shaped crystals to be the $[(Ph_2PCH_2)_2CMeCH_2PPh_2(O)]M(CO)_4$ (M = Mo(**3a**) or W(**3b**)) complexes, where the free phosphine arm was oxidized despite all efforts to exclude oxygen and H_2O. ^{31}P NMR revealed the mixture of crystals to be composed of approximately 80% of the of complex **3a** or **3b**, with the other unsuitable crystals for analysis being (κ^2-Triphos)$M(CO)_4$. Previously, these derivatives have been synthesized by oxidation of the free-phosphine arm in the κ^2-species with H_2O_2.[103] The structures of these two metal complexes are shown in Figure 48. It is worth noting that PPh_3O has been shown to greatly aid the crystallization of organic materials, and hence may account for the preferential well-defined crystals isolated of the oxidized form of the κ^2-species.[106] The non-bonding distances between the phosphine oxide and the nearest CO ligand, O(5)…C(1), of 3.943(4) and 3.88(1) Å for the Mo and W derivatives, respectively, are greater than the sum of the van der Waals radii of 3.25 Å.

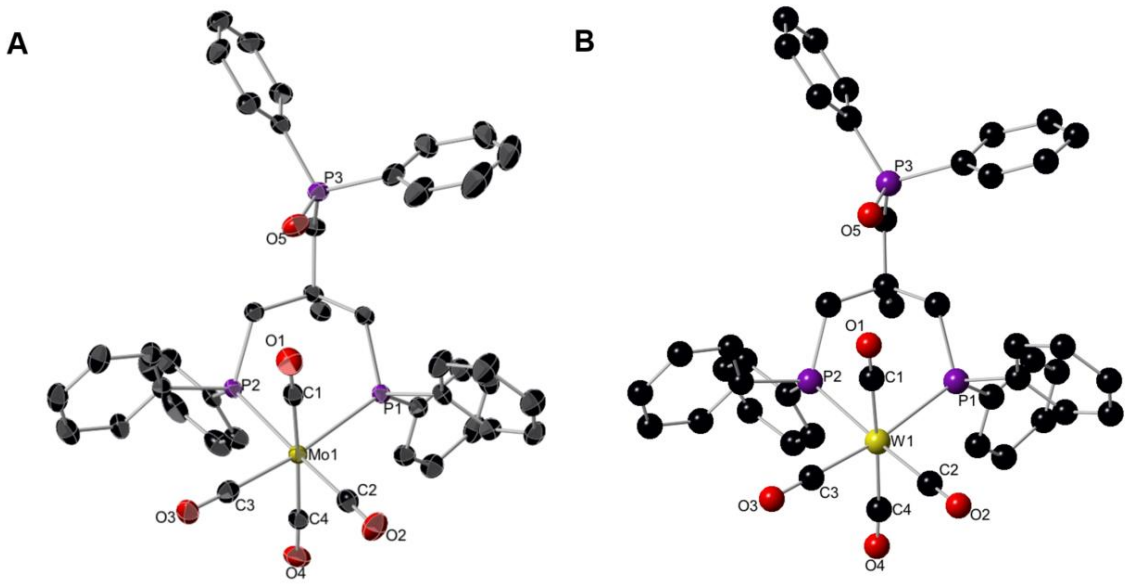

Figure 48 X-ray structures. **A**. Thermal ellipsoid representation of complex 3a with elipsoids at 50% probability surfaces. Hydrogen atoms have been omitted for clarity. **B**. Ball-and-stick drawing of complex 3b.

Kinetic Measurements. Kinetic studies were undertaken by using a rapid-scan and step-scan capable FTIR instrument with our collaborator Dr. Ashfaq Bengali at Texas A&M Qatar. The key results are described below.[100] UV photolysis on (κ^2-Triphos)$W(CO)_4$ in solution can generate a vacant tungsten site *via* photoejection of a CO ligand which is immediately followed by the coordination of the free phosphine arm of the Triphos ligand to give (κ^3-Triphos)$W(CO)_3$ complex (Scheme 15). Photolysis of a CO from the κ^2-complex in the presence of 1-hexene results in IR spectral changes which indicate olefin coordination to the W center with bands appearing at 1944 and 1860 cm^{-1} (Figure 49). These bands are similar to those of the κ^3-complex suggesting the formation of a tricarbonyl species, but as they are blue-shifted, it can be said that the third phosphine

arm of the Triphos ligand remains uncoordinated in this intermediate complex. This transient species, (κ^2-Triphos)$W(CO)_3$(η^2-1-hexene) complex then undergoes intramolecular displacement of the 1-hexene ligand by the free phosphine arm to give (κ^3-Triphos)$W(CO)_3$, as seen by their first-order exponential decay and growth in Figure 49.

Scheme 15

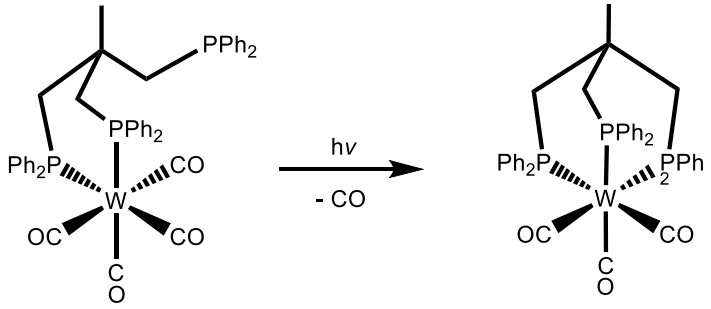

Further evidence of the intermediate complex comes from the observation that the reaction rate varies inversely with 1-hexene concentration (Figure 50). This inverse dependence of k_{obs} on concentration of 1-hexene is consistent with a plausible mechanism that involves reversible dissociation of the 1-hexene ligand prior to the formation of the final (κ^3-Triphos)$W(CO)_3$ product complex (Figure 51). The lifetime of the η^2-alkene species is unaffected by increasing the concentration of the parent tetracarbonyl complex, thereby ruling out an intermolecular process in the displacement of the alkene.

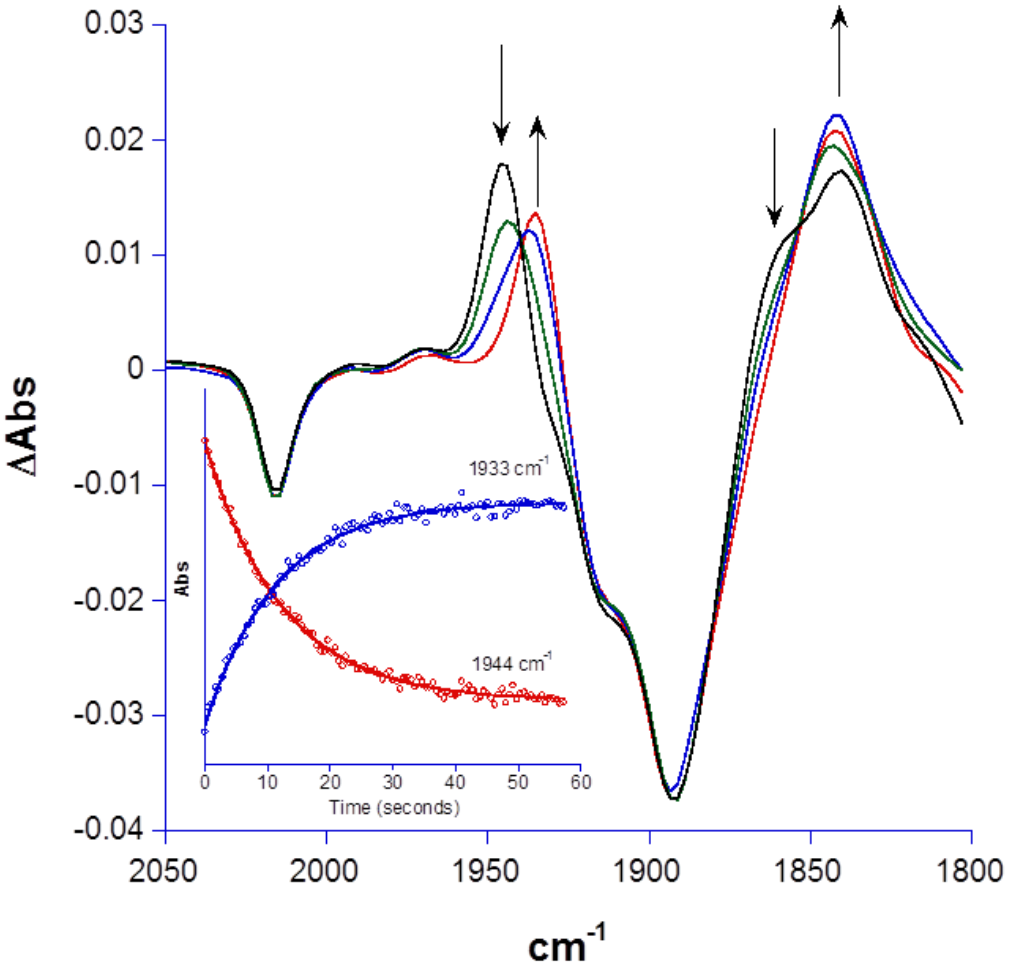

Figure 49 Spectral changes observed upon photolysis of (κ^2-Triphos)W(CO)$_4$ in the presence of [1-hexene] = 3.2 M at 288 K. The peaks at 1944 and 1860 cm^{-1} assigned to the (κ^2-Triphos)W(CO)$_3$(η^2-1-hexene) complex decrease in intensity while those at 1933 cm^{-1} and 1841 cm^{-1} due to the (κ^3-Triphos)W(CO)$_3$ complex grow at the same rate (see inset). The spectra were obtained 0, 5.8, 17.3, and 46.2 seconds after photolysis.

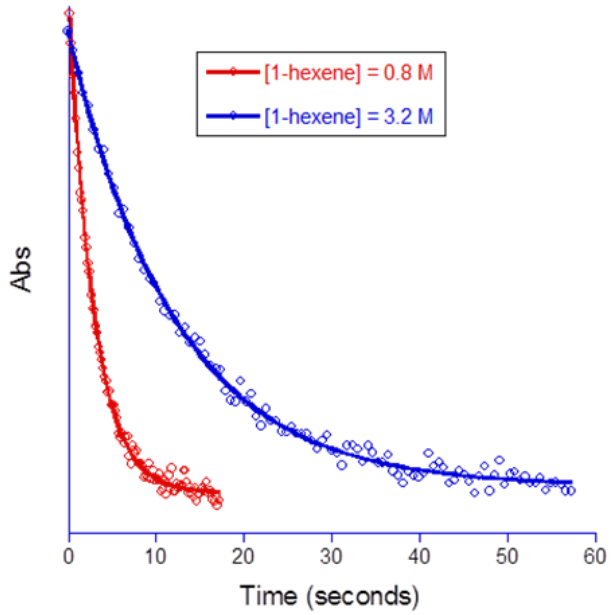

Figure 50 Effect of increasing 1-hexene concentration upon the decay rate of the (κ^2-Triphos)W(CO)$_3$(η^2-1-hexene) complex at 288 K.

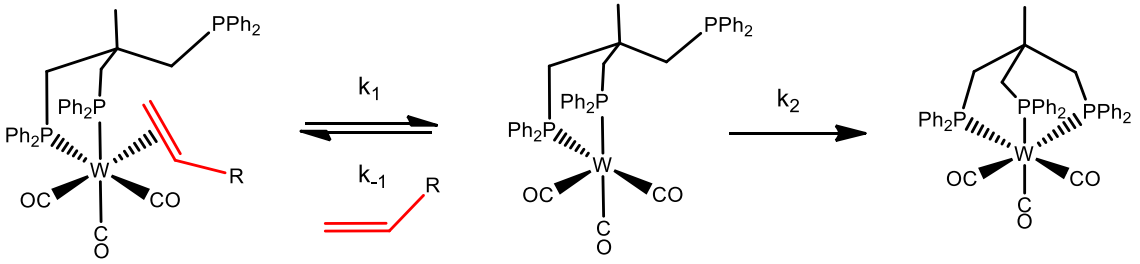

Figure 51 Reversible dissociation of 1-hexene prior to (κ^3-Triphos)W(CO)$_3$ formation.

Experiments were carried out over various concentrations of 1-hexene, and by employing the steady state approximation, the selectivity ratio k', where k' = k_{-1}/k_2, was found to have a value of 20 and be independent of temperature. This is surprising, as it shows the 16-electron (κ^2-Triphos)W(CO)$_3$ intermediate reacts faster with 1-hexene than

with the intramolecular phosphine arm of the Triphos ligand. This temperature independence indicates that the enthalpic barriers are very similar for both reactions, so the kinetic preference is attributed to entropic factors, wherein the steric reorganization of the Triphos ligand involved in $\kappa^2 \rightarrow \kappa^3$ coordination mode is considerably more negative than the bimolecular reaction.

Activation parameters based on the temperature dependence of k_1 were determined *via* Eyring analysis to be $\Delta H^{\ddagger}$ of 26.1 ± 0.4 kcal/mol and a $\Delta S^{\ddagger}$ of 36 ± 3 eu. The strongly positive $\Delta S^{\ddagger}$ is consistent with the dissociative nature of the transition state expected for the k_1 step, and $\Delta H^{\ddagger}$ provides an estimate for the W-(η^2-1-hexene) bond dissociation enthalpy (BDE). This value is consistent with a theoretical estimate of 26.2 kcal/mol for the $(CO)_5W$-(η^2-C_2H_4) BDE.[107] Few experiments conducted with the analogous Mo system under similar conditions showed (κ^2-Triphos)$Mo(CO)_3$(η^2-1-hexene) reacted almost 200 times faster than the W complex. This was expected as Mo-(η^2-1-hexene) BDE is expected to be weaker than that in the W system.[107] Preliminary results on 1-hexene interaction in (κ^3-Triphos)$W(CO)_2$(η^2-1-hexene) shows comparable lifetimes with (κ^2-Triphos)$W(CO)_3$(η^2-1-hexene), but detailed studies could not be obtained due to the poor solubility of the symmetric (κ^3-Triphos)$W(CO)_3$ complex in solvents.

Of particular interest in this study is the photochemical reactions of (κ^2-Triphos)$W(CO)_4$ in the presence of excess CO_2. Upon photolysis of a CO_2-saturated solution of the κ^2-complex, only the formation of (κ^3-Triphos)$W(CO)_3$ was observed with no indication of IR bands for a blue-shifted intermediate. The experiment with the CO_2-saturated solution was repeated in the presence of 1-hexene, and the spectral changes and

rate constants were identical to those determined in the absence of CO_2, i.e. no coupling with the bound 1-hexene was observed. These results strongly support the lack of significant CO_2 interactions with the vacant site in (κ^2-Triphos)$W(CO)_3$, especially when compared with the corresponding binding of an olefin ligand.

By way of contrast, rather strong interaction is observed between triethylsilane and the transient tricarbonyl species afforded upon photolysis of (κ^2-Triphos)$W(CO)_4$. The (κ^2-Triphos)$W(CO)_3$(silane) intermediate gives two ν_{CO} bands similar to those seen in the 1-hexene analog, although as expected these are red-shifted by 5-8 cm^{-1}. However, the initial species reacts with the free-phosphine arm to afford (κ^3-Triphos)$W(CO)_3$ almost 15 times faster than the 1-hexene complex. Given the position of the ν_{CO} bands in the intermediate and its reactivity, this species is most likely (κ^2-Triphos)$W(CO)_3$(η^2-$HSiEt_3$) and not a Si-H activated complex.

Concluding Remarks. We have shown that photolysis of (κ^2-Triphos)$W(CO)_4$ in the presence of 1-hexene affords a short-lived (κ^2-Triphos)$W(CO)_3$(1-hexene) complex which subsequently undergoes loss of the olefin with concomitant formation of the stable (κ^3-Triphos)$W(CO)_3$ derivative. The transient 1-hexene adduct was found to sustain intramolecular displacement of the olefin ligand by the free phosphine arm with a reaction rate which varied inversely with the [1-hexene], indicative of a dissociative process. Furthermore, the unsaturated intermediate was shown to be ~20 times more selective for olefin coordination as compared to the uncoordinated phosphine. The molybdenum analog

was shown to undergo these transformations on a much shorter timescale The activation parameters for the replacement of the 1-hexene ligand in the tungsten complex were determined to be $\Delta H^{\ddagger}$ = 26.1 kcal/mol and $\Delta S^{\ddagger}$ = 36 eu. The enthalpy of activation closely relates to the estimated value of the BDE as expected for a dissociative reaction. Attempts to observe a CO_2 adduct with the transient provided by photolysis of (κ^2-Triphos)$W(CO)_4$ were unsuccessful, indicative of no binding or weak binding with a lifetime of binding less than 10^{-3} sec. Similarly, the kinetic parameters for 1-hexene binding were unaffected by the presence of excessive quantities of CO_2 in solution. That is, CO_2 coordination at the vacant metal site is not competitive with olefin binding. On the other hand, a transient complex (κ^2-Triphos)$W(CO)_3(HSiEt_3)$ was observed upon photolysis of (κ^2-Triphos)$W(CO)_4$ in the presence of triethylsilane at ambient temperature. Based on the ν_{CO} bands in the $HSiEt_3$ adduct and its rapid dissociation, about 15 times more labile than 1-hexene, this species is assumed to be (κ^2-Triphos)$W(CO)_3(\eta^2$-$HSiEt_3)$.

Experimental Section. All reactions were carried out under an argon atmosphere. Dichloromethane was purified by an MBraun Manual Solvent Purification System packed with Alcoa F200 activated alumina desiccant. Decalin (Aldrich) was degassed before use. Methanol and Chloroform were used as purchased from EMD chemicals. The ligand 1,1,1-tris(diphenylphosphinomethyl)ethane or Triphos was purchased from Sigma-Aldrich and the metal-carbonyl precursors, $M(CO)_4(pip)_2$ (M = Mo, W), were prepared as per the literature.[102] NMR spectra were recorded on a Varian INOVA 300 (operating at 299.96 and 121.43 MHz for ^1H and ^{31}P, respectively) and Varian MERCURY 300

(operating at 75.42 MHz for ^{13}C) spectrometers. ^{1}H and ^{13}C NMR spectra were referenced to residual solvent resonances, while ^{31}P NMR spectra were referenced to an external H_3PO_4 in D_2O at 0.0 ppm. Infrared spectra were obtained on a Bruker Tensor 27 FTIR spectrometer. *In situ* IR monitoring was carried out using a Mettler Toledo iC10 ReactIR with an AgX fiber conduit probe. Elemental Analyses were determined by Atlantic Microlab (Norcross, GA).

Synthesis of (κ^2-Triphos)Mo(CO)$_4$

$Mo(CO)_4(pip)_2$ (0.894 g, 2.36 mmol) and Triphos (1.500 g, 2.40 mmol) in dichloromethane (100 mL) were heated to reflux for 30 min. The resulting orange solution was filtered through celite, and the filtrate was reduced in volume to *ca.* 5 mL and treated with methanol to give a tan precipitate. Recrystallization from chloroform/methanol yielded a white product (1.550 g, 79%). IR data in CH_2Cl_2 (ν_{CO}): 1870 (sh), 1901 (s), 1920 (sh), 2020 (m). NMR data in $CDCl_3$: $^{31}P\{^{1}H\}$ δ -27.7 (t, J_{P-P} = 2, 1 P), 19.7 (d, J_{P-P} = 2, 2 P); ^{1}H δ 0.75 (s, 3 H, C*H*$_3$), 2.15 (m, 2 H, C*H*$_2$), 2.43 (dd, $^{2}J_{H-H}$ = 14, $^{2}J_{H-P}$ = 4, 2 H, C*H*$_2$), 2.71 (dd, $^{2}J_{H-H}$ = 14, $^{2}J_{H-P}$ = 9, 2 H, C*H*$_2$), 7.25-7.46 (m, 26 H, C$_6$*H*$_5$), 7.60-7.70 (m, 4 H, C$_6$*H*$_5$); selected $^{13}C\{^{1}H\}$ δ 209.6 (t, $^{2}J_{C-P}$ = 8, 1 C, *C*O), 211.1 (t, $^{2}J_{C-P}$ = 9, 1 C, *C*O), 215.3 (m, 2 C, *trans*-*C*O). Anal. Calcd for $C_{45}H_{39}MoO_4P_3$: C, 64.9; H, 4.7. Found: C, 64.4; H, 4.6%.

Synthesis of (κ^3-Triphos)$Mo(CO)_3$

$Mo(CO)_4(pip)_2$ (0.897 g, 2.37 mmol) and Triphos (1.504 g, 2.41 mmol) in decalin (110 mL) were heated to reflux for 19 h. The resulting brown solid was isolated by filtration and washed with methanol until filtrate ran clear. Recrystallization from chloroform/methanol yielded a white product (1.410 g, 74%). IR data in CH_2Cl_2 (ν_{CO}): 1844 (s), 1938 (s). NMR data in $CDCl_3$: $^{31}P\{^1H\}$ δ 18.2 (s, 3 P); ^1H δ 1.44 (m, 3 H, C*H*$_3$), 2.26 (m, 6 H, C*H*$_2$), 7.08 (t, $^3J_{H-H}$ = 7.2, 12 H, *H*$_m$), 7.18 (t, $^3J_{H-H}$ = 7.2, 6 H, *H*$_p$), 7.35 (m, 12 H, *H*$_o$); ^{13}C NMR data could not be obtained due to low solubility of the compound. Anal. Calcd for $C_{44}H_{39}MoO_3P_3$: C, 65.7; H, 4.9. Found: C, 65.5; H, 4.7%.

Synthesis of (κ^2-Triphos)$W(CO)_4$

$W(CO)_4(pip)_2$ (0.700 g, 1.50 mmol) and Triphos (1.000 g, 1.60 mmol) in dichloromethane (100 mL) were heated to reflux for 4 h. The resulting clear yellow solution was reduced in volume to *ca.* 5 mL and treated with methanol to give a yellow precipitate. Recrystallization from chloroform/methanol yielded a pale-yellow product (0.597 g, 43%). IR data in CH_2Cl_2 (ν_{CO}): 1861 (sh), 1892 (s), 1915 (sh), 2011 (m). NMR data in $CDCl_3$: $^{31}P\{^1H\}$ δ -27.7 (t, J_{P-P} = 2, 1 P), 0.15 [d, J_{P-P} = 2, (J_{P-W} = 226, satellite) 2 P]; ^1H δ 0.76 (s, 3 H, C*H*$_3$), 2.13 (m, 2 H, C*H*$_2$), 2.52 (dd, $^2J_{H-H}$ = 14, $^2J_{H-P}$ = 5, 2 H, C*H*$_2$), 2.81 (dd, $^2J_{H-H}$ = 14, $^2J_{H-P}$ = 10, 2 H, C*H*$_2$), 7.27-7.45 (m, 26 H, C_6H_5), 7.58-7.68 (m, 4 H, C_6H_5); selected $^{13}C\{^1H\}$ δ 202.1 (t, $^2J_{C-P}$ = 7, 1 C, *C*O), 203.5 (t, $^2J_{C-P}$ = 7, 1 C, *C*O), 206.0 (m, 2 C, *trans-C*O). Anal. Calcd for $C_{45}H_{39}O_4P_3W$: C, 58.7; H, 4.3. Found: C, 58.1; H, 4.2%.

Synthesis of (κ^3-Triphos)$W(CO)_3$

$W(CO)_4(pip)_2$ (1.101 g, 2.36 mmol) and Triphos (1.504 g, 2.41 mmol) in decalin (100 mL) were heated to reflux for 20 h. The resulting grey solid was isolated by filtration and washed with ether (2x 25 mL). Recrystallization from chloroform/methanol twice yielded a white product (0.874 g, 42%). IR data in CH_2Cl_2 (ν_{CO}): 1841 (s), 1933 (s). NMR data in $CDCl_3$: $^{31}P\{^1H\}$ δ -1.4 [s, J_{P-W} = 211 (satellite), 3 P]; ^1H δ 1.43 (m, 3 H, C*H*$_3$), 2.35 (m, 6 H, C*H*$_2$), 7.09 (t, $^3J_{H-H}$ = 7.2, 12 H, *H*$_m$), 7.18 (t, $^3J_{H-H}$ = 7.2, 6 H, *H*$_p$), 7.34 (m, 12 H, *H*$_o$); ^{13}C NMR data could not be obtained due to low solubility of the compound. Anal. Calcd for $C_{44}H_{39}O_3P_3W$: C, 59.2; H, 4.4. Found: C, 59.0; H, 4.3%.

Kinetic Measurements

In a typical experiment, the photolysis solution was ≈ 4 mM in (κ^2-Triphos)$W(CO)_4$ dissolved in dichloromethane with varying amounts of 1-hexene. The reactions were conducted over a 25 K temperature range from 278 K to 303 K and the 1-hexene concentration was varied over a 50 fold range (0.08M to 4 M). A Bruker Vertex 80 FTIR equipped with both step-scan and rapid-scan capabilities was used to obtain the IR spectra using a temperature controlled 0.75 mm pathlength transmission cell with CaF_2 windows. Spectra were obtained at 8 cm^{-1} resolution. Photolysis was conducted with 355 nm light from a Nd:YAG laser (Continuum Surelite I-10). Spectral acquisition was initiated following a single shot of the UV laser (30 mJ/pulse) which was collinear with the IR beam and defocused to ensure irradiation of the entire cell volume.

CHAPTER IV

CARBON MONOXIDE INDUCED REDUCTIVE ELIMINATION OF DISULFIDE FROM DINITROSYL IRON COMPLEXES: A MECHANISTIC STUDY*

Introduction

That diatomic molecules in combination with metals play vital roles in a variety of physiological functions is well established. While physiologically beneficial carbon monoxide and nitric oxide concentrations are in picomolar to nanomolar range, increasing concentrations result in cytotoxic effects.[108-110] Under physiological control CO and NO function as important regulatory and signaling molecules, and are members of a class of endogenously-produced gaseotransmitters.[111-117] Much current research is directed at the fundamental biochemistry especially significant in the cardiovascular system, as well as development of compounds as pro-drugs, capable of controlled delivery and release of NO and CO to biological targets—the most important in vasodilation activity being iron in porphyrin environments.[115] As an extensive literature exists for transition metal complexes containing CO and NO, attention has been focused on appropriate combinations of ligands and metals designed for specific pharmacological properties.[25] Indeed, explorations of one class of complexes, dinitrosyl iron complexes (DNICs), are inspired by their natural

---

* Reprinted (adapted) with permission from: Pulukkody, R.; Kyran, S. J.; Bethel, R. D.; Hsieh, C.-H.; Hall, M. B.; Darensbourg, D. J.; Darensbourg, M. Y. *J. Am. Chem. Soc.* **2013**, *135*, 8423. Copyright 2013 American Chemical Society. Pulukkody, R.; Kyran, S. J.; Drummond, M. J.; Hsieh, C.-H.; Hall, M. B.; Darensbourg, D. J.; Darensbourg, M. Y. *Chem. Sci.* **2014**, *5*, 3795. Copyright 2014 The Royal Society of Chemistry.

occurrence,[116] and by the intriguing proposal that they might be the "most abundant nitric oxide-derived cellular adduct", i.e., superceding the S-nitrosothiols (RSNOs).[117] Others have posited that synthetic versions may be developed as NO-release agents.[118]

The chemical properties of CO and NO as ligands to metals are substantially different; the former is viewed as an innocent ligand with weak σ-donor/strong π-acceptor properties in its M-CO bond formation.[119] In contrast, the radical character of NO imparts reactivity that surpasses that of CO, in that its ability to readily switch between the NO^+, •NO, and NO^- forms depends on the redox levels accessible by the metal to which it binds, thereby defining non-innocent ligand binding.[120]

The lifetime of free NO in the aerobic cellular milieu is reported to be too short to account for its observed physiological functions.[121] Therefore, it is expected that transitory derivatives of NO serve for storage, transport and delivery of NO to required sites. Both organic (RSNOs) and inorganic dinitrosyl iron complexes have been proposed for such NO storage/transport functions *in vivo*.[122,123] The biological DNICs are derived *in vivo* from the labile or cellular chelatable iron pool, or by degradation of iron sulfur clusters; the latter generates protein-bound $(cysteinyl\text{-}S)_2Fe(NO)_2$, as high molecular weight, HMW, moieties.[117,124-128] Characterized by a prominent EPR signal at 2.03,[116,118] the HMW form may be rendered mobile in low molecular weight, LMW, forms on exchange with free cysteine or other thiolate-rich biomolecules such as glutathione.[129]

Numerous small molecule models assumed to be relevant to biological DNICs have been synthesized and characterized.[122,130] Synthetic DNIC complexes exist in two redox levels: oxidized, EPR active $\{Fe(NO)_2\}^9$ and the reduced, EPR silent $\{Fe(NO)_2\}^{10}$

(Enemark-Feltham notation).[131] The oxidized form can be found in the neutral $L(X)Fe(NO)_2$ (where for example X = halides, pseudo halides, or thiolate S-donors and L = N-donors or the good sigma donor ligands N-heterocyclic carbenes (NHC) that are apt analogues of imidazoles), and the anionic $X_2Fe(NO)_2^-$ complexes.[132-136] The reduced form can be found in the $L_2Fe(NO)_2$ state, with the paradigm being the 18-electron species, $(OC)_2Fe(NO)_2$, a versatile precursor to $LFe(CO)(NO)_2$ derivatives.[132,137-140] The ligand environment is critical in stabilizing the redox state of the DNIC which in turn is expected to govern its endogenous role as NO storage or releasing agent.[136] The work presented below focuses on developing understanding of mixed ligand environments and mechanisms of ligand exchange processes that might regulate switches in redox levels.

Scheme 16

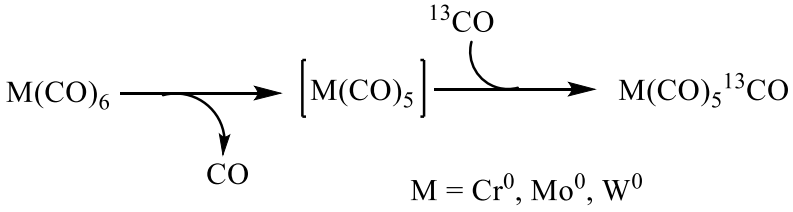

As a poor nucleophile, CO exchange reactions with a metal-bound CO or L typically take place by dissociative mechanisms allowing external CO to be trapped by an open site as in Scheme 16.[141] Recently, we've reported an example of CO displacement of RS● in a dinitrosyliron complex, the kinetics of which followed a second-order rate expression with activation parameters consistent with an associative mechanism, Scheme 17.[142] This process entailed a change in the redox state of the reactant DNIC as the

oxidized state, $\{Fe(NO)_2\}^9$, converted into the reduced analogue, $\{Fe(NO)_2\}^{10}$. Proceeding under mild conditions, the thermodynamics of the reaction is driven by the formation of RSSR as a result of the release of RS●. Computational studies were carried out in pursuit of a reasonable mechanistic proposal for the observed reactivity, resulting in the suggestion that the π-density of the $\{Fe(NO)_2\}$ unit was involved in nucleophilic attack on CO, the latter acting as an electrophile, Figure 52.[142] Theory suggested a side-on approach of CO leading to a 5-coordinate intermediate, species **I** of Figure 52, with the NO ligands accommodating the excess charge. Such nucleophilicity of the iron in $\{Fe(NO)_2\}$, especially in the oxidized $\{Fe(NO)_2\}^9$, was unexpected.[142]

Scheme 17

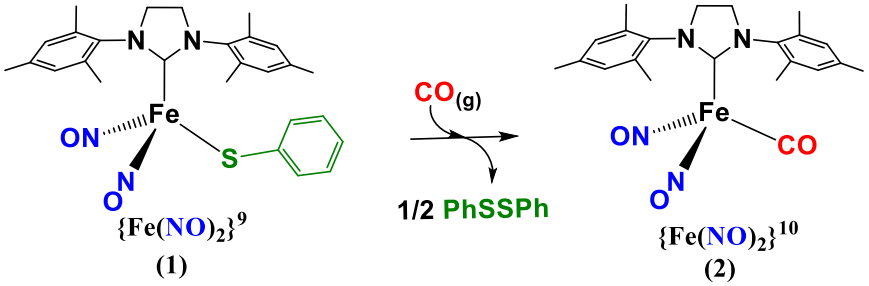

In this chapter, the initial kinetic investigations employed in elucidating the bimolecular mechanism[142] and further experiments designed to test the mechanistic proposal that suggests a unique role of the $\{Fe(NO)_2\}$ unit in the CO-induced disulfide elimination are described.[143] This study was a fruitful collaboration with the M.Y.D. research group, where Dr. Pulukkody prepared and completely characterized all the dinitrosyl iron complexes herein, while Dr. Bethel provided the computational insights.

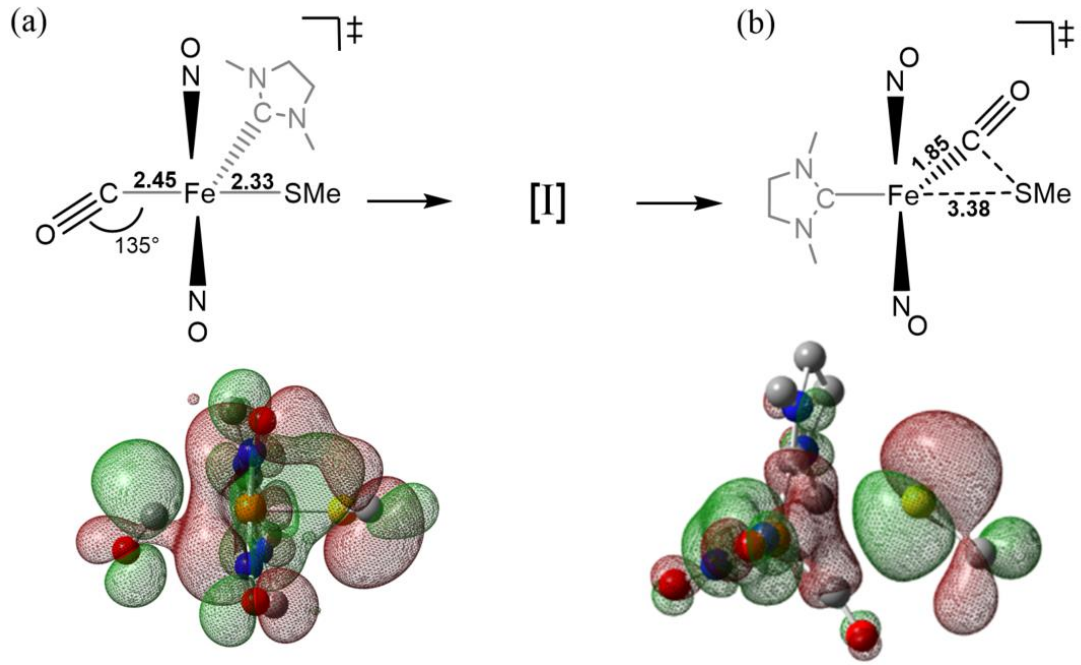

Figure 52 (Top) (a) A sketch of the calculated collision complex,[142] involved in the rate determining step for CO and (NHC)(RS)Fe(NO)$_2$, proceeding through a 5-coordinate intermediate I.[142] Theory finds that as the Fe-CO bond becomes linear as in (b), the Fe-SR bond lengthens, and releases a thiyl radical, either by direct homolytic Fe-S bond cleavage or *via* homolytic C-S cleavage from a transient metallothioester group.[142] (Bottom) Corresponding plots of the transition state SOMOs: (a) the unpaired electron on the {Fe(NO)$_2$} donates into the π^* orbital of the side-on entering CO; and (b) the shift of the unpaired electron releases thiyl radical.[142]

Results and Discussion

Synthesis and Characterization. Homolytic cleavage of (μ-PhS)$_2$[Fe(NO)$_2$]$_2$[144] by two equivalents of the sIMes ligand (freshly prepared by combining 1,3-bis(2,4,6-trimethylphenyl)imidazolinium chloride and NaO^{t}Bu in a 1:1 stoichiometric ratio) leads to the formation of complex **1**, shown in Scheme 17. This preparation is identical to that of the unsaturated NHC or IMes analogue reported earlier.[135] Reaction progress can be monitored *via* IR spectroscopy with notable shifts in the ν_{NO} positions and pattern

indicating the formation of complex **1** from the Roussin's Red Ester, $(\mu\text{-PhS})_2[Fe(NO)_2]_2$, precursor (Figure 53). The room temperature EPR spectrum of complex **1** shows an isotropic signal at g = 2.03, the characteristic signature of the $\{Fe(NO)_2\}^9$ oxidized form of DNICs. Complex **1** is stable under inert atmosphere over several months in both solution and solid states.

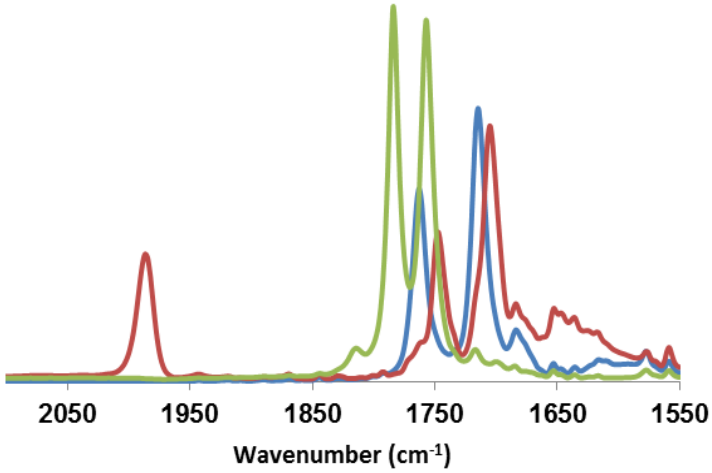

Figure 53 Overlaid IR Spectra of **RRE**, **1** and **2** in THF. [Green: **RRE**: ν_{NO} 1783(s), 1757(s) cm^{-1}], [Blue: **1**: ν_{NO} 1763(s), 1715(vs) cm^{-1}], [Red: **2**: ν_{CO} 1986(s), ν_{NO} 1747(s), 1705(vs) cm^{-1}].

In the presence of $CO_{(g)}$, the oxidized, paramagnetic $\{Fe(NO)_2\}^9$ complex **1** converts to the reduced, diamagnetic $\{Fe(NO)_2\}^{10}$ complex **2**, Scheme 17. The spectral monitor indicated ν_{NO} positions red shifted by ~15 cm^{-1} and the appearance of a new CO band at 1986 cm^{-1}, indicating the formation of the reduced DNIC **2** (Figure 53). The byproduct PhSSPh, confirmed by ^1H NMR and mass spectrometry,[145] is generated by bimolecular

reductive elimination from **1**. The DNIC **2** is fairly air-stable in the solid state, but slowly decomposes in THF solution in the presence of air at room temperature. The DNICs **1** and **2** were obtained as dark purple and brown crystals, respectively, and their molecular structures are compared in Figure 2(a) and 2(b).

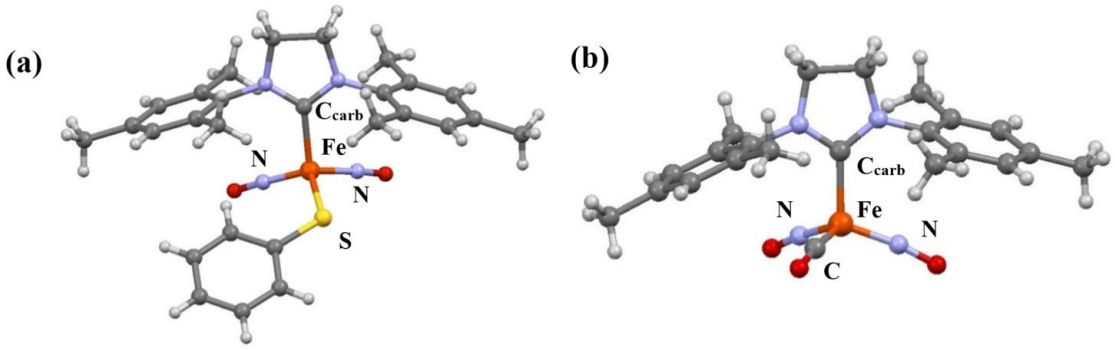

Figure 54 Molecular structures of complexes (a) **1** and (b) **2**in ball-and-stick view.

Kinetic Measurements. The rate of conversion of **1** to **2** is amenable to kinetic and mechanistic studies. This was accomplished via *in situ* IR spectroscopy of toluene solutions of **1**, saturated with CO and maintained under an atmosphere of CO. Figure 55 is a sample three-dimensional stacked plot from *in situ* IR monitoring in toluene at 333 K. The decay of the NO bands and the growth of new NO and CO bands occur at the same rate as expected for the oxidized and reduced DNICs **1** and **2**, respectively (Figure 56).

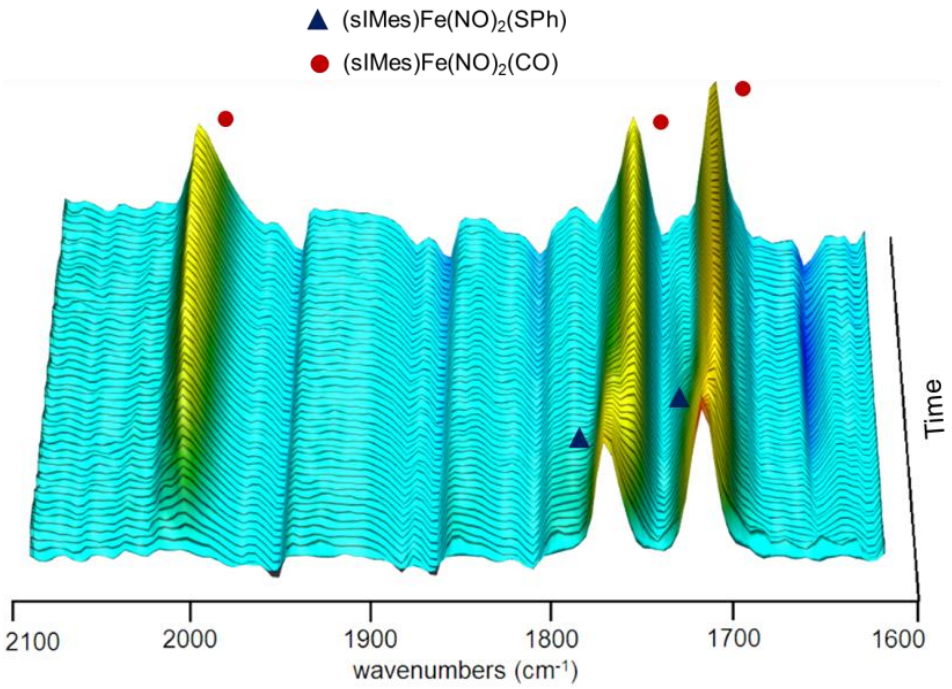

Figure 55 Three-dimensional stacked plot of the reaction of complex **1** with $CO_{(g)}$ at 333 K in toluene.

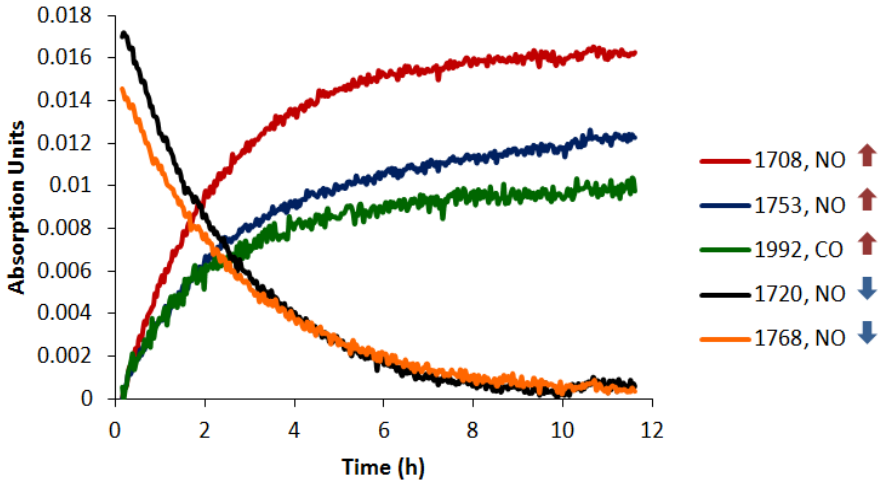

Figure 56 Reaction profiles of infrared bands for the conversion of **1** (ν_{NO} 1708, 1753 cm^{-1}) to **2** (ν_{CO} 1992, ν_{NO} 1720, 1768 cm^{-1})) at 348 K in toluene.

Under the conditions studied, the mole ratio of CO to DNIC in solution is approximately one to one, but, as the reaction is carried out under a CO atmosphere the concentration of CO is constant. Under these conditions the rate was determined to have a first order dependence with respect to the iron complex (Equation 9), as evidenced by the linear natural log plot over three half-lives of the absorption data of the carbonyl band of **2** at 323 K (Figure 57).

$$\text{rate} = k_{obs}\,[\text{Fe}]^1, \text{ where } k_{obs} = k\,[\text{CO}]^n \qquad 9$$

$$\text{rate} = k\,[\text{Fe}]^1\,[\text{CO}]^1 \qquad 10$$

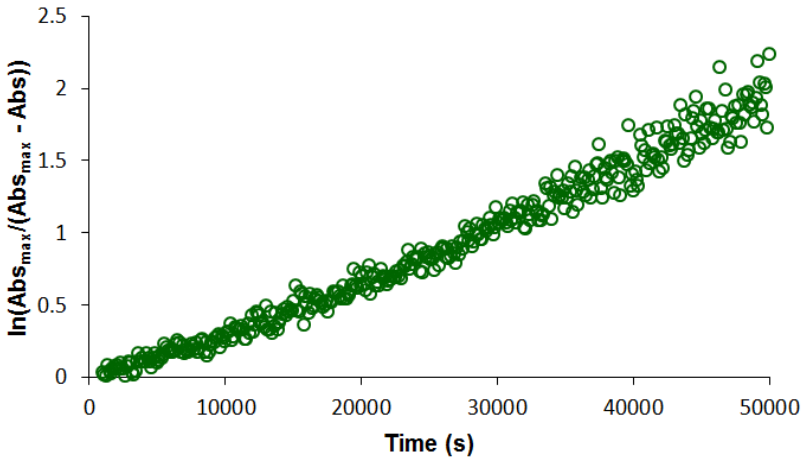

Figure 57 Natural log plot of absorption data versus time of the ν_{CO} of complex **2** at 323 K. A linear trend consistent with a first-order condition in **2** gives a k_{obs} value of 4.03×10^{-5} s^{-1} calculated from the slope.

In order to establish the order of CO dependence in the rate expression in equation 9, reaction rates were monitored at CO pressures of 3.1 and 6.1 atm at 323 K. A plot of the k_{obs} vs [CO] at these pressures is linear with a y-intercept of zero implicating first-order dependence on the concentration of CO (Figure 58). The complete rate expression is thus bimolecular with a first order rate dependence on both complex **1** and CO (Equation 10).

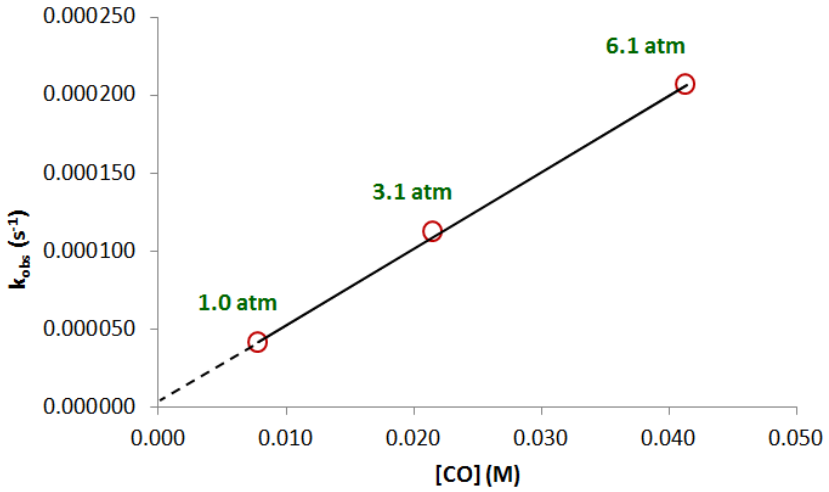

Figure 58 Plot of k_{obs} vs [CO] for the formation of complex **2** at 323 K. The R^2 value of 0.9996.

The temperature dependence of the rate constant, *k*, for the conversion of complex **1** to **2** was measured over a 25 K range under 1 atm of CO (Figure 59) and the resulting *k* values, derived as per Equation 10, are listed in Table 18.

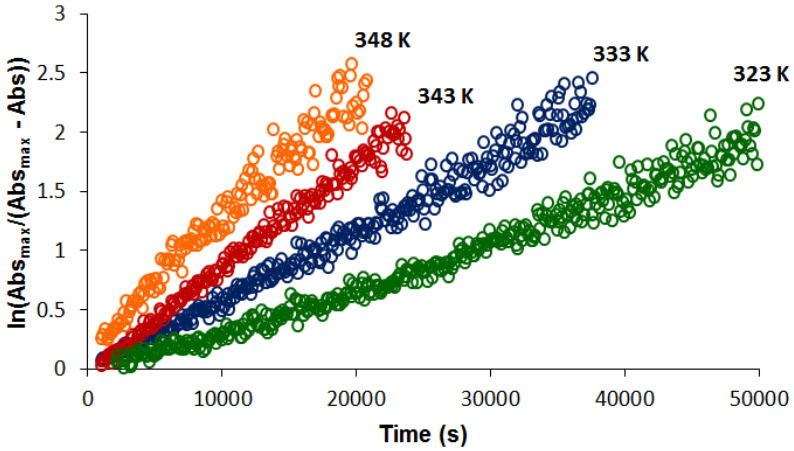

Figure 59 Natural log plots of absorption data versus time of the ν_{CO} of complex **2** at various temperatures.

Table 18 Kinetic parameters obtained from a linear fit of the natural log plots. CO concentrations in toluene at 1 atm were derived from literature.[29]

T (K)	k_{obs} (s^{-1})	[CO] (M)	k (M^{-1} s^{-1})
323.15	4.03 x 10^{-5}	0.00785	5.13 x 10^{-3}
333.15	6.03 x 10^{-5}	0.00798	7.56 x 10^{-3}
343.15	8.81 x 10^{-5}	0.00810	1.09 x 10^{-2}
348.15	1.09 x 10^{-4}	0.00816	1.34 x 10^{-2}

The activation parameters for the formation of complex **2** were determined through an Eyring analysis and found to have values for $\Delta H^{\ddagger}$ of 7.80 ± 0.16 kcal/mol and a $\Delta S^{\ddagger}$ of -45.0 ± 0.5 e.u. (Figure 8). The small $\Delta H^{\ddagger}$ value and large negative $\Delta S^{\ddagger}$ value are indicative of an associative mechanism, consistent with the second order rate expression.

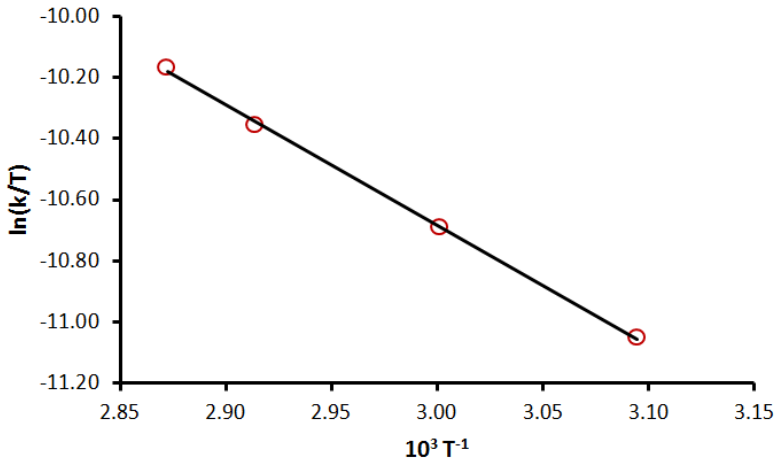

Figure 60 Eyring plot obtained from the temperature dependence of *k*. The R^2 value is 0.999.

para-Substituted Aryl Thiolate DNICs. As theory suggests the {Fe(NO)$_2$} unit to act as a nucleophile in the reaction shown in Scheme 17, a series of analogous {Fe(NO)$_2$}^{9} [(NHC)(*p*-S-C$_6$H$_4$X)Fe(NO)$_2$] complexes were prepared, where the *para*- substituents X were systematically varied from electron donor (EDG) to electron withdrawing groups (EWG) so as to carry out a Hammett analysis of their effects on the electron density at the Fe(NO)$_2$ unit. These complexes were synthesized as described earlier from their corresponding Roussin's Red Ester (Scheme 18). Complexes **1a – 1c** and **1e** were also characterized structurally *via* X-ray diffraction. Although barely within significant limits, there appears to be a gradual decrease of Fe-C_{NHC} bond lengths with the electron withdrawing ability of the *para* substituent on the S-C$_6$H$_4$, concomitant with an increase in the Fe-S bond distance. This correlation is further reflected in the ν_{NO} vibrational spectra. The ν_{NO} positions of the DNIC series (**1a-1e**) show small but systematic shifts to lower wavenumbers over a range of *ca*. 12 cm^{-1} (Figure 61).

Scheme 18

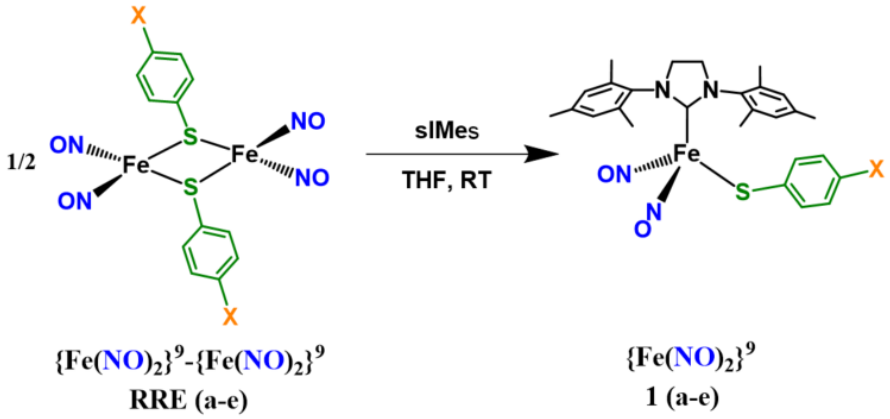

$\{Fe(NO)_2\}^9$-$\{Fe(NO)_2\}^9$
RRE (a-e)

$\{Fe(NO)_2\}^9$
1 (a-e)

	a	b	RRE/1	c	d	e
X	OCH_3	CH_3	H	Cl	CF_3	NO_2
σ_p[41]	-0.268	-0.170	0.000	0.230	0.540	0.778

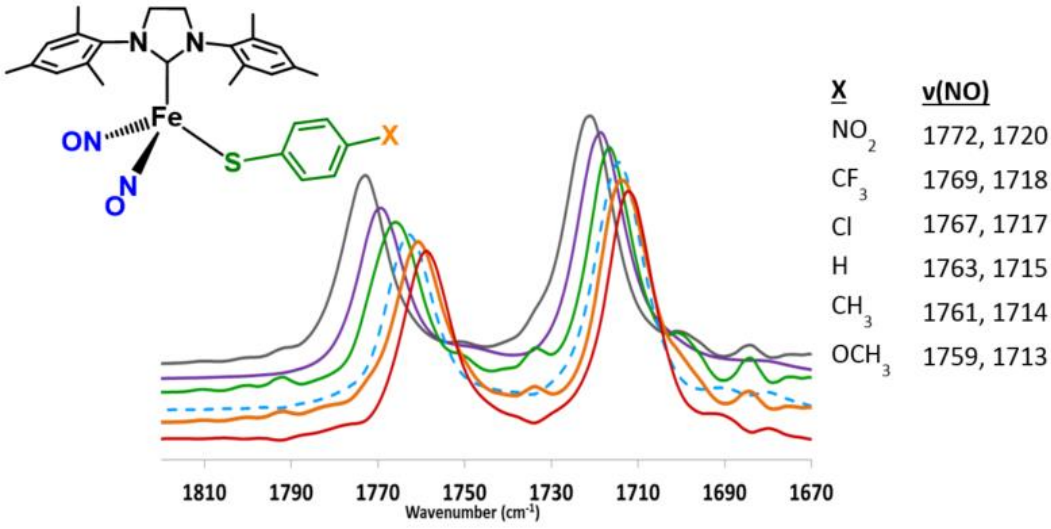

Figure 61 Overlaid IR spectra for **1**, **1a-1e**.

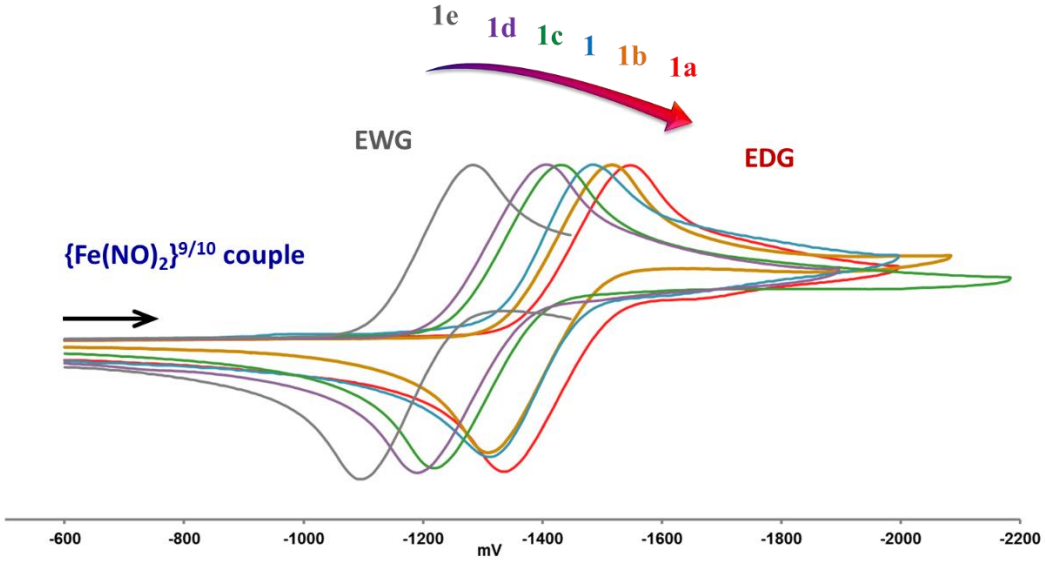

Figure 62 Overlaid cyclic voltammograms (THF solution, scan rate 100 mV/s, 100 mM [*n*-Bu_4N][BF_4] as supporting electrolyte) of **1a** (red), **1b** (brown), **1** (blue), **1c** (green), **1d** (purple), **1e** (grey). All are referenced to Cp_2Fe/Cp_2Fe^+.

The electronic effect of the X-substituent of the $–SC_6H_4X$ series as interpreted from the ν_{NO} IR values is also reflected in the electrochemistry. The unsubstituted analogue, complex **1** [(sIMes)(SPh)Fe$(NO)_2$], shows a reversible redox event at -1.39 V (in THF solution), which is assigned to the $\{Fe(NO)_2\}^{9/10}$ couple. All other derivatives in the series show similar reversible redox events also assigned to the $\{Fe(NO)_2\}^{9/10}$ redox couple. These events range from -1.19 V to -1.44 V for the $–NO_2$, $-CF_3$, -Cl, $-CH_3$ and $–OCH_3$ derivatives respectively. The trend in the $E_{1/2}$ is as expected, shifting to higher negative potentials when moving from electron withdrawing groups to electron donating groups (Figure 62) . There is good correlation between $E_{1/2}$ and the Hammett parameter σ_p

as shown in Figure 63. Correlating along with the ν_{NO} values, these $E_{1/2}$ values are therefore indicative of the changes in electron density occurring at the $Fe(NO)_2$ unit upon changes in the substituent, though present at a remote position.

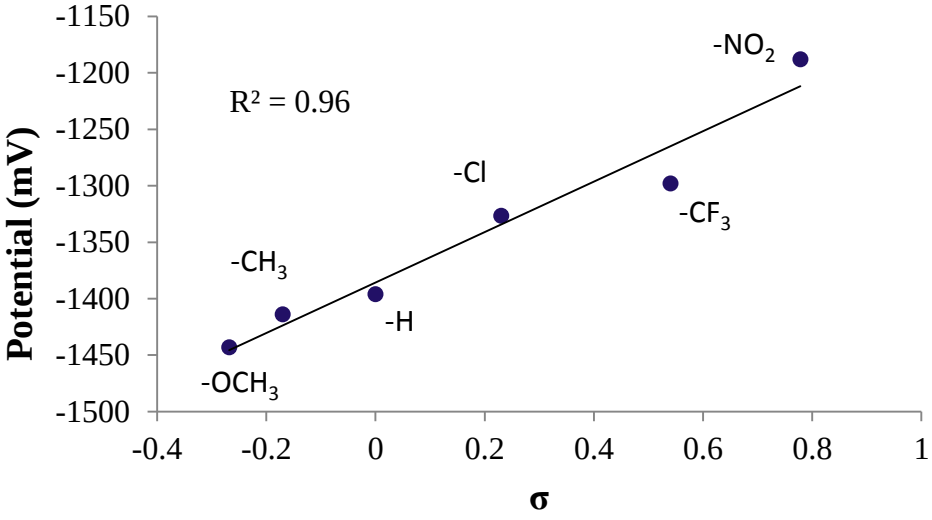

Figure 63 Plot of $E_{1/2}$ for **1a-1e** *v*s the Hammett substituent parameter σ_p. All are referenced to Cp_2Fe/Cp_2Fe^+.

Hammett Analysis. The rates of conversion of complexes **1a-1e** to **2,** were examined using *in situ* IR spectroscopy (Scheme 19). All iron complexes were subject to pseudo-first-order reaction conditions under an excess of CO and the rate constants, *k*, of each reaction were derived from the respective linear natural log plots. The kinetic profiles of **1a-1e** are similar to that of the closely related unsubstituted analogue, complex **1**, described earlier.[142]

Scheme 19

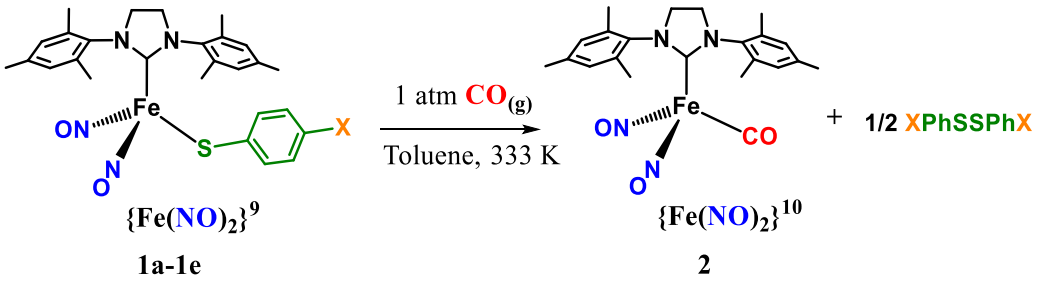

Rate constants (*k*) and $t_{1/2}$ values are listed in Table 19, and indicate that the stronger the electron-withdrawing group on the phenyl thiolate, the slower the formation of the product carbonyl complex, **2**. In the case of the nitro species, **1e** the reaction time is longer than the solution life-time of the reagent, as such, significant decomposition is observed with the progress of the reaction. It is likely that the decomposed species may induce further decomposition in the product, and in fact this is observed by the decrease in product intensity over time. Thus, only the first 10% of the reaction data, which is linear upon logarithmic treatment, was used to calculate the rate constant for **1e**. Though the error in rate measurement could be higher, it can be concluded to have a slower rate than seen for the other complexes. Decomposition was also observed with the trifluoromethane species, **1d** the next strongest electron-withdrawing group in the series, but to a smaller extent. A slight deviation in the trend is seen with the methyl derivative, **1b** where its rate is comparable with the unsubstituted species in this series, **1** or (sIMes)(SPh)Fe$(NO)_2$.

Table 19 Kinetic parameters for reactions of **1a-1e** with CO obtained from linear fits of natural log plots.

Complex	Substituent	k_{obs} x 10^3 (s^{-1})	k x 10^3 ($M^{-1}s^{-1}$)	$t_{½}$ (h)
1a[i]	OCH_3	0.103 ± 0.012	12.9 ± 1.5	1.9
1b[i]	CH_3	0.0555 ± 0.0030	6.95 ± 0.38	3.5
1[40]	H	0.0603	7.56	3.2
1c	Cl	0.0424	5.31	4.5
1d[ii]	CF_3	0.0172	2.16	11.2
1e[ii]	NO_2	0.00270	0.338	71.4

i) Average of 3 trials. ii) Rates based on first 10% of data due to decomposition of reaction mixture over time.

A plot of the rate constants and the Hammett parameter σ_p is linear with a negative slope and a ρ value of -0.831 with an R^2 of 0.901; such correlation is indicative of rate retardation by electron-withdrawing substituents (Figure 64). The nitro species has been omitted for reasons mentioned above, but its inclusion gives a ρ value of -1.293 and an R^2 of 0.869. The ρ value is an indicator of change in charge during the rate-determining step, and its negative value implies a diminution of negative charge at the reaction center. This agrees with the computational prediction where there is loss of negative charge at the $Fe(NO)_2$ unit as a result of its initial nucleophilic attack on an incoming CO molecule. Thus, the facilitation of this reaction by electron-releasing substituents is supportive of the proposed mechanism.

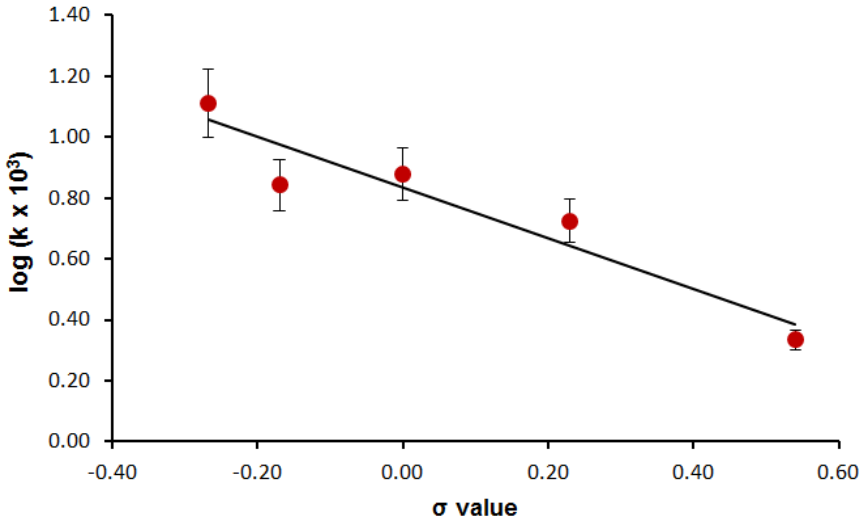

Figure 64 Hammett plot of rate constants from reactions of DNICs (**1a**-**1d**, **1**) with CO. Error bars are 10% of original value. Slope of trend line is -0.831 with an R^2 of 0.901.

Concluding Remarks

For visualizing relationships between structure and reactivity, Hammett correlations are a hallmark of physical organic and physical organometallic chemistry. Such correlations in a series of *para* substituted [(sIMes)(S-C_6H_4X)Fe$(NO)_2$] DNICs (compounds **1a**-**1e**) with variations in the donor characteristics of the aryl thiolate were used to provide a firmer experimental foundation for the unusual theoretical proposal that an oxidized {Fe$(NO)_2$} moiety, i.e. {Fe$(NO)_2$}^{9}, served as a nucleophile towards CO in a process that releases RSSR.[142] Significant electronic rearrangement leads to a reduced {Fe$(NO)_2$} product in the form of [Fe(CO)$(NO)_2$(NHC)].

Although variation of the substituent at the *para* position of the phenyl thiolate takes place remote from the metal center of the {Fe$(NO)_2$}^{9} core, infrared ν_{NO} values and a plot of voltammetric $E_{1/2}$ values with the Hammett parameter σ_p show good correlations,

verifying the presence of systematic changes in electron density as experienced by the $\{Fe(NO)_2\}^9$ core through changes in the S-donor. Having thus established the presence of electronic changes at the metal center between the members of the series of DNICs **1a-1e**, rates of their reaction with $CO_{(g)}$, resulting in the formation of the reduced $\{Fe(NO)_2\}^{10}$ DNIC, [(sIMes)(CO)Fe$(NO)_2$] were examined as monitored by *in situ* IR spectroscopy. A plot of the second-order rate constants and the Hammett parameter σ_p is linear and has a negative slope, indicative of rate retardation with increasing electron-withdrawing nature of the substituents. Together, these results find that subtle, systematic alterations of the electronic character of the $\{Fe(NO)_2\}$ unit moderate the conversion of the $\{Fe(NO)_2\}^9$ into the reduced analogue $\{Fe(NO)_2\}^{10}$ under mild conditions.

Experimental results show that this reaction is sensitive to the nucleophilicity at the metal center, thereby indicating the importance of the CO interaction in the transition state. This study therefore supports the previous computationally derived mechanistic hypothesis of the unique role of the delocalized frontier molecular orbitals of the $Fe(NO)_2$ unit, whereby the reaction is initiated by the overlap of such filled orbitals with the vacant π^* orbitals of the entering CO ligand.[142]

As "cross-talk" between small endogenous gaseotransmitters: CO, NO and H_2S gains rapid interest in the scientific community,[115] the interplay between these molecules and bio-organometallic entities such as DNICs is intriguing. Efforts to understand these processes in the complex biological environment continues to be a challenge, highlighting the importance of the mechanistic understanding obtained in biomimetic studies.

Experimental Section

Kinetic Measurements. *In situ* infrared monitoring was carried out using a Mettler Toledo iC10 ReactIR with an AgX fiber conduit probe having a SiComp ATR crystal. In a typical experiment, a 0.010 M solution of (sIMes)Fe$(NO)_2$(SPh) (**1**) was prepared in a 250 mL 3-neck round bottom flask fitted with the probe by dissolving the compound with 5 mL of CO-saturated toluene under an atmosphere of CO. Once completely dissolved (within 30 s of stirring), the FTIR monitoring was started and the reaction followed until completion. The reactions were conducted over a temperature range from 323 to 348 K; the solubility data of CO was obtained from extrapolation of data in literature.[146,147] The high pressure CO reactions were monitored using an ASI ReactIR 1000 reaction analyses system with a stainless steel Parr autoclave modified with a permanently mounted ATR crystal (SiComp) at the bottom of the reactor.

Synthesis of (sIMes)Fe$(NO)_2$(SPh) (1). Under an argon atmosphere, a 0.27 g (0.80 mmol) sample of 1,3-bis(2,4,6-trimethylphenyl)imidazolidinium chloride and 0.12 g (1.2 mmol) of NaOtBu were dissolved in 20 mL of THF and stirred for 30 min prior to transfer to a Schlenk flask containing 1.0 mmol of the Roussin's Red ester (μ-SPh)$_2$[Fe$(NO)_2]_2$ in 10 mL of THF. Stirring for 30 min resulted in a deep purple solution, which was then dried in vacuo. The resulting dark purple residue (> 90% yield) was dissolved in 10 mL of ether and filtered through celite. The filtrate was dried and redissolved in THF. IR (THF, cm^{-1}) ν_{NO} 1763(s), 1715(vs). Elemental Anal. calculated for $FeC_{27}H_{31}N_4O_2S$ (found) : C, 61.02 (61.08); H, 5.88 (5.98); N, 10.54 (10.33). All other complexes were prepared similarly.[143]

Synthesis of (sIMes)Fe(NO)$_2$(CO) (2). Carbon monoxide was bubbled into a 20 mL THF solution of complex **1** (c.a 0.5 mmol) in a 100 mL Schlenk flask for 10 min. The flask was sealed under 1 atm $CO_{(g)}$ and the solution was stirred overnight at room temperature. The formation of complex **2** was monitored by IR spectroscopy were on a Bruker Tensor 27 FTIR spectrometer in CaF_2 solution cells of 0.1 mm pathlength. A brown colored product was obtained in high yield (> 90%). X-ray quality crystals were obtained from concentrated Et_2O solution at 0 °C. IR (THF, cm^{-1}) ν_{CO} 1986(vs), ν_{NO} 1747(s), 1705(s). Elemental Anal. calculated for $FeC_{22}H_{26}N_4O_3$ (found) : C, 58.68 (59.18); H, 5.82 (5.96); N, 12.44 (12.17). ^{1}H NMR ($CDCl_3$): δ 6.96 (s, aromatic H on Mes), 4.01 (s, NCH_2), 2.29 (s, *o,m,p*-CH_3 on Mes). The diphenyl disulfide formed as the by-product of the above reaction was characterized by ^{1}H NMR spectroscopy. ^{1}H NMR (CD_2Cl_2): PhSSPh δ 7.53(d, SCCH), 7.27 (m); $FeC_{22}H_{26}N_4O_3$ δ 6.98 (s, aromatic H on Mes), 4.02 (s, NCH_2), 2.29 (s, *o,m,p*-CH_3 on mes)

CHAPTER V

CARBON MONOXIDE RELEASING MOLECULES (CORMS)*

While transition metal carbonyl complexes are often used as stoichiometric or catalytic reagents for a variety of chemical transformations,[148] there is increasing interest in their utility as reagents in systems of biological relevance.[149] For example, new radiopharmaceuticals based on the $Re(CO)_3$ and $Tc(CO)_3$ fragments have been synthesized which bind to estrogen receptors.[150] The strong IR absorption of the CO ligands also provides a useful spectroscopic tag which has led to the development of carbonylmetalloimmunoassay procedures.[151] Some metal carbonyl complexes also show promise as anti-cancer drugs.[152] CO gas is known to dilate blood vessels in a manner similar to nitric oxide and has been shown to possess anti-inflammatory and anti-apoptotic properties.[26] Metal carbonyl complexes can be used as CO carriers, thus circumventing the inherent toxicity associated with CO inhalation.[25] Several other beneficial physiological effects of CO have been well documented.[149a,153,26] As a result there have been some early investigations into the use of metal carbonyl complexes as sources of solid CO and therefore as CO releasing molecules (CORMs).[152b,25] For example, among other complexes, $[Ru(CO)_3Cl_2]_2$ and $Ru(CO)_3Cl$(glycinate) have been shown to readily

* Reprinted (adapted) with permission from: Muhammad, S.; Yempally, V.; Anas, M.; Moncho, S.; Kyran, S. J.; Brothers, E. N.; Darensbourg, D. J.; Bengali, A. A. *Inorg. Chem.* **2012**, *51*, 13041. Yempally, V.; Kyran, S. J.; Raju, R. K.; Fan, W. Y.; Brothers, E. N.; Darensbourg, D. J.; Bengali, A. A. *Inorg. Chem.* **2014**, *53*, 4081. Kyran, S. J.; Sanchez, S. G.; Arp, C. J.; Darensbourg, D. J. *Organometallics*, **2015**, *34*, 3598. Copyright 2012, 2014 & 2015, respectively, American Chemical Society.

transfer CO to mygolobin (Mb) to form Mb-CO under physiological conditions.[154] Other CORMs demonstrate therapeutic value in reducing sepsis-induced lethality by inhibiting bacterial growth and respiration.[155]

In the following two sections, rhenium and manganese based CORMs are presented. The investigations were largely carried out by Dr. Bengali's research group at Texas A&M University at Qatar. My contribution in the collaboration primarily involved the synthesis of compounds in analytically pure form for combustion analysis and the structural characterization of the complexes *via* X-ray diffraction studies. The key results from each of these work is highlighted in this chapter.[156,157] Finally, the last section introduces bis(cycloamines) prepared in our labs and its chelation to molybdenum carbonyls.[158] Work done in the Bengali lab show that the ligands employed play a vital role in effectiveness of CORMs (*vide infra*). What makes the bis(cycloamines) as favorable ligands in this area will be addressed.

An Unusually Labile Rhenium Carbonyl Complex

Recently, Bideau and coworkers reported the synthesis of a series of bidentate pyrrole based rhenium tetracarbonyl complexes that have potential utility as radiopharmaceutical reagents due to the incorporation of ^{186}Re or ^{188}Re as a radionuclide Figure 65.[159] Our interest in these complexes was motivated by the reported unusual lability of the *cis* CO ligands in the presence of donor molecules such at PPh_3. Surprisingly, CO substitution by the weakly coordinating THF solvent also occurred readily, even at room temperature. As noted by the authors, the ease of CO loss in these

complexes may lead to their application as CORMs. Given this promising application, it becomes important to investigate both the mechanism of the CO loss pathway.

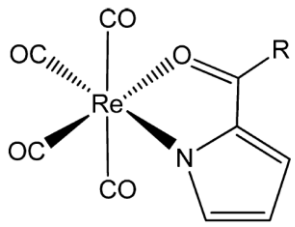

1 (R = H, CH_3, CCl_3, OMe)

Figure 65 Pyrrole- aldehyde/acetyl bound rhenium carbonyls prepared by Bideau and coworkers.[9]

An important characteristic of **1** that might assist in facile CO replacement is the presence of the presumed weak Re-O interaction. This bond could potentially be disrupted by an incoming ligand thereby opening up a coordination site on the Re metal center and provide a low energy pathway for CO loss. This process would be somewhat analogous to an associative "ring slip" mechanism[160] in the substitution of CO from molecules such as $(\eta^5\text{-}C_{10}H_9)Mn(CO)_3$ whereby an open coordination site is generated upon an $\eta^5 \rightarrow \eta^3$ hapticity shift of the hydronaphthalene ring system facilitating incoming ligand binding prior to CO loss.[161] In this study, an experimental and theoretical investigation aimed at understanding the mechanism of CO displacement (Scheme 20) from **1a** and **1b** by PPh_3 and pyridine to form **2a,b** and **3a,b,** respectively. The results provide details about the energetics of this process and lead to the identification of an important intermediate along the reaction pathway.

Scheme 20

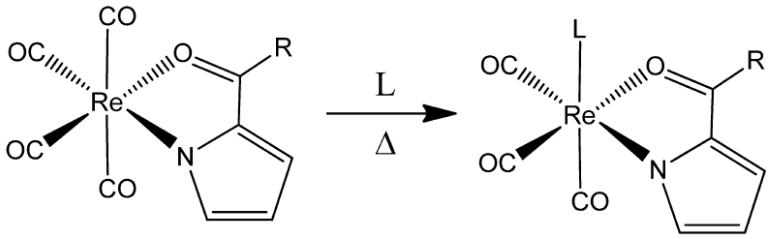

1a (R = H)
1b (R = CF_3)

2a (R = H, L = PPh_3)
2b (R = CF_3, L = PPh_3)
3a (R = H, L = pyridine)
3b (R = CF_3, L = pyridine)

Results and Discussion. Thermal reaction of **1a** with PPh_3 results in the spectral changes shown in Figure 66. The CO stretching bands of **1a** at 2112, 2010, 1993, 1949 cm^{-1} and the aldehyde absorbance at 1571 cm^{-1} exhibit a first-order exponential decrease in intensity and product peaks due to **2a** at 2032, 1939, 1912, and 1580 cm^{-1} increase at the same rate. Observation of three CO stretching absorptions in the product complex is consistent with the previously determined crystal structure of {2-$(CHO)C_4H_3N$}$Re(CO)_3PPh_3$.[159] While the CO ligands have local C_{3v} symmetry, reduction in symmetry due to the pyrrolyl ligand results in the splitting of the E band yielding absorptions at 1939 cm^{-1} and 1912 cm^{-1}. The facial geometry of **2a** indicates loss of a CO ligand that is *cis* to both coordinating atoms of the bidentate pyrrolyl ligand and, as discussed previously,[159] is consistent with the mutual *trans* influence of the CO ligands. As shown in Figure 67, within the first few minutes of the reaction additional peaks are observed to first increase rapidly and then decrease in intensity during the course of the

reaction at 303 K. The complex associated with these absorptions (**IM**) exhibits the temporal profile shown in Figure 68. The reactant species **1a** also has a biexponential time profile with a fast and slow component that matches within a factor of two, the fast growth and slower decay of **IM**. These observations suggest the presence of an intermediate species along the **1a** → **2a** reaction pathway. DFT calculations also confirm the viability of an intermediate complex along the CO displacement channel.

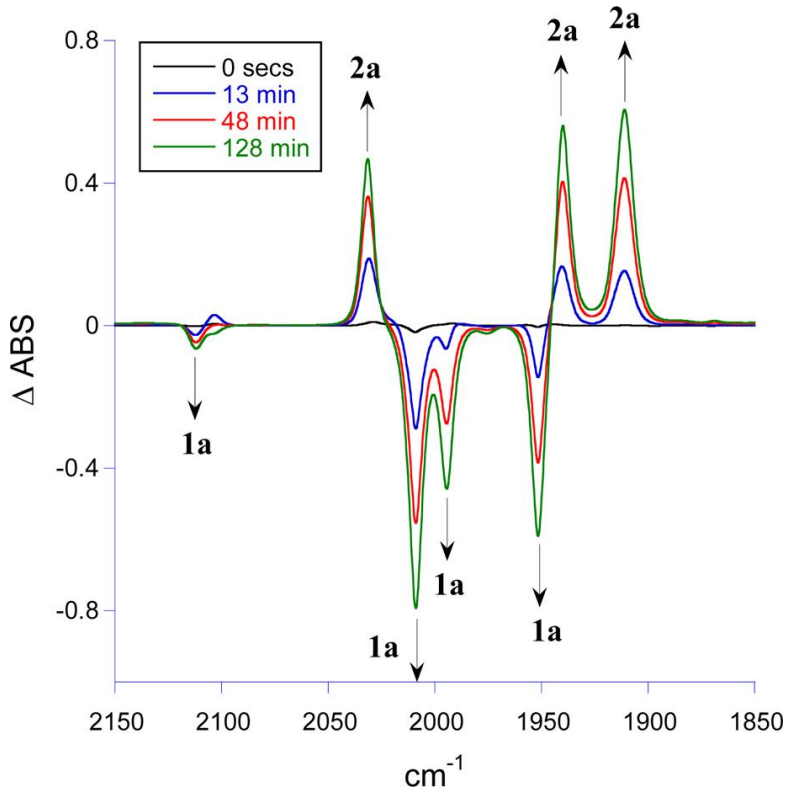

Figure 66 Difference FTIR spectra observed as a function of time upon reaction of a 3 mM solution of **1a** with 0.17 M PPh_3 in heptane at 303 K. The positive peaks are due to the growth of the product complex, **2a**, while the negative peaks are due to the disappearance of the reactant, **1a**.

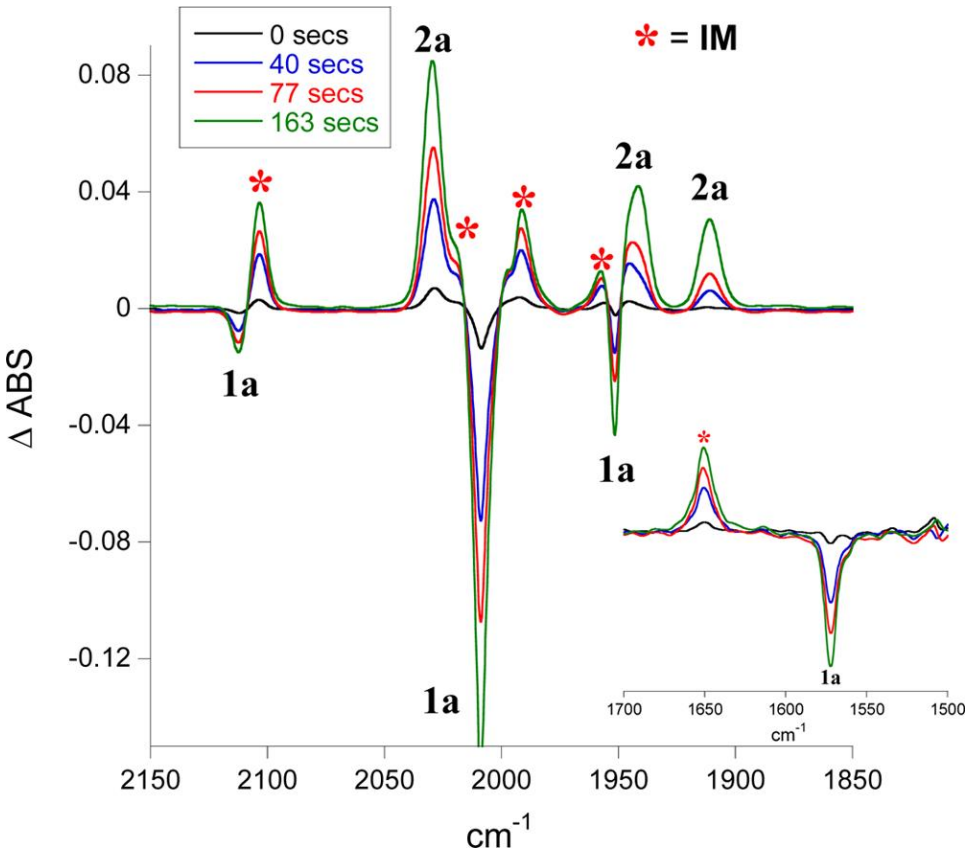

Figure 67 Difference FTIR spectra obtained at the start of the reaction between a 3 mM solution of **1a** and 0.17 M PPh_3 at 303 K in heptane. The peaks marked with **IM** are due to the formation of an intermediate species that grows in rapidly and then decays over the course of the reaction at the same rate as the growth of the product complex **2**a. The inset shows spectral changes in the 1700−1500 cm^{-1} region due to the C═O stretching of the aldehyde.

Four CO stretching bands are observed for **IM** at 2103, 2019, 1990, 1957 cm^{-1} confirming that generation of this intermediate does not require the displacement of a CO ligand from **1a**. Furthermore, the peak at 1651 cm^{-1} associated with this complex is in good agreement with the C=O stretch of the uncoordinated acetylpyrrolyl ligand observed at 1650 cm^{-1}. Put together, this data suggests that the incoming PPh_3 ligand initially

displaces the weakly coordinated aldehyde group of the pyrrolyl ligand to generate an intermediate with the structure shown in Figure 69.

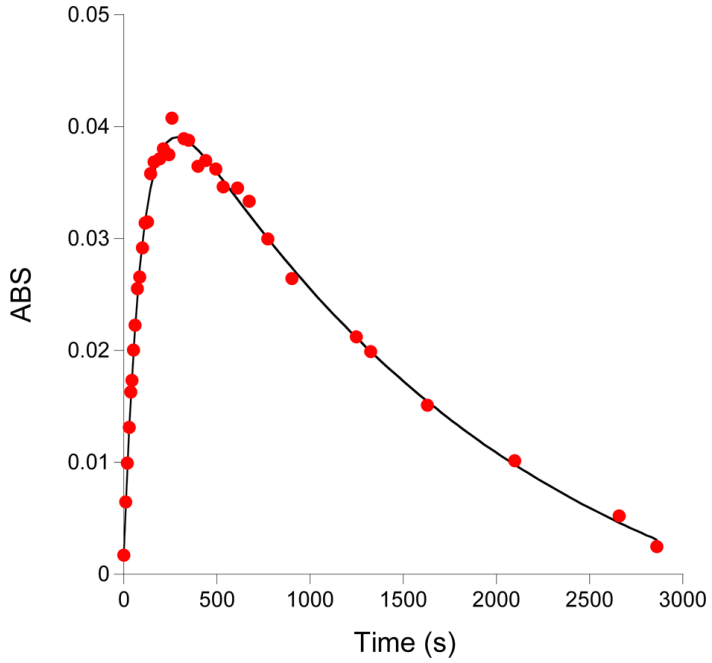

Figure 68 The temporal profile of the intermediate complex, **IM**, monitored at 2103 cm^{-1} obtained upon reaction of a heptane solution of **1**a with 0.17 M PPh_3 at 303 K. The time dependence of this species demonstrates a fast rise followed by a slower decay. The solid black line represents a biexponential fit to the data.

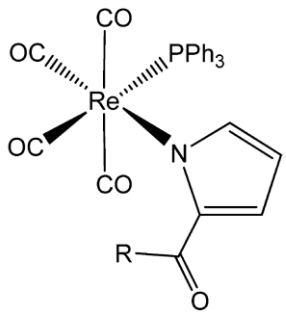

Figure 69 Proposed structure of intermediate.

This intermediate complex then proceeds to form the final product **2a** by loss of a CO molecule that must be *cis* to both the phosphine and N-coordinated pyrrolyl ligands, followed by recoordination of the aldehyde oxygen to the Re center. The overall reaction then appears to follow a **1a → IM → 2a** pathway. To determine whether **IM** is formed reversibly from **1a**, a heptane solution of **1a** and 0.4 M PPh_3 was allowed to react at room temperature for a few minutes and the solution quenched at 263 K. Evaporation of the solvent yielded an amorphous yellow powder together with large white PPh_3 crystals. After hand separation of the PPh_3 crystals, the yellow powder was redissolved in heptane and spectra were acquired at 298 K over a 20 minute time period. As shown in Figure 70, the initial spectrum clearly shows the presence of all three complexes, **1a**, **IM**, and **2a**. Interestingly, **IM** converts completely to the reactant **1a** under these conditions and there is no change in the concentration of **2a**. The data are therefore consistent with the reversible formation of **IM** from **1a** with the equilibrium condition favoring the reactant complex. Furthermore, since conversion of **IM** to **2a** is not observed under these conditions, the overall CO displacement mechanism is consistent with a pre-equilibrium process with the **IM →1a** reaction barrier lower than that for **IM → 2a**. The overall data therefore suggest the reaction mechanism shown in Scheme 21.

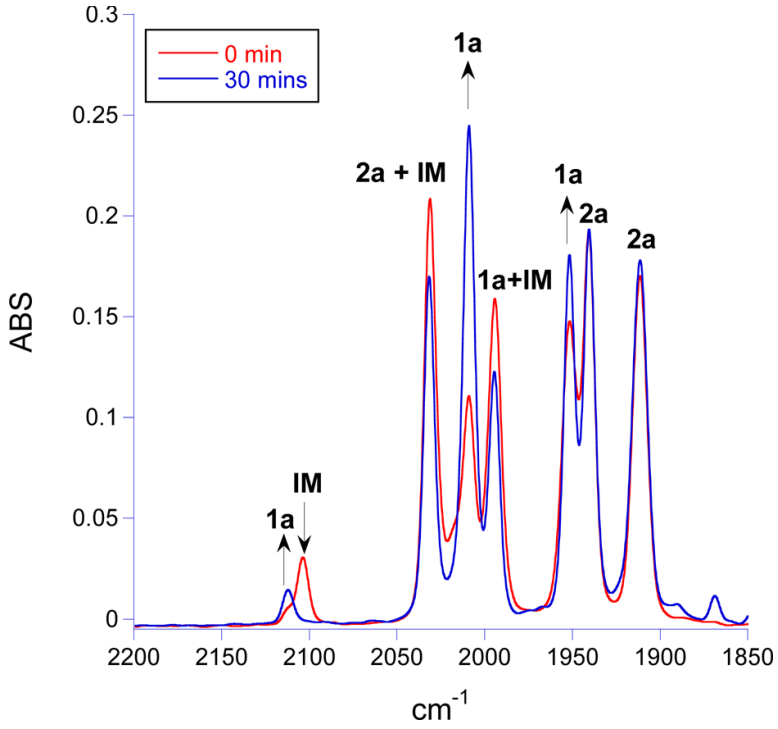

Figure 70 Spectral changes observed when a heptane solution initially containing **1a**, **IM**, and **2a** is left standing at 298 K. The spectra are consistent with complete conversion of **IM** to the reactant **1a** while the concentration of **2a** is left unchanged. Due to the overlap between the CO bands of the various species, the conversion is best observed at 2103 cm^{-1} (**IM**) and 2112 cm^{-1} (**1a**). The intensities of the product bands at 1939 cm^{-1} and 1912 cm^{-1} due to **2a** are unchanged.

Scheme 21

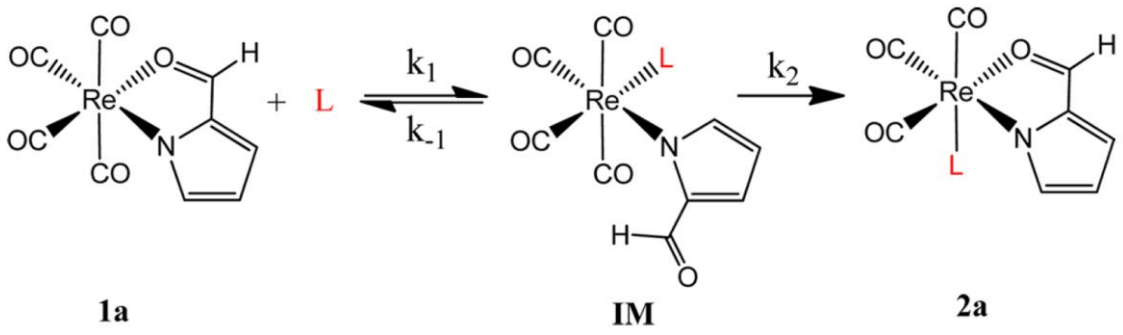

The reaction of **1b** with L = PPh_3 was also studied to ascertain the effect of the electron withdrawing CF_3 group upon the reaction rate and stability of the intermediate. As shown in Figure 71, the rate of CO displacement from **1b** is almost six times faster than from **1a**. The available data does not allow for the origin of this rate enhancement to be determined with certainty. It is possible that the faster rate is due to a shift in the equilibrium towards **IM** as a result of weaker Re-O binding in **1b** or because of differences in the stability of the transition state connecting **IM** to the product complex. During the course of these studies, **2b** was isolated and a crystal structure obtained (Figure 72). The structure of this species is very similar to that of the previously characterized **2a** complex.[159] Of interest however, is the observation that the Re-O bond length in **2b** is 2.185 Å, 0.011 Å longer than in the acetylpyrrolyl complex. This finding is indicative of a weaker Re-O interaction in **2b** as expected.

Solubility limitations with PPh_3 precluded a complete kinetic analysis but was carried out with pyridine as the incoming ligand. The crystal structure of the pyridine complex **3a** formed as the product is shown in Figure 73. An experimental activation enthalpy of 15.4 kcal/mol was determined and is also supported by a theoretical estimate of 13.4 kcal/mol. Computations also assert the identity of the intermediate complex as it is found to be the local minimum on the potential energy surface. A calculated Re-CO bond dissociation energy (BDE) of 30.2 kcal/mol is considerably higher than the activation enthalpy measured in this reaction and supports the occurrence of a lower-energy associative pathway.

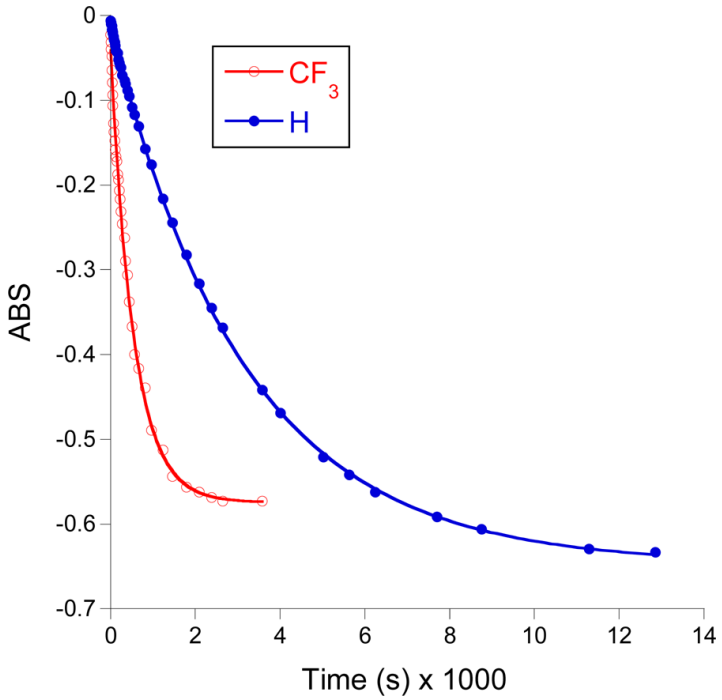

Figure 71 A plot of Abs vs. time for the reaction of **1a** and **1b** with PPh_3 monitored at 2009 cm^{-1} and 2000 cm^{-1}, respectively. A heptane solution of **1a** or **1b** was reacted with 0.17M PPh_3 at 303 K.

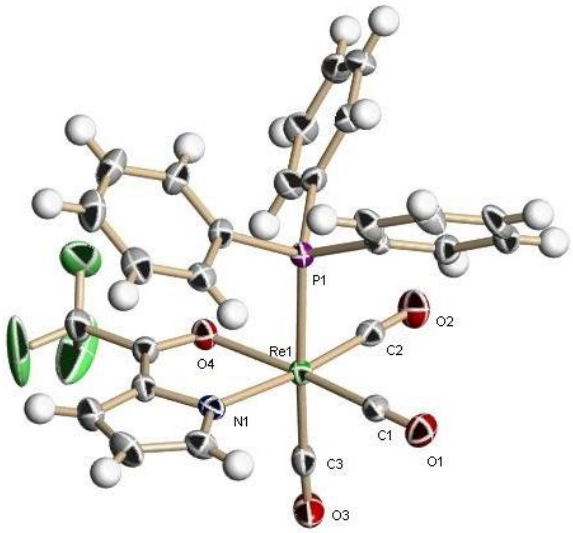

Figure 72 Crystal Structure of {2-$(CF_3CO)C_4H_3N$}$Re(CO)_3(PPh_3)$, **2b**.

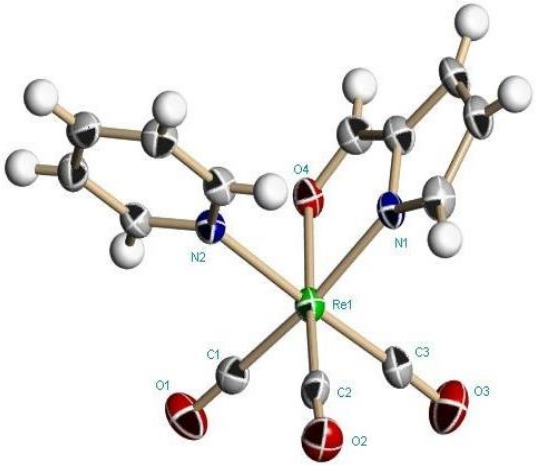

Figure 73 Crystal Structure of {2-(CHO)C_4H_3N}Re$(CO)_3$(pyridine), **3a**.

Conclusions. The thermal displacement of a CO molecule from a Re tetracarbonyl complex bearing a hemi-labile pyrrolyl ligand by PPh_3 and pyridine has been investigated. As reported previously, the CO ligand is found to be unusually labile in this species with the reaction complete within a few hours at room temperature. At the start of the reaction, an intermediate complex is observed which is generated rapidly and then converts to the product tricarbonyl species. This intermediate is identified as the (η^1-N-pyrrolecarboxyaldehyde)Re$(CO)_4$L (L = PPh_3 or pyridine) complex which forms upon the displacement of the aldehyde Re-O bond by the incoming ligand. This species then converts to the final complex by loss of a CO ligand. Theoretical modeling of the reaction using DFT confirms the presence of the intermediate complex along the reaction pathway and the calculated energetic parameters agree well with the experimental values. While the Re-CO bond dissociation energy is calculated to be 30 kcal/mol, the reaction proceeds with a 15.4 kcal/mol enthalpic barrier. It is postulated that the unusual lability of this

complex is due to the presence of the weak aldehyde Re-O link that can easily dissociate to open a coordination site on the metal center and accommodate an incoming ligand prior to CO loss. This associative pathway provides a lower energy reaction channel for the release of CO.

Experimental on Synthesis and Characterizations. The tetracarbonyl rhenium complex with the 2-formylpyrrolyl ligand, {2-(CHO)-C_4H_3N}$Re(CO)_4$ (**1a**) was prepared as per the literature.[159] Solvents were either anhydrous grade (Aldrich) or purified by an MBraun Manual Solvent Purification System packed with Alcoa F200 activated alumina desiccant. NMR spectra were recorded on a Varian INOVA 500 (operating at 499.42, 202.17 and 125.59 MHz for ^1H, ^{31}P and ^{13}C, respectively) or a Bruker Advance II 400 spectrometer. ^1H and ^{13}C NMR spectra were referenced to residual solvent resonances, while ^{31}P NMR spectra were referenced to an external H_3PO_4 in D_2O at 0.0 ppm. Infrared spectra were obtained on a Bruker Tensor 27 or Vertex 80 FTIR spectrometer. X-ray crystallography was done on a Bruker-AXS APEXII CCD diffractometer in a nitrogen cold stream maintained at 110 K. Elemental Analysis for **1b, 2b** and **3a** were determined by Atlantic Microlab (Norcross, GA).

Synthesis of {2-(CF_3CO)-C_4H_3N}$Re(CO)_4$ (**1b**)

$Re(CO)_5Br$ (0.770 g, 1.90 mmol), 2-(trifluoroacetyl)pyrrole (0.312 g, 1.91 mmol) and sodium *tert*-butoxide (0.206 g, 2.14 mmol) in toluene (25 mL) were heated to reflux for 2 h under an argon atmosphere. The resulting vermillion solution was filtered to remove NaBr and the solvent concentrated to give viscous oil. This was purified by a flash

chromatography on silica (pentane/ether, 6/4) to obtain a dark orange oil (small presence of $Re_2(CO)_{10}$ can be removed by a second flash chromatography with pentane/CH_2Cl_2, 9/1) which crystallizes as a dark red solid after complete removal of residual solvent on a rotovap (0.260 g, 30%). IR data in heptane (ν_{CO}): 1583 (m), 1958 (s), 2001 (s), 2014 (s), 2115 (m). NMR data in $CDCl_3$: ^1H δ 6.61 (dd, J = 4.6, 1.3 Hz, 1 H), 7.46 (m, 1 H), 7.70 (m, 1 H); $^{13}C\{^1H\}$ δ 117.9 (q, $^1J_{CF}$ = 280 Hz, 1 C, *C*F_3), 121.5, 128.0 (q, $^4J_{CF}$ = 3 Hz, 1 C), 139.6, 151.9, 172.7 (q, $^2J_{CF}$ = 38 Hz, 1 C, *C*=O), 183.6 (s, 2 C, *C*O), 188.3 (s, 1 C, *C*O), 188.5 (s, 1 C, *C*O). Anal. Calcd for $C_{10}H_3F_3N_1O_5Re_1$: C, 26.1; H, 0.7; N, 3.0. Found: C, 26.2; H, 0.5; N, 3.0%.

Synthesis of {2-(CF_3CO)-C_4H_3N}$Re(CO)_3(PPh_3)$ (**2b**)

A solution of **1b** (0.101 g, 0.219 mmol) in 20 mL hexane was treated with PPh_3 (0.060 g, 0.230 mmol) and refluxed for 1 h under an atmosphere of argon. Upon cooling to room temperature, formation of yellow precipitate was observed. The solution was reduced to a third of the volume and further cooled in a freezer overnight and filtered to give yellow-orange product, (0.103 g, 68%). IR data in CH_2Cl_2 (ν_{CO}): 1582 (m), 1905 (s), 1936 (s), 2032 (s). NMR data in $CDCl_3$: ^1H δ 6.34 (d, J = 4.4, 1 H), 7.01 (m, 1 H), 7.20 (m, 6 H, H_o), 7.30 (m, 1 H), 7.33 (t, J = 8.3 Hz, 6 H, H_m), 7.41 (t, J = 7.3 Hz, 3 H, H_p); ^{31}P δ 20.16; $^{13}C\{^1H\}$ δ 117.9 (q, $^1J_{CF}$ = 280 Hz, 1 C, *C*F_3), 120.6, 126.1, 128.6 (d, J_{CP} = 10 Hz, 6 C, *C*$_6H_5$), 129.3 (d, J_{CP} = 44 Hz, 3 C, *C*$_6H_5$), 130.5 (d, J_{CP} = 2 Hz, 3 C, *C*$_6H_5$), 133.5 (d, J_{CP} = 11 Hz, 6 C, *C*$_6H_5$), 139.0, 150.0, 170.5 (q, $^2J_{CF}$ = 37 Hz, 1 C, *C*=O), 187.6 (d, J_{CP} = 69 Hz, 1 C, *C*O), 195.7 (d, J_{CP} = 67 Hz, 1 C, *C*O), 195.8 (d, J_{CP} = 67 Hz, 1 C, *C*O). Anal. Calcd for $C_{27}H_{18}F_3N_1O_4P_1Re_1$: C, 46.7; H, 2.6; N, 2.0. Found: C, 46.6; H, 2.5; N, 2.0%.

Synthesis of [2-(CHO)-C_4H_3N]$Re(CO)_3$(pyridine) (**3a**)

A solution of **1a** (0.390 g, 0.99 mmol) in 50 mL hexane was treated with pyridine (0.1 mL, 1.24 mmol) and refluxed for 2 h under an atmosphere of argon. Upon cooling to room temperature, formation of yellow precipitate was observed. The solution was further cooled in a freezer overnight and filtered to give yellow product (0.410 g, 93%). IR data in CH_2Cl_2 (ν_{CO}): 1570 (m), 1906 (s), 1927 (s), 2030 (s). NMR data in $CDCl_3$: ^1H δ 6.42 (dd, J = 4.1, 1.4 Hz, 1 H), 7.08 (dd, J = 4.1, 0.9 Hz, 1 H), 7.28 (m, 2 H, pyridine), 7.64 (d, J = 1.4 Hz, 1 H), 7.77 (tt, J = 7.7, 1.7 Hz, 1 H, pyridine), 8.38 (m, 2 H, pyridine), 8.73 (d, J = 1.4 Hz, 1 H, C*H*O); $^{13}C\{^1H\}$ δ 118.1, 124.4, 125.4 (s, 2 C, pyridine), 138.3 (s, 1 C, pyridine), 144.3, 145.0, 152.0 (s, 2 C, pyridine), 181.2 (s, 1 C, *C*HO), 193.1 (s, 1 C, *C*O), 197.3 (s, 1 C, *C*O), 197.6 (s, 1 C, *C*O). Anal. Calcd for $C_{13}H_9N_2O_4Re$: C, 35.2; H, 2.1; N, 6.3. Found: C, 35.2; H, 2.0; N, 6.4%.

Reactivity of a Bulky Diazabutadiene Manganese Carbonyl Complex

The use of a sterically encumbering ligand to facilitate the release of a ligated CO molecule under mild conditions from a metal carbonyl complex is explored in this work. The findings herein suggest a role for steric manipulation of ligand characteristics in the design of CORMs.[157]

Scheme 22

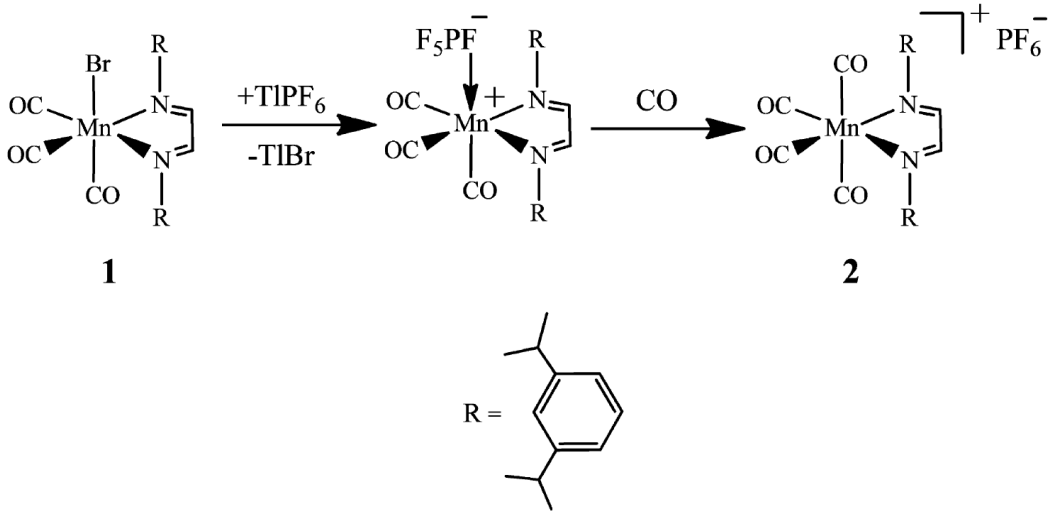

[Mn(CO)$_4$(^{i}Pr$_2$Ph-DAB)][PF$_6$]. A cationic manganese tetracarbonyl complex bearing *N,N'*-bis(2,6-diisopropylphenyl)-1,4-diazabutadiene (^{i}Pr$_2$Ph-DAB) is synthesized by the addition of $TlPF_6$ in presence of CO to a dichloromethane solution of the bromo tricarbonyl analogue shown in Scheme 22. The precursor, **1** is prepared *via* the reaction of the ligand and $Mn(CO)_5Br$. The crystal structure of the tetracarbonyl complex, **2** is shown in Figure 74. As expected of a cationic complex with four strong π accepting ligands, the CO stretching bands of **2** are shifted to significantly higher wavenumbers relative to **1**

(Table 20). The steric influence of the $^{i}P_2Ph$-DAB ligand upon the geometry of **2** is evident in the axial ∠CO−Mn−CO, which at 170.75° is significantly less than that found in analogous complexes where this angle ranges from 174.14° to 178.9°.[162]

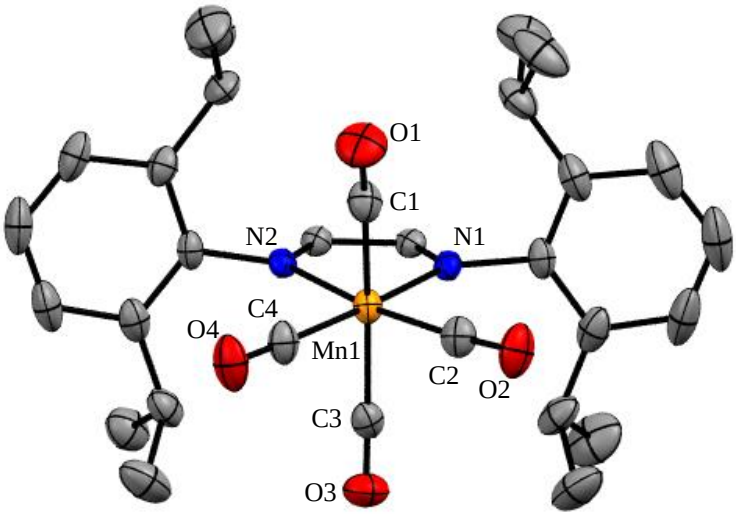

Figure 74 Thermal ellipsoid (probability level at 50%) plot of **2** with select atom labeling. Hydrogen atoms and counteranion omitted for clarity.

Table 20 CO stretching frequencies for manganese complexes in dichloromethane.

Complex	ν_{CO} (cm^{-1})
$Mn(Br)(CO)_3(^{i}Pr_2Ph\text{-}DAB)$ **(1)**	2035, 1971, 1930
$Mn(Br)(CO)_3(bpy)$	2022, 1934, 1912
$[Mn(CO)_4(^{i}Pr_2Ph\text{-}DAB)][PF_6]$ **(2)**	2109, 2042, 2027, 2006
$[Mn(CH_3CN)(CO)_3(^{i}Pr_2Ph\text{-}DAB)][PF_6]$ **(3a)**	2054, 1979, 1963
$[Mn(THF)(CO)_3(^{i}Pr_2Ph\text{-}DAB)][PF_6]$	2055, 1979, 1965
$[Mn(DHF)(CO)_3(^{i}Pr_2Ph\text{-}DAB)][PF_6]$	2053, 1979, 1964
$[Mn(CN^{t}Bu)(CO)_3(^{i}Pr_2Ph\text{-}DAB)][PF_6]$ **(3b)**	2187 (CN), 2051, 1983[a]

[a]broad peak

Thermal Reactivity. The expected weakening of the Mn−CO bonds due to the crowded metal center in **2** is strikingly apparent in the thermal reactivity of this complex. For example, dissolution of the yellow-orange solid in acetonitrile at 288 K results in an instantaneous color change to red. The IR spectrum of this red solution shows three peaks with relative intensities suggestive of a facial tricarbonyl complex. This species was isolated and the crystal structure shown in Figure 75 confirms its identity as the acetonitrile complex $[Mn(CH_3CN)(CO)_3(^iPr_2Ph\text{-}DAB)][PF_6]$ (**3a**).

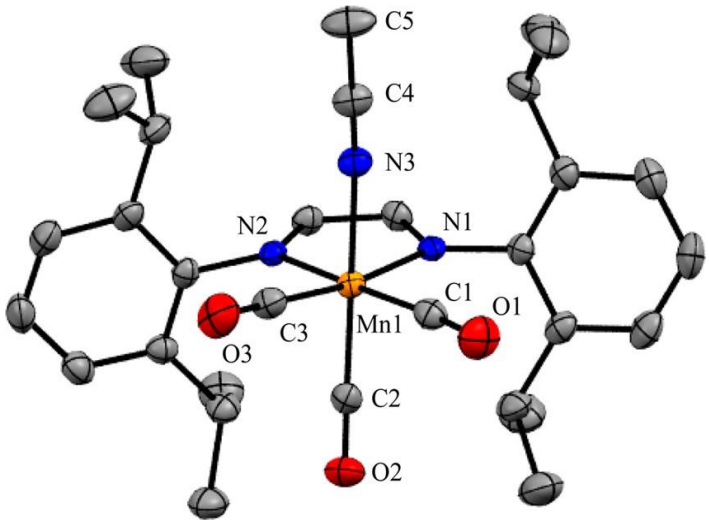

Figure 75 Thermal ellipsoid (probability level at 50%) plot of **3a** with select atom labeling. Hydrogen atoms and counteranion omitted for clarity.

To monitor the formation of the acetonitrile adduct, a dichloromethane solution of **2** was reacted with 0.5 M CH_3CN at 288 K. The IR spectral changes shown in Figure 76 confirm a clean conversion of **2** into **3a** under these conditions. Unfortunately, the mechanism of this substitution reaction and the possibility of estimating the Mn−CO bond

enthalpy could not be investigated, because at higher temperatures and concentrations of CH_3CN, additional unassigned peaks were observed and the rate of decay of **2** did not match the growth of the product. An associative mechanism for CO substitution appears unlikely given the steric bulk of the $^{i}Pr_2$Ph-DAB ligand.

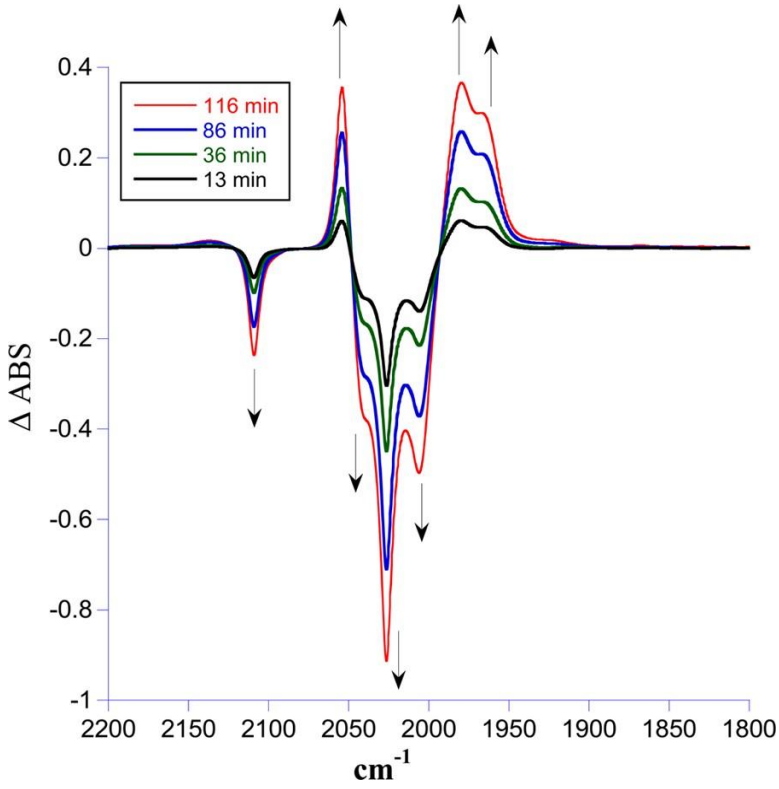

Figure 76 Spectral changes observed upon reaction of a dichloromethane solution of **2** with 0.5 M CH_3CN at 288 K to yield **3a**.

Spectral changes in the infrared observed upon dissolution of **2** in other coordinating solvents such as THF and 2,3dihydrofuran (DHF) suggest the displacement of an axial CO ligand at room temperature to form the [Mn(THF)$(CO)_3$($^{i}Pr_2$Ph-DAB)][PF_6] and [Mn(DHF)$(CO)_3$($^{i}Pr_2$PhDAB)][PF_6] complexes, respectively. The rate of

CO substitution is slower in these solvents compared to CH_3CN. More basic ligands such as pyridine and other amines reacted with **2** to afford a monocarbonyl complex (single peak in the IR spectrum) which was unstable and could not be isolated.

Despite the different donor characteristics of the solvent ligands, the substituted tricarbonyl complexes have similar CO stretching wavenumbers (Table 20). This observation suggests that the electronic environment of the Mn center is not influenced by the ligand donor/acceptor abilities. To ascertain the extent of this insensitivity, the isonitrile ligand CN^tBu, with electronic characteristics significantly different than those of THF and CH_3CN, was used to synthesize the $[Mn(CN^tBu)(CO)_3(^iPr_2Ph\text{-}DAB)][PF_6]$ (**3b**) complex. The crystal structure of **3b** is shown in Figure 77.

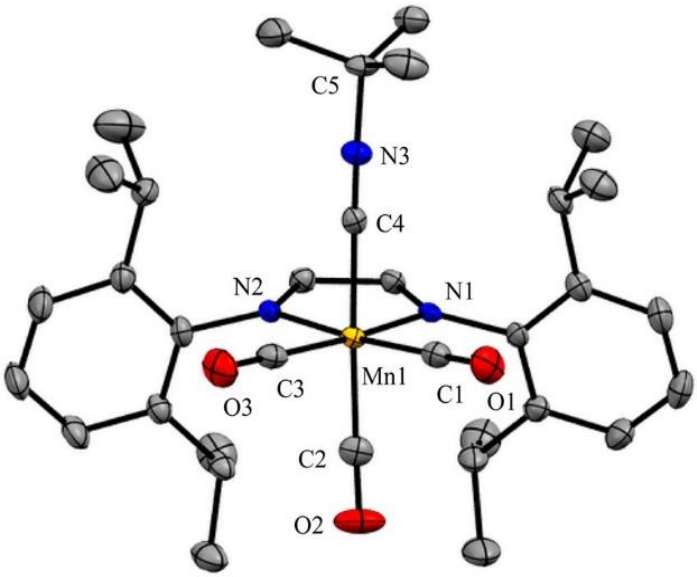

Figure 77 Thermal ellipsoid (probability level 50%) plot of **3b** with select atom labeling. Hydrogen atoms and counteranion omitted for clarity.

Similar to the structures observed for **2** and **3a**, the axial ∠CO−Mn−CNt−Bu = 172.38° showing a large deviation from linearity. Surprisingly, the CO stretching wavenumbers in this species are comparable to those of the other solvated complexes (Table 20). Since DAB ligands are considered to be electron reservoirs,[163] it is possible that they impart a "leveling" effect upon the metal electron density resulting in similar CO stretching wavenumbers for several of the observed complexes. The extreme lability of the CO ligand in **2** is in dramatic contrast to similar complexes such as $[Mn(CO)_4(phen)]^+$ and $[Mn(CO)_4(dppe)]^+$ which demonstrate CO substitution only at high temperatures.[164] For example, $[Mn(CO)_4(dppe)]^+$ is stable for several months in acetonitrile at room temperature.

As shown in Table 21, the Mn−CO bond in **2** is remarkably weak (BDE = 25.3 kcal/mol) especially compared to that in $[Mn(CO)_4(Ph\text{-}DAB)]^+$ (35.4 kcal/mol) and $[Mn(CO)_4(bpy)]^+$ (31.4 kcal/mol). Given the similar Mn−CO BDEs in these latter two complexes, the weaker interaction in **2** is clearly a result of steric rather than electronic differences between the diimine ligands. In a related Mn complex, $(\eta^3allyl)Mn(CO)_4$, increasing the steric bulk of the allyl ligand also resulted in an increase in the rate of CO loss.[165] Since facile loss of coordinated CO ligands is an important characteristic of CORMs, these findings suggest that incorporation of the bulky $^iPr_2$Ph-DAB ligand into metal carbonyl complexes may be useful in the synthesis of viable targets.

Table 21 Calculated Mn−L BDEs for manganese complexes demonstrating the steric influence of the diimine ligand upon the strength of this interaction.

L	$[Mn(L)(CO)_3(^iPr_2Ph\text{-}DAB)]^+$ (kcal/mol)	$[Mn(L)(CO)_3(Ph\text{-}DAB)]^+$ (kcal/mol)
CO	25.3	35.4
CH_3CN	30.1	40.3
THF	26.1	41.6
CNtBu	43.5	52.8

In agreement with experimental findings, the DFT calculations predict that displacement of CO in **2** by CH_3CN and THF is thermodynamically favored with $\Delta G°_{rxn}$ (298 K) = −5.7 kcal/mol and −1.5 kcal/mol, respectively. In all cases, Mn−L BDEs are calculated to be significantly lower in complexes with the larger ($^iPr_2$Ph-DAB) ligand compared to those of the electronically similar yet smaller (Ph-DAB) ligand. Of all the ionic complexes studied, calculations indicate that the strongest interaction is between the Mn center and the isonitrile ligand. This observation is consistent with the greater σ donating ability of isonitrile compared to the other ligands used and, as expected for a cationic complex, suggests a reduced role for π backbonding in stabilizing the Mn-L interaction.

Conclusions. In contrast to other cationic manganese tetracarbonyl complexes which are stable toward thermal displacement of CO, the cationic complex $[Mn(CO)_4(^iPr_2Ph\text{-}DAB)][PF_6]$ undergoes rapid substitution of CO, even by solvent molecules such as CH_3CN and THF. The dissolution of the tetracarbonyl complex in acetonitrile at 288 K results in instantaneous formation of *fac*-$[Mn(CH_3CN)(CO)_3(^iPr_2Ph\text{-}$

DAB)][PF_6] species. The crystal structures of the synthesized complexes are consistent with considerable crowding around the metal center and theoretical calculations using DFT confirm the weakening of the metal−CO interaction is primarily due to the steric bulk of the diimine ligand. These results indicate the possible use of the $^{i}Pr_2$Ph-DAB ligand in the synthesis of reactive metal carbonyl complexes with applications towards CORMs.

Bis(cycloamine) Complexes of Molybdenum Carbonyls

As seen in the prior section, ligand sterics greatly influences the lability of an adjacent CO molecule in manganese carbonyls i.e. increased rate of CO loss is observed from a crowded environment. Below, we introduce bis(cycloamines) and establish their highly sterically demanding nature upon coordination to molybdenum carbonyls through X-ray diffraction analysis.[158] Molybdenum carbonyls are poorer CORMs due to higher electron density than Mn(I) or Re(I) metal centers and as a result bind COs more strongly. Nevertheless, the goal of this study was to ascertain the coordination environment of bis(cycloamines) and molybdenum carbonyls were suitable model complexes.

Introduction. Methylene bridged cyclic amines (Figure 78) are used as heterocyclic building blocks through amino methylations in organic synthesis.[166-171] They can also be employed as organocatalysts in aldol condensations and transesterifications.[172-174] Their use in coordination chemistry as chelating ligands, however, has been largely unexplored. The earliest reported metal complexes, characterized only by infrared spectroscopy, were [CH_2(pyr)$_2$]Mo(CO)$_4$, **1** and

$[CH_2(pip)_2]Mo(CO)_4$, **2** published in a brief communication by Lüttringhaus and Kullick in 1959.[175] Jung et al. have used $CH_2(pip)_2$ as a coligand in the preparation of a benzoquinonatocobalt complex back in 2001.[176] And finally, in a recent 2014 article, Szymańska-Buzar et al. published a crystal structure of the $[CH_2(pip)_2]W(CO)_4$ complex, synthesized photochemically using $W(CO)_6$, thereby establishing the coordinating nature of $CH_2(pip)_2$.[177]

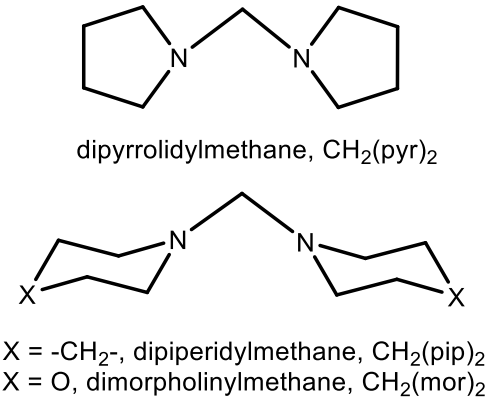

Figure 78 Common methylene bridged cyclic amines.

Preparing these methylene bis(cycloamines) is typically done by refluxing the mono secondary amines with paraformaldehyde in a high-boiling solvent.[166,170,174] Another method involves the transamination with *N,N,N',N'*-tetramethyldiaminomethane using $Sm(NO_3)_2$ or CuCl catalysts.[167] The use of fulvenes as a methylene source has also been noted.[178] In their 2014 work, the authors noticed the formation of dipiperidylmethane from piperidine at room temperature in the presence of the bispiperidine complex, *cis*-$(pip)_2W(CO)_4$ with dichloromethane as solvent.[177] As the authors were involved in studying the catalytic properties of molybdenum and tungsten carbonyls for various

chemical transformations, they had prematurely concluded that the *cis*-$(pip)_2W(CO)_4$ complex acts as the catalyst for this conversion. In reality, the transformation of piperidine to dipiperidylmethane with dichloromethane proceeds on its own (Scheme 23).

Herein, we wish to 1) summarize our efforts in elucidating the reaction conditions involved in preparing dipyrrolidyl- and dipiperidyl- methanes directly from dichloromethane and 2) present the syntheses, structures and complete characterizations of Lüttringhaus and Kullick's molybdenum complexes with said amines as ligands and the varying steric effects they exhibit around the metal center.

Results and Discussion. Our initial interest was driven to understand the role of *cis*-$(pip)_2W(CO)_4$ complex as a catalyst in producing $CH_2(pip)_2$ from piperidine.[177] Upon running a series of experiments (Table 22), it soon became apparent that the metal does not play a role in this chemistry. In fact, both $CH_2(pyr)_2$ and $CH_2(pip)_2$ can be easily prepared by stirring pyrrolidine or piperidine, respectively in dichloromethane at room temperature in the absence of light in good yields, as shown in Scheme 23. The starting amines themselves can double up as a base driving the reaction forward to give methylene bis(cycloamines) along with two equivalents of the respective ammonium chloride salt. In an earlier work, Matsumoto et al. have shown this to occur for various secondary cyclic amines, albeit under high pressures, which is clearly not required.[179] Their use of pressure may stem from alkylated amine byproducts observed in other high pressure organic reactions carried out in dichloromethane. The pressure could accelerate the reaction rate for tertiary amines to produce a chloromethylammonium salt, but it is not required for the

reaction to take place.[180,181] Mills et al. followed up with a detailed NMR study in 1987 showing the reaction of pyrrolidine with dichloromethane to proceed under ambient conditions.[182] They present evidence to the formation of 1-methylenepyrrolidinium chloride after the condensation of the first amine with dichloromethane followed by its rapid reaction with a second amine to yield dipyrrolidylmethane. The reaction of piperidine with various halomethanes have also been described as early as 1964.[183] Rapid formation of dipiperidylmethane is seen to occur with a benzene solution of dibromomethane. More recent examples of alkyl and aromatic amine reactivities without the need of a catalyst or pressing conditions with dichloromethane can also be found in literature.[184,185]

Scheme 23

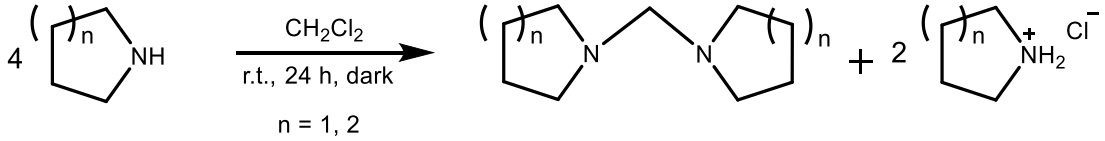

An interesting observation from our test runs was the effect of ambient light on this reaction. While we do not have a complete understanding of its role, what can be said of a reaction under light is its unpredictability, yielding the piperidinium chloride salt as the sole product half the time (Table 22). Thus, all large scale syntheses were carried out in aluminum foil covered flasks. The methylene bis(cycloamines) were spectroscopically pure after removal of salt and excess dichloromethane and can be used for further reactions without the need for distillation.

Table 22 Conditions investigated for the reaction of piperidine with dichloromethane.

Test	Addition of metal complex (mol%)	Stirring under ambient light *vs* darkness	Observed products
1	5% *cis*-$(pip)_2W(CO)_4$	light	only salt
2	5% *cis*-$(pip)_2W(CO)_4$	dark	ligand + salt
3	1% *cis*-$(pip)_2W(CO)_4$	light	ligand + salt
4	1% *cis*-$(pip)_2W(CO)_4$	dark	ligand + salt
5	1% $W(CO)_6$	dark	ligand + salt
6	1% *cis*-$(pip)_2Mo(CO)_4$	light	ligand + salt
7	1% *cis*-$(pip)_2Mo(CO)_4$	dark	ligand + salt
8	-	light	only salt
9	-	dark	ligand + salt
10	-	dark	ligand + salt

Test reactions: 0.25mL piperidine in 20mL CH_2Cl_2 with or without metal addition in an open or Al foil covered vial. Stirred 24 h, excess CH_2Cl_2 removed and product composition determined *via* ^1H NMR on crude mixture.

The chelation of $CH_2(pyr)_2$ and $CH_2(pip)_2$ to molybdenum carbonyls can be achieved either in a refluxing hexane solution for a couple days or in heptane over a few hours yielding the products as yellow solids in moderate yields (Scheme 24). Complex **2**, $[CH_2(pip)_2]Mo(CO)_4$, containing dipiperidylmethane, is air-stable and can be stored in contact with air for long periods of time unlike its well-known bispiperidine analogue, *cis*-$(pip)_2Mo(CO)_4$, **3** which decomposes in the absence of inert atmosphere within a few days. It also exhibits somewhat better solubility than **3** being fully soluble in DMSO, partially soluble in CH_2Cl_2 and THF and minimally soluble in acetone, MeOH and Et_2O. Complex **1**, $[CH_2(pyr)_2]Mo(CO)_4$ has similar if not a slightly poorer solubility in the same solvents and is not air-stable unlike **2**. While some exposure to air is tolerable, storage for longer than a day needs to be under an inert atmosphere.

Scheme 24

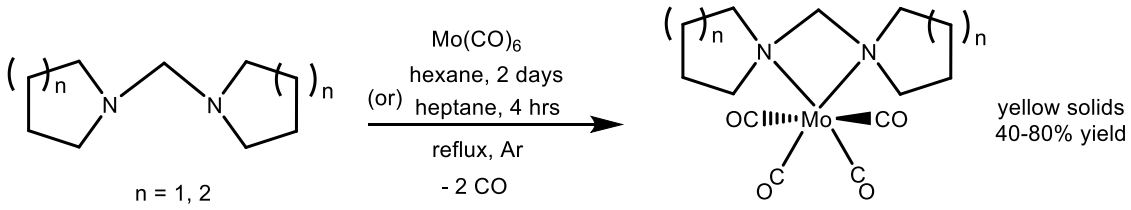

^{1}H NMR spectroscopy shows distinct changes in the chemical shifts of the free ligands versus the coordinated complexes. The bridging methylene protons experience a downfield shift of 1.2 ppm when bound to molybdenum (δ 3.21 → 4.42 ppm, C*H*$_2$(pyr)$_2$; δ 2.86 → 4.09 ppm, C*H*$_2$(pip)$_2$). The methylene protons on the rings become diastereotopic with their signals splitting into pairs upon coordination. Hence, two pairs of multiplets for $CH_2(pyr)_2$ and three pairs of multiplets for $CH_2(pip)_2$ are observed for their complexes. This effect was also noted for the $[CH_2(pip)_2]W(CO)_4$ complex.[177] In the $^{13}C\{^1H\}$ NMR spectra, the bridging methylene carbons have a discrete signal between 80 - 90 ppm for all species. Furthermore, two downfield signals at 206 & 222 ppm representing the axial (*cis* to N) and equatorial (*trans* to N) carbonyl carbons on the molybdenum can be observed for the complexes. Infrared data reveal similar carbonyl stretching frequencies for complexes **1** and **2** indicating the electron donating capability to be nearly identical for both ligands (Figure 79).

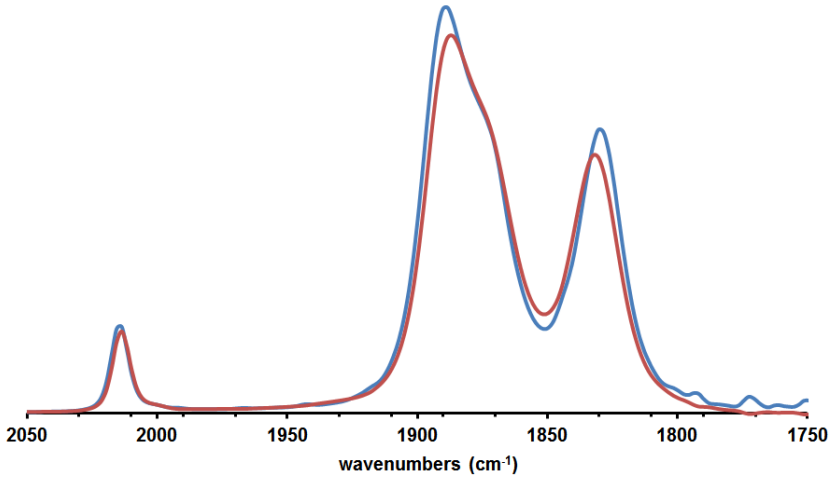

Figure 79 Infrared spectra of $[CH_2(pyr)_2]Mo(CO)_4$, **1** (red) and $[CH_2(pip)_2]Mo(CO)_4$, **2** (blue) complexes in dichloromethane.

Single crystals for X-ray diffraction studies were obtained *via* slow evaporation of an Et_2O and CH_2Cl_2 solutions for complexes **1** and **2**, respectively. Thermal ellipsoid plots and relevant bond distances are shown in Figure 80. Comparison of **2,** $[CH_2(pip)_2]Mo(CO)_4$ with the previously determined structure of **3**,[186] *cis*-$(pip)_2Mo(CO)_4$ shows the $CH_2(pip)_2$ ligand to have a larger steric impact on the surrounding carbonyls leading to a distorted octahedral geometry (Figure 81). With the amines tied back by the methylene group, a small bite angle of 62.55(14)° is observed and the six-membered rings adopt a conformation that points towards the metal center, compressing the equatorial carbonyls and giving a C(2)-Mo(1)-C(2)' angle of 86.0(2)°. The average distance calculated between the equatorial carbonyl carbons and the closest ligand hydrogens is only 2.82 Å. This distance is a bit longer, 2.90 Å, and hence a lesser compression of the equatorial carbonyls, 88.76(13)°, is noted for the tungsten analogue.[177] The angle between

the axial carbonyls of **2** is also compressed, with C(1)-Mo(1)-C(4) measuring 166.9(2)°, about 5° less than what is seen for complex **3**.

The structure of **1** reveals the $CH_2(pyr)_2$ ligand to have a slightly smaller bite angle than $CH_2(pip)_2$ measuring at 61.25(8)°. The five-membered ring size of the pyrrolidyl groups exerts less influence sterically on the equatorial carbonyl carbons with the average distance separating them from the closest ligand hydrogens now at 3.16 Å. Thus, the angle between the equatorial carbonyls is closer to 90° with C(2)-Mo(1)-C(3) measuring 89.28(12)°. The influence on the axial carbonyls, however, remain similar to $CH_2(pip)_2$ with C(1)-Mo(1)-C(4) measuring 166.53(10)°. Co^{II}, Ni^{II} and Zn^{II} complexes bearing the tetradentate N_2O_2 ligand $CH_2(pyr\text{-}2\text{-}COO)_2$, where each pyrrolidyl ring is substituted with a carboxylate group in the 2-position, are the only other structural examples with a *N,N'*-methylene bridged bis(cycloamine)-type ligand.[187,188] The N-M-N angles measure 65.5(1)° (Co^{II}), 67.5(2)° (Ni^{II}) and 63.5(3)° (Zn^{II}), displaying again the severe bite angles imposed by these constrained chelates. Diamines with two carbons separating the nitrogen atoms show a much larger bite angle. The N-Mo-N angle for the less electron-releasing 1,10-phenanthroline ligand in the air-stable complex, $(phen)Mo(CO)_4$, is seen to be 73.62(7)°, while the more electron-donating *N,N,N',N'*-tetramethylethylenediamine ligand reveals a bite angle of 77.98(9)° for its air-stable complex, $(TMEDA)Mo(CO)_4$.[189-192] Moving down the periodic group, methylene bridged phosphines display bite angles towards the higher end of the observed range for methylene bridged amines and larger. For example, dicyclohexylphosphinomethane shows 67.397(17)° and 75.70(2)° for $(dcpm)Mo(CO)_4$ and $(dcpm)NiCl_2$ complexes, respectively.[193,194]

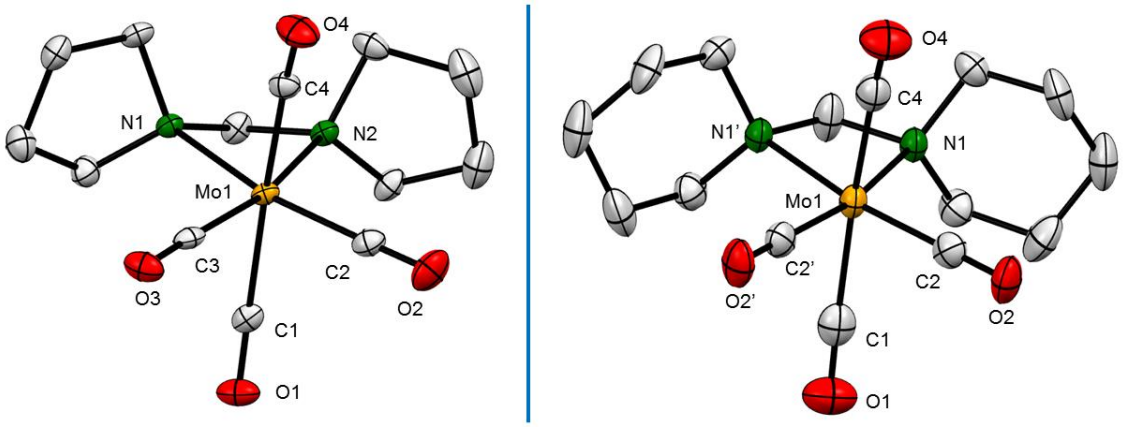

Figure 80 Structures of $[CH_2(pyr)_2]Mo(CO)_4$, **1** (left) and $[CH_2(pip)_2]Mo(CO)_4$, **2** (right). Thermal ellipsoids, probability level 50%, with select atom labeling. Hydrogen atoms omitted for clarity. Select bond distances (Å) - Complex **1**: N-Mo_{ave} = 2.326(2); axial C-O_{ave} = 1.147(3); equatorial C-O_{ave} = 1.166(3). Complex **2**: N-Mo_{ave} = 2.338(3); axial C-O_{ave} = 1.123(7); equatorial C-O_{ave} = 1.157(4).

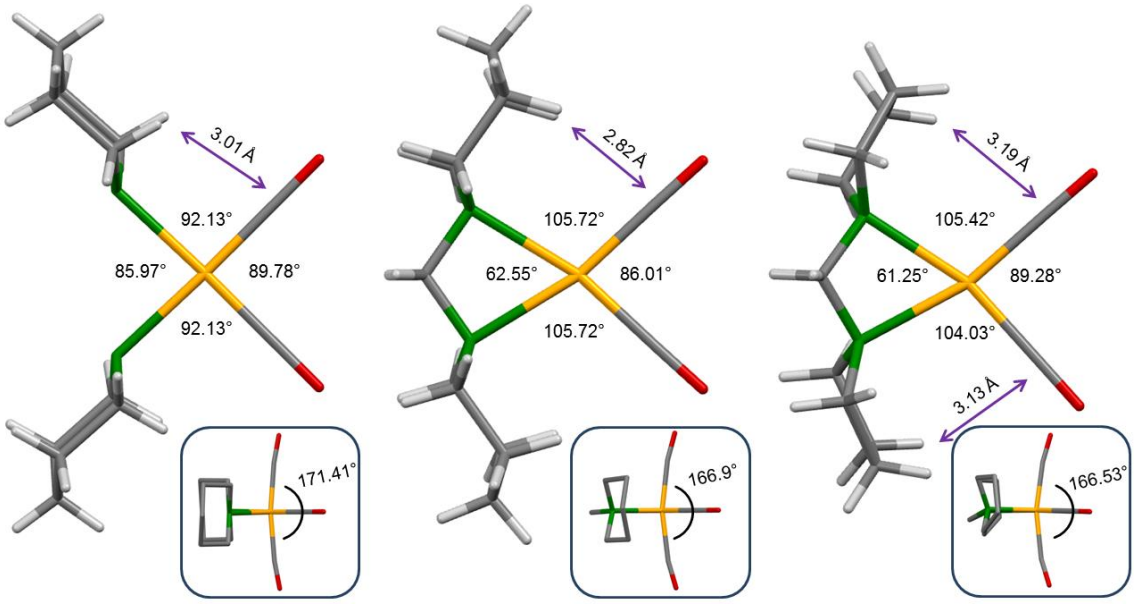

Figure 81 View down the axial carbonyls of *cis*-$(pip)_2Mo(CO)_4$,[21] **3** (left), $[CH_2(pip)_2]Mo(CO)_4$, **2** (center) and $[CH_2(pyr)_2]Mo(CO)_4$, **1** (right). Capped stick representations with angles around the molybdenum center. Average distance to the closest ligand hydrogens from the equatorial carbonyl carbon is shown by arrow. Inset figures display the angle facing away from ligand and between the axial carbonyls.

Conclusions. The search for new ligands, especially those that offer a modular approach to their synthesis, are of constant interest to the inorganic community. We have demonstrated here that a sterically demanding diamine ligand can be prepared by the simple condensation of piperidine with dichloromethane. The coordination environment of the $[CH_2(pip)_2]Mo(CO)_4$ complex is starkly different to its untied *cis*-$(pip)_2Mo(CO)_4$ analogue as a result of the dipiperidylmethane rings now directed around the metal center as seen *via* single-crystal X-ray diffraction studies. The steric effect has less influence on neighboring ligands when the ring size is reduced by one carbon as with the dipyrrolidylmethane complex, $[CH_2(pyr)_2]Mo(CO)_4$. This ligand synthesis can be extended to less basic cyclic amines such as morpholine,[195] while on the other hand, employing substituted piperidines (ex: 3,5-dimethylpiperidine) could introduce even more bulk around the metal center. Sterically encumbering ligands are used in various transition metal chemistry and the surprisingly bulky nature of these methylene bis(cycloamines) with its extreme bite angles could prove useful as a new ligand toolset.

Experimental Section. Piperidine and pyrrolidine were purchased from Alfa Aesar and used as received. $Mo(CO)_6$ was obtained from Strem and GC grade heptane was purchased from EMD chemicals. Dichloromethane and hexane were purified by an MBraun Manual Solvent Purification System packed with Alcoa F200 activated alumina desiccant. NMR spectra were recorded on either a Varian INOVA 300 or 500 MHz spectrometer. ^1H and ^{13}C NMR spectra were referenced to residual solvent resonances.

Infrared spectra were obtained on a Bruker Tensor 27 FTIR spectrometer. Elemental Analyses were determined by Atlantic Microlab (Norcross, GA).

Synthesis of dipiperidylmethane, $CH_2(pip)_2$

Piperidine (10 mL, 8.62 g, 0.101 mol) and CH_2Cl_2 (20 mL) were stirred together in an aluminum foil covered vial. After 24 h, the solution was filtered to remove the white piperidinium chloride salt and the filtrate rotovaped to remove excess CH_2Cl_2. The resulting cloudy oil was treated with THF followed by filtration to precipitate and remove any additional salt. Removal of THF yields a pale yellow liquid product (4.21 g, 91%). Distillation was not required for further experiments. The NMR spectrum is clean and matches that previously reported[177]: ^{1}H ($CDCl_3$) δ 1.43 (m, 4H), 1.55 (m, 8H), 2.42 (m, 8H), 2.86 (s, 2H, NC*H*$_2$N).

Synthesis of dipyrrolidylmethane, $CH_2(pyr)_2$

A similar procedure to $CH_2(pip)_2$ was followed to give $CH_2(pyr)_2$ in greater than 70% yield. When crashing out pyrrolidinium chloride salt, Et_2O is used instead of THF. This salt is very hygroscopic and tends to dissolve in THF. Pure by NMR[182]: ^{1}H ($CDCl_3$) δ 1.76 (m, 8H), 2.57 (m, 8H), 3.20 (s, 2H, NC*H*$_2$N).

Synthesis of $[CH_2(pip)_2]Mo(CO)_4$

$Mo(CO)_6$ (0.200 g, 0.757 mmol) and $CH_2(pip)_2$ (0.150 g, 0.823 mmol) were brought to reflux under an argon atmosphere in heptane (20 mL). After 2 h, a bright yellow product was filtered and washed with hexanes (0.122 g, 41%). IR data in CH_2Cl_2 (ν_{CO}): 1830 (m), 1870 (sh), 1890 (s), 2015 (w). ^{1}H NMR ($CDCl_3$): δ 1.17 (m, 2H), 1.71 (m, 4H), 1.77 (m, 2H), 2.00 (m, 4H), 2.55 (m, 4H), 3.20 (m, 4H), 4.09 (s, 2H, NC*H*$_2$N). ^{13}C{^{1}H}

NMR (d_6-DMSO): δ 22.1, 24.9, 63.7, 89.1 (N*C*H_2N), 206 (*C*O), 222 (*C*O). Anal. Calcd. for $C_{15}H_{22}MoN_2O_4$: C, 46.16; H, 5.68; N, 7.18. Found: C, 45.86; H, 5.60; N, 7.06%.

Synthesis of $[CH_2(pyr)_2]Mo(CO)_4$

$Mo(CO)_6$ (0.157 g, 0.594 mmol) and $CH_2(pyr)_2$ (0.106 g, 0.687 mmol) were brought to reflux under an argon atmosphere in hexane (30 mL). After 3 days, a bright yellow product was filtered and washed with hexanes (0.166 g, 77%). IR data in CH_2Cl_2 (ν_{CO}): 1832 (m), 1870 (sh), 1887 (s), 2014 (w). ^{1}H NMR ($CDCl_3$): δ 1.87 (m, 4H), 2.13 (m, 4H), 2.77 (m, 4H), 3.45 (m, 4H), 4.42 (s, 2H, NCH_2N). $^{13}C\{^1H\}$ NMR (d_6-DMSO): δ 22.5, 63.5, 82.7 (N*C*H_2N), 206 (*C*O), 223 (*C*O). Anal. Calcd. for $C_{13}H_{18}MoN_2O_4$: C, 43.10; H, 5.01; N, 7.73. Found: C, 42.47; H, 5.19; N, 7.61%.

CHAPTER VI

CONCLUSIONS

Ranging from availability to chemical reactivity, carbon monoxide and carbon dioxide are unlike each other in many ways though structurally different by just an oxygen atom. Carbon monoxide is present only in trace amounts on earth, but ironically, it is the second most abundant molecule after dihydrogen in interstellar space. Industrially, CO is a valued commodity and is produced from the partial oxidation of carbonaceous fuel or methane. It is employed in the synthesis of bulk chemicals such as acetic acid and aldehydes to name a few. With an affinity 200 times stronger than oxygen towards red blood cells, CO can cause severe organ damage or death upon prolonged exposure to high concentrations. Interestingly, it was discovered that CO is also produced by enzymes within mammalian cells. At nanomolar concentrations, it functions as a regulatory molecule exhibiting therapeutic properties.

Ongoing efforts focused on developing CO releasing molecules as pharmaceutical drugs are being carried out and metal carbonyls are seen to be good candidates for this purpose. The use of a suitable ligand is vital as it helps labilize a CO from the metal center. Bulky ligands such as *N*,*N'*-bis(2,6-diisopropylphenyl)-1,4-diazabutadiene when coordinated to a manganese tetracarbonyl complex weakens the bond of an adjacent CO ligand. Structurally, the axial carbonyls display significant deviation from linearity with $\angle CO{-}Mn{-}CO \approx 170°$ in the crowded environment. This lends to the release of CO in the presence of a better incoming ligand such as CH_3CN within two hours at a temperature of

288 K as seen spectroscopically. Computations show a bond dissociation energy of 25.3 kcal/mol, about 10 kcal/mol smaller than in the absence of steric congestion. Hemi-labile ligands also facilitate release of CO as is seen with a carboxyaldehyde pyrrolyl bound rhenium tetracarbonyl complex. The weak Re-O bond can break easily allowing a new incoming ligand such as PPh_3 or pyridine to coordinate in its place. As the reaction progresses the aldehyde arm coordinates back on to the rhenium by inducing the release of an adjacent CO through intramolecular interaction. Spectroscopic measurements and computational data estimates the BDE to be as low as 15 kcal/mol for an aldehyde assisted pathway, whereas a regular Re-CO bond dissociation requires around 30 kcal/mol.

There is a rising interest to understand the interplay of gaseotransmitter molecules such as CO and NO in biological systems. An unusual and interesting role of CO is observed in a reaction with a biomimetic dinitrosyl iron complex. The CO induces a reductive elimination of a thiolate species bound to the iron. The surprising feature is the behavior of the CO molecule as the electrophile in this reaction whereby it receives the electron density into its vacant π^* orbitals from the electron rich orbitals of the $Fe(NO)_2$ unit. This theoretical prediction was supported by experimental tests whereby decreasing the nucleophilicity of the $Fe(NO)_2$ unit with electron withdrawing groups drastically reduced the rate of the reaction.

Qualifying as a trace species with less than 1% composition of the earth's atmosphere yet being the fourth most abundant gas, carbon dioxide plays a huge role in the natural carbon cycle and is the major source of carbon in life on earth. It is respired as a waste product by all aerobic organisms and converted to organic materials through

photosynthesis by plants and trees. CO_2 is also released into the atmosphere by burning of fossil fuels, the carbonaceous materials formed by the decay of organic materials exposed to heat and pressure below the earth's surface over millions of years. Since the dawn of the industrial era, anthropogenic emission of CO_2 has elevated its composition from 300 to 400 parts per million upsetting the natural carbon cycle and inducing global warming being a greenhouse gas. It is now widely apparent that strict measures need to be taken to reduce CO_2 emissions and accumulation. The utilization of CO_2 as a C1 precursor in chemical synthesis is seen as a viable solution that can contribute towards this purpose.

Carbon dioxide is a fairly stable and unreactive molecule at room temperature, but with the help of a catalyst and/or higher temperatures it can be transformed into useful chemicals. Currently, CO_2 is employed industrially in the production of select chemicals such as urea which adds value to this waste product, but extensive research needs to be carried out to further expand its utilization. A promising venture is the production of polycarbonates by coupling epoxides with CO_2. While poly(propylene carbonate) and poly(cyclohexene carbonate) are now commercially available through this route, the polymers are only found in niche applications due to their subpar properties when compared to the widely used BPA polycarbonate. To produce CO_2-derived polycarbonates that can compete with BPA PC, larger epoxides with rigid backbones need to be employed. With recent copolymerization studies on CO_2 and 1,4-dihydronaphthalene oxide, high thermal transitions have been realized. It is important to note that bulky ligand frameworks such as in the typical *t*-butyl substituted (salen)Cr^{III} catalysts perform poorly in producing polycarbonate and tend to favor the cyclic carbonate side product. This is seen as a result

of smaller cocatalysts now competing against epoxide binding. The more nucleophilic cocatalyst displace a carboxylated ring-opened monomer to a greater degree which then leads to the formation of cyclic carbonates almost exclusively. When employing the less sterically demanding catalyst such as tetraazaannulene bound Cr^{III} species, there is now more room for the bulker epoxides to be ring-opened and chain-propagate. Thus, higher polymer selectivity and higher activity in comparison to salen systems are observed. Moving forward in this area then necessitates the evolution of current catalysts to handle larger epoxide monomers.

Another important area of CO_2 utilization is its direct coupling with hydrocarbons to yield carboxylic acids which is still in the fundamental stages of research. CO_2 insertion studies compared on a phosphine ligated Ru species bearing both H and Me groups show the carboxylate formation to be thermodynamically more stable than formate formation. This bodes well, as a potential catalytic system needs to selectively insert CO_2 into M-C *vs* M-H bond after a hydrocarbon's oxidative addition across the metal center. Further results also indicate an electron rich environment facilitates faster insertion chemistry.

Ruthenium and iron carbonyl complexes bearing acrylic acid and piperidinium acrylate were synthetically prepared as potential products of CO_2/ethylene coupling. Kinetic studies on the dissociation of these acrylates from the metal center provided an estimate of their bond dissociation energies. It was found that it is easier to remove the acrylates from a ruthenium center by about 5 kcal/mol than from an iron center. Triphos ligated molybdenum and tungsten carbonyls were shown to interact with olefins after photolytically removing a carbonyl and generating a vacant coordination site. Similarly,

ethylene bound ruthenium and iron carbonyls species can also be prepared in the presence of excess ethylene, but no further coupling reaction is observed with CO_2 for either the group 6 or 8 metal carbonyl derivatives. While being excellent infrared tags to follow the progress of a reaction, the carbonyls are also good π-acids that reduce the electron density at the metal center required to activate an olefin towards CO_2 coupling. Also to note is the absence of CO_2 insertion into Ru-H or Ru-Me bonds when an electron withdrawing group, such as chloride, is introduced onto the complex.

In summary, the chemistry of CO and CO_2 are quite different from each other. While the utilization of CO is well-embodied industrially for the production of commodity chemicals, its pharmaceutical application as a therapeutic agent is in the early stages of research. Greater understanding of its biological interactions as well as preparation of suitable CO releasing molecular drugs are of active interest. On the other hand, CO_2 poses a problem with its rising levels in the atmosphere from fossil fuel consumption. Its commercial utilization however has been limited thus far and significant effort needs to be put in to find profitable transformations for the chemical industry. Fundamental studies to understand and develop reactions such as CO_2 and hydrocarbon coupling for carboxylic acid production is one area. Another is the preparation of CO_2-derived polycarbonates that could be employed widely as much of the modern world is made up of plastic.

REFERENCES

1. a) *Carbon Dioxide as Chemical Feedstock*; Aresta, M., Ed.; Wiley: Weinheim, 2010. b) Olivier, J. G. J.; Janssens-Maenhout, G.; Muntean, M.; Peters, J. A. H. W. *Trends in global CO_2 emissions*; The Hauge: PBL Netherlands Environmental Assessment Agency; Ispra: European Commission, Joint Research Centre, 2014. c) Petrenko, V. V.; Martinerie, P.; Novelli, P.; Etheridge, D. M.; Levin, I.; Wang, Z.; Blunier, T.; Chappellaz, J.; Kaiser, J.; Lang, P.; Steele, L. P.; Hammer, S.; Mak J.; Langenfelds, R. L.; Schwander, J.; Severinghaus, J. P.; Witrant, E.; Petron, G.; Battle, M. O.; Forster, G.; Sturges, W. T.; Lamarque, J.-F.; Steffen, K.; White, J. W. C. *Atmos. Chem. Phys.* **2013**, *13*, 7567.
2. National Research Council. *Ocean Acidification: A National Strategy to Meet the Challenges of a Changing Ocean.* Washington DC: The National Academies Press, 2010; p 3.
3. *Carbon Dioxide Capture and Storage*. Metz, B., Davidson, O., Coninck, H., Loos, M., Meyer, L., Eds.; Cambridge University Press: New York, 2005.
4. Several comprehensive reviews cover the copolymerization of epoxides and CO_2. For example, see a) Darensbourg, D. J.; Holtcamp, M. W. *Coord. Chem. Rev.* **1996**, *153*, 155. b) Coates, G. W.; Moore, D. R. *Angew. Chem., Int. Ed.* **2004**, *43*, 6618. c) Sugimoto, H.; Inoue, S. *J. Polym. Sci., Part A: Polym. Chem.* **2004**, *42*, 5561. d) Darensbourg, D. J.; Mackiewicz, R. M.; Phelps, A. L.; Billodeaux, D. R. *Acc. Chem. Res.* **2004**, *37*, 836. e) Chisholm, M. H.; Zhou, Z. *J. Mater. Chem.* **2004**, *14*, 3081.

f) Darensbourg, D. J. *Chem. Rev*. **2007**, *107*, 2388. g) Klaus, S.; Lehenmeier, M. W.; Anderson, C. E.; Rieger, B. *Coord. Chem. Rev*. **2011**, *255*, 1460. h) Kember, M. R.; Buchard, A.; Williams, C. K. *Chem. Commun*. **2011**, *47*, 141. i) Lu, X. B.; Darensbourg, D. J. *Chem. Soc. Rev.* **2012**, *41*, 1462. j) Lu, X.-B.; Ren, W.-M.; Wu, G.-P. *Acc. Chem. Res.* **2012**, *45*, 1721. k) Darensbourg, D. J.; Wilson, S. J. *Green Chem*. **2012**, *14*, 2665. l) Paul, S.; Zhu, Y.; Romain, C.; Brooks, R.; Saini, P. K.; Williams, C. K. *Chem. Commun.* **2015**, *51*, 6459.

5. North, M.; Pasquale, R.; Young, C. *Green Chem*. **2010**, *12*, 1514.
6. a) Inoue, S.; Koinuma, H.; Tsuruta, T. *J. Polym. Sci. B* **1969**, *7*, 287. b) Inoue, S.; Koinuma, H.; Tsuruta, T. *Makromol. Chem.* **1969**, *130*, 210.
7. Liu, L.; Ren, W.-M.; Liu, Y.; Lu, X.-B. *Macromolecules* **2013**, *46*, 1343.
8. a) Noh, E. K.; Na, S. J.; S. S.; Kim, S.-W.; Lee, B. Y. *J. Am. Chem. Soc.* **2007**, *129*, 8082. b) S. S.; Min, J. K.; Seong, J. E.; Na, S. J.; Lee, B. Y. *Angew. Chem. Int. Ed.* **2008**, *47*, 7306.
9. http://www.novomer.com/; http://empowermaterials.com/; http://www.econic-technologies.com/; and http://www.materialscience.bayer.de/Projects-and-Cooperations/CO2-Project. Accessed June 25, 2015.
10. a) Wang, Y.; Fan, J.; Darensbourg, D. J. *Angew. Chem. Int. Ed.* **2015**, *54*, 1. b) Darensbourg, D. J.; Tsai, F.-T. *Macromolecules* **2014**, *47*, 3806. c) Darensbourg, D. J.; Chung, W.-C.; Arp, C. J.; Tsai, F.-T.; Kyran, S. J. *Macromolecules* **2014**, *47*, 7347.

11. Acrylic Acid and Derivatives. *Ullmann's Encyclopedia of Industrial Chemistry* [Online]; Wiley-VCH, Posted October 15, 2011. http://onlinelibrary.wiley.com/doi/10.1002/14356007.a01_161.pub3/abstract (accessed Nov 3, 2012).

12. Broeren, M. Production of Bio-ethylene, 2012. International Energy Agency - Energy Technology Systems Analysis Program Website. http://ieaetsap.org/web/HIGHLIGHTS%20PDF/I13_HL_Bioethylene_Broeren_Mar2012_FINAL9_GSOK.pdf (accessed Nov 3, 2012).

13. a) Hoberg, H.; Schaefer, D. *J. Organomet. Chem.* **1982**, *236*, C28. b) Hoberg, H.; Schaefer, D. *J. Organomet. Chem.* **1983**, *251*, C51.

14. Alvarez, R.; Carmona, E.; Cole-Hamilton, D. J.; Galindo, A.; Gutierrez-Puebla, E.; Monge, A.; Poveda, M. L.; Ruiz, C. *J. Am. Chem. Soc.* **1985**, *107*, 5529.

15. a) Papai, I.; Schubert, G.; Mayer, I.; Besenyei, G.; Aresta, M. *Organometallics* **2004**, *23*, 5252. b) Schubert, G.; Papai, I. *J. Am. Chem. Soc.* **2003**, *125*, 14847.

16. Bernskoetter, W. H.; Tyler, B. T. *Organometallics* **2011**, *30*, 520.

17. Lejkowski M. L.; Lindner R.; Kageyama T.; Bódizs G. É.; Plessow, P. N.; Müller, I. B.; Shäefer. A.; Rominger, F.; Hoffmann. P.; Futter. C.; Schunk, S. A; Limbach, M. *Chem. Eur. J.* **2012**, *18*, 14017.

18. Wolfe, J. M.; Bernskoetter, W. H. *Dalton Trans.* **2012**, *41*, 10763.

19. a) Graham, D. C.; Mitchell, C.; Bruce, M. I.; Metha, G. F.; Bowie, J. H.; Buntine, M. A. *Organometallics* **2007**, *26*, 6784. b) Drees, M.; Cokoja, M.; Kuhn, F. E. *ChemCatChem*, **2012**, *4*, 1703. c) Uhe, A.; Hölscher, M.; Leitner, W. *Chem. Eur. J.* **2012**, *18*, 170.

20. Jessop, P. G.; Hsia, Y.; Ikariya, H.; Noyori, R. *J. Am. Chem. Soc.* **1996**, *118*, 344.

21. Boogaerts, I. I. F.; Nolan, S. P. *J. Am. Chem. Soc.* **2010**, *132*, 8858.

22. Boogaerts, I. I. F.; Fortman, G. C.; Furst, M. R. L.; Cazin, C. S. J.; Nolan, S. P. *Angew. Chem. Int. Ed.* **2010**, *49*, 8674.

23. Carbon Monoxide. *Ullmann's Encyclopedia of Industrial Chemistry* [Online]; Wiley-VCH, Posted Mar 15, 2001. http://onlinelibrary.wiley.com/doi/10.1002/14356007.a05_203/abstract (accessed July 24, 2015).

24. Prockop, L. D.; Chichkova, R. I. *J. Neurol. Sci.* **2007**, *262*, 122.

25. Mann, B. E.; Motterlini, R. *Chem. Commun.* **2007**, 4197.

26. Motterlini, R.; Otterbein, L. E. *Nat. Rev. Drug Discovery* **2010**, *9*, 728.

27. Darensbourg, D. J.; Wilson, S. J. *J. Am. Chem. Soc.* **2011**, *133*, 18610.

28. Darensbourg, D. J.; Wilson, S. J. *Macromolecules* **2013**, *46*, 5929.

29. Liu, Y.; Wang, M.; Ren, W.-M.; He, K.-K.; Xu, Y.-C.; Liu, J.; Lu, X.-B. *Macromolecules* **2014**, *47*, 1269.

30. Darensbourg, D. J.; Yeung, A. D. *Macromolecules* **2013**, *46*, 83.

31. Darensbourg, D. J.; Yarbrough, J. C.; Ortiz, C.; Fang, C. C. *J. Am. Chem. Soc.* **2003**, *125*, 7586.

32. Darensbourg, D. J.; Fang, C. C.; Rodgers, J. L. *Organometallics* **2004**, *23*, 924.

33. Darensbourg, D. J.; Kyran, S. J. *ACS Catal.* **2015**, *5*, 5421.

34. Liu, Y.; Wang, M.; Ren, W.-M.; Xu, Y.-C.; Lu, X.-B. *Angew. Chem. Int. Ed.* **2015**, *54*, 7042.

35. Naphthalene and Hydronaphthalenes. *Ullmann's Encyclopedia of Industrial Chemistry* [Online]; Wiley-VCH, Published March 15, 2003. http://onlinelibrary.wiley.com/doi/10.1002/14356007.a17_001.pub2/abstract. Accessed June 25, 2015.

36. Menzek, A.; Altundaş, A.; Gültekin, D. *J. Chem. Res. (S)*, **2003**, 752.

37. Li, R.; Jansen, D. J.; Datta, A. *Org. Biomol. Chem.* **2009**, *7*, 1921.

38. Darensbourg, D. J.; Mackiewicz, R. M. *J. Am. Chem. Soc.* **2005**, *127*, 14026.

39. Darensbourg, D. J.; Mackiewicz, R. M.; Rodgers, J. L.; Fang, C. C.; Billodeaux, D. R.; Reibenspies, J. H. *Inorg. Chem.* **2004**, *43*, 6024.

40. Shannon, R. D. *Acta Cryst.* **1976**, *A32*, 751.

41. Darensbourg, D. J.; Fitch, S. B. *Inorg. Chem.* **2008**, *47*, 11868.

42. Liu, Y.; Ren, W.-M.; Liu, C.; Fu, S.; Wang, M.; He, K.-K.; Li, R.-R.; Zhang, R.; Lu, X.-B. *Macromolecules* **2014**, *47*, 7775.

43. a) Line, K.; Isupov, M. N.; Littlechild, J. A. *J. Mol. Biol.* **2004**, *338*, 519. b) Connelly, S.; Line, K.; Isupov, M. N.; Littlechild, J. A. *Org. Biomol. Chem.* **2005**, *3*, 3260.

44. Breitmaier, E.; Hanke, R. *Chem. Ber.* **1982**, *115*, 1657.

45. Liu, Y.; Xu, Y.; Jung, S. H.; Chae, J. *Synlett* **2012**, *23*, 2692.

46. Wu, G.-P.; Xu, P.-X.; Lu, X.-B.; Zu, Y.-P.; Wei, S.-H.; Ren, W.-M.; Darensbourg, D. J. *Macromolecules* **2013**, *46*, 2128.

47. Lu, X.-B.; Shi, L.; Wang, Y.-M.; Zhang, R.; Zhang, Y.-J.; Peng, X.-J.; Zhang, Z.-C.; Li, B. *J. Am. Chem. Soc.* **2006**, *128*, 1664.

48. Wu, G.-P.; Wei, S.-H.; Lu, X.-B.; Ren, W.-M.; Darensbourg, D. J. *Macromolecules* **2010**, *43*, 9202.

49. Demadis, K. D.; Meyer, T. J.; White, P. S. *Inorg. Chem.* **1998**, *37*, 3610.

50. Breitmaer, E.; Ullrich, F.-W.; Potthoff, B.; Böhme, R.; Bastian, H. *Synthesis* **1987**, 1.

51. Pawlica, D.; Stojković, M. R.; Sieroń, L.; Piantanida, I.; Eilmes, J. *Tetrahedron* **2006**, *62*, 9156.

52. Darensbourg, D. J.; Kudaroski, R. *Adv. Organomet. Chem.* **1983**, *22*, 129.

53. a) Gibson, D. H. *Chem. Rev.* **1996**, *96*, 2063; b) Gibson, D. H. *Coord. Chem. Rev.* **1999**, *185-186*, 335.

54. Riduan S. N.; Zhang, Y. *Dalton Trans.* **2010**, *39*, 3347.

55. Aresta, M.; Dibenedetto, A. *Dalton Trans.* **2007**, 2975.

56. Louie, J. *Curr. Org. Chem.* **2005**, *9*, 605.

57. Braunstein, P.; Matt, D.; Nobel, D. *Chem. Rev.* **1988**, *88*, 747.

58. Yin, X.; Moss, J. R. *Coord. Chem. Rev.* **1999**, *181*, 27.

59. Leitner, W. *Coord. Chem. Rev.* **1996**, *153*, 257.

60. Jessop, P. G.; Joó, F.; Tai, C.-C. *Coord. Chem. Rev.* **2004**, *248*, 2425.

61. Jessop, P. G.; Ikariya, T.; Nayori, R. *Chem. Rev.* **1995**, *95*, 259.

62. Darensbourg, D. J.; Rokicki, A.; Darensbourg, M. Y. *J. Am. Chem. Soc.* **1981**, *103*, 3223.

63. Darensbourg, D. J.; Rokicki, A. *Organometallics* **1982**, *1*, 1685.

64. Darensbourg, D. J.; Kudaroski, R.; Bauch, C. G.; Pala, M.; Simmons, D.; White, J. N. *J. Am. Chem. Soc.* **1985**, *107*, 7463.

65. Darensbourg, D. J.; Grotsch, G. *J. Am. Chem. Soc.* **1985**, *107*, 7473.

66. Darensbourg, D. J.; Wiegreffe, P. W.; Riordan, C. G. *J. Am. Chem. Soc.* **1990**, *112*, 5759.

67. Darensbourg, D. J.; Wiegreffe, H. P.; Wiegreffe, P. W. *J. Am. Chem. Soc.* **1990**, *112*, 9252.

68. Allen, O. R.; Dalgarno, S. J.; Field, L. D.; Jensen, P.; Willis, A. C. *Organometallics* **2009**, *28*, 2385.

69. Jessop, P. G.; Ikariya, T.; Noyori, R. *Nature* **1994**, *368*, 231.

70. Darensbourg, D. J.; Kyran, S. J.; Yeung, A. D.; Bengali, A. A. *Eur. J. Inorg. Chem.* **2013**, 4024.

71. Lay, E. N.; Taghikhani, V.; Ghotbi, C. *J. Chem. Eng. Data* **2006**, *51*, 2197.

72. Darensbourg, D. J.; Kudaroski, R. *J. Am. Chem. Soc.* **1984**, *106*, 3672.

73. Darensbourg, D. J.; Grotsch, G. *J. Am. Chem. Soc.*, **1985**, *107*, 7473.

74. Cioslowski, J. *J. Am. Chem. Soc.*, **1989**, *111*, 8333.

75. Field, L. D.; Lawrenz, E. T.; Shaw, W. J.; Turner, P. *Inorg. Chem.* **2000**, *39*, 5632.

76. Allen, O. R.; Dalgarno, S. J.; Field, L. D.; Jensen, P.; Turnbull, A. J.; Willis, A. C. *Organometallics* **2008**, *27*, 2092.

77. Field, L. D.; Magill, A. M.; Shearer, T. K.; Dalgarno, S. J.; Turner, P. *Organometallics* **2007**, *26*, 4776.

78. Chatt, J.; Hayter, R. G. *J. Chem. Soc.* **1961**, 2605.

79. CBS-QB3 calculations performed in the gas phase, and with the use of the SMD solvation model, using methanol as the prototypical solvent.

80. a) Darensbourg, D. J.; Ovalles, C. *J. Am. Chem. Soc.* **1984**, *106*, 3750. b) Darensbourg, D. J.; Ovalles, C.; Pela, M. *J. Am. Chem. Soc.* **1983**, *105*, 5937.

81. Thomas, C. A.; Bonilla, R. J.; Huang, Y.; Jessop, P. G. *Can. J. Chem.* **2001**, *79*, 719.

82. a) Alvarez, R.; Carmona, E.; Galindo, A.; Gutierrez, E.; Marin, J. M.; Monge, A.; Poveda, M. L.; Ruiz, C.; Savariault, J. M. *Organometallics* **1989**, *8*, 2430. b) Galindo, A.; Pastor, A.; Perez, P.; Carmona, E. *Organometallics* **1993**, *12*, 4443.

83. a) Lee, S. Y. T.; Cokoja, M.; Drees, M.; Li, Y.; Mink, J.; Herrmann, W. A.; Kuhn, F. E. *ChemSusChem* **2011**, *4*, 1275. b) Bruckmeier, C.; Lehenmeier, M. W.; Reichandt, R.; Vagin, S.; Rieger, B. *Organometallics* **2010**, *29*, 2199.

84. Bomgardner, M. M. *C&E News* **2012**, *90*(35), 8.

85. Burridge, E. *ICIS Chem. Business* **2012**, Oct. 22-28, 36.

86. Li, B.; Kyran, S. J.; Yeung, A. D.; Bengali, A. A.; Darensbourg, D. J. *Inorg. Chem.* **2013**, *52*, 5438.

87. Conder, H. L.; Darensbourg, M. Y. *J. Organomet. Chem.* **1974**, *67*, 93.

88. a) Hug, R.; Poë, A. J.; Chawla, S. *Inorg. Chim. Acta* **1980**, *38*, 121. b) Chen, L.; Poë, A. J. *Inorg. Chem.* **1989**, *28*, 3641.

89. Grevels, F.-W.; Reuvers, J. G. A.; Takats, J. *J. Am. Chem. Soc.* **1981**, *103*, 4069.

90. Kruczynski, L.; LiShingMan, L. K. K.; Takats, J. *J. Am. Chem. Soc.* **1974**, *96*, 4006.

91. Chen, L.; Poë, A. J. *Inorg. Chim. Acta* **1995**, *240*, 399.

92. The *bis* substituted ruthenium product was reported in ref. 91 to be obtained in small, unquantifiable amounts.

93. Smith, G. P.; Laine, R. M. *J. Phys. Chem.*, **1981**, *85*, 1620.

94. Wuu, Y.-M.; Bentsen, J. G.; Brinkley, C. G.; Wrighton, M. S. *Inorg. Chem.* **1987**, *26*, 530.

95. Ferrence, G. M.; Fanwick, P. E.; Kubiak, C. P.; Haines, R. J. *Polyhedron* **1997**, *16*, 1453.

96. As pointed out by a reviewer, the suggestion that a more electron-rich ruthenium center can aim ethylene/CO_2 coupling may be incorrect based on the limited data available in this area.

97. Darensbourg, D. J.; Tappan, J. E. *J. Organomet. Chem.* **1973**, *54*, C39.

98. Desrosiers, M. F.; Wink, D. A.; Trautman, R.; Friedman, A. E.; Ford, P. C. *J. Am. Chem. Soc.* **1986**, *108*, 1917.

99. Weiss, E.; Stark, K.; Lancaster, J. E.; Murdoch, H. D. *Helv. Chim. Acta.* **1963**, *46*, 288.

100. Kyran, S. J.; Muhammad, S.; Knestrick, M.; Bengali, A. A.; Darensbourg, D. J. *Organometallics*, **2012**, *31*, 3163.

101. Chatt, J.; Leigh, G. J.; Thankarajan, N. *J. Organomet. Chem.* **1971**, *29*, 105.

102. Darensbourg, D. J.; Kump, R. L. *Inorg. Chem.* **1978**, *17*, 2680.

103. Fernandez, E. J.; Gimeno, M. C.; Jones, P. G.; Laguna, A.; Laguna, M.; Olmos, E. *J. Chem. Soc., Dalton Trans.* **1996**, 3603.

104. a) Keiter, R. L.; Ye, P.; Keiter, E. A.; Benson, J. W.; Lin, W.; Brandt, D. E.; Southern, J. S.; Rheingold, A. L.; Guzei, I.; Wheeler, K. A.; Cary, L. W. *Inorg. Chim. Acta* **2010**, *364*, 176. b) Darensbourg, D. J.; Wiegreffe, H. P. *Inorg. Chem.* **1990**, *29*, 592. c) Darensbourg, D. J.; Joyce, J. A.; Bischoff, C. J.; Reibenspies, J. H. *Inorg. Chem.* **1991**, *30*, 1137.

105. a) Walter, Q.; Klein, T.; Huttner, G.; Zsolnai, L. *J. Organomet. Chem.* **1993**, *458*, 63. b) Dilsky, S. *J. Organomet. Chem.* **2007**, *692*, 2887.

106. Etter, M. C.; Baures, P. W. *J. Am. Chem. Soc.* **1988**, *110*, 639.

107. Schlappi, D. N.; Cedeño, D. L. *J. Phys. Chem. A* **2009**, *113*, 9692.

108. Miller, M. R.; Megson, I. L. *Br. J. Pharmacol.* **2007**, *151*, 305.

109. Toledo, J. C.; Augusto, O. *Chem. Res. Toxicol.* **2012**, *25*, 975.

110. Wu, L.; Wang, R. *Pharmacol. Rev.* **2005**, *57*, 585.

111. Furchgott, R. F. *Biosci. Rep.* **1999**, *19*, 235.

112. Ignarro, L. J. *Biosci. Rep.* **1999**, *19*, 51.

113. Murad, F. *Biosci. Rep.* **1999**, *19*, 133.

114. Szabo, C. *Sci. Transl. Med.* **2010**, *2*, 54.

115. Kajimura, M.; Fukuda, R.; Bateman, R. M.; Yamamoto T.; Suematsu, M. *Antioxid. Redox Signaling* **2010**, *13*, 157.

116. Vanin, A. F. *Nitric Oxide-Biol. Ch.* **2009**, *21*, 1.

117. Hickok, J. R.; Sahni, S.; Shen, H.; Arvind, A.; Antoniou, C.; Fung L. W. M.; Thomas, D. D. *Free Radical Bio. Med.* **2011**, *51*, 1558.

118. Vanin, A. F.; Chazov, E. I. *Biofizika* **2011**, *56*, 304.

119. Crabtree, R. H. *The Organometallic Chemistry of the Transition Metals*; Wiley, New York, 5th Edn., 2009, Ch. 4, pp. 88.

120. Stamler, J. S.; Singel D. J.; Loscalzo, J. *Science* **1992**, *258*, 1898.

121. Thomas, D. D.; Liu, X.; Kantrow S. P.; Lancaster, J. R. Jr. *Proc. Natl. Acad. Sci. U. S. A.* **2001**, *98*, 355.

122. Lewandowska, H.; Kalinowska, M.; Brzoska, K.; Wojciuk, K.; Wojciuk G.; Kruszewski, M. *Dalton Trans.* **2011**, *40*, 8273.

123. Butler, A. R.; Megson, I. L. *Chem. Rev.* **2002**, *102*, 1155.

124. Toledo, J. C.; Bosworth, C. A.; Hennon, S. W.; Mahtani, H. A.; Bergonia, H. A.; Lancaster, J. R. *J. Biol. Chem.* **2008**, *283*, 28926.

125. D'Autreaux, B.; Horner, O.; Oddou, J. L.; Jeandey, C.; Gambarelli, S.; Berthomieu, C.; Latour J. M.; Michaud-Soret, I. *J. Am. Chem. Soc.* **2004**, *126*, 6005.

126. Foster, H. W.; Cowan, J. A. *J. Am. Chem. Soc.* **1999**, *121*, 4093.

127. Kennedy, M. C.; Antholine W. E.; Beinert, H. *J. Biol. Chem.* **1997**, *272*, 20340.

128. Lee, M. H.; Arosio, P.; Cozzi A.; Chasteen, N. D. *Biochemistry* **1994**, *33*, 3679.

129. Mulsch, A.; Mordvintcev, P.; Vanin A. F.; Busse, R. *FEBS Lett.* **1991**, *294*, 252.

130. Tran, C. T.; Skodje, K. M.; Kim, E. *Prog. Inorg. Chem.* **2014**, *59*, 339.

131. Enemark J. H.; Feltham, R. D. *Coord. Chem. Rev.* **1974**, *13*, 339.

132. Hess, J. L.; Hsieh, C. H.; Reibenspies J. H.; Darensbourg, M. Y. *Inorg. Chem.* **2011**, *50*, 8541.

133. Huang, H. W.; Tsou, C. C.; Kuo T. S.; Liaw, W. F. *Inorg. Chem.* **2008**, *47*, 2196.

134. Lu, T. T.; Tsou, C. C.; Huang, H. W.; Hsu, I. J.; Chen, J. M.; Kuo, T. S.; Wang Y.; Liaw, W. F. *Inorg. Chem.* **2008**, *47*, 6040.

135. Tonzetich, Z. J.; Do L. H.; Lippard, S. J. *J. Am. Chem. Soc.* **2009**, *131*, 7964.

136. Tsai, F. T., Chiou, S. J.; Tsai, M. C.; Huang, H. W.; Chiang M. H.; Liaw, W. F. *Inorg. Chem.* **2005**, *44*, 5872.

137. Tsai, M. L.; Hsieh C. H.; Liaw, W. F. *Inorg. Chem.* **2007**, *46*, 5110.

138. Atkinson, F. L.; Blackwell, H. E.; Brown, N. C.; Connelly, N. G.; Crossley, J. G.; Orpen, A. G.; Rieger A. L.; Rieger, P. H. *J. Chem. Soc. Dalton* **1996**, 3491.

139. McBride, D. W.; Stafford S. L.; Stone, F. G. A. *Inorg. Chem.* **1962**, *1*, 386.

140. Reginato, N.; McCrory, C. T. C.; Pervitsky D.; Li, L. J. *J. Am. Chem. Soc.* **1999**, *121*, 10217.

141. Jordan, R. B. *Reaction Mechanisms of Inorganic and Organometallic Systems*; Oxford University Press, Oxford, 3rd Edn., 2007, Ch. 5, pp 150.

142. Pulukkody, R.; Kyran, S. J.; Bethel, R. D.; Hsieh, C. H.; Hall, M. B.; Darensbourg, D. J.; Darensbourg, M. Y. *J. Am. Chem. Soc.* **2013**, *135*, 8423.

143. Pulukkody, R.; Kyran, S. J.; Drummond, M. J.; Hsieh, C. H.; Hall, M. B.; Darensbourg, D. J.; Darensbourg, M. Y. *Chem. Sci.* **2014**, *5*, 3795.

144. Rauchfuss, T. B.; Weatherill, T. D. *Inorg. Chem.* **1982**, *21*, 827.

145. Hsieh, C.-H.; Darensbourg, M. Y. *J. Am. Chem. Soc.* **2010**, *132*, 14118.

146. Field, L. R.; Wilhelm, E.; Battino, R. *J. Chem. Thermodyn.* **1974**, *6*, 237.

147. Park, J.; Yi, X.; Gasem, K. A. M.; Robinson, R. L., Jr. *J. Chem. Eng. Data* **1995**, *40*, 245.

148. a) Herrmann, W. A.; Cornils, B. *Applied Homogeneous Catalysis with Organometallic Compounds*; Wiley-VCH: Berlin, 2002. b) Masters, C. *Homogeneous Transition-Metal Catalysis*; Chapman Hall: London, 1981. c) Parshall, G. W.; Ittel, S. D. *Homogeneous Catalysis – The Application and Chemistry of Catalysis by Soluble Transition-Metal Complexes*; John Wiley and Sons: New York, 1980. d) Cornils, B.; Herrmann, W. A. *J. Cat*. **2003**, *216*, 23.

149. a) Johnson, T. R.; Mann, B. E.; Clark, J. E.; Foresti, R.; Green, C. J.; Motterlini, R. *Angew. Chem. Int. Ed.* **2003**, *43*, 3722. b) Jaouen, G. *Bioorganometallics. Biomolecules, Labelling, Medicine*; Wiley-VCH: Weinheim, Germany, 2005.

150. a) Ferber, B.; Tos, S.; Vessières, A.; Welter, R.; Jaouen, G. *Organometallics* **2006**, *25*, 5730. b) Le Bideau, F.; Salmain, M.; Top, S.; Jaouen, G. *Chem. Eur. J*. **2001**, *7*, 2289.

151. a) Jaouen, G.; Vessières, A.; Butler, I. S. *Acc. Chem. Res*. **1993**, *26*, 361. b) Jaouen, G.; Top, S.; Vessières, A.; Alberto, R. *J. Organomet. Chem*. **2000**, *600*, 23. c) Salmain, M.; Vessières, A.; Brossier, P.; Butler, I. S.; Jaouen, G. *J. Immunol. Methods* **1992**, *148*, 65.

152. a) Schmidt, K.; Jung, M. Keilitz, R.; Schnurr, B.; Gust, R. *Inorg. Chim. Acta* **2000**, *306*, 6. b) Jaouen, G.; Top, S.; Vessières, A.; Pigeon, P.; Leclercq, G.; Laios, I. *Chem. Commun*. **2001**, 383.

153. a) Alberto, R.; Motterlini, R. *Dalton Trans*. **2007**, 1651. b) Motterlini, R.; Mann, B. E.; Johnson, T. R.; Clark, J. E.; Foresti, R.; Green, C. *J. Curr. Pharm. Des*., **2003**, *9*, 2525.

154. a) Motterlini, R. Clark, J. E.; Foresti, R.; Sarathchandra, P.; Mann, B. E.; Green, C. J. *Circ. Res*. **2002**, *90*, e17. b) Clark, J. E.; Naughton, P.; Shurey, S.; Green, C. J.; Johnson, T. R.; Mann, B. E.; Foresti, R.; Motterlini, R. *Circ. Res*. **2003**, *93*, e2.

155. a) Smith, H.; Mann, B. E.; Motterlini, R.; Poole, R. K. *IUBMB Life* **2011**, *63*, 363. b) Nobre, L. S.; Al-Sahahrour, F., Dopazo, J.; Saraiva, L. M. *Escherichia coli. Microbiology* **2009**, *155*, 813. c) Nobre, L. S.; Seixas, J. D.; Romao, C. C.; Saraiva, L. M. *Antimicrob. Agents Chemother*. **2007**, *51*, 4303. d) Davidge, K. S.; Sanguimetti, G.; Yee, C. H., Cox, A. G.; McLeod, C.W.; Monk, C. E.; Mann, B. E.; Motterlini, R.; Poole, R. K. *J. Biol. Chem*. **2009**, *284*, 4516.

156. Muhammad, S.; Yempally, V.; Anas, M.; Moncho, S.; Kyran, S. J.; Brothers, E. N.; Darensbourg, D. J.; Bengali, A. A. *Inorg. Chem.* **2012**, *51*, 13041.

157. Yempally, V.; Kyran, S. J.; Raju, R. K.; Fan, W. Y.; Brothers, E. N.; Darensbourg, D. J.; Bengali, A. A. *Inorg. Chem.* **2014**, *53*, 4081.

158. Kyran, S. J.; Sanchez, S. G.; Arp, C. J.; Darensbourg, D. J. *Organometallics*, **2015**, *34*, 3598.

159. Mirebeau, J.-H.; Bideau, F. L.; Marrot, J.; Jaouen, G. *Organometallics* **2008**, *27*, 2911.

160. a) Basolo, F. *J. Organomet. Chem*. **1990**, *383*, 579. b) O'Connor, J. M.; Casey, C.P. *Chem. Rev.* **1987**, *87*, 307. (b) Jordan, R. B. *Reaction Mechanisms of Inorganic and Organometallic Systems*; Oxford: New York, 1998, p. 138. c) Schuster-Woldan, H. G.; Basolo, F. *J. Am. Chem. Soc.* **1966**, *88*, 1657.

161. Son, S. U.; Paik, S.-J.; Lee, I. S.; Lee, Y.-A.; Chung, Y. K.; Seok, W. K.; Lee, H. N. *Organometallics* **1999**, *18*, 4114.

162. a) Scheiring, T.; Kaim, W.; Fielder, J. *J. Organomet. Chem.* **2000**, *598*, 136. b) Carriedo, G. A.; Perez-Martínez, J. A.; Miguel, D.; Riera, V.; García-Granda, S.; Perez-Carreño, E. *J. Organomet. Chem.* **1996**, *511*, 77.

163. a) Blackmore, K. J.; Lal, N.; Ziller, J. W.; Heyduk, A. F. *Eur. J. Inorg. Chem.* **2009**, *2009*, 735. b) Lionetti, D.; Medvecz, A. J.; Ugrinova, V.; Quiroz-Guzman, M.; Noll, B. C.; Brown, S. N. *Inorg. Chem.* **2010**, *49*, 4687. c) Lippert, C. A.; Soper, J. D. *Inorg. Chem.* **2010**, *49*, 3682. d) Heneline, M. R.; Clapp, L. A.; Hardcastle, K. I.; Soper, J. D. *Polyhedron* **2010**, *29*, 164.

164. a) Darensbourg, D. J.; Freolich, J. A. *J. Am. Chem. Soc.* **1977**, *99*, 5940. b) Behrens, H.; Lampe, R. J.; Merbach, P.; Moll, M. *J. Organomet. Chem.* **1978**, *159*, 201. c) Uson, R.; Riera, V.; Gimeno, J.; Laguna, M. *Transition Met. Chem.* **1977**, *2*, 123.

165. Palmer, G. T.; Basolo, F. *J. Am. Chem. Soc.* **1985**, *107*, 3122.

166. Love, B. E. *J. Org. Chem.* **2007**, *72*, 630.

167. Shaibakova, M. G.; Makhmudiyarov, G. A.; Ibragimov, A. G.; Dzhemilev, U. M. *Russ. J. Org. Chem.* **2010**, *46*, 43.

168. Prishchenko, A. A.; Livantsov, M. V.; Novikova, O. P.; Livantsova, L. I.; Petrosyan, V. S. *Heteroat. Chem.* **2010**, *21*, 441.

169. Zhou, Y.; Xie, Y.; Yang, L.; Xie, P.; Huang, H. *Tetrahedron Lett.* **2013**, *54*, 2713.

170. Bondarenko, S. P.; Frasinyuk, M. S. *Chem. Nat. Compd.* **2013**, *49*, 841.

171. Hu, J.; Xie, Y.; Huang, H. *Angew. Chem. Int. Ed.* **2014**, *53*, 7272.

172. Cerro-Alarcón, M.; Corma, A.; Iborra, S.; Martínez, C.; Sabater, M. J. *Appl. Catal., A* **2010**, *382*, 36.

173. Boronat, M.; Climent, M. J.; Corma, A.; Iborra, S.; Montón, R.; Sabater, M. J. *Chem. Eur. J.* **2010**, *16*, 1221.

174. Climent, M. J.; Corma, A.; Domínguez, I.; Iborra, S.; Sabater, M. J.; Sastre, G. *J. Catal.* **2007**, *246*, 136.

175. Lüttringhaus, A.; Kullick, W. *Tetrahedron Lett.* **1959**, *1*, 13.

176. Jung, O.-S.; Lee, Y.-A.; Park, S. H.; Kim, Y. J.; Yoo, K. H.; Kim, D. C. *Bull. Chem. Soc. Jpn.* **2001**, *74*, 305.

177. Kocięcka, P.; Kochel, A.; Szymańska-Buzar, T. *Inorg. Chem. Comm.* **2014**, *45*, 105.

178. Taber, D.; Becker, E. I.; Spoerri, P. E. *J. Am. Chem. Soc.* **1954**, *76*, 776.

179. Matsumoto, K.; Hashimoto, S.; Ikemi, Y.; Otani, S. *Heterocycles* **1984**, *22*, 1417.

180. Nevstad, G. O.; Songstad, J. *Acta Chem. Scand., Ser. B* **1984**, *38*, 469.

181. Mas, M.; Sola, J. *Inorg Chim Acta* **1987**, *133*, 217.

182. Mills, J. E.; Maryanoff, C. A.; McComsey, D. F.; Stanzione, R. C.; Scott, L. *J. Org. Chem.*, **1987**, *52*, 1857.

183. Williams, H. *J. Org. Chem.* **1964**, *29*, 2046.

184. Lee, J.-J.; Stanger, K. J.; Noll, B. C.; Gonzalez, C.; Marquez, M.; Smith, B. D. *J. Am. Chem. Soc.* **2005**, *127*, 4184.

185. Rudine, A. B.; Walter, M. G.; Wamser, C. C. *J. Org. Chem.* **2010**, *75*, 4292.

186. a) Grundy, J.; Coles, M. P.; Hitchcock, P. B. *Dalton Trans.* **2003**, 2573. b) The authors overlooked the N-H protons in the empirical formula and therefore did not locate them in the structure of *cis*-$(pip)_2Mo(CO)_4$.

187. Teo, S.-B.; Ng, C.-H.; Teoh, S.-G.; Wei, C. *J. Coord. Chem.* **1995**, *36*, 141.

188. Teo, S.-B.; Teoh, S.-G.; Ng, C.-H. *Polyhedron*, **1995**, *14*, 1447.

189. Bakar, M. A.; Fun, H.-K.; Chinnakali, K.; Teoh, S.-G.; Shawkataly, O. B.; Lopez, F. M. *Acta Crystallogr*. **1993**, *C49*, 582.

190. Kromer, L.; Coelho, A. C.; Bento, I.; Marques, A. R.; Romão, C. C. *J. Organomet. Chem.* **2014**, *760*, 89.

191. Slot, H. J. B.; Murrall, N. W.; Welch, A. J. *Acta Crystallogr*. **1985**, *C41*, 1309.

192. Ardon, M.; Hogarth, G.; Oscroft, D. T. W. *J. Organomet. Chem.* **2004**, *689*, 2429.

193. Hogarth, G.; Kilmartin, J. *J. Organomet. Chem.* **2007**, *692*, 5655.

194. Schultz, M.; Eisenträger, F.; Regius, C.; Rominger, F.; Hanno-Igels, P.; Jakob, P.; Gruber, I.; Hofmann, P. *Organometallics* **2012**, *31*, 207.

195. a) Preparing dimorpholinylmethane requires reflux in dichloromethane over many days. Adding a base could accelerate the reaction as well as convert all the cyclic amine to the desired ligand (see ref. 182) b) Dimorpholinylmethane (CAS# 5625-90-1) and dipiperidylmethane (CAS# 880-09-1) can be purchased commercially from Alfa Aesar. Last checked on May 01, 2015.